OPTOELECTRONIC MODULATION OF MM-WAVE BEAMS USING A PHOTO-INJECTED SEMICONDUCTOR SUBSTRATE

Tom F. Gallacher

A Thesis Submitted for the Degree of PhD
at the
University of St Andrews

2012

Optoelectronic modulation of mm-wave beams using a photo-injected semiconductor substrate

Tom F. Gallacher

This thesis is submitted in partial fulfilment for the degree of
PhD
at the University of St Andrews

March 2012

Declarations

1. Candidates declarations:

I, Tom F. Gallacher, hereby certify that this thesis, which is approximately 43,000 words in length, has been written by me, that it is the record of work carried out by me and that it has not been submitted in any previous application for a higher degree.

I was admitted as a research student in October, 2008 and as a candidate for the degree of PhD in October, 2009; the higher study for which this is a record was carried out in the University of St Andrews between 2008 and 2012.

9th March 2012	Tom F. Gallacher
Date	signature of candidate

2. Supervisors declaration:

I hereby certify that the candidate has fulfilled the conditions of the Resolution and Regulations appropriate for the degree of PhD in the University of St Andrews and that the candidate is qualified to submit this thesis in application for that degree.

9th March 2012	Dr Graham M. Smith
Date	signature of supervisor

9th March 2012	Dr Duncan A. Robertson
Date	signature of supervisor

3. Permission for electronic publication:

In submitting this thesis to the University of St Andrews I understand that I am giving permission for it to be made available for use in accordance with the regulations of the University Library for the time being in force, subject to any copyright vested in the work not being affected thereby. I also understand that the title and the abstract will be published, and that a copy of the work may be made and supplied to any bona fide library or research worker, that my thesis will be electronically accessible for personal or research use unless exempt by award of an embargo as requested below, and that the library has the right to migrate my thesis into new electronic forms as required to ensure continued access to the thesis. I have obtained any third-party copyright permissions that may be required in order to allow such access and migration, or have requested the appropriate embargo below.

The following is an agreed request by candidate and supervisor regarding the electronic publication of this thesis:
Embargo on both the printed copy and electronic copy for the same fixed period of one year on the following ground: publication would preclude future publication;

9th March 2012	Tom F. Gallacher
Date	signature of candidate
9th March 2012	Dr Graham M. Smith
Date	signature of supervisor
9th March 2012	Dr Duncan A. Robertson
Date	signature of supervisor

Abstract

This thesis discusses optoelectronic devices at mm-wave frequencies, focusing on optoelectronic beamforming and non-mechanical beam steering based on an optically excited Fresnel zone plate plasma. The optically controlled zone plate, termed the photo-injected Fresnel zone plate antenna (piFZPA) within this work, is introduced and a comprehensive theoretical framework developed.

The design and optimisation of Fresnel zone plates are detailed, which determine the inherent performance of the piFZPA. A range of zone plates were designed, fabricated, and characterised at 94 GHz with up to 46 dBi gain, -26 dB sidelobe levels, and 67% aperture efficiency being measured for a quarter-wave design.

The control of (sub) mm-wave beams by optical modulation of the complex permittivity of a semiconductor substrate is discussed. The significance of the free-carrier plasma dynamics, the effective lifetime, surface recombination, and the limits of the substrate which are imposed by the spatial resolution of the free-carrier plasma are highlighted, with the optimisation of these parameters discussed.

The passivation quality of high-resistivity silicon wafers were characterised using a mm-wave photoconductance decay method, which yielded lifetime improvements from $\tau_{\text{eff}} = 60\mu\text{s}$ up to $\tau_{\text{eff}} \approx 4,000\ \mu\text{s}$, resulting in lowered recombination velocities ($S = 15\ \text{cm/s}$). W-band characterisations of the passivated wafers illustrate the significance of surface recombination, with measured attenuations of up to 24 dB.

Novel theoretical models are developed throughout this thesis, which yield insight into the requirements of optoelectronic devices, and are shown to agree well with measured data.

The theoretical framework developed details the requirements, limitations, suitability, and design of piFZPAs at any frequency. A range of transmission-type piFZPAs are demonstrated and characterised at 94 GHz, both on-axis and off-axis, based on a novel architecture, with up to 8% aperture efficiency.

Finally, the hybridisation of the piFZPA technique and well established visible display technologies, which has been developed throughout this thesis, enable low-cost, simple, and highly flexible optoelectronic devices, highlighting this method as an attractive solution to adaptive beamforming and non-mechanical steering at mm-wave and submm-wave frequencies.

Acknowledgements

I would like to thank everyone that has helped my over the last three and a half years. In particular, I would like to thank:

Professor John Allen for initial semiconductor discussions.

(Dr) Robert Middleton for all the help, advice, and various discussions which were most helpful; and for all the laughs - I was sad to see you leave!

Dr Cameron Rae for kindly providing the laser facilities which were used to monitor and characterise the lifetimes of passivated wafers. Thank you for letting me clutter your lab!

Dr Arve Holt of IFE, Norway, for inviting me over and letting me see first hand the passivation process, and for letting me give a talk to your group. The results in chapter 4, 5, and 6 would not have been possible if it was not for this kind gesture.

Dr Rune Søndenå for looking after me at IFE, and for passivating the wafers. Thank you for your time, and for very interesting discussions

Dr Dave Stothard and Dave Walsh for loaning me various optics and equipment, and for not chasing me when I didn't give them back! I also want to thank you both for imparting some of your optical wisdom!

Dr Dav Macfarlane for giving me a quick tutorial on the SAFIRE software, and for kindly dismantling your baby; this made the integration of the piFZPA to SAFIRE much quicker than would have been the case if it were just me!

My supervisor, Dr Graham Smith, for putting up with my quirks, for listening to my crazy ideas, and for finding money to buy the lovely projector used throughout this work.

My second supervisor, Dr Duncan Robertson, for proof reading this thesis, your feedback has been most useful.

Dr Dave Bolton for giving me sound advice when times were tough, and for reading the 1st full draft of this thesis - your comments have been most helpful.

Stevie Balfour and Paul Cruickshank for listening to my rants when things didn't work. Stevie thanks for sound mechanical advice which significantly improved my initial designs! I would also like to thank Dr Rob Hunter for producing all the CAD drawings for me.

Dr Chris Hooley for many interesting discussions and help.

And to all of the mm-wave & EPR group for making my time here enjoyable.

Lastly, but by no means least, I would like to thank my beautiful fiancee who has endured my craziness over the last 8 years, and for some reason has not ran a mile! I would not be the person I am today if it were not for your support.

Tom F. Gallacher
March, 2012.

Publications

The following publications and funding have resulted from the work presented within this thesis:

- Gallacher, T. F. *et. al.*, "**Millimetre wave beam steering utilising a photo-injected Fresnel zone plate antenna**", presented at the *International joint conference of the 6th ESA workshop on Millimetre-wave technology and applications and the 4th Global Symposium on Millimetre Waves*, Espoo, Finland, 23rd - 25th May, 2011.

- Gallacher, T. F. *et. al.*, "**Optical modulation of millimetre-wave beams using a semiconductor substrate**", *IEEE Transactions on Microwave Theory and Techniques*, 2012, (In press).

- Gallacher, T. F. *et. al.*, "**Millimeter-wave beam forming and dynamic steering using an optically controlled photo-injected Fresnel zone plate antenna at 94GHz**", to be presented at *SPIE, Defense, Security, and Sensing*, Baltimore, April 2012.

- Gallacher, T. F. *et. al.*, "**Sub-mm wave adaptive beam forming using a photo-injected semiconductor substrate**", to be presented at the *European Microwave week*, Amsterdam, October 2012, as an *invited talk* within the special session on Sub-mm wave beam forming.

- "**Millimetre wave steerable antenna technology demonstrator**", funded by EPSRC UK, Strategic Partners Project, April - June 2012.

Glossary of terms

The following notation is upheld throughout this thesis: boldfaced *hats* ($\hat{\mathbf{a}}$) denote a unit vector; *tilde* ($\tilde{a}$) denote a complex quantity; while *bold* font and/or a overhead arrow ($\mathbf{a}$, $\vec{a}$) denote a vector quantity.

This thesis will also adopt the 'engineering' convention for representing complex quantities as this aligns with relevant texts; thus, the negative sign convention is used, i.e.

$$\tilde{\epsilon}_r = \epsilon_r' - j\epsilon_r''.$$

Terms:

$n,\ N$	zone number, total number of zones
r_n	radii of the nth zone (m)
d_1, d_2	input and output focal lengths of a zone plate lens (m)
F	focal length (m)
λ	free-space wavelength (m)
P	phase-correction constant ($P = 2, 4, 6, \ldots$)
D	zone plate aperture size (m), or semiconductor diffusion coefficient (cm^2/s)
F/D	F-number of a zone plate design
ω_0	centre design (angular) frequency of a zone plate (rad/s), or the beam waist of a Gaussian beam (m)
w	groove depth of a grooved Wood zone plate (m)

t_L	total thickness of a grooved Wood zone plate: $t_L = t_{\mathrm{base}} + w$ (m)
t_{base}	base thickness of the grooved Wood zone plate (m)
ρ, ψ, ξ	spherical coordinates of the feed frame of reference
r, θ, φ	spherical coordinates of the observation point
$G_f(\psi, m)$	feed function
$C_f(r)$	amplitude constant
$L(\psi)$	amplitude divergence factor
$\vec{\mathbf{P}}_d(\psi, \xi)$	feed polarisation vector
k	wavenumber (cm^{-1})
E, M	electric and magnetic fields
$t_{E,M}$	amplitude Fresnel transmission coefficient (oblique incidence) for electric and magnetic polarisations
$r_{E,M}$	amplitude Fresnel reflection coefficient (oblique incidence) for electric and magnetic polarisations
t, r	amplitude Fresnel transmission and reflection coefficients (normal incidence), or amplitude transmission (S_{21}) and reflectivity (S_{11}) through a transmission line
r_0, ϕ_{ref}	zone plate reference radius (m), and reference phase (deg)
$\eta, \eta_i, \eta_s, \eta_p$	aperture efficiency, illumination efficiency, spillover efficiency, and phase efficiency of a zone plate
E_g	semiconductor bandgap energy (eV)
S, S_0, S_d	surface recombination velocity, front (S_0), back (S_d) (cm/s)
d	substrate thickness (m)
α_m	mth root of the continuity transcendental equation
τ_{eff}	effective lifetime (s)
τ_b	bulk lifetime (s)
$\tau_{\mathrm{SRH}}, \tau_{\mathrm{Auger}}, \tau_{\mathrm{rad}}$	characteristic recombination lifetimes: surface defects, Auger, and radiative (s)
U_r, U_g	free-carrier recombination rate, and generation rate (s^{-1})
$\Delta n, \Delta p$	excess free-carrier density of electron and holes (cm^{-3})
n_0, p_0	thermal equilibrium free-carrier density of electrons and holes (cm^{-3})
n_i	intrinsic free-carrier density (cm^{-3})
n, p	free-carrier density for electron and holes (cm^{-3})
I_{opt}	optical irradiance ($\mathrm{mW/cm}^2$)
α_λ	optical absorption coefficient (cm^{-1})
h, c	Planck's constant (Js), and the speed of light in vacuum (m/s)
R	optical reflection coefficient (power)

D_a, τ_a, l_a	ambipolar diffusion coefficient (cm^2/s), effective lifetime (s), and diffusion length (cm)
$\bar{h}(\rho,\xi), h(\rho,\xi)$	Hankel transform and inverse Hanke transform functions
$J_n(x)$	nth order Bessel functions of the first kind of argument x
$\rho, \xi, \eta, \varepsilon, \nu$	3D continuity equation dimensionless quantities
A_1, A_2, A_p	homogeneous and particular coefficients of the 3D continuity equation
N_t	surface defect-state density (cm^{-3})
σ	conductivity ($\mho\mathrm{cm}^{-1}$)
ω	angular frequency (rad/s)
μ_n, μ_p	electron, and hole, mobility ($\mathrm{cm}^2/\mathrm{V}\cdot\mathrm{s}$)
ρ	resistivity ($\Omega\mathrm{cm}$)
$\tilde{\epsilon}_r$	complex relative permittivity (F/m)
$\epsilon_r', \epsilon_r''$	real, and imaginary, parts of the complex permittivity
$\tilde{\mu}_r$	complex relative permeability (H/m)
$\mu_r^{'}, \mu_r^{''}$	real, and imaginary, parts of the complex permeability
$\tan\delta_\varepsilon, \tan\delta_\mu$	permittivity and permeability loss tangents
ω_p	plasma frequency (rad/s)
ϵ_∞'	high frequency ($\omega_p < \omega < h\omega$) relative permittivity
τ_n, τ_p	Drude free-carrier scattering time for electrons and holes (s)
$\tilde{n}$	complex refractive index
η, κ	refractive index, and extinction coefficient
Γ	free-carrier damping frequency (s^{-1})
$\tilde{Z}_L$	complex wave impedance (Ω)
$\tilde{\gamma}$	complex propagation constant
β, α	phase coefficient (rad/m), and (amplitude) attenuation coefficient (Np/m)
$S_{21},\ S_{11}$	transmission, and reflection, S-parameter (dB)
t_g	VNA time-gate specification (s)
R^2	goodness of fit
θ_0, φ_0	scan angle in azimuth and elevation (degs)
ρ_n	radial parameter defining the location on the zone plate aperture (image-space)
ϕ	polar angle defining the angular location on the zone plate aperture (image-space)

Dedicated to my mother,
and in the memory of my late grandmother.

Contents

Creativity is allowing yourself to make mistakes.
Art is knowing which ones to keep.

Scott Adams

chapter 1

Introduction

Millimetre and submillimetre wave applications have continued to grow over the last few decades. In addition to applications such as short-range high data rate communication networks [1], the large bandwidths and compact systems which are achieved at mm-wave and submm-wave frequencies permit high performance, high resolution imagery with good obscurant penetration compared to lower microwave technologies. Due to the current high costs and difficulty of focal plane arrays at these frequencies, applications involving either passive or active imaging all require a steerable or reconfigurable antenna. In addition, the general requirement for rapid beam steering in order to generate real-time imagery, or multi-beam functionality, render mechanical steering mechanisms inadequate and electronic methods are required.

High frame rates, and reconfigurability, span many applications including remote sensing [2,3], automated landing guidance [4–6], brownout mitigation and helicopter collision avoidance [7–12].

Furthermore, recent rises in the threat of terrorism have driven the requirement for high frame-rate imagers, enhancing standard security measures, such as pat-downs or metal detectors, for the use in airports or public places [13–17]. These devices are then aimed at high volume, high through-

put passenger traffic, and must be low-cost, compact, and feature video-rate imagery, whilst also being able to detect concealed threats at reasonable distances.

Example systems include the Agilent technologies 24 GHz reflectarray realtime electronically controlled imager [18], and Pacific Northwest National Laboratory (PNNL) low frequency (< 20 GHz) scanner [19] which combines a switched linear array of transceivers, mechanical scanning in one axis, and digital beamforming for producing high frame rate, diffraction limited images. The portal personnel screener produced by Agilent technologies is an exemplary low frequency system for concealed threat detection, featuring a low profile, light antenna system based on a reconfigurable reflectarray at 24 GHz. The antenna comprises 15,000 electronically controlled patch antennas in a 1 m x 1 m aperture and enables high frame-rates of up to 80 frames per second depending on the resolution and field-of-view, scanning at up to 10 million points per second; high resolution (0.5 cm) imaging of concealed threats can be achieved at 15 frames per second with this device.

Example imagery is shown in Figure 1.1, which demonstrates a personnel wearing an explosive vest (left), and a metallic concealed object located at the centre of the imaged torso (right).

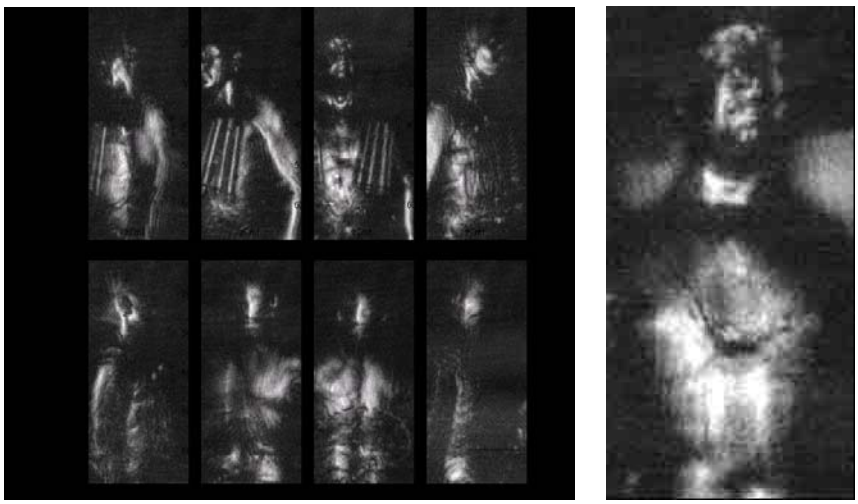

Figure 1.1: Example imagery produced by the Agilent 24 GHz personnel screener. (Reproduced from [18])

However, current antenna technologies at (sub) mm-wave frequencies are restricted by either cost, complexity, reconfigurability, loss, and/or refresh rates, limiting the potential of these applications. Thus alternative techniques and methodologies are required.

1.1 Competing technologies

A large effort has been devoted to finding suitable scanning technologies at (sub) mm-wave frequencies, which has resulted in a vast range of techniques and exotic technologies [8, 20–28]. The following discussion highlights selected methods which have received continued interest over the years, and that have demonstrated promising results.

1. Phased arrays

Phased array antennas have become synonymous with electronic beam steering at microwave frequencies, which feature diverse beam forming capabilities and reduced form factors. However, the requirement for vast numbers of individual components with controllable phase leads to extremely high component numbers, costs and complexity [29–31]. While *passive* architectures offer reduced costs and complexity, *active* designs are required in order to achieve high sensitivity and flexibility. Nonetheless, active designs require individual transmit/receive modules each comprising individual transmitter, low noise and high power amplifiers, circulators and appropriate phase shifters for each radiating antenna element, thus significantly increasing the system cost and complexity.

While monolithic microwave integrated circuits (MMIC) have enabled compact modules for realisation of phased arrays at lower microwave frequencies, current technology at (sub) mm-wave frequencies are prohibitively expensive, lossy, and in the early research stages of development [31]. Furthermore, conventional analogue and digital phase shifters are inherently narrow-band, and thus large arrays or arrays requiring a large instantaneous bandwidth require true time delay (TTD) phase shifters in order to avoid beam degradation and squint [29]. Beam steering then requires control of the length of the TTD

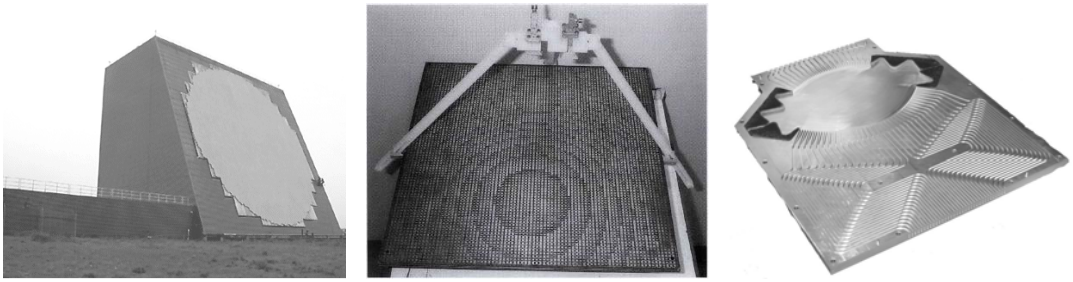

(a) (b) (c)

Figure 1.2: Example reconfigurable antennas: (a) the Dane phased array antenna [35], (b) the Canadian research centre reflectarray antenna [36], and (c) the Army research laboratory Rotman lens [37].

(ideally continuously) such that arbitrary beam scanning can be realised. However, efficient TTD lines are currently immature [32], and thus digitised phase shifters are commonly implemented, which results in degraded performance. The combined high losses and excessive costs of phased arrays has restricted their application to lower microwave frequency applications, commonly implemented at X-band, although integrated device technology (such as CMOS or MMIC) has continued to push phased array architectures into higher mm-wave frequencies [33, 34]. An example phased array antenna operating at 1.5 GHz is shown in Figure 1.2(a).

2. Reflectarrays

Reflectarray antennas represent a hybrid between array antennas and antennas based on geometrical optics, eliminating the need for a complex feed network (c.f. phased arrays), reducing the cost and complexity [38]. The antenna aperture consists of individual passive elements, with controllable phase delay, which re-radiate the incident field from the feed. The controllable phase delay, as above, commonly include PIN or varactor diodes, FET or MEMs switches, liquid crystals, or ferrites [31, 39, 40]. The phase controllers must feature low insertion loss, wide continuous phase control ($0^\circ \rightarrow 360^\circ$), low power consumption, high linearity, and ideally low complexity, with MEMs based switches showing the most promise at mm-wave and submmw-wave frequencies, with limited device lifetimes [31], depending on the fabrication process. Examples of this technology are currently being pursued up to fre-

quencies as high as 650 GHz [41].

While reflectarray technology proves promising for realising rapid beam-steering and adaptive beamforming, vast component numbers (millions of antenna elements and switches) lead to high complexity and costs, thus potentially limiting their suitability for some applications. An example reflectarray antenna operating at 20 GHz and 30 GHz is shown in Figure 1.2(b).

3. Rotman lenses

Electronic scanning antennas based on beamforming networks such as the Rotman lens [42] have shown significant promise at mm-wave and submm-wave frequencies. The required phase shifts across the output aperture are realised by TTD transmission lines and thus Rotman lenses have the potential for larger operational bandwidths than considered in the phased array antenna. In addition, low insertion loss (< 2 dB), and moderate scan loss (~ 4 dB at $30°$) have been demonstrated at mm-wave frequencies. Furthermore, Rotman lens antennas have been demonstrated to yield high sidelobe suppression (< -30 dB) and high gain/directive beams, which can be scanned over an extremely wide field-of-view ($\pm 60°$) [37, 43–45]. Rotman lenses have been demonstrated using microstrip technology at low microwave frequencies up to 40 GHz [46, 47], and are also commonly developed at 77 GHz for use in automotive adaptive and intelligent cruise control applications [45, 48, 49]. Current Rotman lens demonstrations have yet to be commonly demonstrated above 100 GHz.

However, Rotman lenses suffer from possible beam squint, bulky/heavy assemblies, restricted scan angles, and limited scanning to one-dimension, with high numbers of switches being required. As a result, Rotman lenses may thus only be suitable for a limited range of applications. Half of an example Rotman lens operating at 38 GHz is shown in Figure 1.2(c).

1.2 Optoelectronic devices

Significant work has been focused on alternative mm-wave optoelectronic modulators using semiconductor substrates; such interest has included opti-

cally controlled phase shifters, switches, and a range sub-systems focused at optical beamforming and non-mechanical steering, although interest appears to have subsided since the late 90's.

Early work on optoelectronic microwave switches was extensively reported and theorised in the late 1970's by W. Platte [50–54], where microstrp switches have been shown to provide fast switching times at these lower frequencies. However equivalent optically controlled conductance of a semiconductor based switch becomes difficult at higher (sub) mm-wave frequencies due to the increased losses in microstip transmission lines. The use of standard waveguides at these higher frequencies then requires optical modulation of the semiconductor complex permittivity, yielding controlled attenuation through the transmission line [55, 56].

Devices based at higher mm-wave frequencies were extensively studied and demonstrated by Lee *et. al*, with a range of standard waveguide designs featuring an optically excited semiconductor walled section demonstrating high phase shifts ($> 360°/\mathrm{cm}$), whilst also maintaining low insertion loss ($< 1\ \mathrm{dB/cm}$) [55, 57–61].

Various optoelectronic modulators have been reported which demonstrate gating of mm-waves on nanosecond timescales [58, 62]; microwave frequency filters [63–65], and 1D beam steering [66–70] using optically excited gratings; and optically controlled reflectarrays [71, 72] or phased arrays [61, 73]. However, wide adoption of these devices has been impeded by the high irradiance requirements which often limit these devices to non-practical laser devices.

1.3 Prior-art

The work reported within this thesis has been motivated by the optoelectronic approach as first reported by Webb *et. al.* [74–77], which involved an optically controlled Fresnel zone plate. This particular approach to non-mechanical beam steering has the advantage of being flexible, potentially less complex than RF array based devices, and lower cost.

The initial demonstrations of Webb were reported in the mid to late

1990's, and included system demonstrations at 20 GHz [77], 35 GHz [75], and 94 GHz [75, 76].

The architecture used by Webb for each demonstration comprised a bespoke spatial light modulator consisting of an array of near infrared (NIR) LEDs which were driven by a custom controlled optical fibre network. Figure 1.3(a) displays a photograph of the NIR spatial light modulator setup used for the 20 GHz demonstrations; the LED array comprised 3,046 NIR LEDs covering a 350 mm effective aperture.

The demonstrations were the first reports of their kind and successfully illustrated the promising features of this technique, including moderate scan rates ($\sim\ 1,000\ \mathrm{beams/sec}$), high precision beam control ($\Delta\theta = 0.005°$), and wide angle ($\pm 30°$) beam scanning over a 2D area. In particular, this technique may be extended in both aperture size (directivity) and in frequency, although no prior theoretical or experimental work have been presented. Figure 1.3(b) displays the measured off-axis performance up to $30°$ from boresight of the 94 GHz optically controlled Fresnel zone plate measured by Webb *et. al.* The system featured a 146 mm effective diameter and utilised 2,335 NIR LEDs. Figure 1.3(c) displays the measured 2D pattern using the same setup, taken at 1,000 beams per second with the transmitter located on-axis.

While the performance of zone plates are known to be robust against discretisation, or anomalies, in the zone plate structure [78], the limited pixel density of this architecture limits the frequency scalability, inducing off-axis grating lobes, whilst also potentially limiting the pointing resolution of the antenna. In addition, this particular method suffers from high complexity and cost while also being large and bulky, with limited flexibility.

The work presented in this thesis aims to address these limitations by considering the optically excited semiconductor substrate. Control of the free-carrier effective lifetime and the surface recombination velocity can yield improved devices which can then be adapted to suit the requirements of a range of applications, such as high frame rates or lowered irradiance. Furthermore, reduction of the surface recombination velocity permits optical excitation at short visible wavelengths thus enabling the use of convenient, well established visible display technologies, lowering the cost, complexity, and in-

(a)

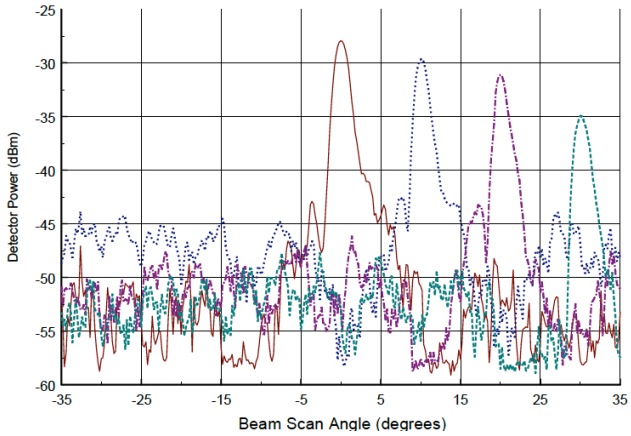

(b)

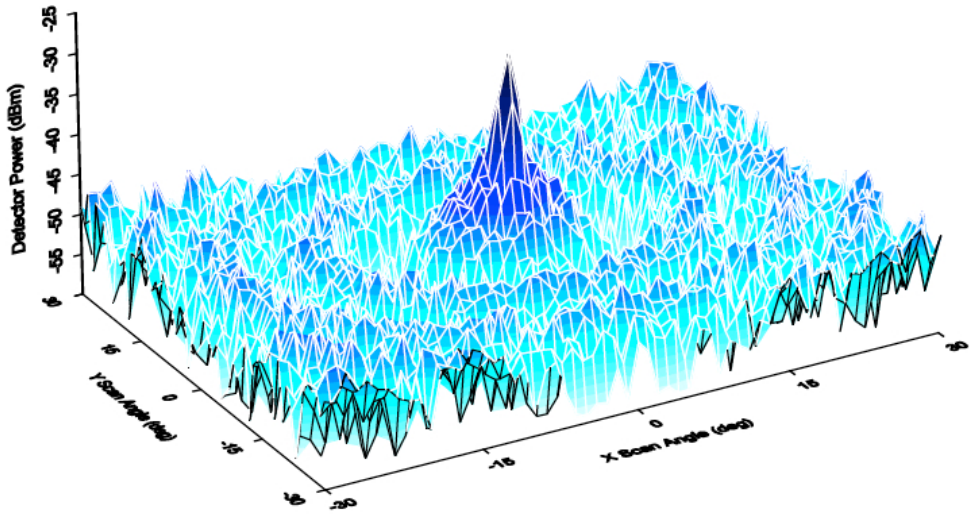

(c)

Figure 1.3: (a) 3,046 NIR LED array spatial light modulator used for 20 GHz demonstrations (reproduced from [77]); (b) measured 94 GHz off-axis performance performed by Webb *et. al.* (reproduced from [75]); and (c) measured 2D 94 GHz antenna pattern using a 2,335 NIR LEDs (reproduced from [75]).

creasing the flexibility and suitability of this technique to higher mm-wave and submm-wave frequencies. For example, Figure 1.4 displays a measured 2D antenna pattern (discussed in Chapter 6) of a F/1.2, 100 mm diameter optically controlled Fresnel zone plate antenna which utilised a standard visible data projector as the optical spatial light modulator and source, where the beam was hopped at 1° increments over a $\pm 30^\circ$ field-of-view in both azimuth and elevation. The extremely high pixel density (>786,000) of the projector, inherent in display technologies, ensures no grating lobes even at high submm-wave frequencies, in addition to offering high resolution masks for precise beam control. This should be compared with the measurements of Webb, i.e. Figure 1.3(c).

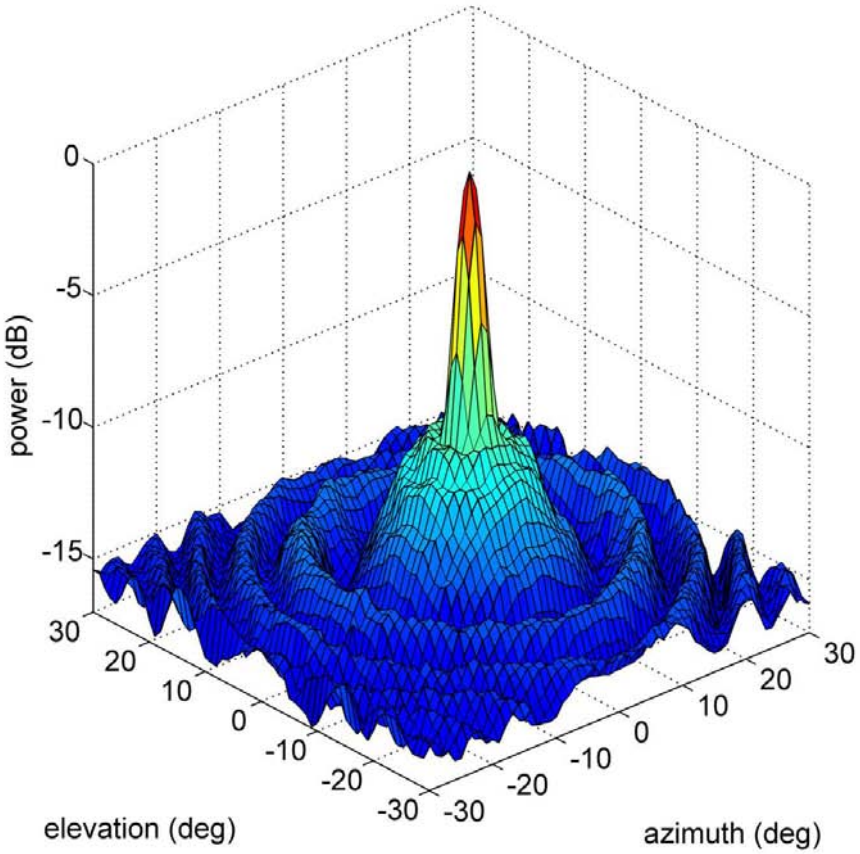

Figure 1.4: Measured 2D antenna pattern for a 94 GHz, 100 mm diameter optically controlled Fresnel zone plate using a data projector as the spatial light modulator and optical source.

Finally, although the work presented by Webb sparked interest in this technique, very little theoretical work has been presented detailing the requirements, limitations, and suitability of this technique to mm-wave and submm-wave frequencies, with little experimental work having been published also. The work presented in this thesis attempts to provide a comprehensive theoretical framework for the optically controlled Fresnel zone plate technique, giving answers to the fundamental questions which have yet to be defined.

1.4 Thesis overview

Different aspects of the optimisation and understanding of optically controlled Fresnel zone plates, or the photo-injected Fresnel zone plate antenna (pi-FZPA), are discussed within each chapter of this thesis. The thesis has the following structure:

Chapter 2 introduces and reviews Fresnel zone plates at mm-wave frequencies. In particular, standard zone plate designs are introduced which are broadly categorised as either Soret (blocking) or Wood (phase correcting) zone plates, each with their own benefits in terms of performance, efficiency, and relative complexity. Optimisation of both zone plate groups are discussed, and a range of zone plates are designed, fabricated, and tested at 94 GHz. Furthermore, an analytical model is developed, which is used to accurately model the overall performance of the grooved zone plate antenna, and is shown to agree well with measured data.

Chapter 3 summarises the general free-carrier dynamics of an opto-excited free-carrier plasma, illustrating the relevant features, and trade-offs, which determine the effective modulation of propagating (sub) mm-wave beams for both pulsed and (quasi-) CW illumination. In addition, the effective free-carrier lifetime and the surface recombination velocity are introduced, representing the most dominant features of the substrate which may be optimised to suit each particular application. Furthermore, the wavelength dependence of the free-carrier plasma is discussed and the optimal choice indicated. A

simple formalism is developed that is used to estimate the effective plasma density within the substrate, which is invaluable for designing optoelectronic modulating devices.

A range of passivation schemes are summarised, which are shown to enable shorter wavelength excitation, resulting in increased system flexibility, and lowered costs. The lifetime stability of two passivation schemes are analysed using a high frequency mm-wave photoconductance decay method (PCD), which has been based on the standard microwave PCD technique. Details of this implementation, and interpretation of the measurements is presented.

Chapter 4 presents the experimental characterisation of a range of silicon substrates at W-band frequencies. The experimental results, which were performed on both un-passivated and passivated wafers, display the marked improvements in controllable attenuation resulting from increased effective plasma densities, arising from the passivation process. The transmission and reflection properties are compared for NIR and visible excitation; the results of these investigations emphasise (and validate) the theoretical understanding of the carrier kinetic processes discussed in Chapter 3.

A fully general analytical model is developed which details the change in transmission line properties of a semiconductor substrate, subject to optical excitation at a range of wavelengths, densities, and effective lifetimes.

Chapter 5 introduces the concept of the photo-injected Fresnel zone plate antenna. A full account of the piFZPA is given, where the two main categories are introduced: transmission- or reflection-type. Both categories represent two distinct approaches to realising piFZPAs, where the transmission-type benefits from simplicity, but at the cost of an increased effective plasma density requirement. The reflection-type offers a reduced plasma density requirement compared to an equivalent transmission-type piFZPA, and also enables higher efficiencies to be achieved, albeit at higher plasma densities; both design requirements and optimisations are discussed. The development of a full composite model, derived from Chapters 2–4, is used as a means of providing answers to the fundamental questions of requirements, performance trade-offs, and limitations for transmission-type piFZPAs, and for the reflection-type piFZPA in conjunction with an ABCD model developed in Chapter 4.

The details of a modified algorithm which enables simple generation of zone plate masks for beam steering is discussed.

Chapter 6 & 7 present the experimental results on a range of piFZPA designs; the results represent the culmination of all prior chapters. The experimental results employ a range of optically controlled semiconductor substrates which demonstrate adaptive beamforming and non-mechanical steering, based on the piFZPA technique. Using a standard visible data projector as a broadband light source and spatial light modulator, the characterisation of several transmission-type piFZPA designs are presented. These realisations demonstrate high fidelity beam control, 2D steering of a mm-wave beam, and active imaging using a 94 GHz FMCW close-range imaging radar. The realisations based on this architecture are believed to be the first demonstrations of their kind, highlighting the potential of realising optoelectronic modulation of (sub) mm-wave beams using low cost, flexible, and well established visible display technologies.

Chapter 8 summarises the key outcomes of the work presented within this thesis. Concluding remarks are made regarding the key optimisation requirements of the piFZPA technique, which are applicable, in general, to methods which involve an optically excited semiconductor substrate. The scalability of this technique both in aperture size and frequency are discussed, highlighting the attractiveness of this technique for a range of applications within the mm-wave and submm-wave frequency bands. Further work is identified, such as experimental measurements which validate some of the numerical results presented; and other technologies which have the potential of yielding dynamic (sub) mm-wave modulation with higher efficiencies than that currently possible with a photoconductive substrate. In particular, key modern technologies are identified which have the possibility of creating low cost reconfigurable antennas with greater than 40% efficiency.

chapter 2

Fresnel zone plates at mm-wave frequencies

This chapter introduces and reviews the concept of Fresnel zone plates. Application of Fresnel zone plates at mm-wave frequencies is summarised and their design and optimisation discussed; errors found within the literature are also highlighted.

The design and characterisation of a range of conventional Fresnel zone plates is presented at 94 GHz.

This chapter forms the foundation required for optimised photo-injected Fresnel zone plates, discussed later in Chapter 5.

2.1 Introduction

Originating from the elementary theory of optics and the propagation of light, theorised by C. Huygens (1690) and A-J. Fresnel (1818), the concept of Fresnel zone plates (FZPs) has been well known and utilised for some time [79].

Construction of FZPs follows from the concept of *half-wave boundaries*, which designate annuli of a given radius such that the phase of an incident wavefront changes across the boundary by up to π radians [79]. FZPs are

commonly grouped into two main categories: blocking, and phase correcting zone plates, which were originally suggested by Lord Rayleigh (1871).

The blocking category are often referred to as the Soret zone plate type, after J-L. Soret (1875), while the phase-correcting type are commonly referred to as Wood zone plates, after R. W. Wood (1898).

The application of FZPs, predominantly exploited at optical wavelengths, was extended into the microwave region in the 1930s, although work was limited to a few published patents [80]. The use of FZPs at higher mm-wave frequencies began in 1960 [81] and was driven by low manufacturing costs, simple fabrication, and their inherent diffraction limited resolution. Furthermore, reduced lens thicknesses, which arise from zoning, also drove development at higher frequencies due to lower absorption loss within the lens material [82].

Understanding of Fresnel zone plate antennas (FZPAs) grew dramatically throughout the 1990s, which was motivated by their application as a low cost solution for DBS (direct broadcast satellite) reception [83].

Resulting from the last four decades, Fresnel zone plates and their application to microwave (and higher frequency) applications has produced a wealth of knowledge within this field, detailed in over one hundred published papers, several patents [84–87], and a collection of books [78, 88–90]. The following discussion details the design and optimisation of both Fresnel zone plate configurations, where particular demonstrations have been highlighted as appropriate. A review of the field of zone plates and their application at microwave and mm-wave frequencies have been detailed over ten years ago [80, 83, 91], and more recently in [78], albeit focused on Fresnel arrays. The design and optimisation of Fresnel zone plates are critical for optimised design of piFZPAs, which are discussed in Chapter 5.

2.2 Blocking (Soret) zone plates

Soret zone plates (SZPs) are the simplest, and the least efficient, of the Fresnel zone plate family, consisting of an aperture containing alternating

transparent and opaque annuli coinciding with the Fresnel half-wave boundaries. SZPs are commonly further sub-divided into either *positive* or *negative* types, given by the construction of an aperture whose phase contribution is either positive or negative [88, 92]. These are illustrated in Figure 2.1(a) and Figure 2.1(b) respectively.

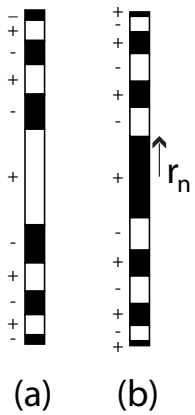

Figure 2.1: Cross-sectional view of SZPs illustrating (a) positive, and (b) negative zone plate types. Black indicates opaque regions, and white transparent. (Reproduced from [88])

The basic SZP offers the lowest focusing gain ($1/\pi^2$ times that of a traditional lens) due to large aperture phase errors of up to π radians, and the disposal of nearly half the available energy from the source. While the efficiency has been shown to dramatically improve for alternate stepped and folded SZP designs [84,89,93–98], the simplicity, low cost, and high resolution of the SZP family makes them suitable for a wide range of applications, such as DBS.

2.2.1 Zone plate design

The equation for calculating zone radii is derived from Fresnel's theory of half-wave boundaries, which requires that the path length change between adjacent zones be equal to $\lambda/2$; from Figure 2.2, this gives

$$n\frac{\lambda}{2} = \sqrt{d_1^2 + r_n^2} + \sqrt{d_2^2 + r_n^2} - (d_1 + d_2). \tag{2.1}$$

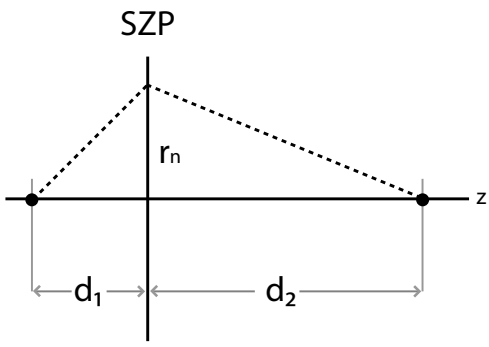

Figure 2.2: Geometry for the construction of the SZP, indicating zone radii, r_n, which is determined by the relative locations of input focal length, d_1, and output focal length d_2.

Rearranging for r_n, (2.1) yields [88]

$$r_n = \frac{1}{2}\left[\left(d_1 + d_2 + \frac{n\lambda}{2}\right)^2 + \left(\frac{d_1^2 - d_2^2}{d_1 + d_2 + n\lambda/2}\right)^2 - 2(d_1^2 - d_2^2)\right]^{1/2}, \quad (2.2)$$

giving the zone radii, r_n, for a SZP which transforms an input spherical phasefront, diverging from distance d_1, to a converging output spherical phasefront focused at a distance d_2. For plane wave illumination: $d_1 \to \infty$, and $d_2 = F$, and (2.2) reduces to the common zone plate expression [88, 89, 99]

$$r_n = \sqrt{n\lambda F + \left(\frac{n\lambda}{2}\right)^2}, \quad (2.3)$$

where F defines the zone plate focal length, λ the design free-space wavelength, and n the zone number.

At optical wavelengths the common situation arises where $F \gg n\lambda/4$, and thus optical zone plates are typically designed with the latter term of (2.3) omitted ($r \propto \sqrt{n}$). Such approximations gives rise to the *geometric* and the *interferometric* zone plate designs, with the former referring to the optical design approximation, and the later to zone plates designed using the full form of (2.3) [100].

At mm-wave frequencies, the design of SZPs should be based on the

interferometric approach, (2.3), otherwise degradations such as multiple focii and spherical aberration ensue [88, 100–104].

2.2.2 Performance and optimisation

The overall performance and optimisation of SZPs are known to differ depending on whether the zone plate is part of the *positive* or *negative* subgroup [92, 97, 105, 106]. For example, *positive* SZPs produce increased gain and sidelobe suppression with lower angular resolution, compared to the *negative* SZP sub-category [92, 105].

In addition, the F-number (F/D) of the SZP design, or the total number of zones N, can have a significant effect on the overall antenna performance. It well known that smaller F/D ratios (larger N) yield increased gain and sidelobe suppression [105].

Figure 2.3(a) displays the results of numerical simulations, which were performed using the vectorial form of the Fresnel-Kirchoff diffraction integral[1] [88, 107, 108], for both *positive* and *negative* SZPs, as a function of F/D. The simulations were performed for a fixed aperture size of 100 mm, with a -11 dB edge taper at 94 GHz. As mentioned above, the gain and sidelobe suppression are shown to increase (globally) as $\mathrm{F/D} \rightarrow 0$ for the *negative* SZP, while only the sidelobe suppression is shown to increase for the *positive* SZP. A smaller size of the central zone as F/D is reduced gives rise to the lowered focusing gain for the *positive* SZP [79], while the smaller central zone reduces the apodization of the *negative* SZP, thus increasing the gain. The *negative* SZP is also shown to feature improved angular resolution over the *positive* SZP, inline with [92].

Local discontinuity, and gain reductions, arise from the change of the outermost zone from transparent to opaque, where maximum gain occurs for a fully transparent zone [109].

Figure 2.3(b) displays example far-field patterns calculated using the vectorial Fresnel-Kirchoff diffraction integral for SZPs with a 200 mm aperture, with either a 200 mm (F/D = 1) or 400 mm (F/D = 2) focal length. The dis-

[1] Note in Ref. [88], eq. (5.18) displays an error: The $\cos\varphi$ term should read $\sin\varphi$.

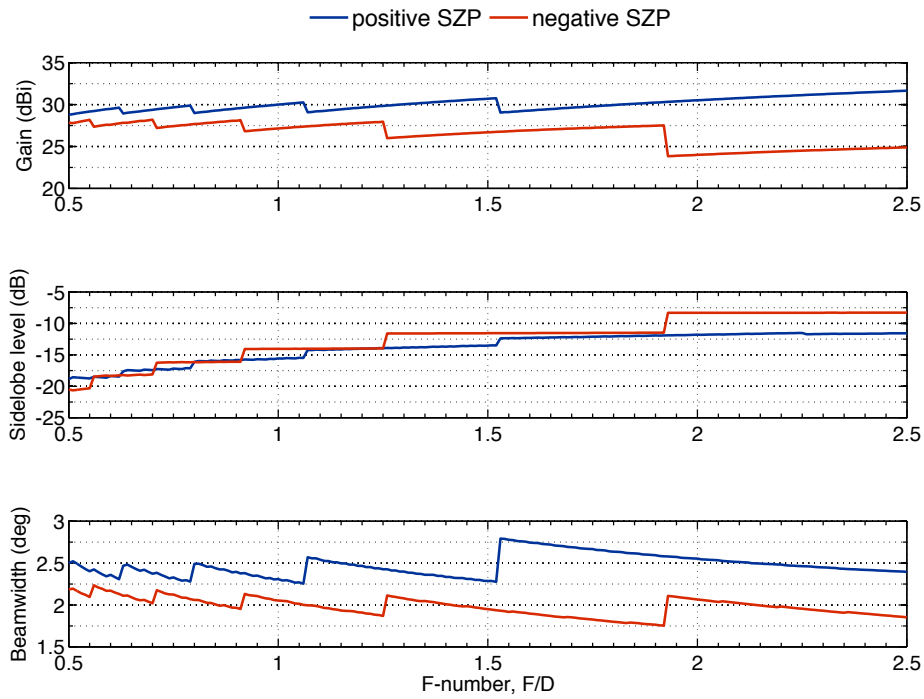

(a)

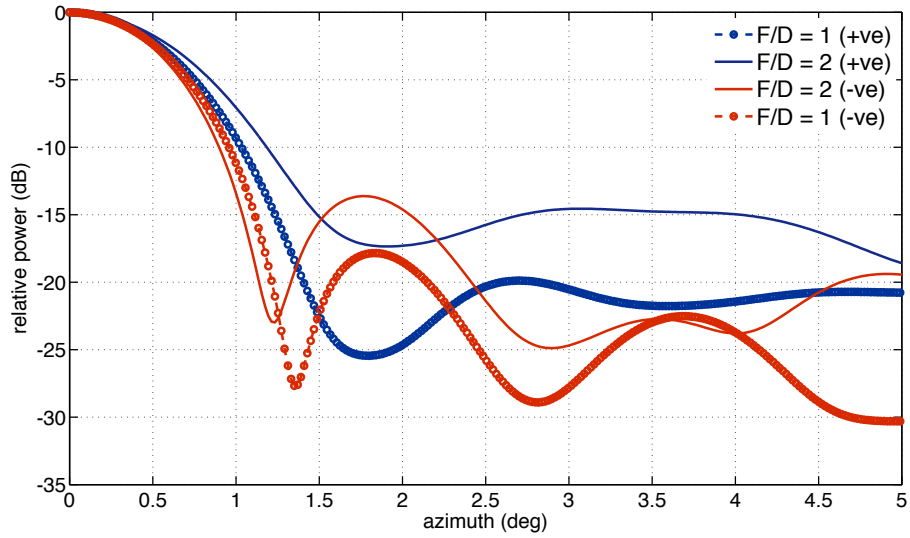

(b)

Figure 2.3: SZP simulated performance variation: (a) displays the gain, sidelobe level, and beamwidth for a range of F/D designs, comparing both *positive* and *negative* zone plate configurations (fixed D = 100 mm); (b) normalised far-field patterns for F/D = 1, 2 for both zone plate types.

tinction between both SZP sub-categories, and the relative number of zones, as discussed, are evident from the simulated far-field patterns[2].

Finally, the zoning of zone plates are known to reduce their bandwidth [110], giving rise to a frequency dependent focal length (c.f. (2.3)). This can be advantageous for quasi-optical techniques involving focal isolation or frequency and spatial filtering [110–112]. However for most applications, reduced bandwidths (compared with traditional lenses) are un-favourable.

The bandwidth of a SZP can be approximated by

$$\Delta\omega = \frac{\omega_0}{N}, \tag{2.4}$$

arising from a $\lambda/4$ tolerance in the pathlength change due to chromatic aberration [100]. Here, $\Delta\omega = |\omega - \omega_0|$, with angular centre frequency ω_0, and the total number of zones N. As an example, a 150 mm aperture, F/1 SZP with a design frequency of 94 GHz which produces N = 11.10 zones, yields an 8.5 GHz bandwidth, or 9%, much less than an ordinary lens ($> 40\%$).

2.3 Phase correcting (Wood) zone plates

In comparison to SZPs, Wood zone plates (WZPs) yield increased efficiency arising from the introduction of an additional phase retardation of up to π radians in place of alternating blocking zones. At mm-wave frequencies, the phase-correction mechanism is commonly introduced by a grooved dielectric plate [88], or a planar structure of alternating permittivities [113]; the latter being known as the Wood-Wiltse zone plate.

In addition, increased stepping of the grooved dielectric, or an increased number of alternating permittivities, is known to further enhance the overall focusing efficiency due to reduced phase error across the aperture. The reduction of the phase error is commonly denoted by a phase-correcting constant P, where λ/P denotes the wave correction scheme used. For example, the simplest half-wave design results for $P = 2$; quarter-wave correction for $P = 4$; and eighth-wave correction for $P = 8$. This results in an increase in

[2]patterns have been normalised

phase efficiency from 40.5% ($P = 2$) up to 95% ($P = 8$), with a 100% phase efficiency being obtained from a traditional lens [95, 114].

The design of WZPs follows similarly that of SZPs with the addition of the phase-correcting constant, P, groove depth, w, and lens thickness t_L. WZPs similarly divide into *positive* and *negative* sub-groups, as shown in Figure 2.4. The distinction in performance between both types varies less significantly than for the SZPs [115], and thus WZPs typically adopt a single sub-group.

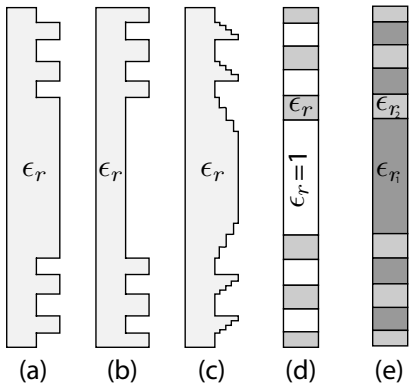

Figure 2.4: Cross-sectional view of Wood zone plate antennas indicating (a) negative $P = 2$ zone plate, (b) positive $P = 2$ zone plate, and (c) positive $P = 4$ zone plate designs. Additionally, Wood-Wiltse zone plates are shown for (d) alternating dielectric/air, and (e) alternating dielectric (both are $P = 2$ designs).

The Wood-Wiltse zone plate type was initially introduced to circumvent problems commonly encountered for WZP designs, such as shadowing effects and the accumulation of lossy materials within the grooves. However, shadowing degradations have since been shown to be only significant for fast ($F/D < 0.5$) grooved WZP designs [113, 116], with the accumulation of lossy material only posing a significant risk in certain circumstances.

2.3.1 Zone plate design

The calculation of zone radii of WZPs closely follows the discussion detailed in Section 2.2.1. The generalised design equation for the Pth correction scheme is given by [117],

$$r_n = \frac{1}{2}\left[\left(d_1 + d_2 + \frac{n\lambda}{P}\right)^2 + \left(\frac{d_1^2 - d_2^2}{d_1 + d_2 + n\lambda/P}\right)^2 - 2(d_1^2 - d_2^2)\right]^{1/2}, \quad (2.5)$$

which reduces to

$$r_n = \sqrt{\frac{2n\lambda F}{P} + \left(\frac{n\lambda}{P}\right)^2} \quad (2.6)$$

for the plane-wave illumination case[3] [118], where (2.2) and (2.3) detail the zone dimensioning for the half-wave correction (P = 2) case.

The dielectric width of the phase-correction mechanism is written as [119]

$$w = \frac{\lambda}{P(\sqrt{\epsilon_{r2}^{'}} - \sqrt{\epsilon_{r1}^{'}})}, \qquad \epsilon_{r2}^{'} > \epsilon_{r1}^{'}, \quad (2.7)$$

which specifies the width of the Wood-Wiltse lens. For the case of a grooved dielectric, $\epsilon_{r1}^{'} = 1$ (air) and (2.7) reduces to[4] [99, 113]

$$w = \frac{\lambda}{P(\sqrt{\epsilon_r'} - 1)}. \quad (2.8)$$

While there exists no closed form solution for optimising the grooved WZP [120], for the Wood-Wiltse zone plate, it has been shown that for the $P = 2$ case, maximum gain occurs when [119]:

$$\frac{\epsilon_{r2}^{'}}{\epsilon_{r1}^{'}} = \left(\frac{k+1}{k}\right)^2. \quad (2.9)$$

The right hand side of (2.9) originates from the matched dielectric thickness which yields the maximum transmission, due to an integer number of standing waves, k (see Chapter 4). For higher order correction schemes ($P > 2$), the optimised design requires a full rigorous approach where the required phase change produced by propagation through a dielectric of permittivity $\epsilon_{rn}^{'}$ (n = 1, 2, . . . P) is performed such that the phase change matches

[3] with typographical errors in [88, 113]
[4] with typographical errors in [88]

the phase-correction scheme [119, 121, 122].

2.3.2 Modified Fresnel-Kirchhoff diffraction integral

Using the Fresnel-Kirchhoff diffraction integral, the far-field patterns of a WZP antenna can be numerically simulated. Current methods outlined in the literature appear to concentrate on the Wood-Wiltse design[5] [88, 119, 121, 123, 124], with the simplest method applying a phase correcting factor, $e^{j2\pi/P}$, to the SZP Fresnel-Kirchhoff formalism [99, 125]. However, this method is only sufficient for designs satisfying (2.9), which may not always be the case. In addition, using the above methods which account for the phase shift produced by the dielectric medium (nicely outlined in [108]) are still insufficient for a grooved WZP, as they unanimously neglect the effects of a supporting base. These methods describe insufficiently the optimum dielectric substrate thickness of the full lens.

The following summarises a numerical model devised to fully simulate the far-field antenna patterns of a grooved dielectric WZP. Details of the derivation have been left for discussion in Appendix A. The limitations of this physical optics (PO) approach are to relatively slow F/D designs ($F/D > 0.5$) and reasonable off-axis angles ($< 30°$). The limitations arise from the PO field equivalence principle, and the approximation of a local plane wave which is used when deriving the Fresnel reflection coefficients of the dielectric medium. Larger deviations, and smaller F/D ratios, can be simulated using techniques such as UTD (geometrical optics), which were first derived by Baggen for the SZP [109], and van Houten for the dielectric Wood-Wiltse zone plate [108, 124]. Validation of the accuracy of UTD at large offset angles has been theoretically studied [126], and experimentally demonstrated [127].

The antenna geometry of the grooved dielectric WZP antenna is depicted in Figure 2.5. For simplicity, the input field from the feed, $G_f(\psi, m)$, is modelled as an idealised feed, represented by a raised cosine function [128]

[5] all with various typographical errors.

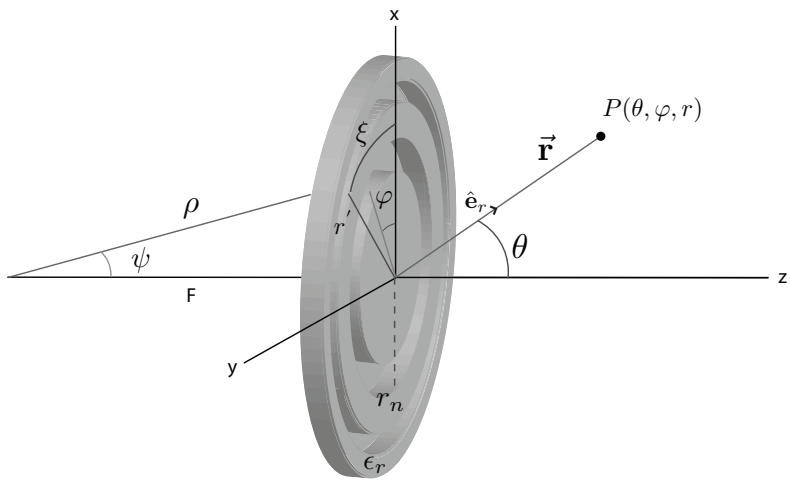

Figure 2.5: Geometry of a transmission-type grooved dielectric WZP illuminated by an axially symmetric, idealised, feed.

$$G_f(\psi, m) = \begin{cases} 2(m+1)\cos^m(\psi) & \text{if } 0 \leq \psi \leq \pi/2 \\ 0 & \text{if } \psi \geq \pi/2 \end{cases}, \tag{2.10}$$

where m defines the field taper, and ψ the angle of the aperture. ρ, ψ, ξ denote the coordinates of the frame containing the feed and antenna, whilst r, θ, φ denote the coordinates of the far-field observation point, P.

Summarising Appendix A, the electric-field vector at the output aperture of the dielectric is given by

$$\mathbf{E}_d(\psi, \xi, m) = \left(\frac{P_t \eta_0}{2\pi}\right)^{1/2} \sqrt{G_f(\psi, m)} \frac{e^{-jkL(\psi)}}{L(\psi)} \cos\psi \cdot \vec{\mathbf{P}}_d(\psi, \xi), \tag{2.11}$$

where P_t is the power transmitted by the antenna, and η_0 is the intrinsic impedance of free-space ($120\pi\ \Omega$). The amplitude divergence factor, $L(\psi)$, is given from geometry:

$$L(\psi) = \frac{F}{\cos\psi} + \frac{\tilde{\epsilon}_r t_L}{\sqrt{\tilde{\epsilon}_r - \sin^2\psi}}, \tag{2.12}$$

with lens thickness,

$$t_L = t_{\text{base}} + w, \tag{2.13}$$

where $\tilde{\epsilon}_r$, F, t_{base}, and w define the (complex) permittivity, focal length, lens base thickness, and groove depth (2.8), respectively.

The feed polarisation, $\vec{\mathbf{P}}_d(\psi, \xi)$, is chosen as the so-called Huygens source [109], which is written as [121]

$$\vec{\mathbf{P}}_d(\psi, \xi) = -t_M \cos\xi \cdot \hat{\mathbf{e}}_\psi + t_E \sin\xi \cdot \hat{\mathbf{e}}_\xi, \tag{2.14}$$

where t_E, t_M are the polarisation-dependent Fresnel transmission coefficients, for electric and magnetic polarisations, respectively, and ξ is the polar angle of the feed/zone plate aperture. Expressions for t_E, t_M are given in Appendix A.

Applying the Fresnel-Kirchhoff diffraction integral to (2.11) yields the general expression for the far-field pattern,

$$\vec{\mathbf{E}}_d(\theta, \varphi) = C_f(r)\hat{\mathbf{e}}_r(\theta, \varphi) \times \iint_{A'} \left[\hat{\mathbf{n}} \text{ x } \vec{\mathbf{P}}_d(\psi, \xi)\right] \frac{e^{-jkL(\psi)}}{L(\psi)} e^{jk\hat{\mathbf{e}}_r(\theta,\varphi)\cdot\hat{\mathbf{r}}''} \mathrm{d}A''. \tag{2.15}$$

where $\hat{\mathbf{e}}_r, \hat{\mathbf{n}}, \hat{\mathbf{r}}'$ are unit vectors, and $C_f(r)$ is given by

$$C_f(r) = \frac{jke^{-jkr}}{2\pi r}\sqrt{\frac{P_t}{2\pi}\eta_0}, \tag{2.16}$$

with distance to the far-field observation point given by r. Solving the ξ integral analytically, and collecting terms, the components of the electric-field (θ, φ), given by

$$\mathbf{E}(\mathbf{r}, m) = \mathbf{E}_\theta(\mathbf{r}, m) \cdot \hat{\mathbf{e}}_\theta + \mathbf{E}_\varphi(\mathbf{r}, m) \cdot \hat{\mathbf{e}}_\varphi, \tag{2.17}$$

can be shown (outlined in Appendix A) to yield

$$E_\theta(\theta, \varphi) \;=\; -\pi C_f \cos\varphi \sum_m \int_{\psi_m}^{\psi_{m+1}} O_d(\psi) e^{M_d(\psi)} I_\theta(\theta, \psi) \mathrm{d}\psi \tag{2.18}$$

$$E_\varphi(\theta,\varphi) = -\pi C_f \sin\varphi\cos\theta \sum_m \int_{\psi_m}^{\psi_{m+1}} O_d(\psi) e^{M_d(\psi)} I_\varphi(\theta,\psi)\mathrm{d}\psi, \quad (2.19)$$

with

$$M_d(\psi) = -jkL(\psi) \quad (2.20)$$

$$N_d(\theta,\psi) = k\sin\theta\left(F\tan\psi + \frac{\tilde{\epsilon}_r t_L \sin\psi}{\sqrt{\tilde{\epsilon}_r - \sin^2\psi}}\right) \quad (2.21)$$

$$O_d(\psi) = \sqrt{G_f(\psi,m)}\left(F\tan\psi + \frac{\tilde{\epsilon}_r t_L \sin\psi}{\sqrt{\tilde{\epsilon}_r - \sin^2\psi}}\right) \quad (2.22)$$

where $C_f(r)$ is defined by (2.16), and k is the wavenumber. The components $I_\theta(\theta,\psi), I_\varphi(\theta,\psi)$ are defined as

$$I_\theta(\theta,\psi) = -(t_M\cos\psi + t_E)J_0[N_d(\theta,\psi)]\ldots + (t_M\cos\psi - t_E)J_2[N_d(\theta,\psi)] \quad (2.23)$$

$$I_\varphi(\theta,\psi) = (t_M\cos\psi + t_E)J_0[N_d(\theta,\psi)]\ldots + (t_M\cos\psi - t_E)J_2[N_d(\theta,\psi)], \quad (2.24)$$

where $J_0[x], J_2[x]$ are the zeroth and second order Bessel functions of the first kind, of argument x, respectively.

The gain, co- and cross- polar, patterns are then given by standard expressions found in the literature [88, 108, 119, 121].

Figure 2.6 displays a comparison of the far-field antenna pattern for an 88 mm diameter, F/1.2, *positive* WZP computed by two methods. The comparison is shown for both the vectorial Fresnel-Kirchhoff diffraction integral outlined above, implemented in Matlab, and the Finite Integration Technique incorporated into the CST transient solver [129]. The comparison shows excellent agreement in the mainlobe, with similar levels for the sidelobe envelope. Differences between both methods can be attributed to the difference in feeds, and the approximations used in the derivation of the Fresnel-Kirchhoff

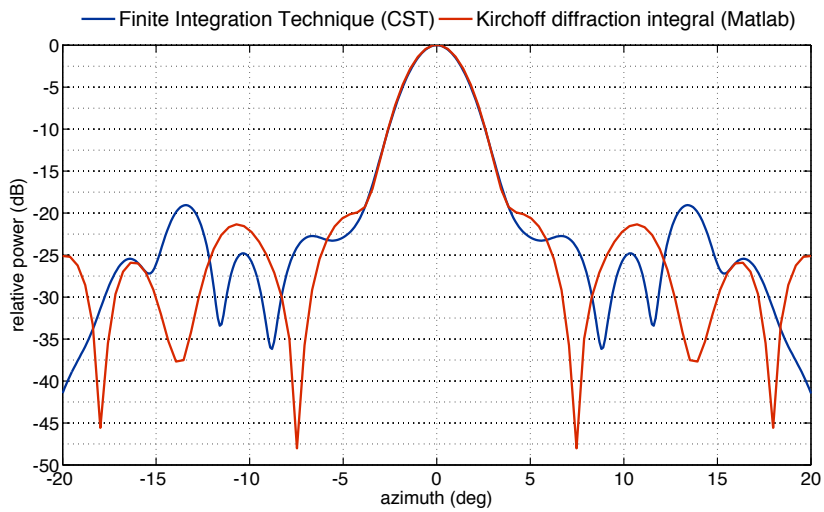

Figure 2.6: Simulated (and normalised) far-field H-plane patterns for a grooved dielectric WZP, comparing the vectorial Fresnel-Kirchhoff diffraction integral method and the general Finite Integration Technique (FIT) available within the CST EM simulation environment. The comparison shows good agreement between both methods.

model. In addition, slight errors are expected to have been introduced within the CST simulations as a result of the coarse mesh, which was used in order to reduce the simulation time (∼8 hrs).

2.3.3 Performance and Optimisation

The optimisation of WZPs is similarly dependent on the F/D ratio, whilst additionally including the lens permittivity(ies) and base thickness. The choice of lens thickness, for the case of the Wood-Wiltse zone plate, has been briefly discussed above; and the relative change in sidelobe/gain performance follows Section 2.2.2. The significance of an appropriate lens material, and its effect on the overall gain and efficiency, can be investigated for a grooved WZP using the modified Fresnel-Kirchhoff model. The phase, illumination, and aperture efficiency are defined in Appendix B, which have been derived for the grooved dielectric WZP case.

Figure 2.7 displays the phase, illumination, and aperture efficiency for a 100 mm aperture, F/D $= 2$, $P = 2$, 5 mm thick grooved WZP antenna as a function of lens permittivity for $2 \geq \epsilon_r' \geq 5$. Keeping all other parameters

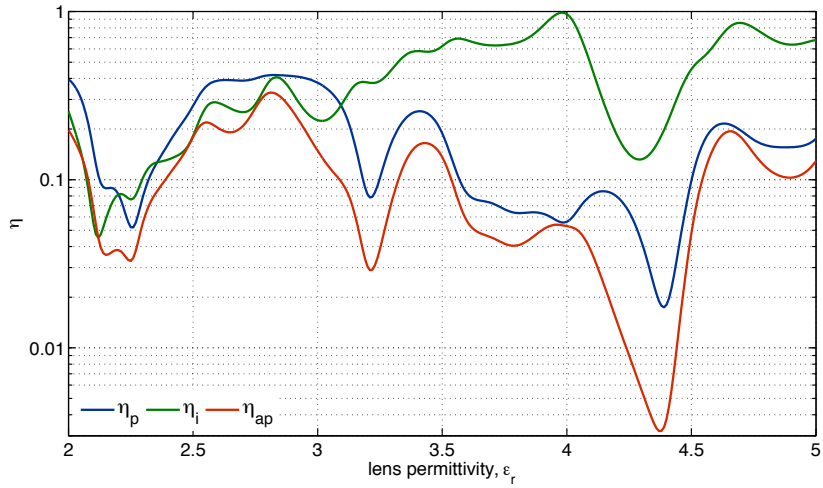

Figure 2.7: Simulated zone plate efficiency for a 100 mm aperture, F/D = 2, 5 mm thick WZP as a function of lens permittivity ϵ_r. Efficiencies include: phase efficiency, η_p; illumination efficiency, η_i; and overall antenna efficiency, η_{ap}.

constant[6], the efficiencies are shown to vary considerably[7] as the permittivity of the lens is changed. In addition, the phase efficiency of the zone plate is shown to only achieve the theoretical maximum ($\sim 40\%$) for lens permittivities $\epsilon_r' = 2$, and $2.5 \geq \epsilon_r' \geq 3.0$ – for this particular design. Furthermore, the overall aperture efficiency shows a strong correlation to the phase efficiency, as clearly indicated with a lens permittivity of $\epsilon_r' = 3.98$, where the illumination efficiency of $\eta_i = 0.99$ and phase efficiency $\eta_p = 0.06$ yield an aperture efficiency of $\eta_{ap} = 0.05$. Due to this correlation, the phase efficiency is often used to indicate the performance of WZPs.

The corresponding change in antenna gain (dBi), based on the simulations of Figure 2.7, is shown in Figure 2.8(a). The change in gain follows a similar trend, and changes over a 20 dBi range within the range of permittivities simulated. The maximum gain is found for lens permittivities $\epsilon_r' = 2.0$ and in the range $2.5 \geq \epsilon_r' \geq 3.0$, corresponding to the peak in phase efficiency. Various common materials have been identified on the figure, which include[8]:

[6] adjusting the groove depth, w, with each change in permittivity

[7] certain selections of ϵ_r' for this zone plate thickness result in a poor interference condition, which results in a drop in gain.

[8] complex components ignored. However, the model works equally well in all situations

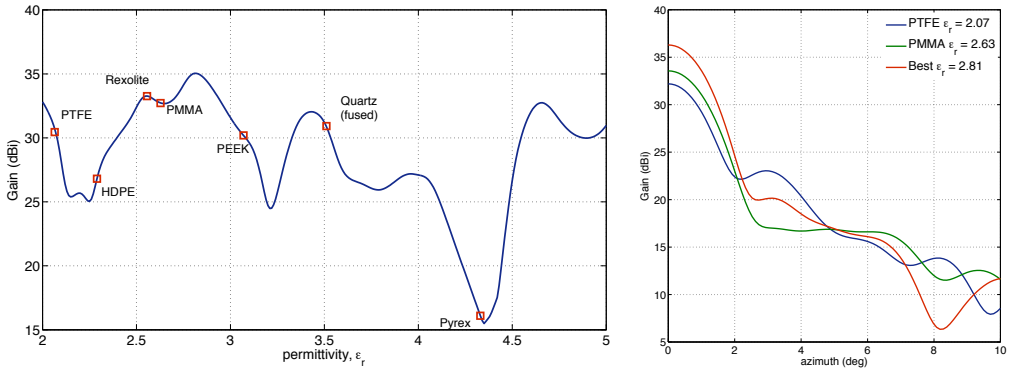

(a) (b)

Figure 2.8: (a) Simulated gain as a function of lens permittivity, ϵ_r, for a 100 mm diameter, F/2, grooved dielectric WZP. (b) Corresponding H-plane far-field patterns at select lens permittivities.

PTFE ($\epsilon_r' = 2.07$), HDPE ($\epsilon_r' = 2.29$), Rexolite ($\epsilon_r' = 2.56$), PMMA ($\epsilon_r' = 2.63$), PEEK ($\epsilon_r' = 3.07$), fused Quartz ($\epsilon_r' = 3.51$), and pyrex ($\epsilon_r' = 4.33$). The W-band measured permittivities of HDPE, PMMA and PEEK were taken from [130]; and the permittivities of PTFE, Rexolite, Quartz and pyrex from [131]. The corresponding far-field patterns for the best case ($\epsilon_r' = 2.81$ with this design), PTFE, and PMMA are shown in Figure 2.8(b).

These simulations indicate the significance of the choice of lens permittivity and the effect on overall gain for a grooved WZP. Furthermore, no closed form solution exists for optimisation of the lens thickness (and permittivity), and thus optimisation must be accomplished iteratively [120, 132].

Finally, WZPs also benefit from increased bandwidths due to the increased phase efficiency; modification of (2.4) yields [99, 108]

$$\Delta\omega = \frac{P\omega_0}{N}, \tag{2.25}$$

where P, N retain their usual meaning. The WZP then yields approximately double the bandwidth of a SZP, for any choice of phase correction scheme, P. Using the same example as before, a 150 mm aperture, F/1, 94 GHz WZP yields an approximate 17.0 GHz bandwidth, or 18% ($P \geq 2$).

2.4 Large aperture Wood zone plate antennas

The following section details the design, fabrication and characterisation of two phase-correcting zone plates at 94 GHz.

2.4.1 Design

The designs comprised two Wood zone plate antennas (WZPAs): a half-wave correction (P = 2) and quarter-wave correction (P = 4) scheme. The effective aperture sizes were chosen to match a 300 mm diameter Cassegrain antenna which was tested during the establishment of the mm-wave far-field antenna test range. Available WR10 feeds resulted in a input focal length of approximately 490 mm (F/1.63), corresponding to a -13 dB edge taper.

The lens material was selected using the Kirchoff diffraction formulation outlined in Section 2.3.2, where the antenna performance was simulated for a range of materials. The initial materials considered included Rexolite 1422, polytetrafluoroethylene (PTFE), and high density polyethylene (HDPE). Although simulations suggested the lowest performance, HDPE was chosen due to its immediate availability, and its extremely low cost.

Characterisations of the HDPE ($\epsilon_r' = 2.29$ at 94 GHz) lenses yielded reasonable performance with an average peak sidelobe level of -17.4 ± 0.6 dB with 38.0 ± 0.1 dBi gain, for the P = 2 design, and -21.5 ± 0.2 dB peak sidelobe

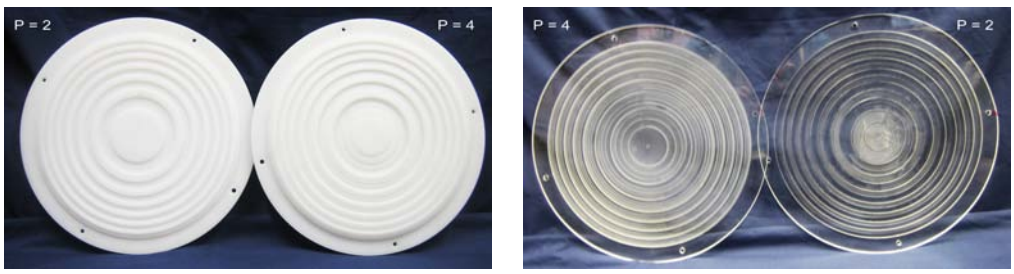

(a) (b)

Figure 2.9: Photograph of both WZPA designs, half-wave (P = 2) and quarter-wave (P = 4) correction. The image shows both designs for both material types, (a) HDPE and (b) PMMA.

level with 40.2 ± 0.1 dB gain, for the P = 4 design. However, poor precision achieved during fabrication of the HDPE grooves, and the large (16 - 19 mm) lens thickness, which ensured structural rigidity, resulted in a broadening of the mainlobe at the -10 dB level in both designs. For these reasons, the design was repeated with a different lens material. Polymethyl methacrylate (PMMA), or acrylic/perspex® ($\epsilon_r' = 2.63$ at 94 GHz), was chosen given its extremely low cost, and good mechanical properties. Additionally, Figure 2.8(a) suggests potentially good performance for a lens of this permittivity. The performance as a function of lens thickness was modelled using the numerical method of Section 2.3.2. These simulations showed small changes of less than 5 dBi in gain, and 2 dB in sidelobe levels, for a change in PMMA thickness, t_L, from 4 mm to 12 mm. The new zone plate design was then chosen near the centre of the simulated thickness range, representing a compromise in sidelobe performance and gain whilst minimising the cost of the material, $t_L = 6$ mm.

Both WZPAs as constructed from both materials are shown in Figure 2.9, and comprise a 350 mm effective aperture. The excess outer ring was used for mounting to a support frame for testing.

The zone radii were calculated using (2.6), and the groove depth using (2.8), for both the P = 2 and P = 4 design, with F = 490 mm, $\lambda = 3.19$ mm, and $\epsilon_r' = 2.63$. This resulted in 14.07 zones for the half-wave correction design, and 28.13 zones for the quarter-wave correction design. The calculated zone radii are given[9] in Table 2.1. The groove depths were calculated as $w = 2.57$ mm for the P = 2 case, and $w = 0,\ 1.28,\ 2.56,\ 3.84$ mm for the P = 4 case.

2.4.2 Far-field antenna patterns

A conventional far-field antenna test range was established in order to measure the performance of a range of antennas. The range could support antennas with dimensions of up to 0.5 m, measured at 94 GHz. Separation between transmitter and the antenna-under-test (AUT) was greater than the standard

[9] partial zones have been rounded up to the next integer.

Table 2.1: WZPA zone radii with F = 490 mm, D = 300 mm, $\lambda = 3.19$ mm design for both P = 2, 4.

Zone number	r_n (P = 2)	r_n (P = 4)
n = 1	39.58	27.97
n = 2	56.02	39.58
n = 3	68.66	48.49
n = 4	79.35	56.02
n = 5	88.79	62.65
n = 6	97.34	68.66
n = 7	105.22	74.19
n = 8	112.58	79.35
n = 9	119.5	84.20
n = 10	126.07	88.79
n = 11	132.33	93.16
n = 12	138.22	97.34
n = 13	144.08	101.35
n = 14	149.64	105.22
n = 15	150.00	108.96
n = 16	-	112.58
n = 17	-	116.09
n = 18	-	119.5
n = 19	-	122.83
n = 20	-	126.07
n = 21	-	129.23
n = 22	-	132.33
n = 23	-	135.35
n = 24	-	138.32
n = 25	-	141.23
n = 26	-	144.08
n = 27	-	146.89
n = 28	-	149.64
n = 29	-	150.00

Rayleigh range ($2D^2/\lambda$) [133], which yields less than 5% measurement error of the true antenna response [134].

Antenna measurements were performed with the AUT operating in receive mode. The test range comprised a small fixed transmitter, and a heterodyne receiver attached to the AUT. The transmitter consisted of a 94 GHz Gunn oscillator (Farran Technologies GN-10), isolator, and a WR10 20 dBi corrugated feed horn. The small transmitter was placed atop a tall tripod support, located at a distance greater than the Rayleigh range, for the given AUT. The transmitter was powered from a small 18 V rechargeable battery pack, where power to the Gunn oscillator was regulated using a standard voltage regulator circuit. The heterodyne receiver consisted of a similar 94 GHz Gunn local oscillator (LO), a W-band balanced mixer (Farran Technologies BMC-10), DC-block, two (optional) low-noise amplifiers (Mini-circuits ZFL-500LN), with 14 dB gain at the chosen IF (≈ 400 MHz), and a spectrum analyser (HP8591E). The LO Gunn oscillator voltage was similarly regulated, and which was used to control the IF frequency using variable resistors incorporated into the regulator design. The IF spectrum obtained on the spectrum analyser was then recorded via a host computer using a GPIB interface. The test range yielded approximately 60 dB dynamic range.

The angular response of the AUT was then measured by characterising the received power as a function of rotation angle of the antenna around its vertical axis using a single axis turntable[10] (Parker Automation 21204RTMP). The turntable and measurements were automated via software control, which was developed using the ANSI C programming language.

A customised lens holder, and feed bracket were designed and fabricated, which offered accurate alignment of the lens and WR10 corrugated feedhorn. The antenna was placed at a height of 1.7 m ($> 4D$) above the ground, with the transmitter located approximately 60 m from the zone plates (far-field ~ 56 m). Figure 2.10 displays a photograph of the P = 4 WZPA located in the test range.

Figure 2.11 displays the measured far-field patterns for both the E- and H- planes for the P = 2, PMMA WZPA. Measurements were performed with

[10]accompanied by a STT57 stepper motor, and PDX15 controller.

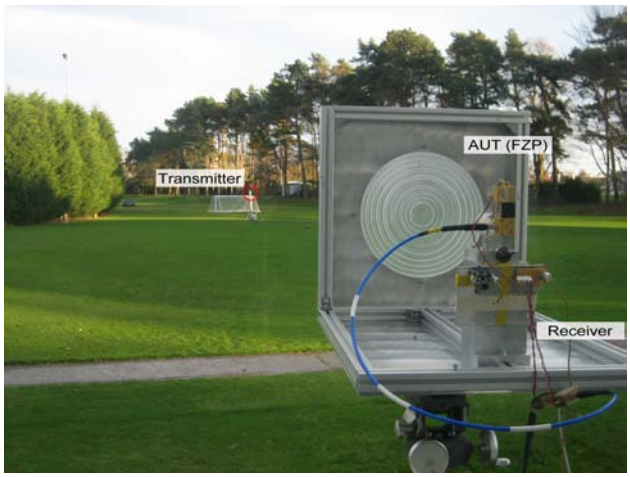

Figure 2.10: Photograph of the far-field test range used to measure the antenna performance of the WZPAs; the antenna-under-test (AUT) was the PMMA, P = 4, WZPA. The WZPA was orientated with the grooves facing the receiver, although measurements on both orientations showed negligible variations in the measured pattern for this design. The transmitter, indicated in the figure, was located approximately 60 m from the AUT.

a $40°$ field-of-view at $0.25°$ angular increments shown in Figure 2.11(a), and a $10°$ field-of-view at $0.10°$ angular increments shown in Figure 2.11(b).

The measured data indicates a highly symmetrical mainlobe, with excellent agreement between both planes. The average peak sidelobe level was measured as -22.3 ± 0.2 dB. The half power beam width, in both planes, was calculated using a least means square (LMS) algorithm and a fundamental Gaussian mode fitted to the top 4 dB of the mainlobe, which yielded $\theta_{\mathrm{hpbw}} = 0.79°$ ($R^2 = 1.00$, or goodness of fit) for both the E- and H-planes. This gives [133] a directivity of $D = 47.6$ dBi. The gain of the antenna was measured using the gain transfer method [135], and was found to be 42.4 ± 0.1 dBi, averaged between both planes. This gives an aperture efficiency of $\eta_{ap} = 30\%$, where numerical simulations suggest (Appendix B) an overall aperture efficiency of 27%.

Figure 2.11(c) shows a comparison between the measured H-plane data and numerical simulations performed using the Kirchoff diffraction integral method. The simulations were performed with: F = 490 mm, D = 300 mm, edge taper = -13 dB, t_L = 5.9 mm, and $\tilde{\epsilon}_r = 2.630 - 0.029j$. The compar-

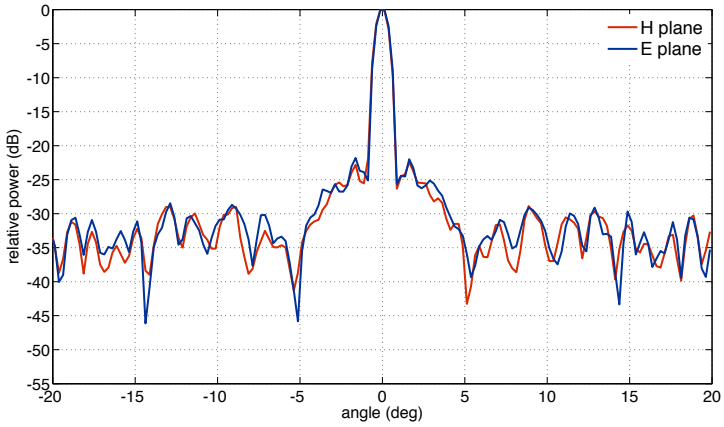

(a)

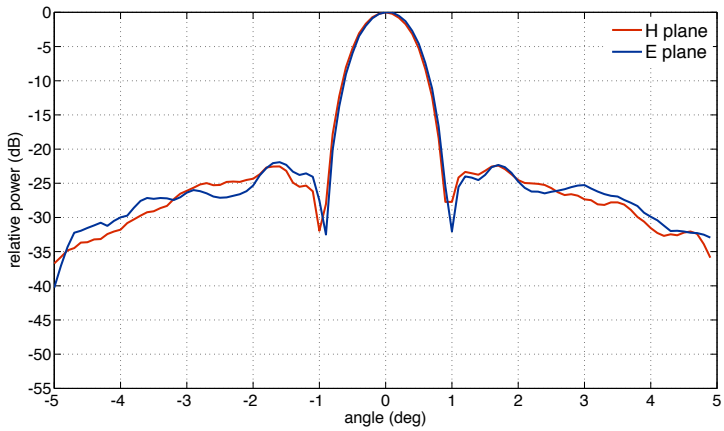

(b)

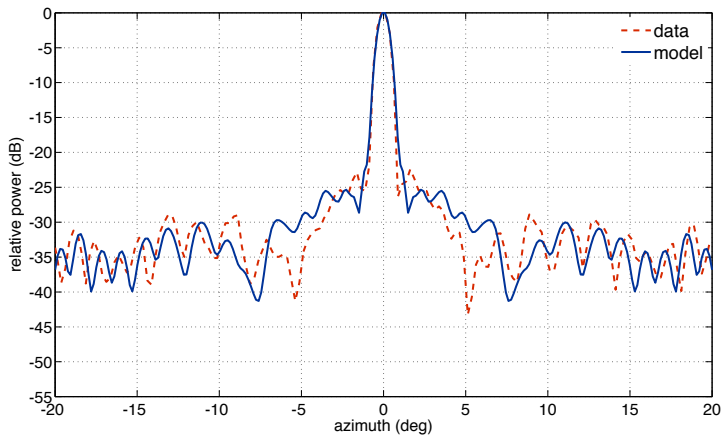

(c)

Figure 2.11: (a) Measured principle plane patterns for the $P = 2$, 300 mm, PMMA WZPA over $\pm$ 20° field-of-view, and (b) $\pm$ 10° field-of-view. (c) comparison between measured, and simulated, H-plane pattern using the Fresnel-Kirchoff model described earlier.

ison demonstrates excellent agreement around the mainlobe and the general sidelobe level, with similar patterns observed in both sidelobe envelopes. The sidelobe structure is shown to be less accurate close to the mainlobe, but still presents good agreement with the general trend and levels. Numerical simulations suggested a gain of 41.8 dBi, agreeing very well with the measured gain.

Figure 2.12 displays the principle plane patterns for the quarter-wave (P = 4) WZPA, measured as above. Similarly, Figure 2.12(a) displays the E- and H- plane patterns over a $40°$ field-of-view at $0.25°$ angular increments, with a $10°$ field-of-view at $0.10°$ angular increments shown in Figure 2.12(b).

The measured principle plane patterns, again, demonstrate excellent symmetry between both planes, with a well formed mainlobe; the marginal asymmetry in the low-level close-in sidelobes is a result of nearby foliage on a single direction of the test-range. The average peak sidelobe level is measured as -26.0 ± 1.5 dB, with a half-power beamwidth of $\theta_{\mathrm{hpbw}} = 0.79°$ ($R^2 = 0.99$), and $\theta_{\mathrm{hpbw}} = 0.81°$ ($R^2 = 1.00$) for the E- and H- plane, respectively. This gives a directivity of $D = 47.5$ dB. The gain was measured to be 45.8 ± 0.1 dBi, using the gain transfer method as before, which yields an aperture efficiency of $\eta_{ap} = 67\%$. This, again, agrees well with numerical simulations which suggest an aperture efficiency of 68%.

Figure 2.12(c) displays the comparison between the measured H-plane pattern and numerical simulations using the Kirchoff method, as before, all parameters remaining the same with P updated from 2 to 4. Numerical simulations suggest a gain of 47.5 dBi, which agrees well with the measured gain.

The slight asymmetry of the mainlobe for the P = 4 WZPA is believed to result from manufacturing tolerances, where the reduced groove widths, and depths, increased the difficulty in maintaining high accuracy whilst machining a plastic sheet. These problems are indicative of the restrictions imposed on realising greater than $P = 8$ designs, where increased manufacturing problems are significant in comparison to the improvements of the antenna gain obtained. The measurements discussed in Figure 2.12 suggest that even $P = 4$ designs present potential manufacturing difficulties, and thus the choice of

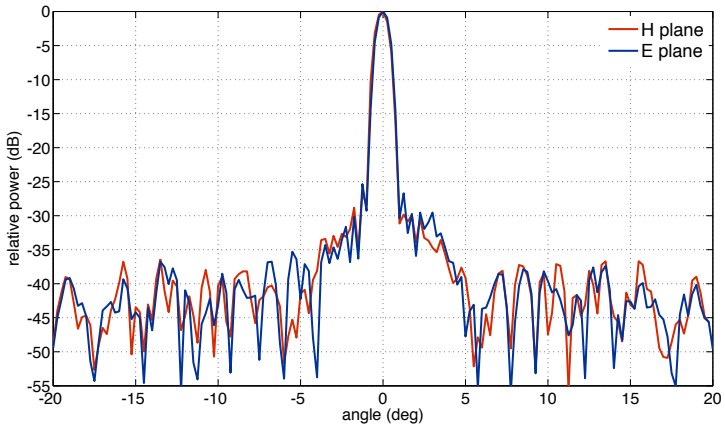

(a)

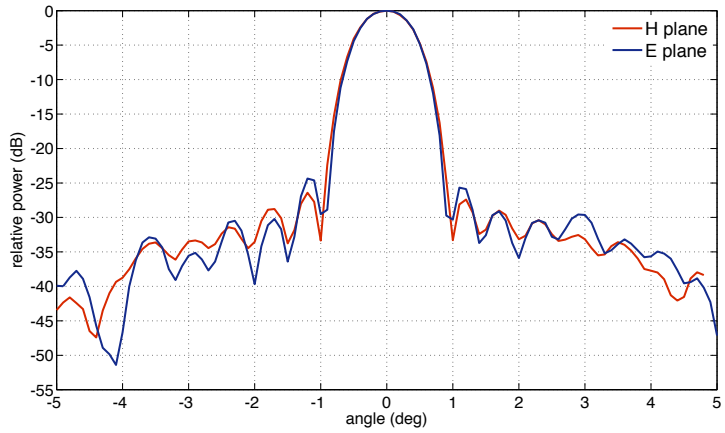

(b)

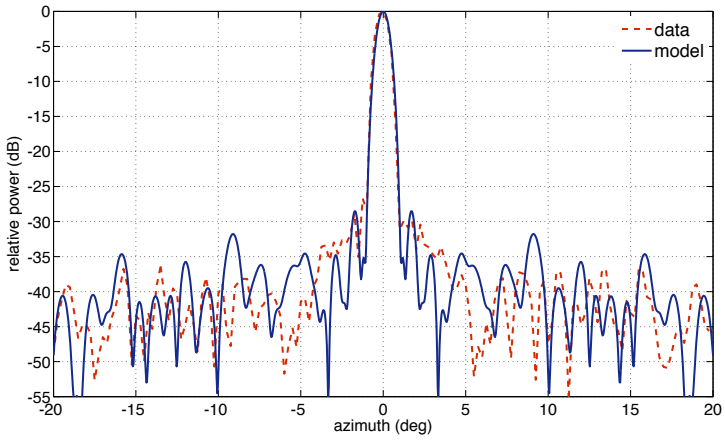

(c)

Figure 2.12: (a) Measured principle plane patterns for the $P = 4$, 300 mm, PMMA WZPA over $\pm\ 20°$ field-of-view, and (b) $\pm\ 10°$ field-of-view. (c) comparison between measured, and simulated, H-plane pattern using the Fresnel-Kirchoff model described earlier.

suitable dielectrics with good mechanical properties can be critical to the improvements offered by such designs.

2.5 Summary

An outline of the design of both blocking and phase-correcting Fresnel zone plates has been presented. Details of the optimisation and the limitations of each Fresnel zone plate type have been outlined, where the phase-correcting zone plates are shown to offer improved efficiency, bandwidth, and increased performance.

A new numerical model has been developed, which may be used to simulate the far-field performance of a grooved dielectric phase-correcting zone plate antenna, with arbitrary dielectric thickness, and permittivity. Using this model, and the optimisation required for the appropriate lens material, a range of phase-correcting zone plates were designed, fabricated, and characterised at 94 GHz. Details of the characterisation of each zone plate lens have been given, and are shown to agree well with the new numerical model.

Finally, the design and optimisation of zone plates, which has been outlined in this chapter, are critical for realising an optimised piFZPA. Further, the numerical Fresnel-Kirchoff model which has been introduced provides an important component to a model which is used to analyse the requirements of the piFZPA. The details of the piFZPA requirements, design and optimisation are discussed in Chapter 5, with the experimental characterisation of several designs detailed in Chapter 6.

chapter 3

Opto-excited semiconductors: free-carrier effective lifetime and carrier kinetics

Semiconductor substrate integral parameters such as the free-carrier lifetime, surface recombination rate, and defect-state density play a pivotal role in the modulation of (sub) mm-wave beams propagating through the substrate. The opto-excited properties of the substrate involve a complex spatial and temporal dependence that are dominated by surface recombination and diffusion effects, which result in lowered effective free-carrier plasma densities, and thus modular control of propagating (sub) mm-wave beams.

The following chapter presents an overview of the complex opto-excited free-carrier system, which yields insight into the limitations of optoelectronic modulation of propagating (mm-wave) beams. The discussion will focus on the effective lifetime parameter, τ_{eff}, arguably the most important control parameter; surface recombination effects, which lead to reduced effective lifetimes, and which in turn leads to increased optical irradiance requirements; and finally, free-carrier diffusion effects, which lead to increased effective free-carrier plasma densities and limited plasma spatial resolution.

3.1 Introduction

Illumination of a semiconductor substrate with photons whose energy exceeds the semiconductor bandgap ($E > E_g$), depicted in Figure 3.1, results in the generation of a free-carrier electron-hole plasma, the density of which is linearly dependent on the minority-carrier lifetime. The free-carrier lifetime parameter is well regarded as the most important substrate parameter in most applications due to its influence on several substrate characteristics. In particular, for optoelectronic mm-wave devices the free-carrier lifetime dictates the free-carrier plasma density, free-carrier diffusion and thus spatial resolution, and free-carrier kinetics. The free-carrier lifetime is also taken as an indicator to the overall quality of the semiconductor substrate, with its relative magnitude being determined by both the density of defect-states in the bulk and at the surface of the substrate, and to a lesser extent the band structure of the semiconductor. The density of surface defect-states is known to dominate the relative effective lifetime of a given substrate. The following discussion focuses on the density of surface defect-states of a given optoelec-

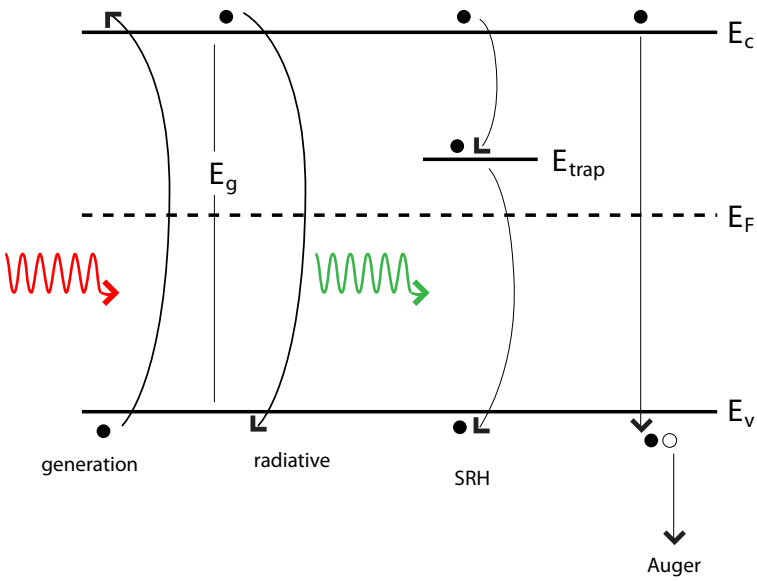

Figure 3.1: Energy band diagram highlighting important features of the semiconductor substrate, including the recombination and generation processes.

tronic device, where increased modulation of propagating mm-wave beams, by excitation at shorter-wavelengths, can be realised with reduced surface defect-state densities, thus increasing the attractiveness of such devices at (sub) mm-wave frequencies.

Excitation of a free-carrier plasma which results from an increased generation rate above thermal equilibrium, U_g, correspondingly results in an increased recombination rate (above thermal equilibrium), U_r, until a new equilibrium is attained. The rate of recombination, U_r, is a function of the free-carrier plasma density, and includes several recombination mechanisms that reduce the opto-excited plasma density; these include radiative, defect-state, or Auger recombination [136] (see Figure 3.1). In general, each loss mechanism features a unique characteristic injection-level dependent lifetime. As a result, the free-carrier lifetime is commonly referred to the *effective* lifetime, which is the cumulative sum of each individual characteristic lifetime, subject to the substrate properties. In addition, each recombination mechanism can be separated into both volume (bulk) or surface effects [137, 138].

Bulk recombination can be suitably controlled by proper high quality growth methods, such as the float-zone technique, which lowers the impurity concentration and bulk defect levels, thus increasing the defect-state lifetime. In comparison, Auger recombination is characteristically a high-injection process, which dominates for free-carrier plasma densities exceeding $\approx 10^{17}\ \mathrm{cm}^{-3}$ [136]. Comparatively, radiative recombination (fluorescence) can be neglected for indirect bandgap semiconductors (such as silicon), where the requirement for additional phonon excitations in order to conserve momentum reduce the probability of recombination [139]. Loss mechanisms which are then attributed to defect-level recombination at, or near, the substrate surface dominate the effective lifetime. Surface defect-level recombination, or Shockley-Read-Hall (SRH) recombination [140, 141], is a significant source of lowered lifetimes in **all** wafers, and results from surface impurities, lattice defects, or non-saturated (*dangling*) bonds.

The relative lifetime of the surface recombination mechanism is typically denoted by the surface recombination velocity (SRV), S $(\mathrm{cm/s})$, the effects of which are given by the roots of the transcendental equation

$$\cot\left(\frac{\alpha_m d}{2}\right) = \frac{2D}{Sd} \cdot \frac{\alpha_m d}{2}, \tag{3.1}$$

with substrate thickness, d, carrier diffusion coefficient, D, SRV, S, and the mth root, α_m, indicating the mth surface decay mode [138,142]. The lifetime of each mth characteristic decay mode, which are both injection-level and temporally dependent, are such that $\tau_1 > \tau_2 > \ldots \tau_m$. Thus, under (quasi-) CW irradiation, the surface component of the effective lifetime is given by the fundamental mode of surface recombination, τ_1, or [142, 143]:

$$\frac{1}{\tau_s} = \alpha_1^2 D, \tag{3.2}$$

which yields the effective lifetime:

$$\frac{1}{\tau_{\text{eff}}} = \left(\frac{1}{\tau_{SRH}} + \frac{1}{\tau_{Auger}} + \frac{1}{\tau_{rad}}\right) + \frac{1}{\tau_s} \tag{3.3}$$

$$\frac{1}{\tau_{\text{eff}}} = \frac{1}{\tau_b} + \frac{1}{\tau_s}, \tag{3.4}$$

with bulk lifetime, τ_b; this gives the common effective lifetime expression

$$\frac{1}{\tau_{\text{eff}}} = \frac{1}{\tau_b} + \alpha_1^2 D. \tag{3.5}$$

Thus, it is clear from (3.1) and (3.5) that the effective lifetime of a given substrate will be dependent on both the SRV and the substrate thickness, d. The severity of this dependency can be found by analysing (3.1) for different values of S, and d. Figure 3.2 displays the corresponding changes to the effective lifetime as a function of both parameters.

Figure 3.2(a) displays the normalised (relative to the bulk lifetime) effective lifetime as a function of the substrate thickness, d, highlighting the significance of the SRV as d is reduced. It is observed that for a given SRV, the effect of surface recombination becomes less significant as the substrate thickness increases, which is attributed to the diffusion limited response of the excited free-carrier plasma. In addition, the overall reduction in τ_{eff} is shown to reduce as the SRV is decreased.

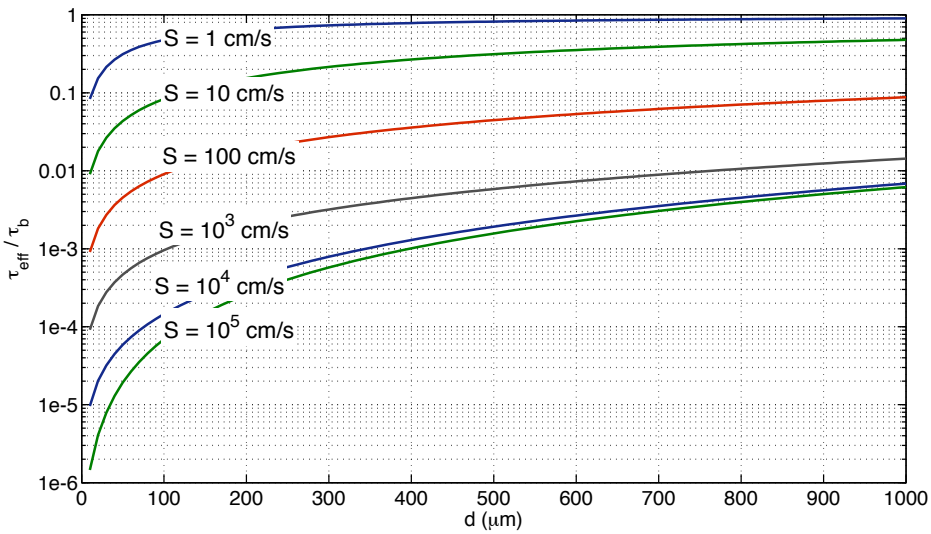

(a)

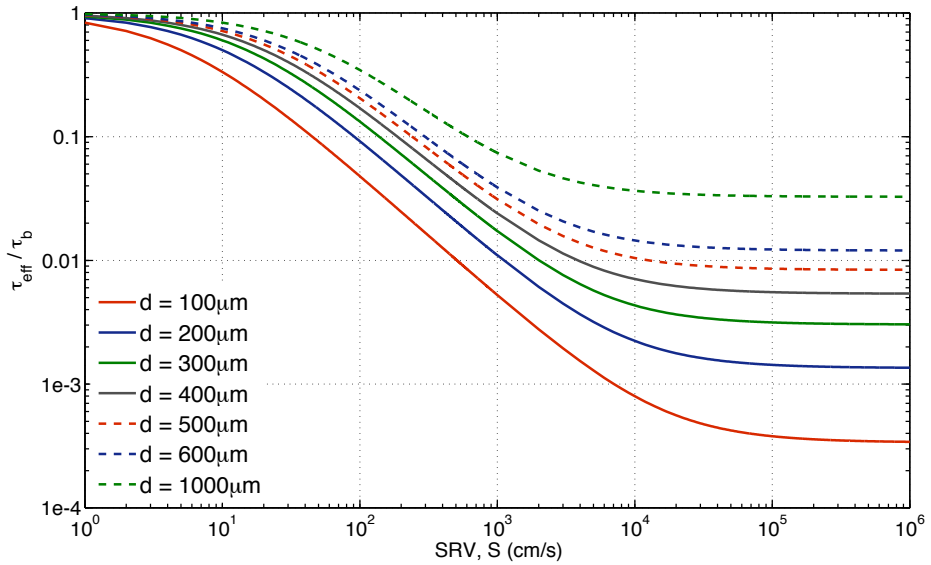

(b)

Figure 3.2: Simulated effective lifetime, τ_{eff}, as a function of (b) SRV, S (cm/s), and (a) wafer thickenss, d. Both figures have been normalised to the substrate bulk lifetime, τ_b.

Figure 3.2(b) displays the normalised effective lifetime for a high resistivity substrate as a function of SRV. It is shown that an increase in the SRV results in large reductions of the effective lifetime; the saturation level again indicating the diffusion limited case. It is also observed that the diffusion limited saturation point occurs for lower values of S, as the substrate thickness is increased.

Saturation of the recombination rate by either an infinitely large SRV or substrate thickness results in two asymptotic solutions to (3.1). The combination of both solutions has been shown to give a simplified form for the effective lifetime [136, 144]:

$$\frac{1}{\tau_{\text{eff}}} = \frac{1}{\tau_b} + \left(\frac{d}{2S} + \frac{1}{D} \left[\frac{d}{\pi} \right]^2 \right)^{-1}, \tag{3.6}$$

which indicates the non-diffusion and diffusion limited recombination cases.

From Figure 3.2, surface recombination is shown to significantly influence the overall magnitude of the effective lifetime parameter. The relative change, or degradation, of the effective lifetime parameter is equivalent to a change in the effective plasma density, thus suppressing the modulation of mm-wave propagation constants for a given illumination level. Optimising the influence of surface recombination, with either increased substrate thicknesses or lowered SRVs, is critical for increasing the impact of optoelectronic modulation of the complex permittivity at a given optical irradiance. In most circumstances, lowered SRVs are to be preferred for several reasons which will be discussed.

3.2 Effective free-carrier plasma density

Optoelectronic modulation of the transmission properties of an opto-excited semiconductor substrate is determined by the complex permittivity of the substrate. Thus, the modulation is determined by the effective free-carrier plasma density throughout the substrate, knowledge of which is required for the design and analysis of reconfigurable devices. However, calculation of this

parameter proves to be complex due to the range of carrier dynamic processes which take place under optical excitation. No closed form solution exists as a result, and thus only an approximation to the photo-injected density is possible.

The following method of estimating the effective optically excited free-carrier plasma density has been derived for (quasi-) CW irradiation, i.e. a stationary state. Assuming charge neutrality, with no surface recombination, and excitation by a delta function, the free-carrier plasma density is given by the common expression, under equilibrium,

$$U_r = U_g \tag{3.7}$$

$$\frac{\Delta n}{\tau_{\text{eff}}} = (1-R)\frac{I_{\text{opt}}\lambda\alpha_\lambda}{hc}; \tag{3.8}$$

with

$$E_{\text{photon}} = \frac{hc}{\lambda}, \tag{3.9}$$

and where I_{opt} defines the incident optical excitation density (mW/cm^2) at wavelength λ; α_λ defines the wavelength dependent absorption coefficient within the semiconductor; $h,\ c$ define Planck's constant, and the speed of light in a vacuum; τ_{eff} defines the effective lifetime; $(1-R)$ defines the optical power transmission across the air/semiconductor interface, where R denotes the (power) reflection coefficient, given later by (4.11); and Δn denotes the free-carrier plasma density[1] (electrons, Δn, and holes, Δp).
Re-arranging for the excess carrier density, Δn, yields the common expression

$$\Delta n_0 = (1-R)\frac{I_{\text{opt}}\lambda\alpha_\lambda}{hc}\tau_{\text{eff}}, \tag{3.10}$$

assuming perfect quantum efficiency; the subscript 0 has been added to represent the initial peak free-carrier density.

However, (3.10) generally overestimates the effective free-carrier plasma density, which is reduced due to surface recombination and diffusion effects.

[1] Δn is chosen as representing the excess carrier density, since $\Delta n = \Delta p$

Neglecting lateral diffusion, i.e. orthogonal to the optical excitation direction, the spatial distribution can be approximated using a 1D analysis.

Integration of the free-carrier plasma distribution, generated by an optical excitation source of a given wavelength (assuming CW conditions), throughout the substrate thickness gives the effective plasma density optically excited within the substrate. The spatial distribution, or profile, of a free-carrier plasma generated by optical excitation of a semiconductor substrate is governed by the 1D ambipolar diffusion equation [145]

$$D_a \frac{\partial^2}{\partial z^2} \Delta n(z) = \frac{\Delta n(z)}{\tau_a} - G e^{-\alpha_\lambda z}, \tag{3.11}$$

which has been shown to yield [53]

$$\Delta n(z) = \frac{\Delta n_0}{1 - \alpha_\lambda^2 L_a^2} \left[e^{-\alpha_\lambda z} - \frac{\alpha_\lambda L_a^2 + S\tau_{\text{eff}}}{L_a + S\tau_{\text{eff}}} e^{-z/L_a} \right] \quad 0 \leq z \leq \infty \tag{3.12}$$

where under low-injection, the ambipolar diffusion coefficient, D_a, and lifetime parameter, τ_a, attain their minority carrier values [145]. The free-carrier generation rate, G, is given by $\Delta n_0/\tau_{\text{eff}}$, with Δn_0 being defined by (3.10). The parameters L_a, S define the ambipolar diffusion length and SRV respectively. These are typically $L_a = 170\ \mu\text{m}$ ($\tau \approx 10\ \mu\text{s}$) and $S > 10^6\ \text{cm/s}$ for low quality silicon. The effective plasma density, Δn_{eff}, follows the summation over the substrate thickness:

$$\Delta n_{\text{eff}} = \frac{1}{d} \int_0^d \Delta n(z)\ \mathrm{d}z \tag{3.13}$$

$$= \frac{\Delta n_0}{d(1 - \alpha_\lambda L_a^2)} \left[\frac{1}{\alpha_\lambda} \left(1 - e^{-\alpha_\lambda d}\right) - \frac{\alpha_\lambda L_a^2 + S\tau_{\text{eff}}}{L_a + S\tau_{\text{eff}}} L_a \left(1 - e^{-d/L_a}\right) \right]. \tag{3.14}$$

where the initial plasma density, Δn_0, is given by (3.10).

Using the measured optical wavelength-dependent absorption coefficient,

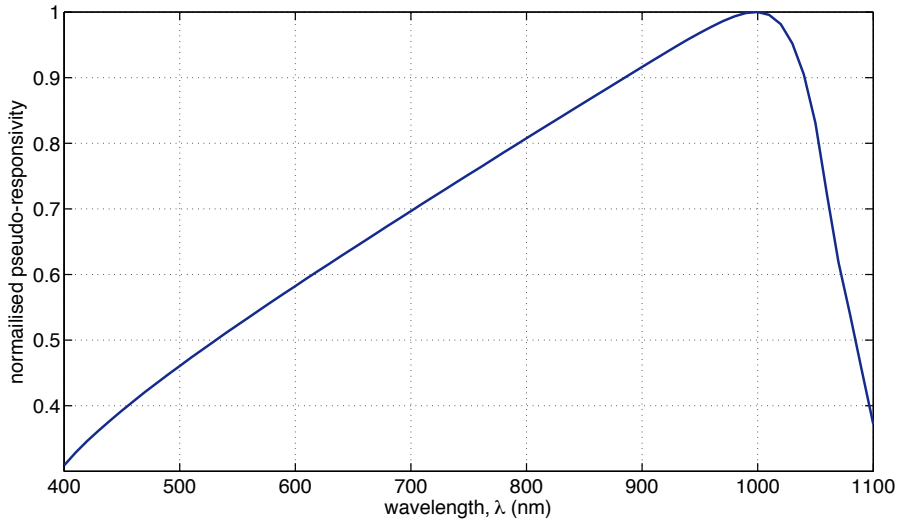

(a)

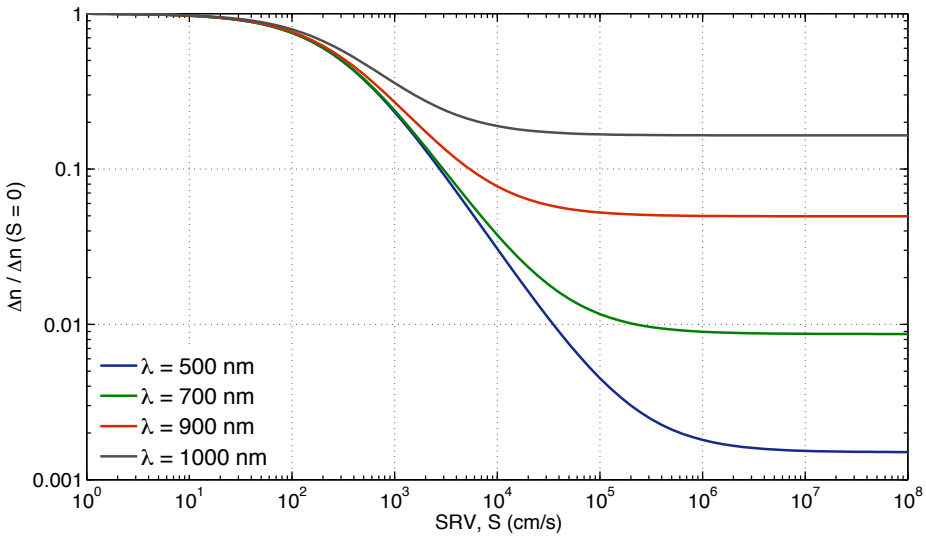

(b)

Figure 3.3: (a) Simulated normalised excess carrier density as a function of excitation wavelength, λ. (b) normalised excess carrier density as a function of SRV, for a range of wavelengths, λ; substrate thickness, $d = 500\ \mu\mathrm{m}$

α_λ, from Green and Keevers [146] the effective plasma density as a function of wavelength can be calculated. This yields the spectral response of the silicon substrate, with the peak being determined by the values of α_λ. For the data of Green and Keevers, the peak response of silicon, shown in Figure 3.3(a), corresponds to $\approx 1\ \mu\mathrm{m}$, or near the silicon bandgap.

Equation (3.14) can also be used to indicate the wavelength dependence of the effective plasma density as a function of the SRV; this is shown in Figure 3.3(b). It is observed that in all cases, the effective plasma density is reduced as the SRV increases until a saturation level is reached, corresponding to the diffusion limited case, as observed in Figure 3.2(b). Furthermore, the point of saturation is shown to vary as a function of excitation wavelength, which results from the change in absorption coefficient, i.e. shorter wavelengths yield increased carrier concentrations nearer the surface.

However, and most importantly, the relative change in the effective plasma density is shown to be independent of the excitation wavelength for $S < 500\ \mathrm{cm/s}$, where Figure 3.3(b) represents one particular substrate thickness. Hence, for reasonable surface qualities, the effective plasma density can be equally generated by shorter-wavelength excitation as conventional near-bandgap wavelengths, albeit requiring a modest increase in the irradiation level due to the reduced responsivity of the substrate. This subtlety is an important result as shorter (visible) wavelength excitation extends optoelectronic modulation of the substrate to more conventional technologies, thus reducing the complexity, cost, and increasing flexibility.

3.3 Free-carrier plasma dynamics

The effective plasma density dependent complex permittivity of an opto-excited substrate is a function of both time and space, owing to the dynamic change in carrier recombination and diffusion processes. Thus, the modulation of mm-wave propagation within an opto-excited substrate at mm-wave frequencies changes as a function of time, and spatial distribution of the optically excited plasma. The following sections describe the temporal variation

of the plasma distribution as a result of pulsed excitation, followed by a discussion on the spatial distribution of the plasma in the (quasi-) CW state. Each discussion indicates the dependence on both surface recombination and diffusion effects.

3.3.1 Transient response

Although this thesis will be particularly focused on the (quasi-) CW operation, it will be pertinent to discuss the transient case. In addition to helping understand the interpretation of the lifetime measurements discussed in Section 3.5, consideration of the transient case will also help identify some key features of the effective lifetime.

The transient response ($t_{\mathrm{pulse}} \ll \tau_{\mathrm{eff}}$) of a free-carrier plasma was first described mathematically by McKelvey [142] and further developed by Luke and Cheng [143]. Although the analysis was performed for low-level injection, the results of the analysis are still useful for current discussions.

The transient response of the effective plasma density is obtained, as above, by integrating the spatial plasma profile over the substrate thickness, $1/d \int_0^d \Delta n(x,t)\ \mathrm{d}x$, which has been shown to yield the following solution for a Gaussian pulse [143]

$$\begin{aligned}
\Delta n(t) \;=\; & \frac{4\Delta n_0 e^{-\alpha_\lambda d/2}}{d} \sum_{m=1}^{\infty} \frac{\sin\left(\frac{\alpha_\lambda d}{2}\right) e^{\left(0.5[\sigma\tau_m]^2\right)}}{\left(\alpha_\lambda^2+\alpha_m^2\right)\left(\alpha_m d+\sin(\alpha_m d)\right)} \\
& \mathrm{x}\left[\alpha_\lambda \sinh\left(\frac{\alpha_\lambda d}{2}\right)\cos\left(\frac{\alpha_m d}{2}\right)\right. \\
& \qquad \left. + \alpha_m \cosh\left(\frac{\alpha_\lambda d}{2}\right)\sin\left(\frac{\alpha_m d}{2}\right)\right]\ldots \\
& \mathrm{x}\left[\mathrm{erf}\left(\frac{t_0}{\sqrt{2}\sigma}+\frac{\sigma}{\sqrt{2}}\tau_m\right)\right. \\
& \qquad \left. - \mathrm{erf}\left(-\frac{(t-t_0)}{\sqrt{2}\sigma}+\frac{\sigma}{\sqrt{2}}\tau_m\right)\right] e^{-\tau_m(t-t_0)}, \qquad (3.15)
\end{aligned}$$

where the full spatial and temporal plasma distribution is denoted by $\Delta n(x,t)$ [142, 143, 147], and where 2σ defines the pulse width, t_0 the peak point (in time) of the pulse, τ_m the lifetime of the mth decay mode (see (3.4)), and $\mathrm{erf}(x)$ the error function $2/\sqrt{\pi}\int_0^x e^{-t^2}\,\mathrm{d}t$.

Figure 3.4(a) displays the simulated decay transient of an opto-excited substrate using (3.15) with: $2\sigma = 0.3\ \mu\mathrm{s}$, $t_0 = 0.6\ \mu\mathrm{s}$, $\tau_b = 1,000\ \mu\mathrm{s}$, $S = 10^3, 10^6\ \mathrm{cm/s}$, $d = 600\ \mu\mathrm{m}$, and for $\lambda = 500, 700, 900, 1000\ \mathrm{nm}$, which highlights several features of the free-carrier plasma.

Firstly, the transient decay is shown to be initially non-linear, which results from the higher order surface decay modes. Such surface effects are shown to be pronounced for shorter wavelengths and higher SRVs, due to the increased concentration of excess carriers generated near the surface. The wavelength dependent non-linear decay can be utilised for separating the measured bulk and surface lifetimes of a given sample, either by a multi-wavelength pump-probe method [148–150], or the multi-slope technique [143, 151, 152].

Secondly, the effective lifetime, indicated by the decay asymptote, is shown to be independent of wavelength, corresponding to the fundamental surface decay mode; the decay asymptote is shown in Figure 3.4(b), which displays the normalised instantaneous lifetime, τ_0/τ_b, for each excitation wavelength. The wavelength invariance may not be initially intuitive given the varying significance of S with excitation wavelength, but is equally an important result, with several practical advantages.

Finally, the time for decay to below a predefined threshold is shown to change depending on excitation wavelength and SRV. Modulating the substrate at the maximum refresh rate of the opto-excited plasma, commonly accepted as $1/\tau_{\mathrm{eff}}$, can thus lead to a reduced dynamic range in the optically modulated beam. For example, using (3.6) with $d = 600\ \mu\mathrm{m}, \mathrm{S} = 10^6\ \mathrm{cm/s}$, giving an effective lifetime of $\tau_{\mathrm{eff}} = 12\ \mu\mathrm{s}$, corresponds to a decay of between 60% and 80% of the initial plasma density, depending on the excitation wavelength. In effect, the general refresh rate of the plasma instead becomes $\approx 1/2\tau_{\mathrm{eff}}$ in order to ensure sufficient decay; increased refresh rates may be achieved by implementing shorter excitation wavelengths, albeit slightly depending on the substrate SRV.

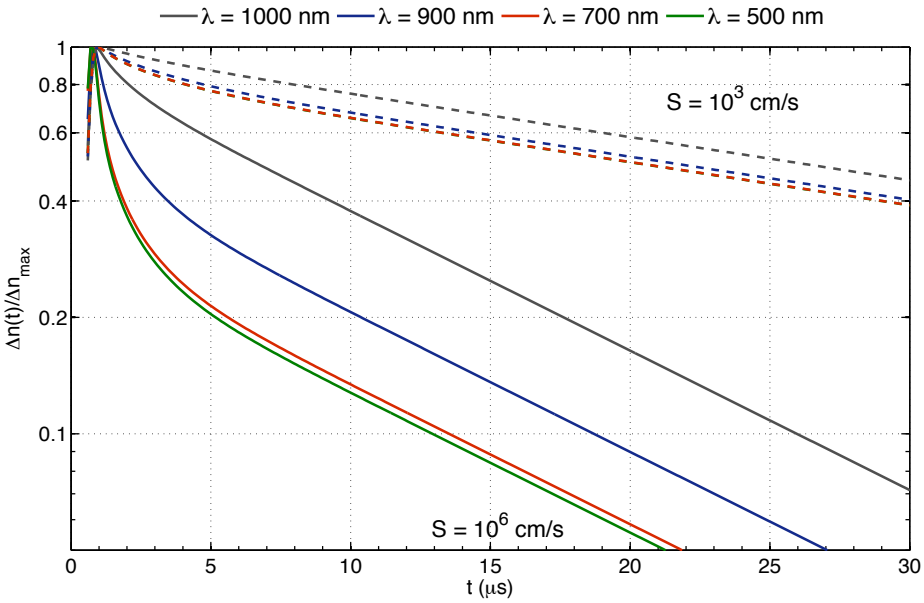

(a)

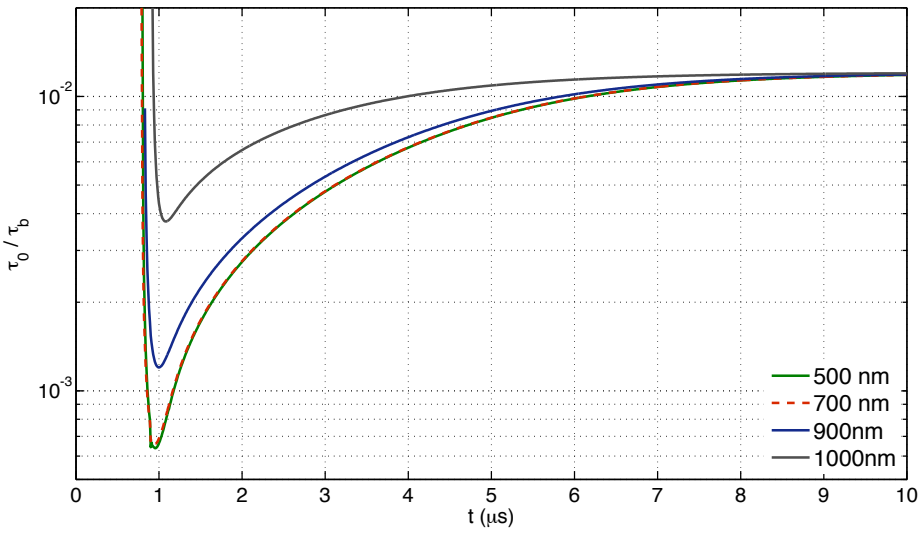

(b)

Figure 3.4: (a) Simulated decay transient for an optically excited plasma with excitation wavelengths $\lambda = 500, 700, 900, 1000$ nm. The transients are shown for $S = 10^3$ (- -), and 10^6 cm/s (–). (b) Simulated instantaneous lifetime, τ_0 for (a) with $S = 10^6$ cm/s. ($1/\tau_0 = -\frac{\mathrm{d}}{\mathrm{d}t}\ln[\Delta n(t)]$; see [143], eq. (11), (12a-b).)

3.3.2 Steady-state response

Having discussed the temporal properties of the free-carrier plasma under pulsed excitation, it is now relevant to discuss the spatial distribution and the corresponding effects on the effective plasma density under (quasi-) CW illumination.

The 3D spatial distribution of an opto-excited plasma is described by the time-independent ambipolar continuity equation. Using a zero-field, quasi-neutral approximation this can be written as [145, 153]

$$D_a \nabla^2 \Delta n(r,z) - \frac{\Delta n(r,z)}{\tau_a} = -G(r,z), \tag{3.16}$$

where $G(r,z)$ defines the generating function, D_a the ambipolar diffusion coefficient, τ_a the ambipolar effective lifetime, and $\Delta n(r,z)$ the excess electron-hole plasma density. The ambipolar parameters are a function of excess carrier density, Δn, and are given by [145]

$$D_a = \frac{(p+n)D_n D_p}{pD_p + nD_n} \tag{3.17}$$

$$\tau_a = \frac{p+n+2n_i}{p_0+n_0+\Delta n}\tau_{\text{eff}}, \tag{3.18}$$

where n_0, p_0 define the thermal equilibrium electron and hole concentrations, n, p the total excess carrier concentrations of electrons and holes, and n_i defines the intrinsic carrier concentration as given by the law of mass action [139, 145]. Under low-injection, the ambipolar parameters reduce to their minority counter parts, and are independent of Δn. While the solution of (3.16) is commonly treated in a 1D approximation [52, 53, 65], it will be pertinent for later discussions to include radial diffusion effects when understanding the limitations of an optically encoded mask, such as a Fresnel zone plate. The particular method used for solving (3.16) follows from the method reported by Gary *et al.* [153]. In this method the complexity is reduced by appealing to the rotational symmetry of the problem. Using cylindrical geometry, the solution to (3.16) can be found by utilising the Han-

kel transform [154], where transformation to Hankel space yields a simplified analysis [153, 155, 156].

Within the scope of this thesis the most appropriate generation function, $G(r, z)$, would be that which represents uniform illumination, i.e. a top-hat function ($G(r) = \Theta(r),\ 0 \leq r \leq a$). However, fast Fourier transformations of the top-hat function result in long computation times and problems with Gibbs phenomena due to discontinuities in the illuminating function. While the computation time could be reduced by implementing particular fast Hankel transform algorithms [157–160], Gibbs phenomena often lead to difficult interpretation of diffusion effects, which are of interest due to being an indicator of spatial limitations of the optically excited plasma. To ameliorate these problems, a continuous generation function was adopted, chosen to be a Gaussian profile, as originally discussed by Gary *et. al.*. The 3D generation function, $G(r, z)$, is then given by the product of a radial Gaussian beam and Beer's law [161], and thus (3.16) can be re-written as

$$D_a \nabla^2 \Delta n(r, z) - \frac{\Delta n(r, z)}{\tau_a} = -g \exp\left(\frac{-2r^2}{\omega_0^2} - \alpha z\right), \tag{3.19}$$

where ω_0 defines the Gaussian beam waist, and g defines the initial generation rate, i.e. $\Delta n_0/\tau_{\text{eff}}$ with Δn_0 being defined by (3.10).

Inserting the cylindrical from of the Laplacian, normalising all distances by the ambipolar diffusion length $L_a = (D_a \tau_a)^{1/2}$, and with: $\rho = r/L_a$, $\xi = z/L_a$, $\eta = \sqrt{2} L_a/\omega_0$, $\varepsilon = \alpha_\lambda L_a$, $\delta n = g\tau_a$, and using $h(\rho, \xi) = \Delta n(r, z)/\delta n$ as representing the plasma distribution in Hankel space, (3.19) then gives the following dimensionless form of the ambipolar continuity equation in 3-dimensions

$$\begin{aligned} &\frac{\partial^2}{\partial \xi^2} h(\rho, \xi) + \frac{\partial^2}{\partial \rho^2} h(\rho, \xi) + \ldots \\ &\qquad \ldots \frac{1}{\rho} \frac{\partial}{\partial \rho} h(\rho, \xi) - h(\rho, \xi) = -\exp\left(\eta^2 \rho^2 - \varepsilon \xi\right). \end{aligned} \tag{3.20}$$

Using the standard Hankel transforms [154]

$$\bar{h}(\nu,\xi) = \int_0^\infty \rho J_0(\nu\rho) h(\rho,\xi) \mathrm{d}\rho \tag{3.21a}$$

$$h(\rho,\xi) = \int_0^\infty \nu J_0(\nu\rho) \bar{h}(\nu,\xi) \mathrm{d}\rho, \tag{3.21b}$$

and noting the standard relations [153]

$$\int_0^\infty \rho J_0(\nu\rho) \left[\frac{\partial^2}{\partial\rho^2} h(\rho,\xi) + \frac{1}{\rho}\frac{\partial}{\partial\rho} h(\rho,\xi)\right] \mathrm{d}\rho = -\nu^2 \bar{h}(\nu,\xi) \tag{3.22}$$

$$\int_0^\infty \rho J_0(\nu\rho) \left[-\exp\left(-\eta^2\rho^2 - \varepsilon\xi\right)\right] \mathrm{d}\rho = -\frac{\exp\left(-\nu^2/4\eta^2 - \varepsilon\xi\right)}{2\eta^2}, \tag{3.23}$$

(3.20) reduces to a 2nd order ordinary differential equation

$$\frac{\mathrm{d}^2}{\mathrm{d}\xi^2}\bar{h}(\nu,\xi) - (\nu^2+1)\bar{h}(\nu,\xi) = -\frac{\exp\left(-\nu^2/4\eta^2 - \varepsilon\xi\right)}{2\eta^2}. \tag{3.24}$$

This standard form has the general solution

$$\bar{h}(\nu,\xi) = A_1 e^{\left(-\xi\sqrt{\nu^2+1}\right)} + A_2 e^{\left(\xi\sqrt{\nu^2+1}\right)} + A_p e^{\left(-\frac{\nu^2}{4\eta^2} - \varepsilon\xi\right)}, \tag{3.25}$$

obtained from the sum of the homogenous and particular solutions. The constant A_p follows from the particular solution, and can be shown to be given by

$$A_p = \left[2\eta^2(\nu^2 + 1 - \varepsilon^2)\right]^{-1}. \tag{3.26}$$

The coefficients A_1, A_2 are found from the surface recombination boundary conditions; in Hankel space, these can be written as [153]

$$\begin{aligned} S_0\bar{h}(\nu,\xi=0) &= \chi\frac{\partial}{\partial\xi}\bar{h}(\nu,\xi)\Big|_{\xi=0} \\ S_d\bar{h}(\nu,\xi=b) &= -\chi\frac{\partial}{\partial\xi}\bar{h}(\nu,\xi)\Big|_{\xi=b} \end{aligned} \tag{3.27}$$

where S_0, S_d define the SRV at the front and back surfaces, and $b = d/L_a$, $\chi = L_a/\tau_a$. Using (3.27) and substituting the expression for $\bar{h}(\nu, \xi)$ gives two simultaneous equations which can be solved to give expressions for the coefficients A_1, A_2, which are dependent on the surface recombinations at the front and back surfaces. This can be shown to give

$$A_2 = \gamma \frac{(S_0 + \chi\varepsilon)(S_b - \chi\varpi)e^{-b\varpi} + (\chi\varepsilon - S_b)(S_0 + \chi\varpi)e^{-\varepsilon b}}{(S_b + \chi\varpi)(S_0 + \chi\varpi)e^{b\varpi} - (S_0 - \chi\varpi)(S_b - \chi\varpi)e^{-b\varpi}} \quad (3.28)$$

$$A_1 = -\frac{A_2(S_0 - \chi\varpi) + \gamma(S_0 + \chi\varepsilon)}{S_0 + \chi\varpi}, \quad (3.29)$$

where the following parameters have been introduced for simplification:

$$\gamma = A_p \exp\left(-\frac{\nu^2}{4\eta^2} - \varepsilon\xi\right) \quad (3.30)$$

$$\varpi = \sqrt{\nu^2 + 1}. \quad (3.31)$$

The spatial distribution of the free-carrier plasma, $\Delta n(r, z)$, is then obtained by performing the inverse Hankel transform, (3.21), which was performed using the *quadl* function in Matlab.

For completeness, the solutions to the above transforms for a top-hat illumination function are given in Appendix C.

The Hankel transform method then serves as an invaluable tool for investigating the spatial limitations imposed by the semiconductor substrate.

3.3.2.1 Longitudinal profile dependence

The first profile dependence to be discussed will be that of the longitudinal component, or the excess carrier concentration throughout the wafer. For all simulations discussed, a high-resistivity silicon substrate is assumed. This method, however, is equally applicable to any other semiconductor.

The penetration depth of the excess carrier profile is typically expressed via the absorption coefficient, i.e. $1/\alpha_\lambda$, which is valid only in situations where diffusion effects are negligible (e.g. transient response). For situations in

which diffusion is non-negligible, the plasma penetration depth through the substrate increases, as shown in Figure 3.5. The simulations were performed with $\lambda = 1000$ nm and $d = 500$ μm, using the lifetime parameters outlined in Table 3.1. The diffusion, and its significance, is dependent on the (effective) ambipolar lifetime, given by $L_a = (D_a \tau_a)^{1/2}$.

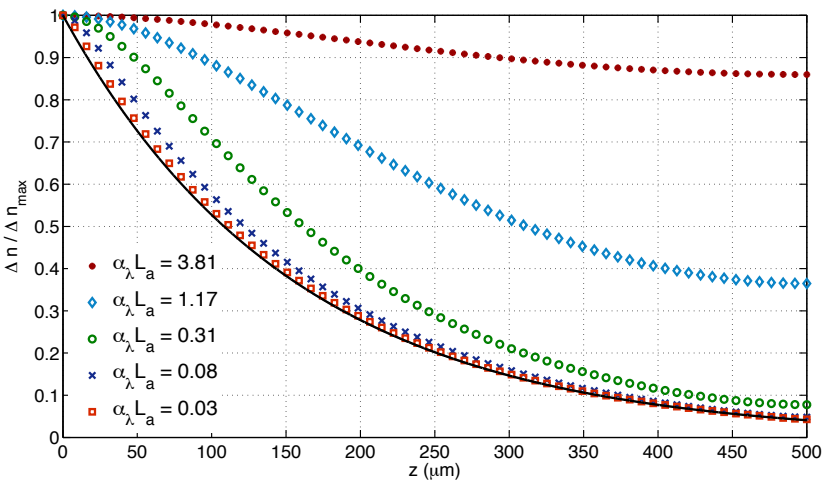

Figure 3.5: Simulated longitudinal (r = 0) excess carrier profile as a function of the ambipolar effective lifetime (or L_a), indicating the non-negligible diffusion as $\alpha_\lambda L_a \geq 1$. Solid line represents the ideal $1/\alpha_\lambda$ decay, defined by Beer's law.

The plasma penetration depth is determined either by the ambipolar diffusion length or the absorption depth, given by Beer's law, depending on which is larger, the former being true when $\alpha_\lambda L_a > 1$, shown in Figure 3.5; diffusion then becomes significant in substrates of large effective lifetimes.

Figure 3.6 displays the three-dimensional plasma profile within a silicon substrate with an effective lifetime of $\tau_{\text{eff}} = 10,\ 100$, and 1000 μs, with an optical excitation wavelength of $\lambda = 800$ nm. The silicon wafer was of 5 cm diameter, and was excited by an optical Gaussian beam, with a $\omega_0 = 1$ cm beam waist. The increase in effective lifetime, and thus diffusion length,

Table 3.1: Simulated effective lifetimes.

τ_{eff}	100 μs	10 μs	1 μs	0.1 μs	0.01 μs
$\alpha_\lambda L_a$	3.81	1.17	0.31	0.08	0.03

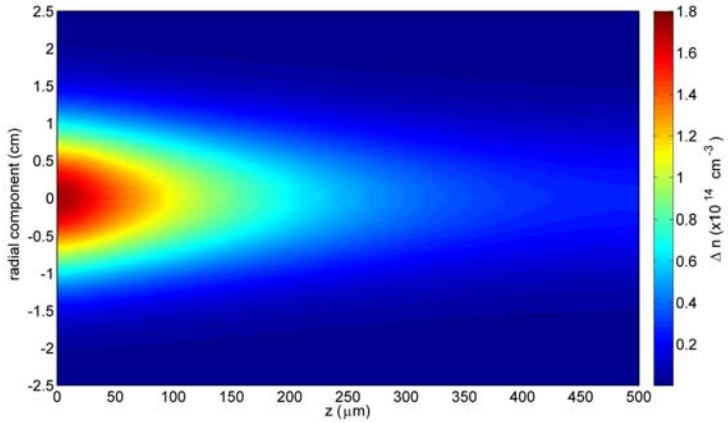

(a) $\tau_{\text{eff}} = 10\ \mu\text{s}$

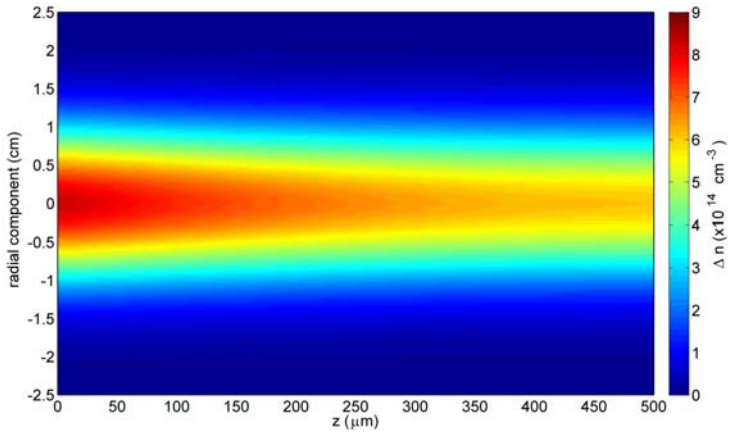

(b) $\tau_{\text{eff}} = 100\ \mu\text{s}$

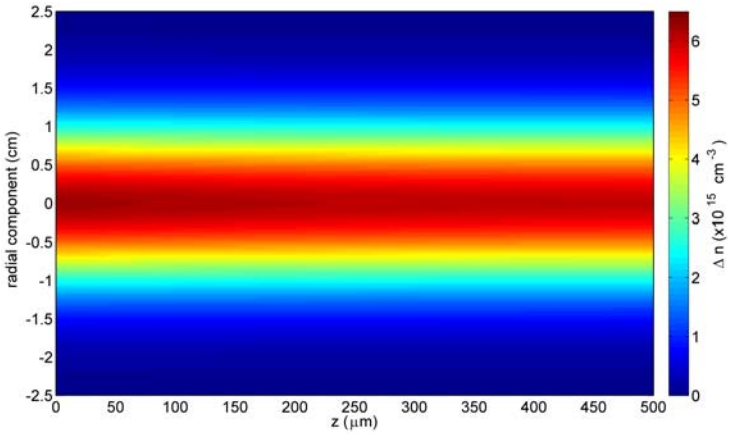

(c) $\tau_{\text{eff}} = 1000\ \mu\text{s}$

Figure 3.6: Simulated 3D excess carrier profile throughout a high-resistivity silicon wafer with Dia = 5 cm, $d = 500\ \mu\text{m}$, and $\lambda = 800\ \text{nm}$, $\omega_0 = 1\ \text{cm}$. Increased carrier penetration is observed for higher lifetime substrates.

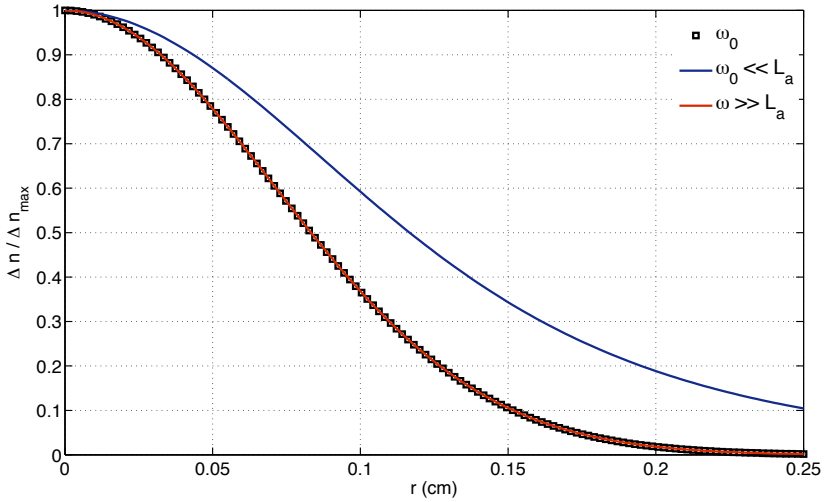

Figure 3.7: Simulated radial component of the excess carrier density generated by a Gaussian beam, ω_0.

increases both the maximum excess carrier density ($\Delta n(r,z) = \Delta n(0,0)$), and the penetration depth within the wafer. The diffusion length[2] L_a becomes comparable to the wafer thickness at $\tau_{\text{eff}} = 100\ \mu\text{s}$ ($L_a \geq 597\ \mu\text{m}$), and greatly exceeds the wafer thickness for $\tau_{\text{eff}} = 1000\ \mu\text{s}$ ($L_a \geq 1891\ \mu\text{m}$).

An increase in carrier penetration thus results in an increased effective plasma density, yielding an overall increased change in the substrate complex permittivity.

3.3.2.2 Lateral profile dependence

While larger plasma penetration depths yield an increased effective plasma density, increased diffusion can limit its spatial resolution. This then poses potential limits to the *optical encoding efficiency* of the projected mask. The lateral diffusion limits are illustrated using the above 3D Hankel formulation.

Figure 3.7 displays the normalised excess plasma density[3] as a function of radial coordinates, where the spatial feature of interest is denoted by the Gaussian beam waist, ω_0. It is shown that the spatial resolution of the 'projected mask' is limited by the ambipolar diffusion length, L_a, as above. In

[2]dependent on the injected plasma density, and thus irradiance
[3]ignoring plasma density reductions due to increased diffusion

particular, diffusion effects are shown to be negligible when the spatial features are much greater than the diffusion length of the substrate ($\omega_0 \gg L_a$). In contrast, masks which feature spatial components that are smaller than the diffusion length ($\omega_0 \ll L_a$), result in non-negligible diffusion effects; the opto-excited plasma density then follows the optical mask limited to a spatial resolution L_a, with a corresponding drop in the effective plasma density.

Figure 3.8 displays the 3D plasma density for both $\omega_0 >> L_a$ – Figure 3.8(a) – and $\omega_0 << L_a$ – Figure 3.8(b). Ignoring the relative increase in penetration depth, the plasma profile is shown to diffuse out to an outer bound which is defined by the diffusion length; this is shown by the light blue segment in the figure which approximately denotes the beam waist (i.e. 1/e point). In addition, the increased diffusion in the latter case also leads to a lowered effective plasma density, which ultimately results in a reduced change in the complex permittivity of the substrate.

Hence, while an increase in the effective lifetime yields increased effective plasma densities, through increased plasma penetration and the direct dependence of (3.10), larger effective lifetimes can lead to limited plasma spatial resolution, thus restricting transfer of a given mask to the opto-excited plasma. Limited plasma transfer, or *pattern wash-out*, can lead to reduced performance from the opto-excited device, which is discussed further in Chapter 5 for the piFZPA.

Thus, it is clear that there exists a trade-off between the maximal modulation of the complex permittivity at a given level of irradiance, and the spatial resolution of the plasma. The optimisation of the substrate is then determined by the intended application, whereby the penetration depth, and thus effective plasma density, are reduced in order to maintain spatial resolution, at the expense of an increased irradiance.

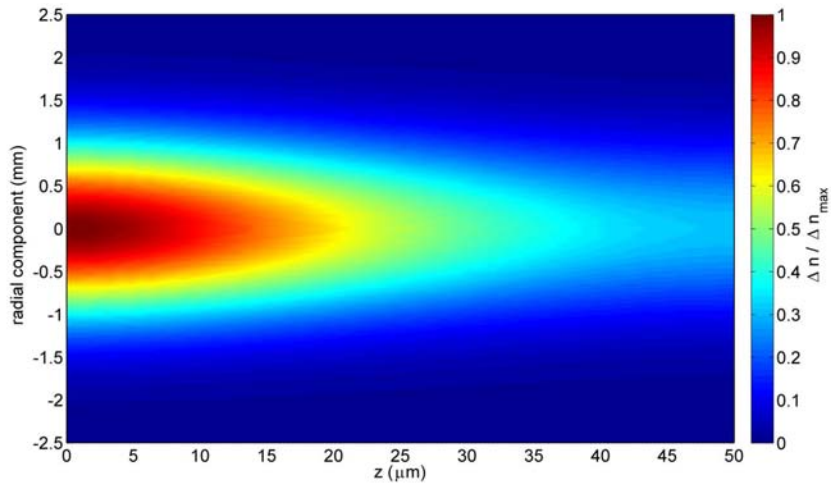

(a) $\omega_0 \gg L_a$

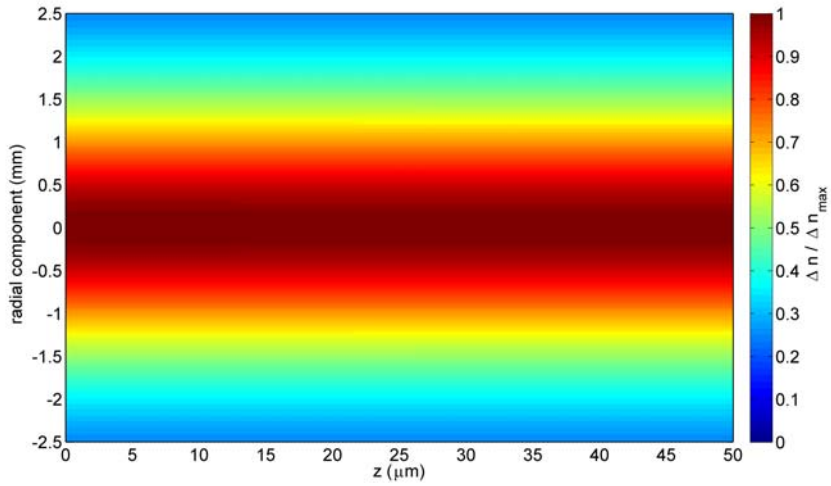

(b) $\omega_0 \ll L_a$

Figure 3.8: Simulated 3D excess carrier profile throughout a 5 mm diameter, $50\ \mu\mathrm{m}$ silicon wafer at various effective lifetimes. The excitation wavelength was 800 nm, with a beam waist of 1 mm, in both cases; zero SRV has also been assumed ($S = 0\ \mathrm{cm/s}$).

3.3.2.3 Non-zero surface recombination

Previous discussions have assumed a perfect surface, i.e. $S = 0\ \mathrm{cm/s}$. The following section highlights the changes to the spatial distribution of the free-carrier plasma, and the corresponding change in the effective plasma density as a result of non-zero surface recombination velocities; the following plasma distributions have been obtained using the above Hankel method with $S \neq 0\ \mathrm{cm/s}$.

Figure 3.9 displays the 3D plasma density for a high-resistivity, 5 cm diameter wafer, with $d = 500\ \mu\mathrm{m}$, $\omega_0 = 2\ \mathrm{cm}$, $\lambda = 800\ \mathrm{nm}$, $I_{\mathrm{opt}} = 100\ \mathrm{mW/cm^2}$, at a range of front and rear SRVs, S_0, S_d. It is shown for an increased front SRV, from $0\ \mathrm{cm/s}$ to $10^6\ \mathrm{cm/s}$ (with $S_d = 0\ \mathrm{cm/s}$), the density of the plasma at the front surface decreases, yielding a peak plasma density at $d > 0$. The peak plasma density is also shown to drop by up to two orders of magnitude as a result of the increased SRV. Comparatively, an increased rear SRV (with $S_0 = 0\ \mathrm{cm/s}$) is shown to reduce the plasma density at the rear significantly for increased values of S, where the overall peak plasma density is shown to be reduced by a factor of ~ 3, much lower than was observed for increased values of S_0. In addition, the rear surface density is shown to approach zero, for increased values of S_d ($10^6\ \mathrm{cm/s}$), which results from the diffusion limited carrier transport to the rear surface. Thus, it can be expected that higher rear SRVs in thin substrates ($d \ll L_a$) would suffer increased carrier losses, due to non-diffusion limited recombination. This is commonly found in solar cells, which require increased passivation quality of the rear surface.

The change in the free-carrier plasma distribution and density for increased SRVs highlights the requirement for minimised SRVs in order to achieve effective modulation of propagating (sub) mm-wave beams, at a given irradiance.

3.4 Lifetime control: wafer passivation

Free-carrier recombination which is dominated by SRH defects, described previously, has been shown to be dependent on both the opto-excited plasma density, Δn, and the defect-state density, N_t, i.e. $S = S(\Delta n, N_t)$, which yields

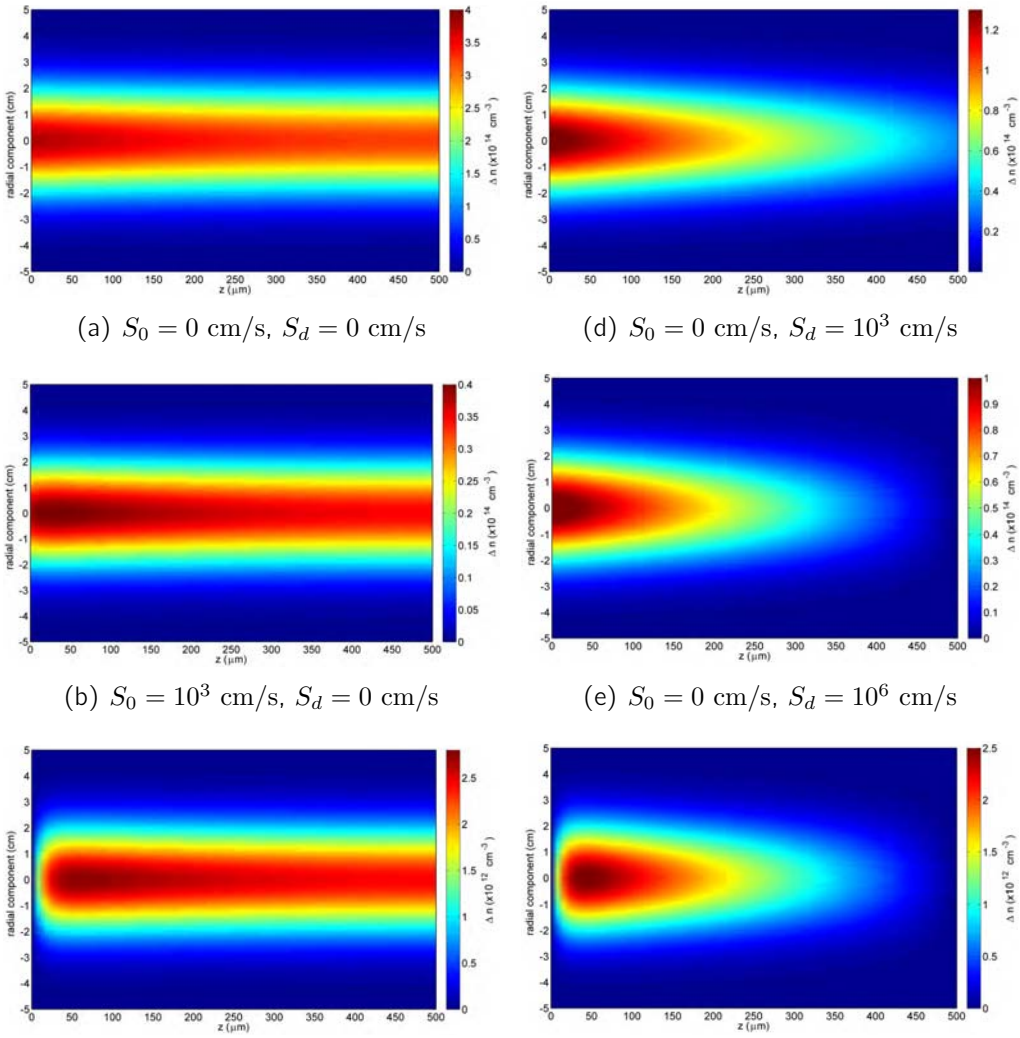

(a) $S_0 = 0$ cm/s, $S_d = 0$ cm/s

(d) $S_0 = 0$ cm/s, $S_d = 10^3$ cm/s

(b) $S_0 = 10^3$ cm/s, $S_d = 0$ cm/s

(e) $S_0 = 0$ cm/s, $S_d = 10^6$ cm/s

(c) $S_0 = 10^6$ cm/s, $S_d = 0$ cm/s

(f) $S_0 = 10^6$ cm/s, $S_d = 10^6$ cm/s

Figure 3.9: Simulated 3D plasma density as a function of front and back SRV, S_0, S_d respectively. Substrate was a 5 cm diameter, 500 μm thick wafer illuminated by a wavelength of $\lambda = 800$ nm, with $I_{\text{opt}} = 100$ mW/cm^2, and with a beam waist, $\omega_0 = 2$ cm. (a)–(c) $S_0 = 0 \rightarrow 10^6$ cm/s with $S_d = 0$ cm/s, (a),(d)–(e) $S_d = 0 \rightarrow 10^6$ cm/s with $S_0 = 0$ cm/s, and (f) $S_0 = S_d = 10^6$ cm/s.

two main passivation mechanisms for reducing the SRV [140, 141, 162, 163].

The following summary presents a brief discussion of various passivation techniques including the growth, or deposition, of a thin film onto the wafer surface, which reduces the defect state density, and the creation of an internal-electric field, reducing the excess carrier density near the surface(s). Whilst a range of excellent passivation qualities have been reported, based on the immersion of the substrate sample within a range of solvents [164, 165], these particular methods suffer from rapid degradation of the surface quality and are thus only suitable for process characterisation.

3.4.1 Reduction of the surface defect-state density

The reduction in SRVs by a thermally grown, or chemically deposited, film onto the wafer surface yields improved effective lifetimes by reducing the surface defect density, N_t. Many potential passivation films have been investigated within the photovoltaic community, with current industry standards involving either the deposition of amorphous silicon (a-Si), silicon nitride ($\mathrm{SiN_x}$), or a thermally grown oxide layer ($\mathrm{SiO_2}$). While alternative films involving amorphous silicon carbide [166, 167], and various organic layers [168–171] have shown great potential with continued interest over the years, this particular discussion will briefly outline the three industry standards, as presenting the most relevance to this work.

Thermally grown oxide layers ($\mathrm{Si-SiO_2}$) have long been the industry standard due to their high passivation qualities (low SRV) and long term stability [162, 172–174]. Further, enhanced passivation quality on both n-type and p-type substrates has been demonstrated by a post high temperature aluminium anneal (*alneal*), due to the space-charge region created which induces an internal surface-state field (see Section 3.4.2), in addition to a lowered $\mathrm{Si-SiO_2}$ interface defect density [162, 175]. Both methods have shown to commonly yield reduced SRVs of $10 < S(\mathrm{cm/s}) < 500$, depending on wafer type [162].

However, the thermal oxide process, in addition to requiring highly clean environment (low cleamroom class), is inherently a high temperature tech-

nique ($\geq 1,000\ ^{\circ}\mathrm{C}$), requiring processing times of several hours. Such conditions pose problems for lower quality substrates such as Cz-Si, p-Si, and ribbon-Si, where high temperatures can lead to increased lattice defects and/or impurities [162,163,172]. While good passivation results ($S \approx 50\,\mathrm{cm/s}$) have been shown for a lower-temperature ($900\ ^{\circ}\mathrm{C}$) oxide layer grown in a nitric acid environment [176], oxide layer passivation has yet to be demonstrated at low temperatures and short processing times. Thus, oxide passivation remains a typically expensive passivation technique with less suitability to lower resistivity wafers.

Alternative low temperature ($< 500\ ^{\circ}\mathrm{C}$) methods include the passivation of silicon nitride ($\mathrm{SiN_x}$) or amorphous silicon (a-Si) films.

Passivation by thin-layer deposition of $\mathrm{SiN_x}$ films has recently been adopted as an industry standard due to its low temperature and extremely short processing times (few mins per surface). In addition, several studies have shown nitride passivation to be comparable to oxide methods [162, 172, 177–181], with SRVs of $S < 100\ \mathrm{cm/s}$ being typical. Furthermore, the positive space-charge region present in nitride films is known to enhance the passivation quality of n-type substrates due to the internal field-effect [163, 182–184], where improvements over a wide-range of substrate specifications have been shown to be maintained by the passivation of nitride stacks [185–187].

Nitride passivation methods are subject to optimisation of temperature and of the process gas mixture (ammonia, silane, and/or nitrogen) [178,188], where variations in the deposition process have shown varying improvements, with high frequency (13.56 MHz) plasma enhanced chemical vapour deposition (PECVD) yielding improved passivation and stability over lower frequency ($100 - 500\ \mathrm{kHz}$) PECVD techniques, due to reduced surface defects introduced by plasma interactions [177,179]. Recent advances in indirect- PECVD passivation techniques have also shown continued improvements in the nitride passivation quality [172, 178, 188].

Most significantly, nitride passivation layers have shown prolonged stability against UV irradiation ($< 400\ \mathrm{nm}$), thus driving their adoption for outdoor solar cells; this is also of interest for the scope of this work, where lower maintenance passivation methods are obviously beneficial.

Nitride passivation layers are also known to yield reasonable thermal stability against further high temperature processing steps (such as metallisation), which can be increased by suitable thermal stacks [187]; and are known to produce enhanced passivation quality with low temperature anneals due to increased diffusion of hydrogen [162, 181, 188, 189].

Thin film deposition of amorphous silicon (a-Si) has recently emerged as a potential passivation method, attractive because of its lowered processing temperatures ($200\ ^{\circ}\mathrm{C}$), short processing times (minutes), and the excellent passivation qualities ($S \sim 10\ \mathrm{cm/s}$) observed for both p- and n-type substrates [190–192]. Similarly, a-Si passivation followed by a short low temperature anneal is also known to yield enhanced passivation qualities due to a likewise diffusion of hydrogen [192–194]. a-Si deposition similarly requires optimisation of the temperature and process gases (silane, ammonia, and/or hydrogen) for each substrate.

In contrast to nitride passivation, a-Si layers yield increased UV sensitivity, thus reducing their long term stability, whilst also suffering from reduced thermal stability, limiting post-passivation processing steps such as metallisation [195].

Finally, thin film passivation is increasingly being combined into varying stack structures which combine the benefits of each individual layer, thus yielding improved thermal stability, passivation quality, substrate suitability (n- and p-type), and UV resistance [186, 187, 196].

3.4.2 Reduction of the surface excess carrier density

Internal surface-field passivation, which lowers the minority carrier density near the surface, is commonly achieved by creating surface junctions, or by implementing a doping profile below the substrate surface [162, 197, 198]. Internal field passivation methods have a continued interest, particularly in the photovoltaic community, due to their high passivation quality and applicability to a wide range of substrate types. Standard high-low junctions ($\mathrm{p}^{+}\ \mathrm{p}$ or $\mathrm{n}^{+}\ \mathrm{n}$) created by boron, phosphorous, or aluminium alloy diffused along the substrate surface yield reasonable SRVs with $200 < S < 2,000\ \mathrm{cm/s}$ [162],

which can be improved ($S \leq 50\ \mathrm{cm/s}$) by combined stack passivation. However, in general, surface-field passivations require a further high temperature anneal for increased passivation qualities [195, 199] and thus suffer from the aforementioned problems.

Field-effect passivations, which involve a reduction of one charge carrier type by means on an internal electric field, are most commonly achieved by passivation of charged films [200]. A wide range of charged films thus yield the flexibility to passivate a variety of n- and p-type materials.

One prominent low temperature ($\approx 200 - 300\ ^{\circ}\mathrm{C}$) field-effect passivation technique appears to be that of atomic-layer-deposited (ALD) aluminium oxide ($\mathrm{Al_2O_3}$), which requires the deposition of ultra-thin ($< 100\ nm$) films created by chemical reactions between trimethyl-aluminium [$\mathrm{Al(CH_3)_3}$], water, ozone, and/or oxygen in repeated cycles. This gives films of high uniformity, the thickness of which is highly controllable, which are also highly stable against UV irradiation, and also featuring good surface passivation qualities with $S \leq 200\ \mathrm{cm/s}$ [201–204]. Processing times for ALD of $\mathrm{Al_2O_3}$ are also moderate in comparison to nitride and oxide deposition times, of order a few tens of minutes depending on the number of processing cycles and/or film thickness.

However, ALD $\mathrm{Al_2O_3}$ suffers from reduced thermal resistance against further high temperature processing steps, similar to a-Si films, and thus further high temperature processing, such as metallisation, will be comparatively limited. As before, combination of suitable nitride stacks have shown increased thermal stability, whilst maintaining low SRVs [203, 205]. While ALD aluminium oxide has shown to yield low SRVs, high reflectivity at optical wavelengths render such passivations potentially unsuitable for reconfigurable mm-wave devices, which would require simultaneous illumination from a single surface for both optical and mm-wave beams. This has limited applicability for a range of optoelectronic applications, such as the photo-injected Fresnel zone plate.

Thus, low temperature thin film deposition techniques seem most appropriate as passivation solutions for reconfigurable mm-wave applications, pertaining – at least – to the scope of this thesis.

3.5 Lifetime stability characterisation

The following section details the experimental investigation of the long-term lifetime stability of a range of high-resistivity wafers, passivated by either thin-film hydrogenated a-Si or hydrogenated $\mathrm{SiN_x}$. These methods were chosen as presenting to be the most promising, whilst also being industry standards[4]. The lifetime characterisation was performed by successive lifetime measurements on each sample using a modified experimental arrangement based on the non-contact microwave photoconductance method (μ-PCD) [138, 206–209].

The modified experimental configuration is introduced, and the experimental results of the long-term stability of each passivated wafer obtained over a 12 month period discussed.

3.5.1 Experimental configuration

The experimental modification to the standard $\mu-$PCD method involved replacing the standard reflectivity of microwaves (commonly 2 - 30 GHz) by a high frequency mm-wave source, operating at 94 GHz. The mm-wave source and receiver hardware consisted of a 94 GHz Gunn oscillator (Farran Technology, GN-10), an isolator (Elva-1 IS-10/94), standard 3-port circulator, 94 GHz detector diode (Farran Technology WDP-10), and a pulsed Neodymium-doped Yttrium Orthovanadate ($\mathrm{Nd:YVO_4}$) diode-pumped solid-state laser (DPSSL) as the illuminating source ($\lambda = 1064\ \mathrm{nm}$). The modified configuration is hereinafter referred to as the mm-PCD method.

The output of the DPSSL was free-space coupled into the end of a 300 $\mu\mathrm{m}$ optical fibre using a combination of optical lenses, which produced a large output focal length; the output optics included additional controllable mirrors, used to tune the free-space coupling into the open-ended fibre. The output coupling was adjusted to ensure constant average power for each measurement. The plastic cladding of the opposite end of the fibre was removed, and the fibre core placed through a small opening drilled into the side of

[4]The primary focus of this thesis was not to investigate novel passivation methods.

a standard H-plane WR10 90° bend. This allowed for simultaneous illumination of the wafer by both the optical illumination (1064 nm), and the mm-wave (3.19 mm) sources. The experimental configuration is illustrated in Figure 3.10.

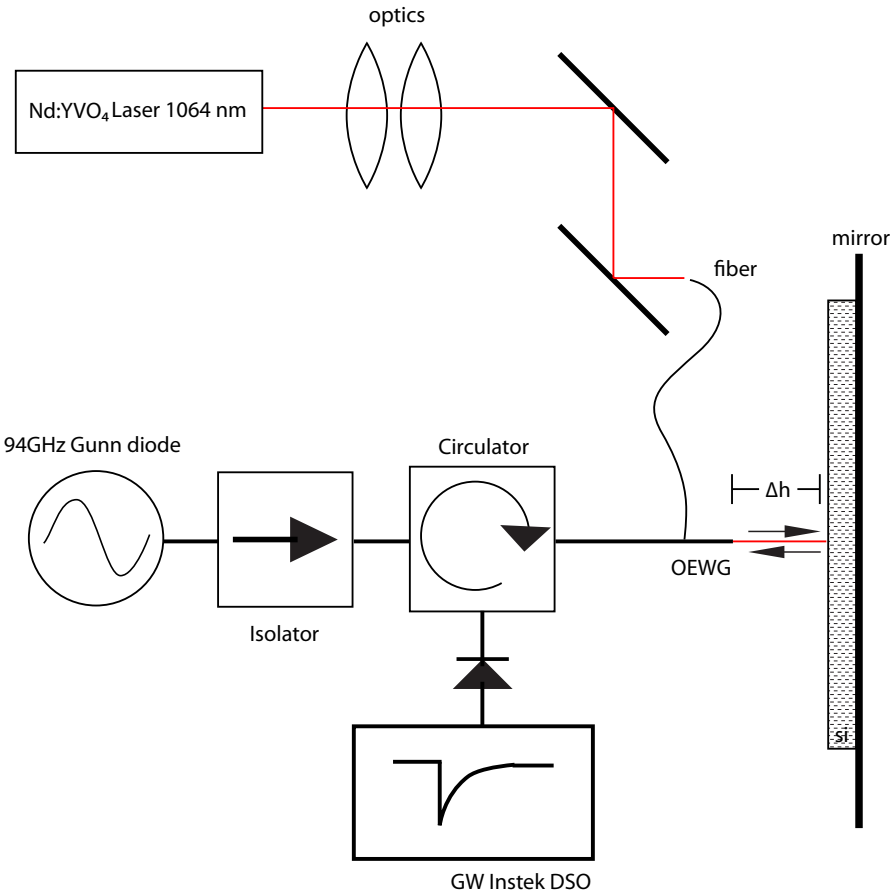

Figure 3.10: Diagram indicating the experimental configuration of the mm-PCD technique utilised for characterising the lifetimes of tested wafers. The change in conductivity is provided by short laser pulses from a Neodymium Vanadate DPSS laser. The change in mm-wave reflectivity is then observed on a digital storage oscilloscope, using a diode detector. The sensitivity is increased by optimising the matching condition of the etalon, controlled by the separation of the wafer and open-ended waveguide (OEWG), $\Delta\mathrm{h}$.

Testing each wafer individually, the wafer-under-test was placed atop a laboratory-jack (not shown in figure) separated by cleanroom wipes, used to protect the wafer surfaces. The lab-jack was then used to tune the separation

(Δh) of the wafer below the open-ended waveguide (OEWG) for maximum sensitivity; the separation of the wafer and reflector (lab-jack) was assumed as 0 mm. Separation of both wafer and reflector are known to be crucial for optimised $\mu-$PCD sensitivity, and linearity [207]; however in this particular implementation, wafer thicknesses were such $(3\lambda/4)$ that the mm-wave reflectivity of the etalon produced by the dielectric silicon wafer and reflector were matched for maximum reflection at 94 GHz (see Chapter 4). Thus, there was no additional requirement of optimisation of the etalon by varying the reflector separation.

While the standard $\mu-$PCD method is known to be an inherent small-signal technique, requiring low-injection to satisfy the linear dependence of the reflected microwave power [136, 207], the higher mm-wave frequency requires higher excitation densities in order to satisfy the corresponding linear reflectivity region (Chapter 4). The high-resistivity of the measured samples then required high-injection in order to satisfy the mm-wave linear reflectivity region, and thus possible errors may have been introduced due to non-invariant carrier mobilities [138]; however, such errors were found to be small in most cases.

The DPSSL produced short pulse widths of approximately 7 ns, with a 70 Hz repetition rate, and a 1064 nm peak wavelength, producing approximately $220\ \mu\mathrm{W}$ average power. The repetition rate was set by the upper bound of the lifetimes to be measured, which was estimated as 4 - 5 ms. Furthermore, pulse rates less than $1/\tau_{\mathrm{eff}}$ are required in order to circumvent potential errors introduced by non-full decay transients [206].

The mm-wave recovery response was captured using a digital storage oscilloscope (GW Instek GDS-2204 DSO, 200 MHz bandwidth), which offered quick acquisition and the ability to perform several averages of each trace. The DSO was triggered from the pulse driver of the DPSSL. Each wafer was measured at 10 different locations across the wafer in order to (partially) account for the spatial lifetime inhomogeneity across the wafer. This was important for the stability measurements, as the inhomogeneity could falsely infer degradation between consecutive measurements. While the small illumination area of the $\mu-$PCD method permits full wafer mapping of the

carrier lifetime (c.f. QSSPC), attempts using an in-house 2-axis controller used for other characterisations proved unsuccessful due to hardware, time, and fluctuating sensitivity limitations. Thus, the ten measurements per wafer represented a compromise between correcting for the lifetime inhomogeneity, and the time taken to perform each characterisation (10 mins per wafer); each location was selected randomly by moving the lab-jack and wafer assembly under the OEWG.

Each measured response of the mm-wave reflectivity voltage was saved to disk, and processed at a later stage in Matlab.

3.5.2 Extracting the effective free-carrier lifetime, τ_{eff}

The complex dependency of the decay transients on several sample parameters can lead to inaccurate and difficult interpretation of the measured lifetimes using the $\mu-$PCD/mm-PCD method [210–214]. In addition, the measured effective lifetimes obtained by transient decay methods correspond to a *differential* lifetime, i.e.

$$\tau(\Delta n) = \frac{\Delta n(t)}{-\partial \Delta n(t)/\partial t}, \tag{3.32}$$

where measured lifetimes can either under or over estimate the actual lifetime of the sample, which, in general, changes as a function of injection level [138]. Thus alternative methods must be adopted, such as the quasi-steady state photoconductance (QSSPC) method [138, 215] or a small signal light biased transient measurement [138, 212, 213], where the injection level can be determined. Owing to a compromise between the effects of free-carrier trapping and Auger recombination, effective lifetimes are given at an injection level of $10^{15}\ \mathrm{cm}^{-3}$ as standard.

For measured samples used within the scope of this work, the measured injection level dependence of the effective lifetime indicated an almost invariant effective lifetime at injection levels corresponding to the linear mm-wave reflectivity region ($\approx 10^{14} - 10^{16}\ \mathrm{cm}^{-3}$), shown in Figure 3.11. Thus, measured differential lifetimes can be assumed to approximate that of the actual

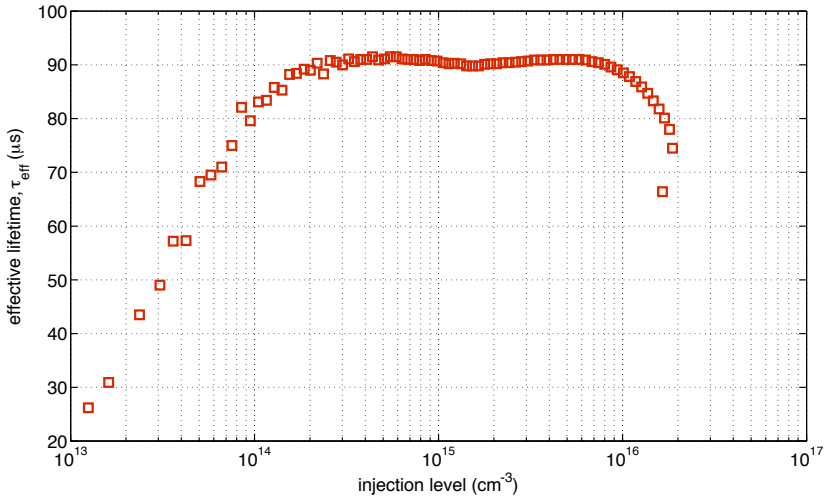

Figure 3.11: Example measured injection level dependence of the actual free-carrier lifetime using the QSSPC method (courtesy of IFE, Norway).

free-carrier effective lifetime [216].

Using Matlab, the recovery traces for each measurement and each wafer were processed using a bespoke algorithm. The algorithm featured several components which were primarily tasked to isolating a single transient, and formatting the data as it was recorded from the digital oscilloscope. Single decay transients were isolated using numerical differentiation which was used to locate large discontinuities arising from sudden changes in the excess plasma density of the substrate. Finally, a series of pre-defined threshold limits were used in conjunction with numerical derivates that analysed the rate of change of gradients within the transient. Large changes in the transient gradient, located at the beginning and end portions of the measured response, indicating multiple-time constant exponential decay and were thus truncated with the remaining central section used for determination of the effective lifetime. In essence, approximately 35% of the initial decay was ignored, with the portion of the latter region changing depending on the non-linearity of the decay.

The measurements were consistently performed with a negative *decay* transient, which was set by altering the displacement height Δh, thus changing the conductivity relative to the background of the etalon [207].

The ideal exponential decay transient can then be modelled by the follow-

ing exponential

$$\Delta R = \Delta R_0 \left[1 - \exp\left(-t/\tau_{\text{eff}}\right)\right], \tag{3.33}$$

where ΔR_0 represents an arbitrary amplitude constant and τ_{eff} defines the effective free-carrier lifetime of a finite region on the wafer, limited by the spot size of the illuminating laser. The mm-PCD transient was then linearised for the sake of linear least-squares fitting

$$\begin{aligned} \Delta R^{'} &= \ln\left[1 - \Delta R/\Delta R_0\right] \\ &= B\mathrm{x} + \mathrm{C}, \end{aligned} \tag{3.34}$$

which gives the effective free-carrier lifetime τ_{eff} from a linear fit, $\tau_{\text{eff}} = -1/\mathrm{B}$. The linear fit was accomplished via a LMS to a first-order polynomial using the Matlab function *polyfit*.

Figure 3.12 displays the decay transients for two wafers: (a) a relatively low quality passivated wafer with an effective lifetime of $\tau_{\text{eff}} = 99\ \mu\text{s}$, and (b) a high quality passivated wafer with an effective lifetime of $\tau_{\text{eff}} = 1450\ \mu\text{s}$. Both examples demonstrate regions of non-linear decay, where initial non-linearities are expected to have arisen from free-carrier scattering (Auger) and non-linear reflectivity effects, whereas non-linear transients observed at the end of the measured traces resulted from free-carrier trapping (bulk SRH), and potentially non-linear reflectivity effects, depending on the relative magnitude of τ_{eff}. In both cases, the analytical model of Luke and Cheng (Section 3.3.1) has been included, which shows excellent agreement near the linear region. The simulations assumed: $d = 600\ \mu\text{m}$, $\tau_b = 5500\mu\text{s}$, $D = 30\ \text{cm}^2/\text{s}$, $\lambda = 1064\ \text{nm}$ and $t_p = 7\ \text{ns}$. These simulations were found to yield $S = 80\ \text{cm/s}$ for the lower quality wafer ($\tau_{\text{eff}} = 99\ \mu\text{s}$), and $S = 0.1\ \text{cm/s}$ for the high quality wafer ($\tau_{\text{eff}} = 1450\ \mu\text{s}$). However, these give different values than those suggested by (3.6), which yields $S = 298\ \text{cm/s}$, and $S = 15\ \text{cm/s}$ respectively; the disagreement of the transient analysis model is expected to arise from the low-injection assumption made during formulation of the model,

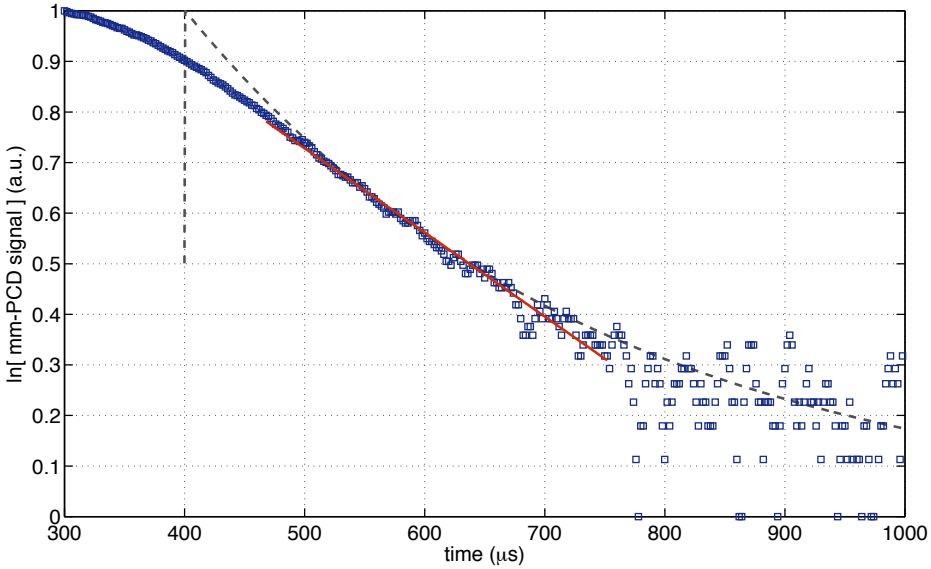

(a)

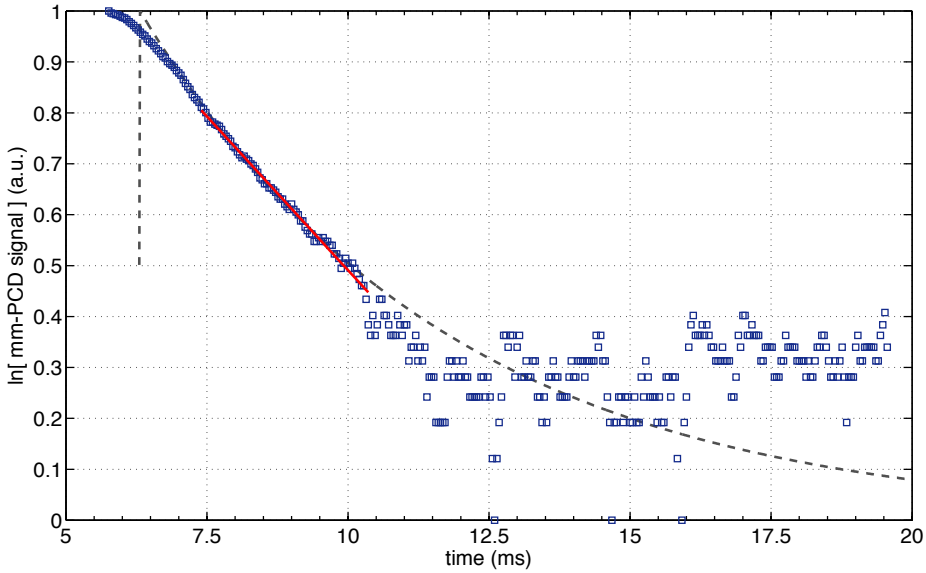

(b)

Figure 3.12: Measured and fitted (dashed line) decay transients for passivated wafers with (a) a $\tau_{\text{eff}} = 99\ \mu\text{s}$ ($w4$), and (b) a $\tau_{\text{eff}} = 1450\ \mu\text{s}$ ($w1$), effective lifetimes. Red line indicates the fit produced by the bespoke algorithm for each data set.

which may not fully apply in this case due to the extremely high resistivity of the wafers ($N_D \approx 10^{11}$ cm^{-3}). Equation (3.6) is thus taken as the guide for the following measurements. Figure 3.12 also displays the linear fit produced by the algorithm discussed above, and shows excellent location and fitting to the linear region of the transient.

Figure 3.13 displays the measured and fitted transients from measurements performed on wafer $w3$ during the study, where the spatial inhomogeneity resulted in a statistical spread in the measured effective lifetimes, illustrated by the variation in the fitted gradients.

It should be noted that while the injection level variance of the carrier mobilities has been found to be negligible in most cases, it has been observed that such effects can be significant for exceptionally high carrier lifetimes, and thus a small portion of the data set has such errors included in the analysis. Such data is expected to imply longer lifetime due to the 'concave' decay transients obtained. Exclusion of such data was impractical due to the number of transients taken; however, continued improvements of the experimental setup – lowered irradiation levels – have minimised such errors in the following analysis.

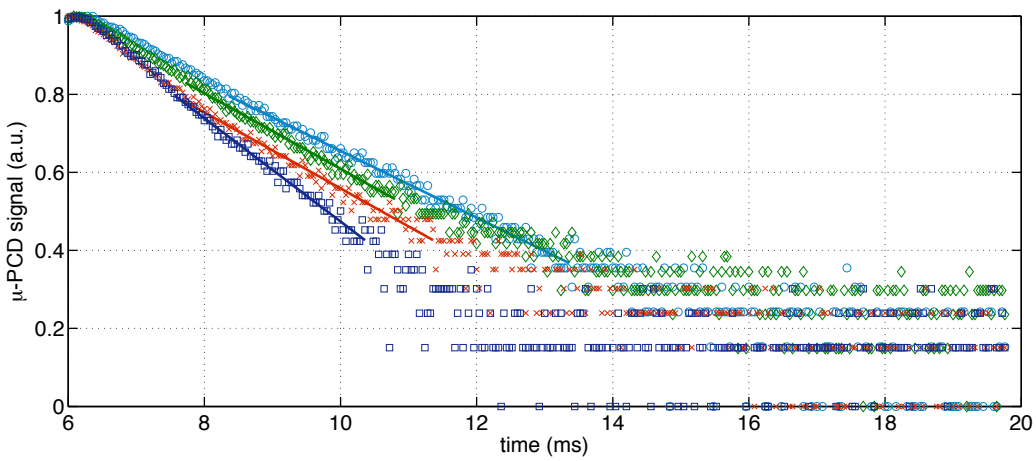

Figure 3.13: Measured decay transients for several locations on a single wafer ($w3$), indicating the statistical variation in τ_{eff} as a result of defect inhomogeneity. Fitted lifetimes are shown as solid lines.

3.5.3 Lifetime stability characterisation of a-Si:H and SiN_x:H passivated silicon wafers

Lifetime degradation characterisations were performed on a batch of six single-side polished silicon wafers of $675\ \mu\mathrm{m}$ thickness, and $\rho > 10,000\ \Omega\mathrm{cm}$ resistivity, which were supplied by TOPSiL Semiconductors AG [217]. The bulk lifetime of the wafer batch, as measured by TOPSiL, was stated to be $\tau_b = 5500\ \mu\mathrm{s}$.

Lifetime stability investigations of the passivation treatments were limited to two particular methods: hydrogenated amorphous silicon (a-Si:H) and hydrogenated silicon nitride ($\mathrm{SiN_x}$:H). Both passivations were performed during a visit to the solar cell research labs, Institute for Energy Technology, in Norway. The passivations were both applied by high frequency (13.56 MHz) direct-PECVD. The wafers were subject to a pre-plasma clean and etching process used to ensure pure silicon surfaces, pre-deposition. Long etching times were additionally used to remove an unknown surface finish from one side of each wafer. The pre-processing steps were performed as follows.

The rough single-sided surface finish was removed by 6 x 2 minute etchings in a CP5 chemical polish ($\mathrm{HNO_3 : CH_3COOH : HF}$), 10:5:2 ratio, each followed by a cleanse in a deionized water (DI) bath. This thinned the wafers by up to[5] 100 $\mu\mathrm{m}$. Oxide layers were removed by a 2 minute bath in Hydrofluoric acid (HF), 5% concentration, followed by a cleanse in a DI water bath. Organic layers were then removed by a chemical etch in Piranha solution ($\mathrm{H_2SO_4 : H_2O_2}$), 4:1 ratio, for 8 minutes; followed by a DI water cleanse. The initial pre-clean was then completed by a final HF bath for 2 minutes in 5% concentration followed by a DI water cleanse.

The wafers were then transferred into a higher quality cleanroom facility where the PECVD instrument (Oxford instruments SEMLAB133) was located. Before passivation in the PECVD unit, the wafers were cleaned in a further 5% HF bath for 2 minutes, and cleansed in a DI water bath.

Five out of the six wafers received passivation by a-Si:H films. The de-

[5] This represents a theoretical maximum and a general rule of thumb, and varies depending on the crystal orientation of the wafer.

position was performed at 230 $^{\circ}\mathrm{C}$ for 10 minutes per side, per wafer; this resulted in approximately 80 nm of passivation film on each side. Between each surface passivation, the wafers were subject to a further cleanse in a HF/DI bath, as above.

The final wafer was passivated by thin-film deposition of $\mathrm{SiN_x}$:H, deposited at 400 $^{\circ}\mathrm{C}$ for 5 minutes per surface, per wafer; no HF/DI cleanse was performed between each surface passivation. Again, this resulted in approximately 80 nm of thin film being deposited on each wafer surface.

As a result of chamber contamination, some wafers featured small dust speckles; while this would have reduced the lifetime at each site, the range of cover on each contaminated wafer was small, and thus did not significantly degrade the overall performance of the wafers.

The wafers were then annealed in a hot furnace at 450 $^{\circ}\mathrm{C}$ for approximately 1 minute, under an inert atmosphere of predominantly Nitrogen and Hydrogen. This allowed for hydrogenation of the wafers, further increasing the effective lifetime.

The wafers were then labeled $w0 \rightarrow w6$, where $w1 \rightarrow w5$ referred to wafers treated by the a-Si:H method, and w6 to the single wafer passivated by the $\mathrm{SiN_x}$:H method. Wafer $w0$ referred to one wafer, un-passivated, which was then used for reference.

Figure 3.14 displays the lifetime map measured at IFE for wafer $w0$, illustrating the lifetime inhomogeneity across the wafer. The lifetime map was obtained using a commercial $\mu-$PCD mapping instrument (SemiLab WT-2000), performed using a grid spacing of 2 mm, with an excitation wavelength of $\lambda = 904\ \mathrm{nm}$. The mean lifetime across the wafer was measured as $\tau_{\mathrm{eff}} = 36.4 \pm 14.9\ \mu\mathrm{s}\ (w0)$.

Similarly, Figure 3.15 displays the lifetime maps for (a) a-Si:H ($w1$) passivation, and (b) $\mathrm{SiN_x}$:H ($w6$) passivation. Both show large increases in the effective carrier lifetime, with similar spatial inhomogeneity. The amorphous silicon passivation – Figure 3.15(a) – yielded an effective lifetime of $\tau_{\mathrm{eff}} = 1825.4 \pm 881.0\ \mu\mathrm{s}$ (w1), as measured by SemiLab WT-2000, where the map was taken in 1 mm lateral steps. The silicon nitride passivation – Figure 3.15(b) – yielded an effective lifetime of $\tau_{\mathrm{eff}} = 3418.2 \pm 1005.2\ \mu\mathrm{s}$

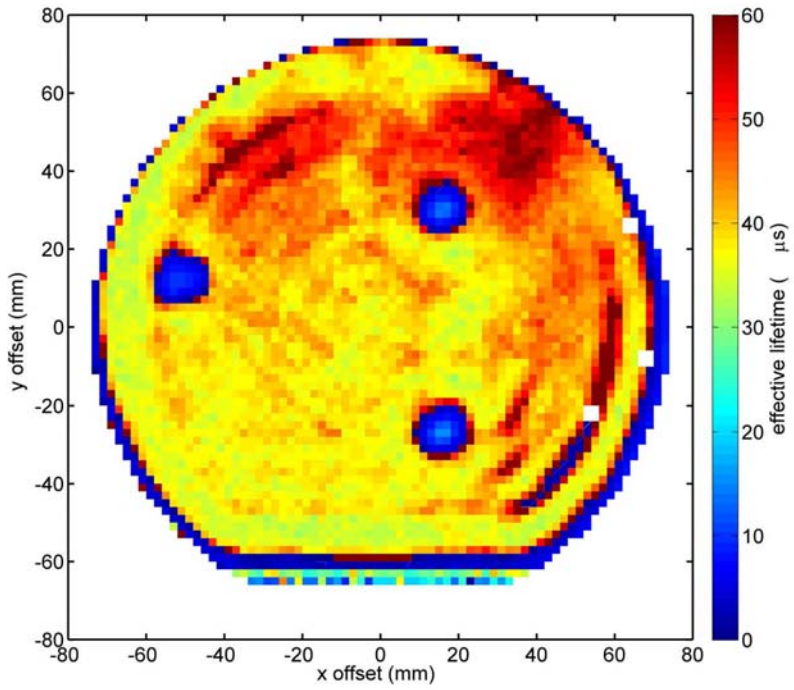

Figure 3.14: Measured lifetime map of wafer $w0$, taken at IFE Norway. The mean effective lifetime was measured as 36.4 μs.

(w6), with 2 mm lateral steps. It is important to note the improved lifetime homogeneity of $w6$ as evident in Figure 3.15, which is likely to be more of a function of prior handling of this particular wafer in respect to other wafers, than a correlation to improved passivation homogeneity over the a-Si method.

The three circular 'defects' observed in Figure 3.14, Figure 3.15(b), and partially evident in Figure 3.15(a), are interference with support rods located as part of the vacuum table; these are observed due to the high resistivity of the wafers, and are not normally visible for solar grade wafers.

The lifetime stability of the passivated wafers was then investigated over a 49 week period using the experimental configuration outlined in Section 3.5.1, and the processing algorithm of Section 3.5.2. Ten measurements per wafer were taken as a means to reduce the masking of degradation by the spatial inhomogeneity, as evident in Figure 3.15. Due to the time taken to establish the measuring facility and processing software, the characterisations began 10 weeks after passivation and ran through until week 49.

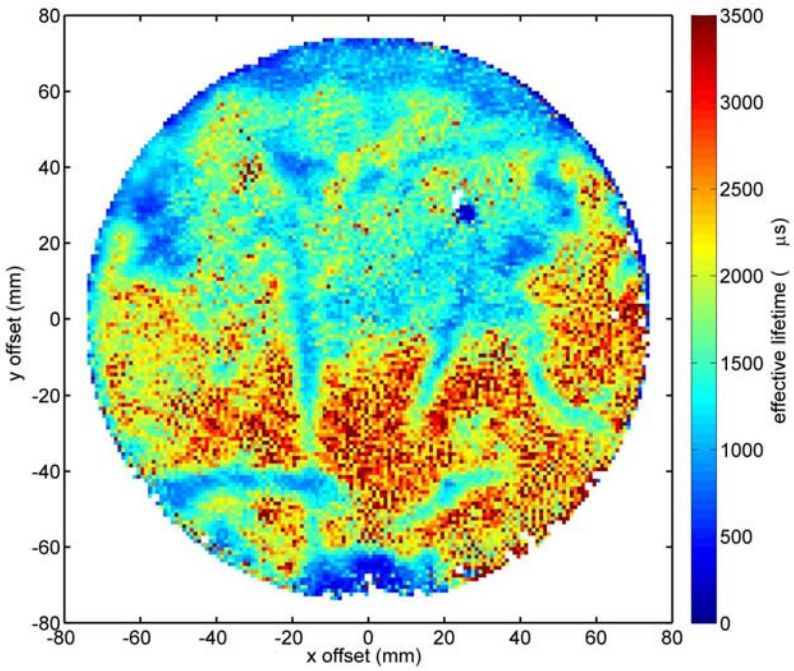

(a) w1: $\alpha - \mathrm{Si:H}$ passivation

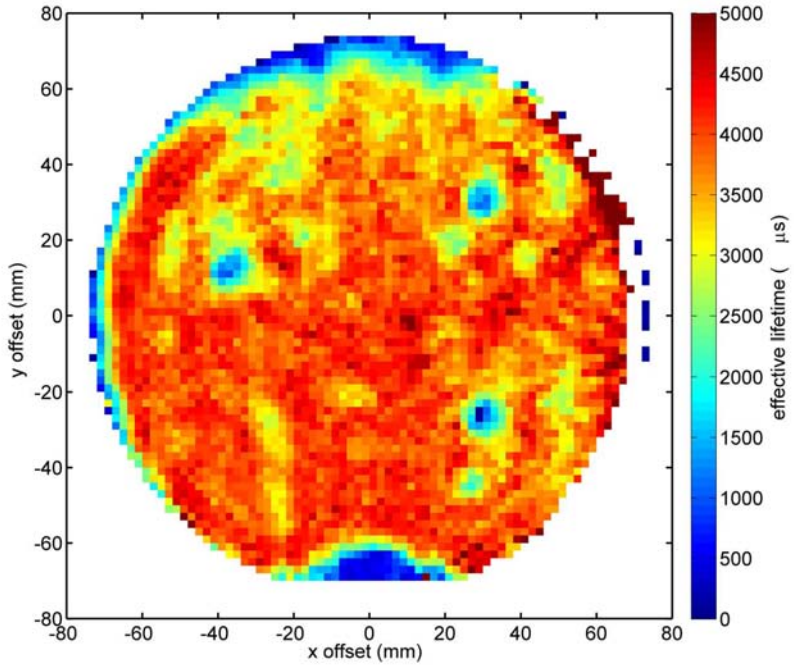

(b) w6: $\mathrm{SiN_x:H}$ passivation

Figure 3.15: Measured lifetime maps for (a) $\alpha - \mathrm{Si:H}$ passivation ($w1$), and (b) $\mathrm{SiN_x:H}$ passivation ($w6$). The measured average effective lifetime across each wafer was measured as 1825 μs for $w1$, and 3418 μs for $w6$.

Figure 3.16 indicates the results of the lifetime stability study, representing over 3,000 measured decay transients spanning a 40 week period. Each data point represents the statistical average of the 10 measurements taken, where error bars, obtained from the statistical spread across the 10 measurements, highlight the spatial lifetime inhomogeneity.

The results of the passivation shows the wafer batch to split into two categories: a high quality group, with $\tau_{\text{eff}} > 1$ ms; and a low quality group, with $\tau_{\text{eff}} < 1$ ms. The separation of the passivated wafers is likely to result from inherent defects of the silicon crystal, and surface defects (e.g. scratches), which were identified by photo-luminescence measurements[6]. Large improve-

[6]data not available, measurements performed at IFE Norway

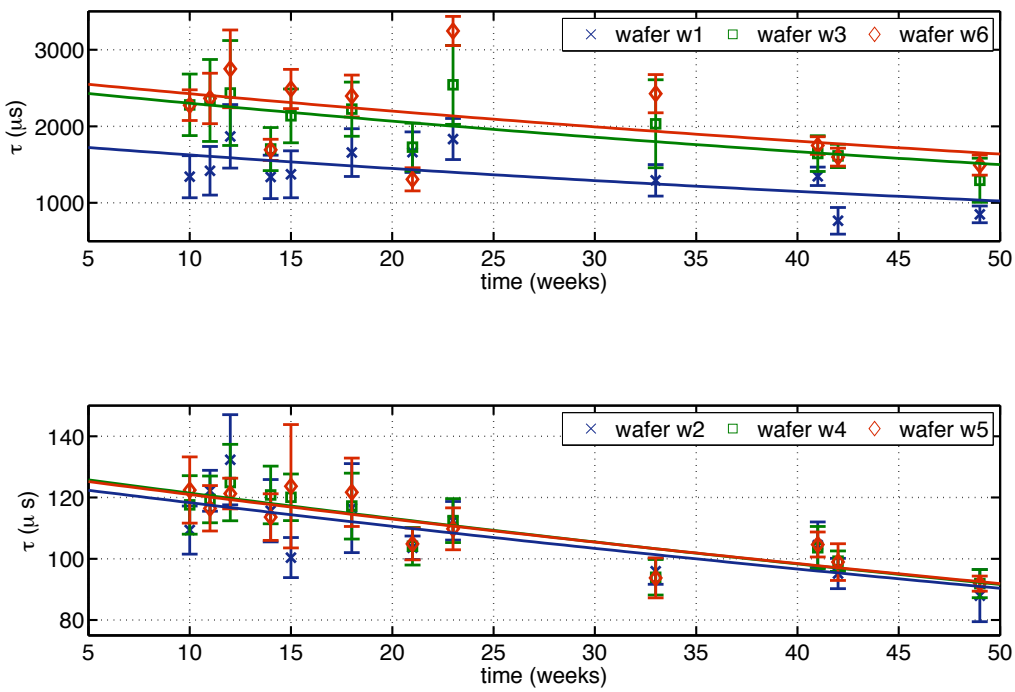

Figure 3.16: Measured lifetime stability for a range of 6 wafers passivated by either amorphous silicon, or silicon nitride films. Each data point represents a 10-point spatial average across each wafer. Both groups of passivation quality are shown to decay over comparable timeframes, approaching an equilibrium level, which is greater than the original untreated state. Wafers $w1$ and $w2$ are represented by the blue data points; wafers $w3$ and $w4$ by the green data points; and wafers $w5$ and $w6$ by the red data points in each subfigure.

ments in the effective lifetime were observed from the mm-PCD measurements, resulting from lowered SRVs; an SRV of $S = 15\ \mathrm{cm/s}$ was calculated using (3.6) for the largest improvements. Thus, effective optoelectronic control of these substrates by high-absorption visible excitation can be expected as a result. Such applications are discussed in later chapters.

The lifetime stability study indicated a slow decay of the passivation over the period of the measurements. The decay constants are comparable between each wafer within each category. For the high quality wafers, a decay constant of 93.8 ± 5.1 weeks was found, and 145.5 ± 2.1 weeks for the low lifetime wafers. Over a 2 year period, this leads to an decay to an effective lifetime of $877\ \mu\mathrm{s}$ for the high quality wafers, and $65\ \mu\mathrm{s}$ for the low quality wafers. However, the observed decay is expected to include errors introduced in the experimental setup, such as limitations of the mm-PCD measurement method, and the lifetime extraction algorithm. Thus the decay of the passivation layers are expected to offer longer term stability than initially suggested, which are expected to reach an asymptotic state [218].

Furthermore, the passivation quality can be 'reset' to a limited extent by further low temperature anneals, using the same method as outlined above [218]. Thus, it can be concluded that the large, and tuneable, improvements (both τ_{eff} and the SRV) to the semiconductor substrates by the thin film deposition methods result in an invaluable low-maintenance solution for yielding highly efficient optoelectronic devices, which can be tailored for a wide range of applications.

3.6 Summary

The significance of surface recombination effects has been discussed, and the resulting *effective* lifetime parameter introduced. The significance of the effective lifetime parameter has been highlighted, defining the optically excited plasma density, plasma penetration depth, and plasma spatial resolution. While maximal values of the free-carrier effective lifetime yields increased effective plasma densities, which results in large modulation of mm-wave beams

at a given irradiation level, associated problems may be arise from to the limited plasma resolution. Thus, there exists a compromise between the required level of irradiance, and the degree of transfer of the spatial mask to the excited plasma, which must be chosen based on application requirements.

Suitable methods of controlling the SRV, and thus effective lifetime parameter, have been discussed with techniques involving thin film deposition of silicon nitride proving to be the most promising. Silicon nitride passivation is known to feature high UV and thermal stability, excellent passivation quality, and long term stability, which has been experimentally shown to be of order two years using a high frequency mm-wave photoconductance decay method.

Characterisations on a range of high-resistivity wafers have shown dramatic improvements in the effective free-carrier lifetime, which increased from $60\ \mu\mathrm{s}$ in the un-treated state, up to $4,000\ \mu\mathrm{s}$ in some cases. Corresponding reductions in the SRVs have been approximately inferred from the measurements, with improvements ranging from $S > 10^6\ \mathrm{cm/s}$ in the un-treated case, to $S = 15\ \mathrm{cm/s}$ in some of the best cases. These wafers can then be expected to produce efficient optoelectronic devices based on short (visible) wavelength excitation due to the improved SRVs.

The particular features of an opto-excited semiconductor substrate can be widely modified which can then be implemented for realising practical optoelectronic devices. The tailored improvements are shown to be efficient, long term stable, and are of low maintenance. These devices thus serve as a valuable vehicle for a wide range of high performance applications.

chapter 4

W-band characterisation of optically excited silicon wafers

The transmission and reflection properties of a range of silicon wafers, both in the un-illuminated (dark) and in the opto-excited state, were characterised across the W-band frequency range. A quasi-optical semiconductor transmission line model is introduced and discussed which was used to indicate the dependence of the optical irradiance and the transmission/reflection properties through the substrate at mm-wave frequencies. The characterisation results are presented and compared to simulations using the developed opto-excited transmission line model.

4.1 Introduction

The transmission line measurements were based on a standard quasi-optical (QO) measurement configuration. The setup used a 2-port configured vector network analyser (VNA) for measuring the transmission and reflection properties of the semiconductor in both the dark, and opto-excited, states. Using the characteristic interferograms produced by the Fabry-Pérot resonance within the silicon substrate, it was possible to accurately measure the

complex permittivity of the opto-excited (and dark) substrate. Similar techniques have long been established for accurately characterising a variety of materials at microwave and mm-wave frequencies [130, 219–221].

The following section introduces the quasi-optical (QO) transmission line model used to simulate the transmission and reflection properties through an opto-excited substrate. This model serves as a invaluable tool for investigating the effective transmission (or reflection) properties of an opto-excited substrate, and has been used throughout this work.

4.2 Plane-wave propagation through lossy, conducting media

While the problem of plane wave propagation through a conducting, lossy medium is commonly treated in standard texts [222, 223], in almost all cases the solution to the wave-equation is reduced to particular examples which benefit from one of the following simplifications:

1. Low-loss dielectric/bad conductor: $\tilde{\epsilon} \simeq \epsilon'$, and $\sigma < \omega\epsilon'$
2. Lossy dielectric: $\tilde{\epsilon} = \epsilon' - j\epsilon''$, $\sigma \ll \epsilon''$
3. Good conductor: $\sigma > \omega\epsilon'$, $\sigma \gg \epsilon''$,

where ϵ' denotes the real part of the complex permittivity, ϵ'' its complex part, ω the propagating frequency, and σ the conductivity of the medium.

However, the problem of mm-wave propagation through an optically excited semiconductor substrate requires a full general approach, as the opto-excited substrate can be ascribed to either simplification, depending on the photo-induced plasma density. For example, a high-resistivity (low-doping) silicon wafer is well described by simplification (1) in the absence of an external stimulus, simplification (2) when optically excited above an excess carrier density of $\Delta n \geq 10^{15}\mathrm{cm}^{-3}$, and simplification (3) in the presence of high irradiation levels generating a plasma density exceeding $10^{17}\mathrm{cm}^{-3}$. Most impor-

tantly, the substrate can not be adequately described by either simplification for intermediate plasma densities.

Thus, a general approach is required to fully indicate the mm-wave propagation effects through a variably excited semiconductor substrate. The following treatment presents such an approach with no low-loss or low/high-conductivity approximations, and when faced with situations where the above simplifications apply, the general solution becomes that of the solutions derived using the simplifications.

The characteristic response of a medium to the application of an external electric field is governed by the material permittivity. The complex permittivity, $\tilde{\epsilon_r}$, relative to the permittivity of free-space ($\epsilon_0 = 8.85 \text{ x}10^{-12} \text{ F/m}$), encompasses both dispersion and dissipative losses [222]

$$\tilde{\epsilon_r} = \epsilon_r' - j\left(\epsilon_r'' + \frac{\sigma}{\omega\epsilon_0}\right), \tag{4.1}$$

$$= \epsilon_r' - j\epsilon_t''. \tag{4.2}$$

where ϵ_t''denotes the total loss within the medium, i.e. the sum of the complex components. For the case of a semiconductor substrate, the free carrier conductivity is given as [139]

$$\sigma = \rho^{-1} = q\left(\Delta n_n \mu_n + \Delta n_p \mu_p\right), \tag{4.3}$$

where ρ, Δn_i, and μ_i define the (silicon) resistivity, carrier density, and the charge carrier mobility respectively. The unit electron charge is defined as $q = 1.6 \text{ x}10^{-19} \text{ C}$.

Similarly, the material magnetic response to an externally applied magnetic field is described by the permeability, which may also be complex and dispersive, depending on the material and frequency range. It will be assumed that the semiconductor substrate is non-magnetic, in which case the complex relative permeability becomes

$$\tilde{\mu_r} = 1 - 0j.$$

For materials exhibiting loss, it is customary to present the loss in the form of the loss tangent, which is defined by the angle of the permittivity vector in the complex plane. In the general case, the dielectric loss tangent is defined as

$$\tan\delta_\epsilon = \frac{\epsilon_r'' + \sigma/\omega\epsilon_0}{\epsilon_r'} = \frac{\epsilon_t''}{\epsilon_r'} \tag{4.4}$$

and similarly for the magnetic response

$$\tan\delta_\mu = \frac{\mu_r''}{\mu_r'}. \tag{4.5}$$

Assuming low-loss dielectric conditions, (4.4) reduces to the form commonly found in the literature,

$$\tan\delta_\epsilon = \frac{\epsilon_r''}{\epsilon_r'}. \tag{4.6}$$

The relative permittivity of the semiconductor substrate is given by the Lorentz-Drude model [58, 224]:

$$\tilde{\epsilon_r} = \epsilon_\infty' \left[1 - \sum_i \left(\frac{\omega_i^2}{\omega^2 + \Gamma_i^2} \right) + \frac{j}{\omega} \sum_i \left(\frac{\omega_i^2 \Gamma_i}{\omega^2 + \Gamma_i^2} \right) \right], \tag{4.7}$$

with the free-carrier damping frequency Γ_i, and the free-carrier resonance frequency ω_i for electrons (n) or holes (p). Here, ϵ_∞' describes the background polarisability of the bound charges in the high frequency regime[1] [224, 225].

The photo-induced free-carrier plasma (Chapter 3) can be characterised by its unique resonance frequency, ω_p, which is known as the plasma resonance frequency, which is defined by

$$\omega_p^2 = \sum_i \omega_i^2 = \sum_i \frac{\Delta n_i q^2}{m_i^* \epsilon_0 \epsilon_\infty'}, \tag{4.8}$$

where m_i^* corresponds to the effective mass of the free-carrier type *i* (electrons or holes), with all other terms having been defined above.

[1] $\omega_p < \omega < 2\pi hf$.

The damping frequency, Γ_i, of (4.7) can be calculated from the Drude free-carrier momentum scattering time, τ_i, for the ith carrier type, given by

$$\tau_i = \frac{\mu_i m_i^*}{q}, \tag{4.9}$$

which defines the mean-free time for the momentum loss of the ith carrier type, and $\Gamma_i = 1/\tau_i$; all terms retaining their usual meanings.

4.2.1 Free-carrier plasma frequency, ω_p

The optical properties of solids, such as metals and heavily doped semiconductors, are associated with the relative density of the free-carrier plasma through the plasma resonance frequency ω_p ($\propto (\Delta n)^{1/2}$). The following discussion contrasts the differences between these two commonly treated examples and the opto-excited semiconductor substrate. The transmission properties for materials exhibiting a relative low density free-carrier plasma are found to exhibit attenuation that varies slowly as a function of the plasma injection level, compared to a high reflectivity edge found in the standard metal and heavily doped semiconductor cases. The slow varying attenuation of the opto-excited substrate can be advantageous to their application at higher mm-wave and submm-wave frequencies, which is further discussed in Chapter 8.

4.2.1.1 High frequency limit, $\omega \gg \Gamma$

The *high frequency limit* occurs when the propagating angular frequency becomes much greater than the free-carrier damping frequency, i.e. $\omega \gg \Gamma$; an example of which is the optical properties of solids measured in the infrared to visible region. In the high frequency limit, (4.7) reduces to

$$\tilde{\epsilon_r} = \epsilon'_\infty \left(1 - \frac{\omega_p^2}{\omega^2}\right), \tag{4.10}$$

which gives rise to a frequency-dependant metallic effect, where it is assumed that $\omega, \omega_p \gg \Gamma$. For $\omega < \omega_p$, the relative permittivity drops below zero; the refractive index, $\tilde{n} = \sqrt{\tilde{\epsilon_r}}$, then becomes complex for $\omega < \omega_p$, and real for

$\omega > \omega_p$. The material then acts as a perfect reflector for frequencies below the plasma resonance, and as a dielectric above.

The (power) reflectivity, R, is given by

$$R = \left| \frac{(\eta - 1)^2 + \kappa^2}{(\eta + 1)^2 + \kappa^2} \right|, \tag{4.11}$$

where the complex refractive index is defined by

$$\tilde{n} = \sqrt{\tilde{\epsilon}_r} = \eta - j\kappa, \tag{4.12}$$

with index of refraction η, and coefficient of extinction κ.

The frequency-dependent behaviour of (4.10) gives rise to the plasma edge observed in metals and heavily doped semiconductors, where the doping density dependence is commonly utilised for the determination of the free-carrier effective mass for heavily-doped semiconductors [225–227].

Figure 4.1 displays the plasma edge for a heavily doped silicon wafer, at a range of dopant densities (or ω_p). The non-zero reflectivity beyond the plasma edge results from the high (> 1) permittivity of the wafer, producing reflectiv-

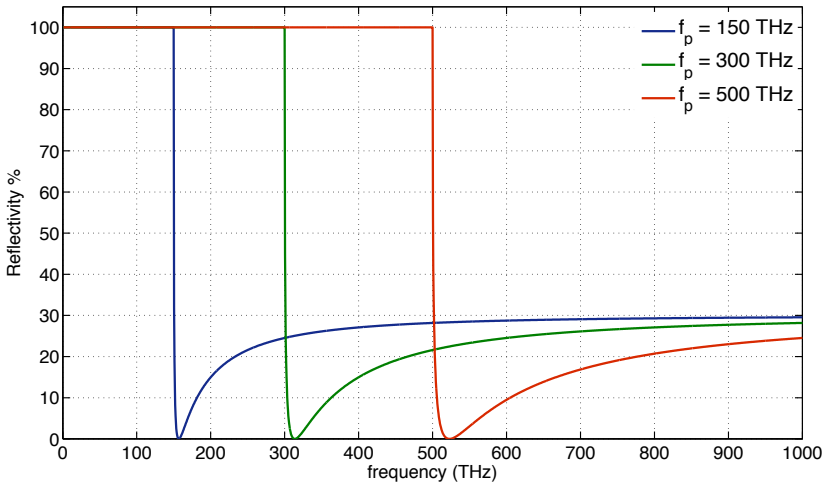

Figure 4.1: Simulated reflectivity from a semi-infinite, heavily-doped semiconductor substrate. The zero reflectivity point indicates the free-carrier plasma resonance, ω_p. Simulations are shown for a range of doping densities (or ω_p), where $f_p = 150$ THz (Δn $\approx$ 5 x10^{20}cm^{-3}), $f_p = 300$ THz (Δn $\approx$ 2 x10^{21}cm^{-3}), and $f_p = 500$ THz (Δn $\approx$ 6 x10^{21}cm^{-3}).

ity from the surface of the dielectric. The plasma resonance corresponds to the zero in the reflectivity, as shown in Figure 4.1, where $\omega(R=0) \approx \omega_p$ [225].

4.2.1.2 Low frequency limit, $\omega \ll \Gamma$

The *low frequency limit* occurs for propagating frequencies below the free-carrier damping frequency[2], $\omega \ll \Gamma$, in which case (4.7) reduces to

$$\tilde{\epsilon_r} = \epsilon'_\infty \left(1 - \frac{\omega_p^2}{\Gamma^2} - j\frac{\omega_p^2}{\omega\Gamma}\right). \tag{4.13}$$

The Drude free-carrier contribution ($\mathrm{Im}[\tilde{\epsilon_r}]$) then becomes important in the low frequency limit, arising from the $1/\omega$ dependence. In cases where the excess carrier densities are large, the optical constants become both large and similar in magnitude, $\eta \approx \kappa$, and thus similar to Section 4.2.1.1, the material behaves as a perfect reflector; this gives rise to the skin depth of a lossy medium

$$\delta_{\mathrm{skin}} = 1/\alpha, \tag{4.14}$$

where α denotes the absorption coefficient[3]. The absorption coefficient is defined by Beer's law [161], and is given later for the general case.

4.2.1.3 Pseudo low frequency limit, $\omega, \omega_p \ll \Gamma$

The *pseudo low frequency limit* pertains to media in which both the propagating frequency and the plasma frequency are less than the free-carrier damping frequency, i.e. $\omega, \omega_p \ll \Gamma$. Millimetre-wave and submm-wave propagation through a lightly doped ($< 10^{17}\ \mathrm{cm}^{-3}$) silicon substrate is one particular example in which the pseudo low frequency limit applies, where $\Gamma \approx 2\ \mathrm{THz}$ or the Drude free-carrier momentum scattering time, $\tau_i = 10^{-13}\ \mathrm{s}$ [225,228]. As a result of the low doping density, the assumption $\omega_p > \Gamma_i$ becomes invalid[4],

[2] again, $\omega_p > \Gamma$ is assumed in the literature, and thus $\epsilon''_r \gg \epsilon'_r$.

[3] α_λ (Chapter 3) and α are used to distinguish between the optical and mm-wave propagation effects, respectively, when both are discussed.

[4] although valid for large free-carrier plasma densities, however, optical excitation to such densities require high irradiances which are out the scope of this thesis.

which leads to gradual changes in the optical properties at (sub) mm-wave frequencies, as the free-carrier plasma density increases (c.f. high frequency limit).

Under dark-state conditions, or for reasonable irradiance, the free-carrier Drude contribution is negligible, due to $\omega_p < \Gamma$, and thus in contrast to Section 4.2.1.2 and from (4.13), the silicon substrate behaves as a low-loss dielectric, giving rise to the low insertion loss observed for high-resistivity silicon substrates.

The increase in the free-carrier plasma density, by application of above bandgap optical excitation, results in an increased plasma resonance ($\omega_p \propto \sqrt{\Delta n}$), and from (4.13) results in a quadratic increase in the dielectric loss of the material. Figure 4.2(a) displays the frequency-dependent loss tangent ($\tan \delta_\epsilon$) for a range of propagating frequencies, where the change in loss is shown.

Further, the combination of the low frequency limit, and the low plasma frequency ($\omega_p < \Gamma$) contribute to the absence of the plasma edge, such that the change in reflectivity changes smoothly as ω_p (Δn) is increased. Figure 4.2(b) displays the reflectivity as a function of plasma frequency for a lightly-doped silicon substrate, for propagating frequencies, f, in the mm-wave and submm-wave range; for comparison to the high-frequency limit, a propagating frequency of 100 THz has been included. As the plasma frequency (density) increases the reflectivity is shown to approach unity, indicating that $\eta \approx \kappa$, i.e. the substrate becomes metallic. This region corresponds to the case where the optical irradiance becomes sufficient such that $\omega_p \geq \Gamma$ ($< 10^{16}\ \mathrm{cm}^{-3}$ here), and thus the traditional low frequency limit applies. However, in almost all practical cases, except those involving high powered laser sources, this region is typically never encountered.

Hence, as a result of the absence of a free-carrier plasma edge and the absence of a metallic effect, for practical levels of irradiance in the pseudo low frequency limit, the modulation of (sub) mm-wave beams via an opto-excited semiconductor substrate thus relies on the gradual control of the free-carrier loss, by suitable optical excitation.

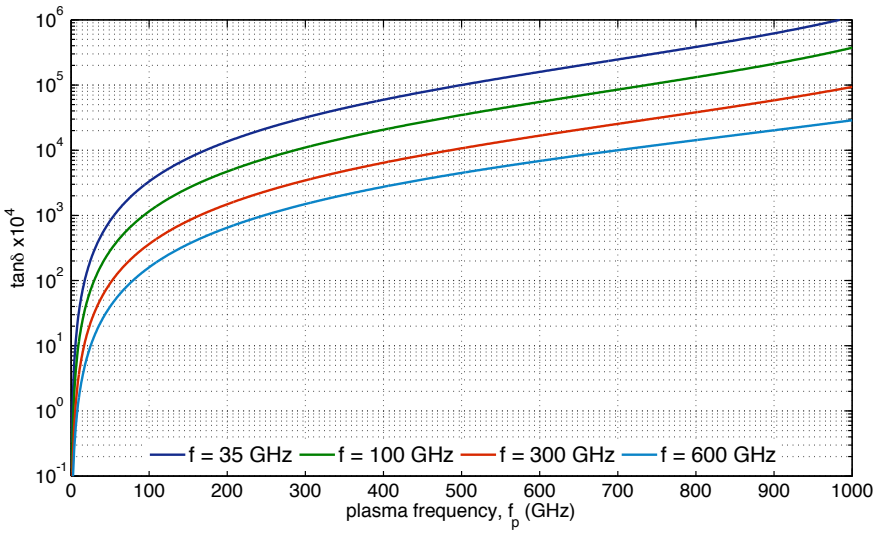

(a)

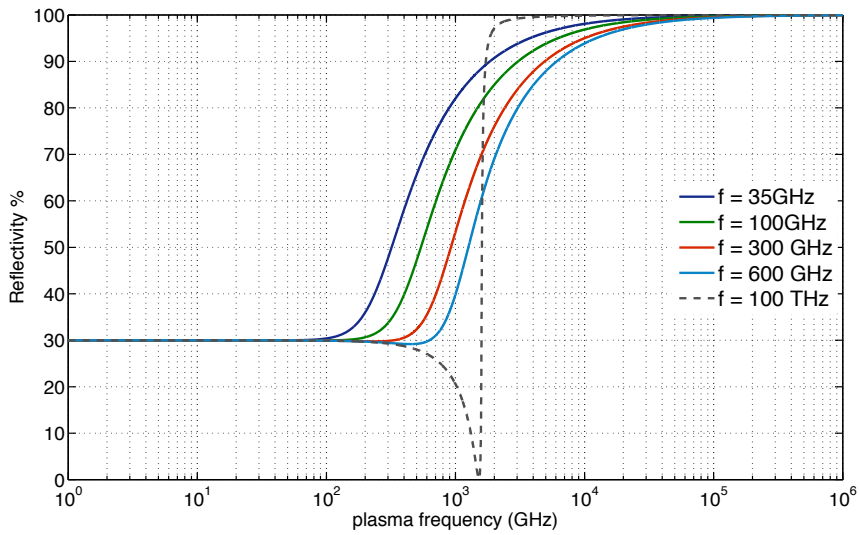

(b)

Figure 4.2: Simulations highlighting the plasma frequency dependence, ω_p, of the (a) loss tangent, and (b) the reflectivity, as a range of propagating frequencies, f.

4.2.2 QO transmission line model: ABCD matrix method

The opto-excited silicon transmission line model is formulated using the above complex permittivity, and the standard ABCD transmission line matrix method [110, 229]. The quasi-optical silicon transmission line was modelled as a lossy transmission line with plane wave propagation, which can be represented as [229]

$$\begin{bmatrix} A & B \\ C & D \end{bmatrix} = \begin{bmatrix} \cosh\tilde{\gamma}l & \tilde{Z}_L \sinh\tilde{\gamma}l \\ \frac{1}{\tilde{Z}_L}\sinh\tilde{\gamma}l & \cosh\tilde{\gamma}l \end{bmatrix}, \tag{4.15}$$

with transmission line element length l, generalised (complex) wave impedance $\tilde{Z}_L = \sqrt{\tilde{\mu}/\tilde{\epsilon}}$, and complex propagation constant

$$\tilde{\gamma} = \alpha + j\beta. \tag{4.16}$$

The complex propagation constant $\tilde{\gamma}$, is defined by the absorption coefficient α (Np/m), and the phase coefficient β (rad/m).

Accounting for both conductive and dielectric loss, the general expressions for attenuation and the phase coefficient are [230]

$$\alpha = \frac{2\pi}{\lambda_0}\sqrt{\epsilon_r'\mu_r'} \cdot \sqrt{\frac{1 - \tan\delta_\epsilon \cdot \tan\delta_\mu}{1 - \tan^2\frac{\delta_\epsilon+\delta_\mu}{2}}} \cdot \tan\frac{\delta_\epsilon + \delta_\mu}{2} \tag{4.17}$$

and

$$\beta = \frac{2\pi}{\lambda_0}\sqrt{\epsilon_r'\mu_r'} \cdot \sqrt{\frac{1 - \tan\delta_\epsilon \cdot \tan\delta_\mu}{1 - \tan^2\frac{\delta_\epsilon+\delta_\mu}{2}}} \cdot \tan\frac{\delta_\epsilon + \delta_\mu}{2} \tag{4.18}$$

which for a non-magnetic material become

$$\alpha = \frac{2\pi}{\lambda_0}\sqrt{\epsilon_r'} \cdot \sqrt{\frac{1}{1 - \tan^2\frac{\delta_\epsilon}{2}}} \cdot \tan\frac{\delta_\epsilon}{2} \tag{4.19}$$

and

$$\beta = \frac{2\pi}{\lambda_0}\sqrt{\epsilon_r'} \cdot \sqrt{\frac{1}{1 - \tan^2\frac{\delta_\epsilon}{2}}}. \tag{4.20}$$

Equations (4.19), (4.20) reduce to their common forms when dealing with optical properties of solids in the high frequency limit, with $\omega \gg \omega_p$, which are [161]

$$\alpha = \frac{2\pi\kappa}{\lambda_0}, \tag{4.21}$$

$$\beta = \frac{2\pi\eta}{\lambda_0}, \tag{4.22}$$

where, $\epsilon_r' \approx \epsilon_\infty'$, and $\kappa \ll \eta$. However, these are strictly only valid in the high frequency limit, and thus the general expression should be used in the case of lightly-doped, opto-excited semiconductor substrates.

For completeness, the complex refractive index can be obtained from the complex permittivity using [161]

$$\eta = \left[\frac{1}{2}\left(\epsilon_r' + \sqrt{\epsilon_r'^2 + \epsilon_t''^2}\right)\right]^{1/2}, \tag{4.23}$$

and

$$\kappa = \left[\frac{1}{2}\left(-\epsilon_r' + \sqrt{\epsilon_r'^2 + \epsilon_t''^2}\right)\right]^{1/2}, \tag{4.24}$$

with the total dielectric loss, $\epsilon_t'' = \epsilon_r'' + \sigma/\omega\epsilon_0$.

Finally, the transmission (S_{21}) and reflection (S_{11}) coefficients are obtained [229] from the ABCD matrix using,

$$S_{21}(dB) = 20\log_{10}\left[\frac{2}{A+B+C+D}\right] \tag{4.25}$$

and

$$S_{11}(dB) = 20\log_{10}\left[\frac{A+B-C-D}{A+B+C+D}\right]. \tag{4.26}$$

Equation (4.25) and (4.26) define the transmission and reflection power components and thus the logarithm is preceded by a factor of 20 to convert from the field components, inherently treated by the ABCD matrix method.

4.2.3 QO transmission line model involving an opto-excited semiconductor substrate

Combining the Lorentz-Drude model, the complex propagation parameters, and the lossy ABCD matrix provides a generalised analytical model detailing the transmission line properties for an optically excited semiconductor substrate, at a given (sub) mm-wave frequency. This gives insight into the free-carrier plasma density requirements for (sub) mm-wave modulation.

The following details the transmission line properties for a high-resistivity silicon substrate at 94 GHz, where the following substrate parameters have been assumed, based on standard literature values [58, 139]; these are summarised in Table 4.1.

Table 4.1: Assumed characteristic parameters for a high-resistivity silicon substrate. †m_e corresponds to the rest mass of an electron.

Parameter	Γ_n^{-1}	Γ_p^{-1}	m_n^*	m_p^*	μ_n	μ_p	ϵ'_∞
(units)	$\mathrm{x10^{-13}\ s^{-1}}$		kg		$\mathrm{cm^2/V \cdot s}$		
Value	2.2	1.3	$0.259m_e$	$0.380m_e$	1500	600	11.7

Optical excitation of a semiconductor substrate, resulting in an increased electron-hole plasma density, alters the complex refractive index (permittivity) of the bulk material. The change in complex refractive index, shown in Figure 4.3, results in an increase in the extinction coefficient, κ, due to increased free-carrier Drude contribution. At sufficiently large excitation densities ($\omega_p \geq \Gamma$) the significant free-carrier Drude contribution yields a metallic effect ($\eta \approx \kappa$), arising from the transition into the low-frequency limit.

In addition, the Fabry-Pérot etalon produced by the transmission line containing a finite-thickness semiconductor substrate yields a range of wafer thicknesses which correspond to either maximum transmission, minimum reflection, or vice-versa; the corresponding matched thicknesses are given by

$$d = \frac{m\lambda}{4\sqrt{\epsilon'_r}} \qquad m = 2, 4, 6, ... \tag{4.27}$$

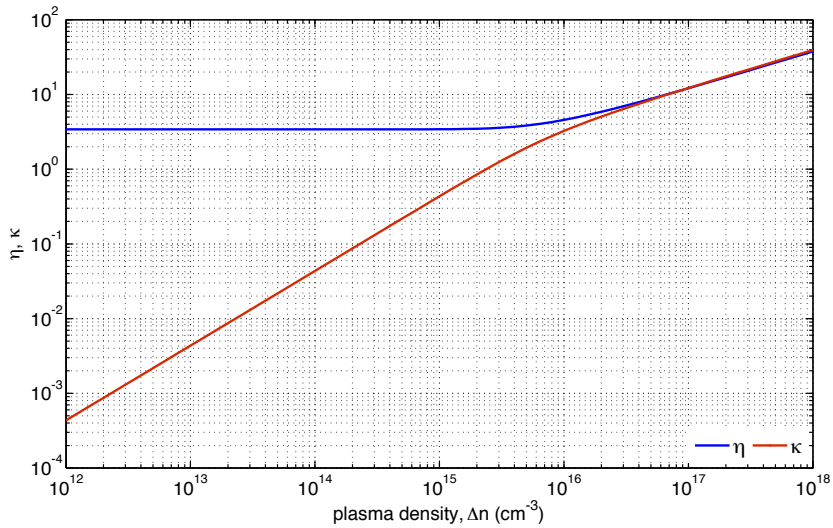

Figure 4.3: Simulated complex refractive index of a high-resistivity silicon substrate, as a function of plasma density, N_c. A zero SRV, and homogeneous plasma profile is assumed.

and

$$d = \frac{m\lambda}{4\sqrt{\epsilon_r'}} \qquad m = 1, 3, 5, ... \tag{4.28}$$

where substrate thicknesses given by (4.27) yield maximum transmission, and (4.28) maximum reflection.

The change in the transmission line properties of the semiconductor substrate, subject to the optical modulation of the complex refractive index, can then be determined from the ABCD matrix. Figure 4.4 displays the simulated transmittance (S_{21}) and reflectance (S_{11}) of a high-resistivity, $932\ \mu\mathrm{m}$ thick silicon substrate as a function of optical irradiance, I_{opt}, across the whole W-band frequency range; zero SRV, and a homogeneous plasma profile have been assumed. The effective carrier lifetime has been taken as $500\ \mu\mathrm{s}$, with an optical excitation wavelength of $\lambda = 900\ \mathrm{nm}$. Conversion between the irradiation density and the photo-induced free-carrier plasma density is given by (3.14).

Figure 4.4 indicates several features of the opto-excited substrate transmission line. First, as the photo-induced free-carrier plasma density is in-

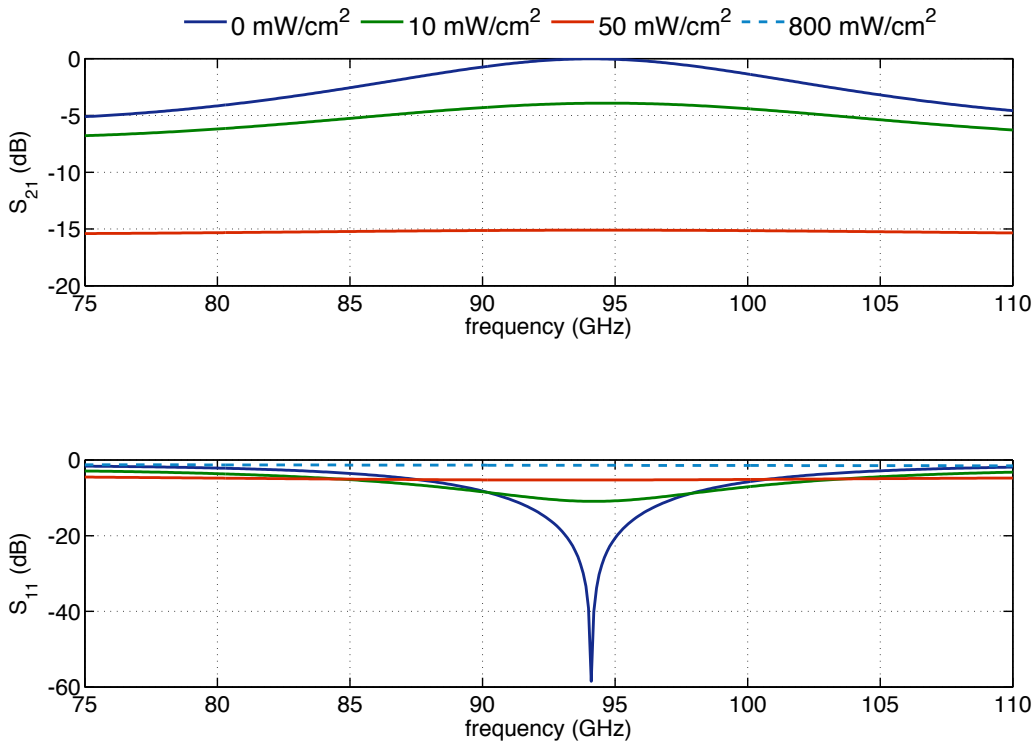

Figure 4.4: Simulated transmittance (S_{21}) and reflectance (S_{11}) interferograms through a high-resistivity, $932\ \mu\mathrm{m}$ thick, silicon substrate with an effective free-carrier lifetime of $500\ \mu\mathrm{s}$. The interferograms are displayed at several irradiance levels at an excitation wavelength of $\lambda = 900\ \mathrm{nm}$. The irradiances correspond to the following plasma densities: $0\ \mathrm{mW/cm^2} \rightarrow 10^{12}\ \mathrm{cm^{-3}}$, $10\ \mathrm{mW/cm^2} \rightarrow 1.65\ \mathrm{x10^{14}\ cm^{-3}}$, $50\ \mathrm{mW/cm^2} \rightarrow 8.24\ \mathrm{x10^{14}\ cm^{-3}}$, and $800\ \mathrm{mW/cm^2} \rightarrow 1.32\ \mathrm{x10^{16}\ cm^{-3}}$, which can be calculated using (3.14).

creased, the increased Drude contribution ($\kappa \gg 0$) yields increased attenuation, as would be expected. Secondly, larger changes in reflection than in transmission are observed due to the increased finesse of the reflection interferogram. The pronounced changes in reflection will be beneficial for realising improved piFZPAs, due to the reduced plasma density requirements, which is discussed in Chapter 5. Finally, for sufficiently high irradiances, which generate high free-carrier plasma densities, the substrate becomes metallic-like, with an increased surface reflectivity. The increased reflectivity is illustrated for an irradiation level of $800\ \mathrm{mW/cm^2}$, which generates an approximate plasma density of $10^{16}\ \mathrm{cm^{-3}}$, where from Figure 4.3 $\eta \approx \kappa$. The trans-

mittance trace for an irradiation level of $800\ \mathrm{mW/cm^2}$ has been omitted to maintain clarity, as the mean transmittance over W-band was approximately $S_{21}(800\ \mathrm{mW/cm^2}) \approx -105\ \mathrm{dB}$.

4.3 QO Transmission line characterisation of high-resistivity silicon wafers

This section details measurements performed on a range of silicon wafers as a function of optical excitation density, and wavelength. The results highlight the significance of the substrate surface recombination velocity (chapter 3) on the corresponding modulation of (sub) mm-wave beams, and are also compared to the analytical model developed in the previous sections, which are shown to be in excellent agreement.

4.3.1 Quasi-optical vector network analyser

A quasi-optical (QO) transmission line and a vector network analyser were used for measuring the transmission line properties of the opto-excited silicon wafers. The wafers used in this work were high resistivity ($\rho > 10\ k\Omega\mathrm{cm}$) Float-zone silicon, which ensured low insertion loss in the dark-state. The transmission line characteristics were also measured alongside a single wafer which was available from previous, independent, work. All wafers were procured (coincidentally) from TOPSiL Semiconductor Materials AS [217], and the known wafer parameters for each batch are given in Table 4.2. The wafer batches have been designated stocks A and B, where stock A defines the original single wafer, and stock B the wafers obtained for this work; the Stock B wafers are referred to as $w1 \rightarrow w6$ (Chapter 3) once passivated. The large effective lifetime for the un-treated wafer from Stock A arises due to the increased wafer thickness, thus surface recombination is diffusion limited.

The 4-port vector network analyser[5] (VNA) included W-band extension

[5]Anritsu ME7808B broadband VNA

Table 4.2: Silicon wafer details used throughout the characterisations performed. Stock B designates the wafers used for realising the piFZPA. †pre-passivation.

Stock	Thickness (μm)	Diameter (mm)	Resistivity (Ωcm)	Lifetime Bulk (μs)	Lifetime Effective (μs)
A	4100	87.80	$\sim 12,000$	-	793
B†	675	150.00	$\sim 15,000$	5500	60

heads[6] which allowed characterisation across the extended W-band region, 65 - 110 GHz. However, measurements in the 65 - 75 GHz were typically unreliable and have thus been omitted throughout. Characterisations were restricted to a 2-port configuration giving the transmission, S_{21}, and reflection, S_{11}, parameters. The free-space QO transmission line provided a convenient configuration for coupling the silicon substrates to an external optical source, with the addition of relevant optics.

The QO-VNA setup is illustrated in Figure 4.5(a). The (W-band) coupling optics consisted of a standard pair of identical aspherical 88 mm aperture blazed HDPE lenses, which were characterised and found to produce a small focal region of 32 mm in diameter (1/e), with an output focal length of approximately 340 mm; this gives in a depth of focus of ± 117 mm from the beam waist[7] [231]. This configuration ensured low diffraction effects, and plane-wave illumination at the semiconductor substrate. Standing-wave reflections from the optic mounts and feedhorns were minimised by implementing the time-gate method.

Measurements were referenced to the free-space transmission through the QO transmission line for the transmission measurements, and to a planar mirror for the reflection measurements. The measured interferograms then gave accurate account of the transmission line properties of the dark and opto-excited states of the semiconductor substrate.

Using the analytical model described above, a non-linear unconstrained local minimisation routine was performed on each interferogram. Using the

[6] Anritsu 3742-EW

[7] less than 10% increase in beam radius, ω, from the beam waist, ω_0

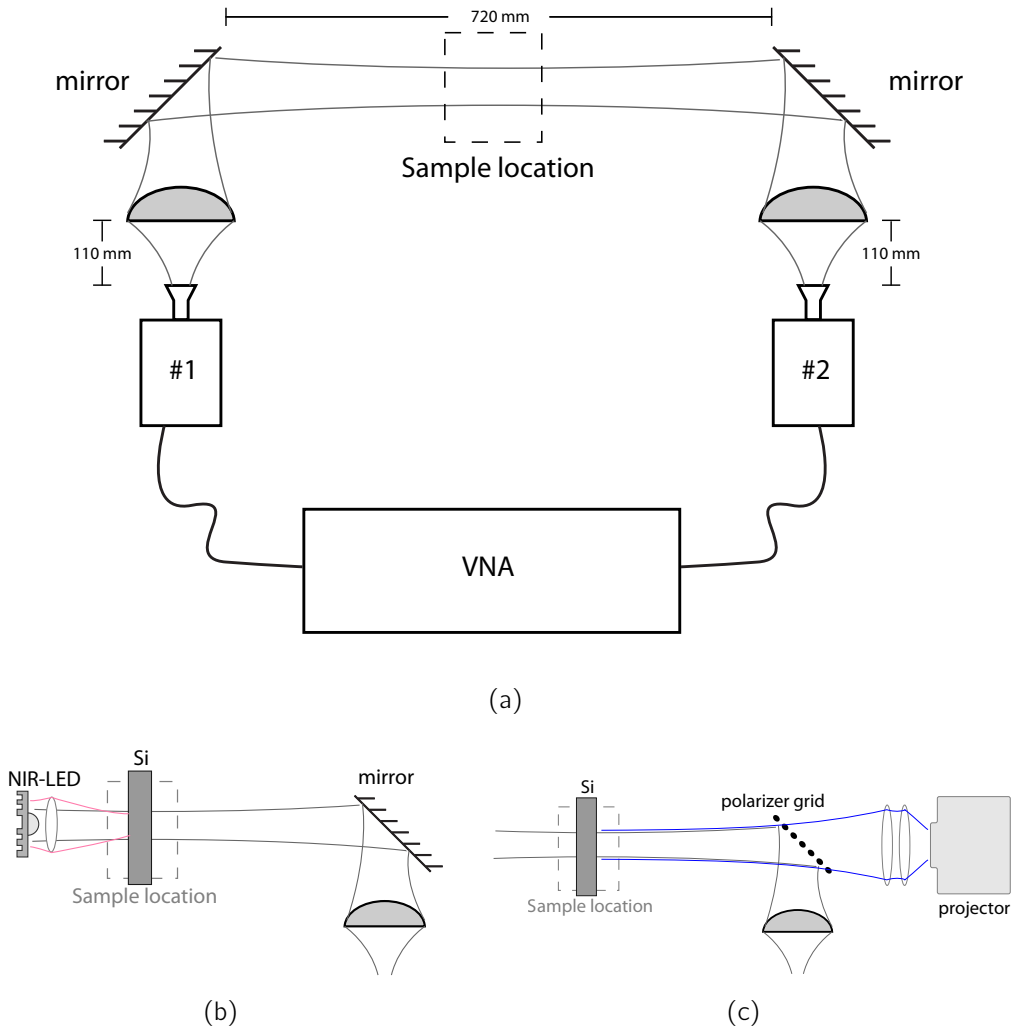

Figure 4.5: W-band QO-VNA configuration used for free-space transmission line silicon wafer characterisations; the wafers were placed at sample the location. (a) depicts the basic QO-VNA setup, (b) the NIR illumination arrangement, with a single high power Osram NIR-LED, and (c) the visible irradiation arrangement, using a high power data projector as the source.

fminsearch function in Matlab and a LMS algorithm, the extraction routine then provided the complex permittivity and thickness for the semiconductor substrate. Whilst this routine runs a simultaneous extraction of both $\tilde{\epsilon}_r$, d, the strong correlation to the substrate thickness resulted in accurate determination of the complex permittivity. This approach was also extended to the opto-excited state, where the algorithm then extracted the complex permittivity (and effective irradiance), given the initial thickness specification. The opto-excited plasma density can be inferred from the Lorentz-Drude model.

4.3.2 Characterisation pre-wafer passivation

Measurements on both wafer stocks were performed in both the dark, and opto-excited state. Dark state measurements were used to extract the base permittivity and wafer thickness, for comparison with the expected values. These then formed the initial parameters for the opto-excited state measurements, where the extraction algorithm then gave the optically induced complex permittivity.

4.3.2.1 Dark state

The first dark state characterisations were performed on the single A stock wafer, designated A1. Using a standard permittivity of $\epsilon_r' = 11.7$, and a measured wafer thickness of $d = 4,200 \pm 5\ \mu\mathrm{m}$, the interferograms were fitted using the above algorithm. The algorithm can be used to fit either the transmittance, or reflectance interferograms. In almost all cases, the reflectance interferogram was used because of its increased finesse, which then limits the possible error on d. The time-gate specification for the reflectance measurement was located, $t_g = 2.139 \pm 0.271\ \mathrm{ns}$.

Figure 4.6 displays the measured, and best fit, interferograms for wafer A1. For illustration, the time-gate was omitted in the transmittance measurement, which highlights the significance of standing wave reflections. The numerical fitting of the interferograms produced accurate fits to the model with $R^2 = 0.84$ (S_{21}) and $R^2 = 0.92$ (S_{11}), where the low R^2 for the transmittance resulted from the scatter in the data, due to reflections. The best

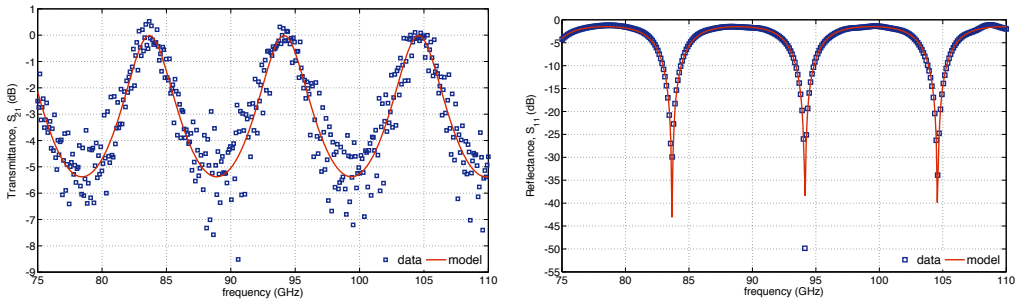

(a) (b)

Figure 4.6: Measured, and modelled transmission line interferograms for wafer A1, where (a) displays the transmittance, and (b) the reflectance interferograms. The large scatter in the transmittance measurements results from no time-gate inclusion.

fit interferograms produced a substrate thickness of $d = 4,192.6\mu m$, and a complex permittivity

$$\tilde{\epsilon}_r = 11.7 - 8 \text{ x}10^{-4}\text{j}, \quad \tan\delta \text{ x}10^4 = 0.676.$$

The above process was then repeated for a single stock B wafer, where the starting parameters $\epsilon_r' = 11.7$ and wafer thickness $d = 675 \pm 15$ μm were used. The wafer thickness and tolerance were taken from the supplied specification sheet. Both interferograms were made utilising the time-gate technique; the transmittance measurement was performed with a time-gate specification, $t_g = 4.357 \pm 0.616$ ns, and the reflectance measurement with a time-gate of $t_g = 2.152 \pm 0.342$ ns. The measured and modelled interferograms for the stock B wafer are shown in Figure 4.7.

The best fit interferograms yielded $R^2 = 1.00$ (S_{21}) and $R^2 = 0.93$ (S_{11}), where reduced reflections give rise to an improved agreement between data and model. The substrate details from the best fit gave a substrate thickness, $d = 673.5$ μm, and a complex permittivity,

$$\tilde{\epsilon}_r = 11.7 - 8 \text{ x}10^{-4}\text{j}, \qquad \tan\delta \text{ x}10^4 = 0.676,$$

where the similarity between both wafer permittivities results from the comparable resistivities.

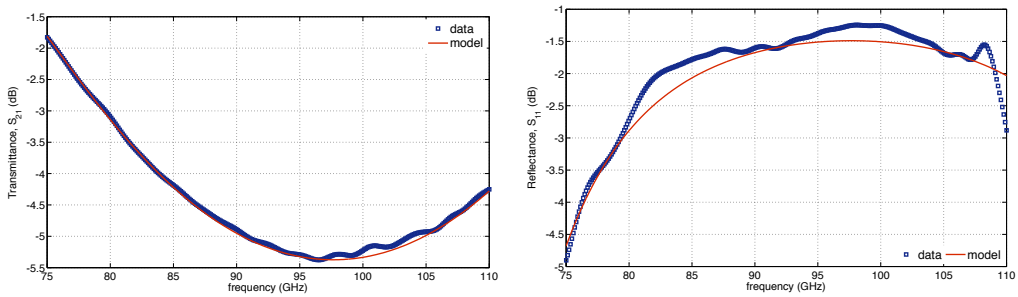

(a) (b)

Figure 4.7: Transmission line measurements on a 675 μm, stock B, silicon wafer. Figure (a) illustrates the transmission interferogram, and (b) the reflection interferogram. The thinner wafer supports fewer cycles in the interferograms and is shown to be optimised for maximum reflection at 98GHz.

4.3.2.2 Opto-excited state

The above procedure was then repeated for both the stock A and B wafers in the optically excited state. Both wafers were characterised under NIR illumination using an Osram SFH-4751 3W IR-LED source, and visible illumination using a Sanyo PLC-XM150 6,000 ANSI lumens XGA data projector as the source, at a range of illuminating densities.

Taking wafer A1 first, the QO-VNA setup was slightly modified to include the NIR LED as shown in Figure 4.5(b). The coupling of the NIR to the wafer surface was improved by using an additional focusing lens (Ledil Oy CA10861-Iris-IR), which reduced the half-power beamwidth to $\pm 5.5°$ from the original $\pm 70°$. However, while the high power LED is expected to produce approximately 1.5 W CW excitation at 960 nm, the low fill factor over the mm-wave focal region resulted in a significantly reduced effective plasma density. Thus, the effects of the excitation with the NIR were marginal.

The irradiance was measured using a thermal power meter (Melles Griot 13PEM0001). The measured irradiance of the NIR LED gave an estimate of the effective power density due to the spatial non-uniformity of the output beam, where the non-uniformity resulted in reduced effective irradiance, producing very little change (< 0.3 dB transmission) in the measured transmission properties. Figure 4.8 displays the measured and modelled reflection

interferogram for the thick stock A wafer with the NIR LED positioned behind the wafer. The short separation distance produced a half-power illuminated spot of approximately 8 mm (FWHM), at normal incidence, with a peak irradiance of $54\ \mathrm{mW/cm^2}$.

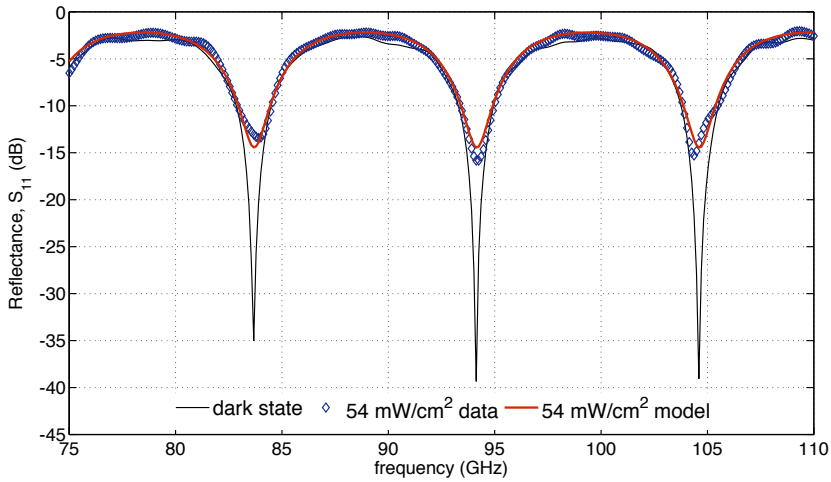

Figure 4.8: Measured and modelled reflectance interferogram for wafer A1 under $54\ \mathrm{mW/cm^2}$ NIR illumination. The null is shown to drop by up to 25 dB at 94 GHz.

The numerical fit the the opto-excited interferogram yielded a complex permittivity of ($R^2 = 0.98$)

$$\tilde{\epsilon}_r = 11.693 - 0.131j, \qquad \tan\delta\ \mathrm{x}10^4 = 112.03,$$

where the substrate thickness was fixed. A loss tangent of this magnitude corresponds to an effective plasma density, $\Delta n \approx 4\ \mathrm{x}10^{13}\ \mathrm{cm}^{-3}$. The reflection null is shown to degrade by up to 25 dB, at 94 GHz, indicating sufficient irradiation to alter the complex refractive index such that the the matching condition of the etalon is destroyed. The reflectance interferograms were measured with a time-gate of $t_g = 2.139 \pm 0.271\ \mathrm{ns}$ which isolated the silicon wafer from the LED assembly.

In comparison, the thin stock B wafers did not yield a discernible change in the transmission properties due to their thickness, high SRV, and the low filling factor of the NIR LED source over the mm-wave focal spot.

The characterisations were repeated at visible wavelengths, where the im-

proved illumination uniformity produced by the projector optics yielded better results. The Sanyo data projector was used to project a single primary colour onto the wafer, which was assumed to be monochromatic during the modelling. The monochromatic simplification used throughout the modelling, and the measured power levels, thus represent an under-estimation to the optically induced plasma. However, this has been found to be sufficient to within a few dB of the measured change due to the large errors associated with the assumed substrate parameters.

The monochromatic wavelengths were taken as the peak of the primary colour band, as obtained by measuring the spectral output of the projector. The spectral output of the Sanyo projector is shown in Figure 4.9 – in addition to the NIR output – and was measured using an optical spectral analyser (Yokogawa AG-6315B OSA).

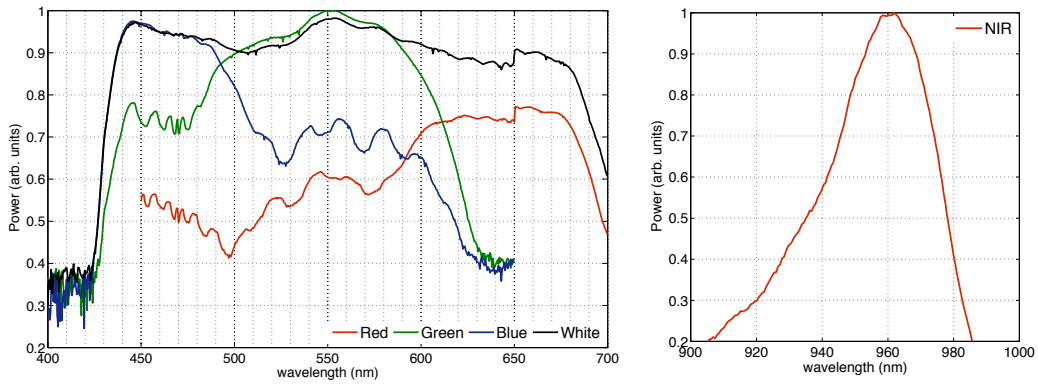

Figure 4.9: Measured spectral output from the Sanyo PLC-XM150 projector, and the Osram NIR LED.

The 'peak' wavelengths were then: 445 nm for blue; 550 nm for green; 650 nm for red; and 550 nm for full white projection. The irradiance was then controlled either by varying the opacity of the projected image to a black background, or by varying the projected image height (size). In addition, the irradiance was maximised by reducing the distance to the projector focal plane by incorporating additional optics. The additional optics consisted of standard 77 mm diameter Hoya camera lenses, which where either +2, +3, or +4 diopters depending on the projected image height. The modified setup

of the QO-VNA is shown in Figure 4.5(c), where a vertical polariser grid was used to simultaneously illuminate the surface of the substrate with both mm-wave and optical wavelengths. The polariser grid resulted in a loss of approximately 50% of the optical irradiance, however, the high output from the projector meant that it was still suitable for initial investigations. Improved optical transmission, whilst maintaining good mm-wave reflectivity was later achieved by replacing the polariser grid with a indium tin oxide coated polymer film. The use of this transparent reflector is discussed in Chapter 6.

Figure 4.10 displays the optically excited interferograms for a stock B wafer, where the dark reference has been subtracted from the measured data in order to maximise clarity in the figure. The illumination height of the projected coloured images were 60 mm (80 mm width), with 100% opacity (full power), where the measured irradiance was found to be uniform over the illuminated area. The time-gate was $t_g = 4.295 \pm 0.496$ ns for the transmittance, and $t_g = 2.206 \pm 0.313$ ns for the reflectance measurements. The peak attenuation observed, which is shown for $218\ \mathrm{mW/cm^2}$ white illumination, corresponds to an approximate plasma density of $\Delta n = 2.6\ \mathrm{x}10^{13}\ \mathrm{cm}^{-3}$, indicating very little change in the permittivity. The small change observed resulted from the dominance of the surface recombination effects, discussed previously in Chapter 3. The largest attenuation, at 94 GHz, was measured as 0.27 dB.

Hence, for sufficient spatial modulation at mm-wave frequencies, the surface recombination effects must be reduced, for both visible and NIR excitation for the current (stock B) substrate thickness.

4.3.3 Characterisation post-wafer passivation

The above measurement procedure was then repeated using the six passivated wafers, $w1 \rightarrow w6$, from stock B. The passivation details were outlined, along with the corresponding improvements to the effective lifetime and SRV, in Chapter 3. The combined effects of an increased effective lifetime, and reduced SRV, resulted in an increased opto-excited plasma density for a given irradiation level. Hence, the propagation effects increased significantly.

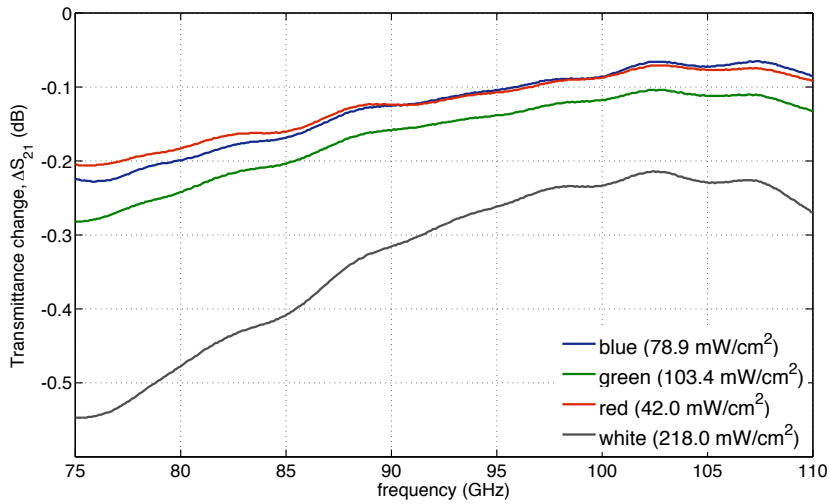

(a)

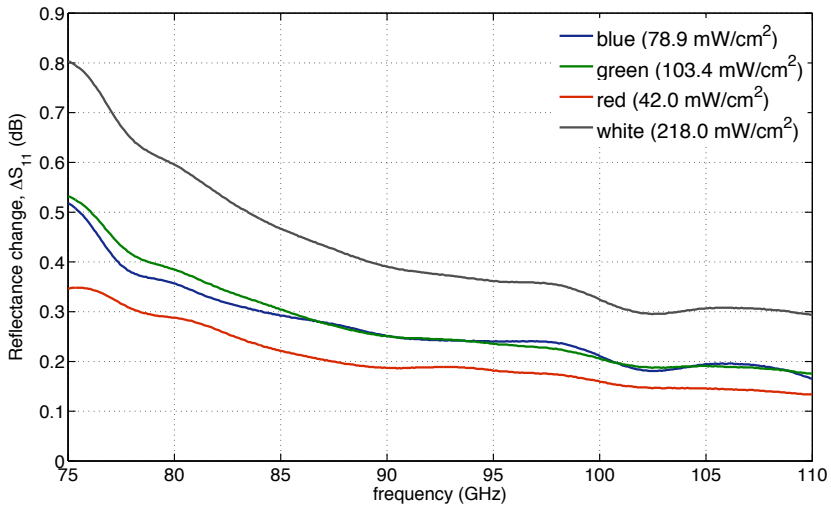

(b)

Figure 4.10: Measured change in (a) transmission and (b) reflection interferograms for a single stock B wafer under high density visible excitation. The illumination density varied from $80\ \mathrm{mW/cm^2}$ (blue) up to $218\ \mathrm{mW/cm^2}$ (white).

4.3.3.1 Dark state

Dark state measurements were initially repeated in order to ascertain the new wafer thicknesses, which were reduced during the passivation process; mechanical measurement of the wafer thicknesses was avoided due to the surface damage that would ensue. In all cases, the initial starting parameters for the modelling algorithm were $\epsilon_r' = 11.7$, and $d = 675\ \mu\mathrm{m}$.

Experimental data was modelled against the reflection interferogram as before. Figure 4.11 displays the measured and modelled interferograms for both the transmittance and reflectance measurements. While the models were generated based on the fit to the reflectance data, the agreement with the transmittance data appears consistently better across all wafers. This suggests that there may have been some error introduced into the reflection measurement, or reference. The mean goodness of fits for the reflectance data yielded $R^2 = 0.90 \pm 0.02$, with $R^2 = 0.97 \pm 0.02$ for the transmission data. The time-gate was set as $t_g = 4.131 \pm 0.250\ \mathrm{ns}$ for the transmittance, and $t_g = 2.014 \pm 0.200\ \mathrm{ns}$ for the reflectance measurements. Using the transmittance data, the error associated in the obtained thickness is no more than 4% compared to the reflectance data results, highlighting the robustness of the fitting algorithm; the largest source of error being related to errors incurred in the reflection measurements. The complex permittivity was found to be unchanged by the passivation process, as should be expected due to the negligible passivation layer thickness ($\sim \mathrm{nm} \ll \lambda$).

The wafer thicknesses obtained from the modelling are given in Table 4.3.

Table 4.3: Stock B silicon wafers: post-passivation wafer thickness. †error corresponds to maximum error case, Err = 4%.

Wafer	d† (μm)	[$R^2(S_{21})$]	Wafer	d† (μm)	[$R^2(S_{21})$]
$w1$	594.20 ± 23.76	[0.98]	$w4$	589.26 ± 23.56	[0.99]
$w2$	589.74 ± 23.60	[0.99]	$w5$	593.93 ± 23.76	[0.99]
$w3$	599.91 ± 24.00	[0.96]	$w6$	597.02 ± 23.88	[0.88]

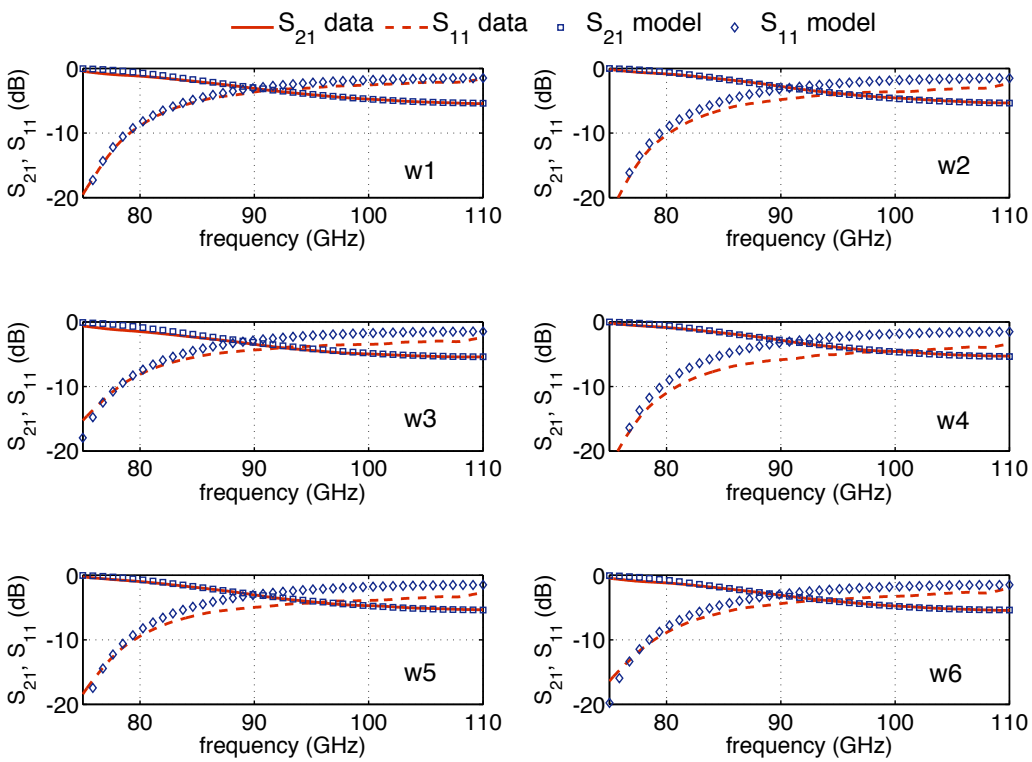

Figure 4.11: Dark state interferograms for each passivated stock B wafer. The new thickness for each wafer, post- passivation is determined from numerical simulation based on the reflection interferogram. Initial guess parameters were $\epsilon_r' = 11.7$, $d = 675\mu m$, and $I_{\text{opt}} = 0$.

4.3.3.2 Opto-excited state

The passivated wafers were re-characterised at visible and NIR illuminating wavelengths using the same sources, as above.

Beginning with the NIR measurements, the measurement configuration remained as Figure 4.5(b) where measurements were performed with two LEDs/lenses in order to improve coupling efficiency; the measured peak irradiation density was approximately $130\ \text{mW/cm}^2$.

Figure 4.12 displays the measured transmittance interferograms for each of the six passivated stock B wafers ($w1 \rightarrow w6$). The time-gate was $t_g = 4.295 \pm 0.496$ ns. The division of the passivation/wafer quality (Chaper 3) gave rise to a modest, and large, change in transmission through the set of wafers, as shown in the Figures 4.12(a), 4.12(b) respectively. The dotted lines

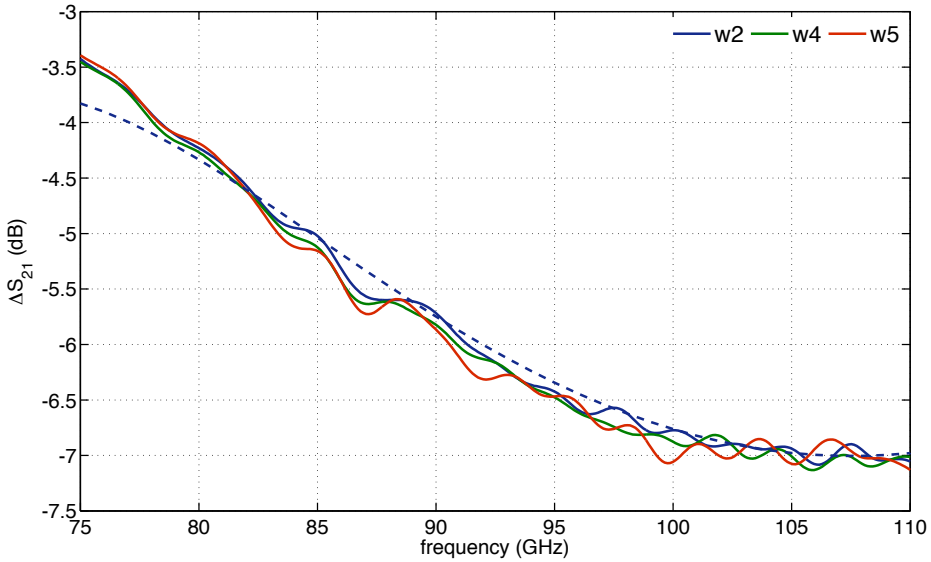

(a)

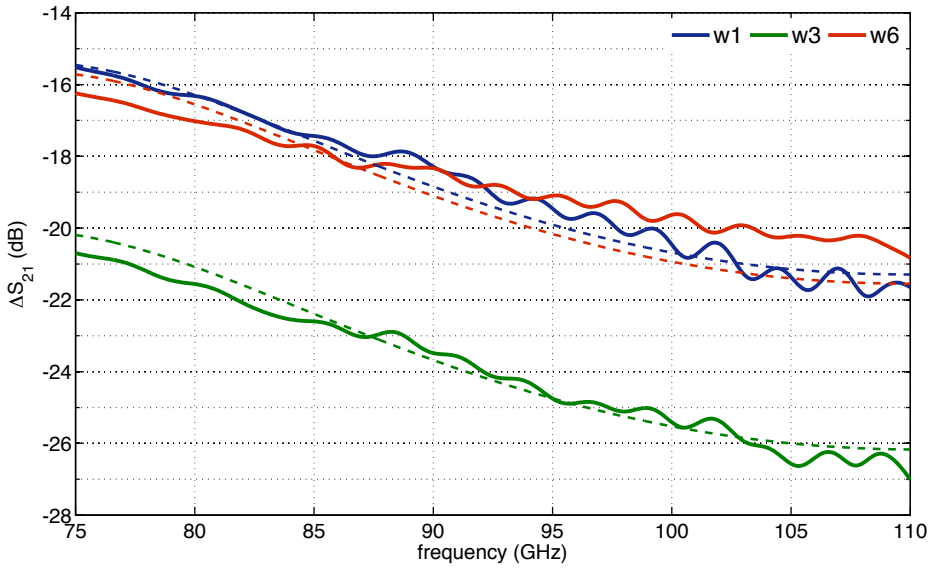

(b)

Figure 4.12: Measured (solid line) and modelled (dashed line) change in transmittance interferograms for each stock B wafer, with NIR optical excitation. (a) displays a modest attenuation corresponding to the lower quality passivated wafers, and (b) the maximum in reduced transmission corresponding to the high quality wafers.

represent the best fit model to the data, and are shown to agree well for all wafers. Due to the similarities between wafers $w2$, $w4$, and $w5$, only a single model has been included. All models assume zero SRV, and a homogeneous plasma.

The effective lifetimes were based on the QSSPC measurements, which were performed at the IFE institute, as the mm-PCD (Chapter 3) had not been completed at the time of measurement. The effective lifetimes were measured as: $\tau_{\text{eff}}(w1) = 2500\ \mu\text{s}$, $\tau_{\text{eff}}(w3) = 4700\ \mu\text{s}$, $\tau_{\text{eff}}(w6) = 2600\ \mu\text{s}$, and $\tau_{\text{eff}}(w2) \approx \tau_{\text{eff}}(w4) \approx \tau_{\text{eff}}(w5) \approx 120\ \mu\text{s}$. An irradiance of $27\ \text{mW/cm}^2$ was used in all cases representing a 21% coupling efficiency, compared to 7% found for earlier measurements utilising a single NIR LED and lens. The lowest attenuation observed ($w2, w3, w4$) at 94 GHz was measured as 6.4 dB, corresponding to a loss tangent $\tan\delta_\epsilon\ \text{x}10^4 = 1,638$ ($\Delta n = 6.0\ \text{x}10^{14}\ \text{cm}^{-3}$). The maximum attenuation observed ($w3$) was measured as 24.6 dB (94 GHz), corresponding to a loss tangent of $\tan\delta_\epsilon\ \text{x}10^4 = 11,037$ ($\Delta n = 3.0\ \text{x}10^{15}\ \text{cm}^{-3}$), thus obviously representing a significant improvement over the un-treated case.

The visible illumination measurements were repeated as above using the setup of Figure 4.5(c). The projector height was increased to 90 mm, resulting in a reduced irradiance. Figure 4.13 displays the transmittance interferogram measured for wafer $w6$, with a time-gate of $t_g = 4.152 \pm 0.366$ ns. The optical irradiance was reduced by approximately 75% for the new projected area. The effective lifetime of the wafer was measured as approximately $\tau_{\text{eff}} = 1,500\ \mu\text{s}$ (Chapter 3), lowered due to the delay between the irradiation measurements ($\approx$ 40 wks).

The transmission through the opto-excited wafer was found to have reduced significantly as a result of the wafer passivation. The lowest attenuation, produced by blue irradiation, was measured as 8.2 dB at 94 GHz, which corresponds to a loss tangent $\tan\delta_\epsilon\ \text{x}10^4 = 1,360$ ($\Delta n = 8.7\ \text{x}10^{14}\ \text{cm}^{-3}$). The maximum visible attenuation was measured for white light irradiation, due largely to a higher illumination density, and was found to be 14.7 dB (at 94 GHz), with a loss tangent $\tan\delta_\epsilon\ \text{x}10^4 = 4,476$ ($\Delta n = 1.6\ \text{x}10^{15}\ \text{cm}^{-3}$).

The change in transmission for irradiation by the NIR sources has been in-

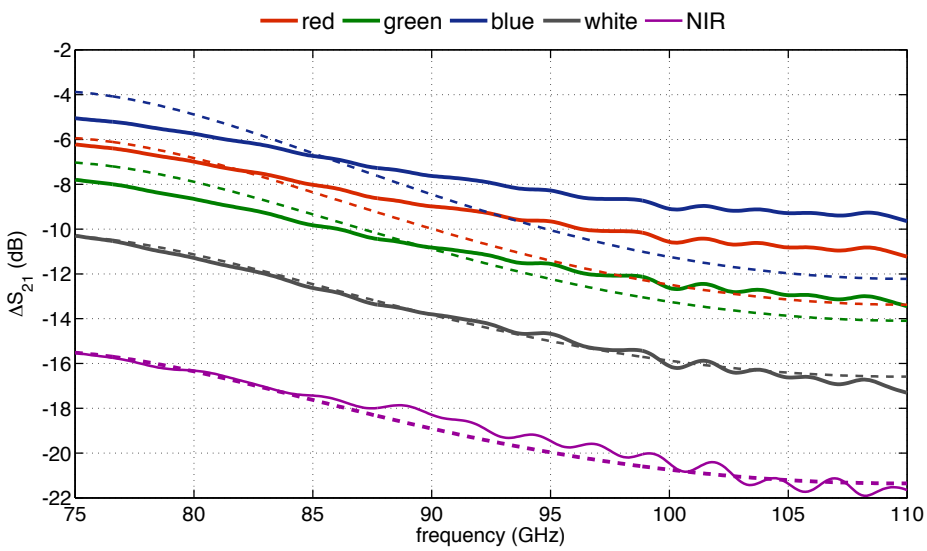

Figure 4.13: Measured (solid line) and modelled (dashed line) change in transmittance interferograms for wafer $w6$ at various illuminating wavelengths, and densities. The irradiances were measured to be approximately: $15\ \mathrm{mW/cm^2}$ red, $17\ \mathrm{mW/cm^2}$ blue, $31\ \mathrm{mW/cm^2}$ green, $65\ \mathrm{mW/cm^2}$ white, and $27\ \mathrm{mW/cm^2}$ NIR.

cluded for comparison. The attenuation is shown to be larger for $27\ \mathrm{mW/cm^2}$ NIR illumination density, than for the visible, which is expected due to the responsivity of the silicon substrate (see Figure 3.3(a)). The attenuation was measured as 19.2 dB (at 94 GHz) for the NIR source, which resulted in a loss tangent $\tan\delta_\epsilon\ \mathrm{x}10^4 = 7,645$ ($N_c = 2.2\ \mathrm{x}10^{15}\ \mathrm{cm}^{-3}$).

The dotted lines in Figure 4.13 indicate the analytical model for the visible and NIR transmittance data. The agreement between model and data is shown to be excellent for the NIR and white irradiation cases, and less accurate for the primary colour cases. The discrepancy is believed to result from the validity, and accuracy of the plasma homogeneity and monochromatic excitation assumptions in these cases.

To emphasis the wavelength dependency of the opto-excited plasma in the silicon samples, a simple scalar attenuation measurement was performed at 94 GHz using a QO transmission line and a power meter (Boonton 4220). The Sanyo data projector was used as the source, and the intensity was measured by altering the opacity of the image; the projection height remained fixed. Figure 4.14 displays the measured attenuation through wafer $w6$ as a function

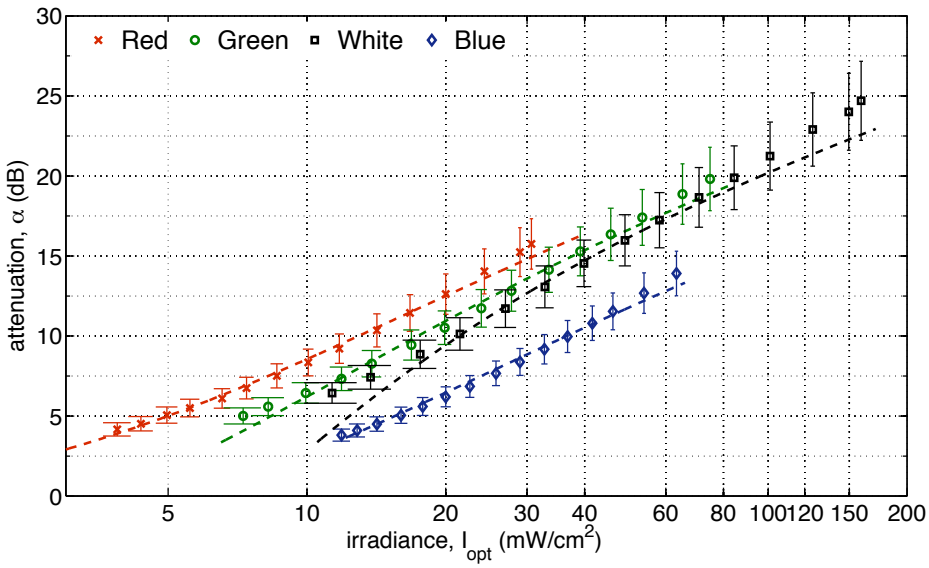

Figure 4.14: Measured (points) and simulated (dotted lines) attenuation through a passivated silicon wafer ($w6$) at 94 GHz, where the effective lifetime was measured as $\tau_{\text{eff}} \approx 1800\ \mu\text{s}$. The model and data show good agreement over the measured range, where slight deviations are attributed to the simplification of the analytical model.

of irradiance, over a range of illuminating wavelengths. The effective lifetime of the wafer, at the time of measurement, was approximately $\tau_{\text{eff}} = 1800\ \mu\text{s}$.

The dotted lines in Figure 4.14 represent the calculated silicon attenuation, at 94 GHz, modelled using the Lorentz-Drude complex permittivity (4.7), the expression for the effective plasma density (3.14), and the general attenuation expression (4.19). The comparison between the model and data shows good agreement, where slight deviations arose from experimental errors and the monochromatic simplification of the model. Figure 4.14 clearly indicates the wavelength dependence, as suggested by Figure 3.3(a), of the opto-excited plasma density: a larger plasma density is generated for a longer wavelength illumination, supporting the optimal illumination region (minimum irradiance) as being close to the bandgap.

4.4 Summary

This chapter has presented the quasi-optical transmission line characterisation of a range of high-resistivity silicon wafers, at a range of illuminating densities, and wavelengths. A generalised analytical model describing the transmission and reflection properties of an optically excited semiconductor substrate has been introduced, and shown to give excellent agreement with measured data. The model can then be used to infer the optically excited plasma density of a given substrate, which when combined with the generalised ABCD matrix method can indicate the resulting transmission properties, as a function of frequency.

Following from the discussions presented in Chapter 3, the significance of the effective lifetime parameter, and the SRV, have also been demonstrated, by comparing the transmission line properties of wafers before and after passivation; the significance of the SRV and τ_{eff} parameters have been demonstrated experimentally. In the un-passivated case, the presence of a high SRV ($S \geq 10^6$ cm/s), giving a significant reduction in the effective lifetime, τ_{eff} (Figure 3.2), resulted in a lowered optically excited plasma density, at a given irradiation level, thus reducing the overall change in the measured mm-wave attenuation. Further, the significant reduction in the short wavelength opto-excited plasma density due to a high SRV, resulted in very little measured attenuation for visible excitation.

The significant increase in optically excited plasma densities for a range of wafers that were passivated has been shown. The marked reduction in the SRV, yielding a higher effective lifetime, has shown generous changes in the transmission line properties through the treated wafers, with high attenuation changes of up to 25 dB (at 94 GHz) having been observed for NIR excitation. Wafers of sufficient thickness, such that $L_a > d$, and large reductions in the SRV have shown substantial effective plasma generation, producing high attenuations with visible excitations, agreeing with Figure 3.3(b).

Plasma generation by visible excitation has been shown experimentally to require from an increase in the required irradiance, compared to NIR excitation, due to the spectral response of the silicon sample (Chapter 3). The

maximum change in attenuation at 94 GHz observed for excitation at visible wavelengths was measured as 15 dB for white illumination, using the data projector, some weeks post passivation. This is a significant result which extends the possibility of generating dynamic spatial mm-wave modulators using excitation at visible wavelengths, based on well established display technologies.

chapter 5

The photo-injected Fresnel zone plate

The remainder of this thesis will focus on the design and application of the photo-injected Fresnel zone plate technique for adaptive, and non-mechanical beam steering, at mm-wave frequencies. This method proves to be simple, low-cost, and highly flexible (given correct consideration to the semiconductor substrate) compared to alternative (opto) electronic methods.

Design of photo-injected Fresnel zone plate antennas are not fully characterised by a closed set of design equations due to limitations imposed by the semiconductor substrate. The following discussion highlights the various design concepts, their impact on the plasma density requirements, and highlights the limits imposed by the semiconductor substrate. A variety of analytical techniques from previous chapters will be combined throughout this discussion, giving valuable insight into the optimisation and limitations of this particular non-mechanical method of beam steering, indicating its suitability at (sub) mm-wave frequencies.

5.1 Introduction

The photo-injected Fresnel zone plate antenna (piFZPA) method features full 3D scanning and adaptive beam forming, whilst maintaining reasonable costs and potentially low complexity, and is applicable at both mm-wave and submm-wave frequencies. This method also proves to be fast with high output beam fidelity, thus serving as an attractive solution for a wide range of applications. One significant drawback of this technique, however, is the interrelation of the required optical power and the corresponding scan rate of the antenna; whilst refresh rates, limited by the effective carrier lifetime of the substrate, can be as high as GHz (or more), the substantial increase in optical power required to achieve this performance often limits the refresh rate, in practice, to several tens of kHz. Thus, while passivation of the substrate can reduce the required level of irradiance (longer lifetimes), the increased lifetime results in slower scan speeds. Hence a compromise exists, the optimisation of which will be dictated by the application requirements. In addition, this method suffers from a fundamentally low aperture efficiency due to large phase errors associated with the limited half-wave correction zone plate design (Chapter 2). However, these limitations can be minimised, and are often out-weighed by the flexibility, speed, fidelity, and relatively low-cost of this technique, so that the piFZPA method continues to be a potentially attractive solution for a host of applications.

The original demonstrations of the piFZPA technique were first performed over 15 years ago by Webb *et al.* [74–77], which resulted in several patents [232–235]. However, very little theoretical work has been presented since these initial demonstrations, and thus a full, and definitive, understanding to the requirements, limitations, and suitability at mm-wave (and higher) frequencies is yet unknown. The following discussion builds on previous chapters to develop a theoretical framework for an optimised piFZPA design, and attempts to address the fundamental questions which have yet to be answered. While the discussion focuses on application at mm-wave frequencies, the basic principles are extended in Chapter 8 to highlight the requirements and suitability at submm-wave frequencies. Experimental characterisation of sev-

eral piFZPA designs based on a transmission-type piFZPA configuration are discussed in the next chapter.

5.2 Transmission-type

Design of piFZPAs are ascribed to either one of two main designations: transmission, or reflection, types. Transmission-type designs are inherently simpler in construction, and additionally do not induce degradations due to aperture blockage, and are thus suitable for smaller aperture sizes.

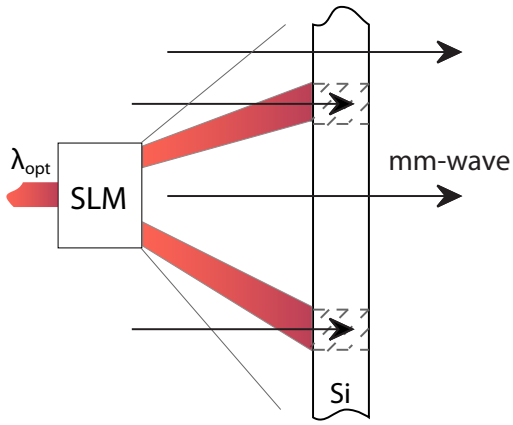

Figure 5.1: Depiction of the transmission-type piFZPA representing a reconfigurable blocking-type zone plate analogue.

The basic transmission-type piFZPA is depicted in Figure 5.1. In the basic form, the transmission-type piFZPA comprises an optical source, optical spatial light modulator (SLM), semiconductor substrate, relevant mm-wave hardware for transmit/receive, and a suitable means of illuminating the substrate by both optical and mm-wave beams; this can include an optically transparent mm-wave reflector (a dichroic filter), or other design such as the LED configuration used by Webb [235].

The optical source then excites a free-carrier plasma with distinct spatial features which are defined, in this particular application, by the zone plate mask (Section 5.4), encoded by means of the optical SLM. Using the optically transparent mm-wave reflector to physically align both optical and

mm-wave beams, a mm-wave beam is propagated through the semiconductor substrate using relevant quasi-optical components (such as a feedhorn, or lens). Reconfiguration of the zone mask via the SLM then enables (optical) reconfiguration of the mm-wave beam using the opto-excited plasma. This enables the realisation of a generalised mm-wave SLM capable of producing adaptive beamforming and non-mechanical beam steering.

5.2.1 Design

While these design equations have been encountered previously, they will be restated within the current context in order to provide clarity and continuity.

Design of transmission-type piFZPAs requires calculation of both the zone plate design (Chapter 2) and the substrate thickness (Chapter 4). The zone plate design produces the overall antenna performance, whilst appropriate substrate thicknesses are required in order to minimise loss through the substrate. Optimal substrate thicknesses, which minimise transmission loss, can be calculated from the transmission etalon expression introduced in Chapter 4, which is given by (4.27):

$$d = \frac{m\lambda}{2\sqrt{\epsilon_r'}} \qquad m = 1, 2, 3, ... \tag{5.1}$$

where for the piFZPA, ϵ_r' denotes the substrate dark permittivity, with $\epsilon_r' = 11.7$ for silicon. Similarly as before, λ is the free-space design (centre) wavelength of the mm-wave beam.

The zone plate radii, r_n, are calculated given the focal length (F) and aperture size (D) of the antenna (2.3):

$$r_n = \left[n\lambda F + \left(\frac{n\lambda}{2}\right)^2 \right]^{1/2}, \tag{5.2}$$

or

$$r_n = \left[n\lambda\sqrt{F^2 + r_0^2} + \left(\frac{n\lambda}{2}\right)^2 + r_0^2 \right]^{1/2}, \tag{5.3}$$

for a non-zero reference radius, r_0, given by (D.1) as discussed in Appendix D.

While the design of the piFZPA follows these simple design equations, substrate limitations define the piFZPA designs which can be realised in practice. For example, reasonable irradiation level requirements, requiring an increased effective lifetime, τ_{eff}, impose a corresponding plasma resolution limit (L_a) which then determines the zone plate design that can be supported by the substrate. As such, the zone plate design: choice of feed, edge taper, and F/D ratio, will depend on the relative substrate effective lifetime, and thus the optimised design will be dependent on the given application requirements and the optical budget.

Furthermore, the limitation of controlling propagating mm-wave beams by changes in attenuation (i.e. photoconductivity) restrict transmission-type piFZPA designs to low efficiency zone plate types (c.f. Soret zone plates), and thus the maximum efficiency for a transmission-type piFZPA is similarly 10%. Such low efficiency, resulting in 10 dB insertion loss, representing the optimal case, potentially limits this configuration to systems which benefit from high signal-to-noise ratios, such as radar or active imaging.

5.2.2 Composite Fresnel-Kirchhoff diffraction integral

While the far-field performance of the transmission-type zone plate antenna can be inferred from the basic Fresnel-Kirchhoff diffraction integral, as implemented by Webb [76], or by a modified approach based on the optically projected binary mask [236], no prior method appears to have been introduced which can also account for the opto-excited state of the substrate, in addition to the zone plate design, i.e. a complete piFZPA model. Thus, previously employed methods can not accurately address some of the fundamental questions which pertain to the zone plate and opto-excited substrate hybridisation.

The following section details a new composite Fresnel-Kirchhoff approach developed for this purpose. This approach is based on a modified form of the Fresnel-Kirchhoff method introduced in Chapter 2, which has been extended to include the semiconductor substrate parameters based on analytical models

which were previously introduced in Chapter 3 and Chapter 4. The core of the new approach follows the derivation of the modified Fresnel-Kirchhoff diffraction integral described in Appendix A, which will also be used for reference throughout.

The analysis which follows is based loosely on the geometry of Figure 2.5 where the piFZPA dielectric lens is of uniform thickness, similar to the Wood-Wiltse lens antenna. Thus some modifications to the formalism have been adopted based on previous Wood-Wiltse models. In the case of the piFZPA, the alternating permittivities of the zone plate are replaced by alternating zones of the dark state substrate ($\epsilon_r' = 11.7$, for silicon), and the opto-excited complex permittivity of the substrate.

Following Chapter 4, the opto-excited complex permittivity of the substrate is given by the Lorentz-Drude formula (4.7), which is re-stated for completeness:

$$\tilde{\epsilon_r} = \epsilon_\infty' \left[1 - \sum_i \left(\frac{\omega_i^2}{\omega^2 + \Gamma_i^2} \right) + \frac{j}{\omega} \sum_i \left(\frac{\omega_i^2 \Gamma_i}{\omega^2 + \Gamma_i^2} \right) \right], \tag{5.4}$$

where all terms have been defined previously in Chapter 4.

The electric field vector at the output aperture of the piFZPA can be represented by the general form of the Fresnel-Kirchhoff integral, (2.15):

$$\vec{\mathbf{E}}_d(\theta, \varphi) = C_f(r) \hat{\mathbf{e}}_r(\theta, \varphi) \times \iint_{A'} \left[\hat{\mathbf{n}} \times \vec{\mathbf{P}}_d(\psi, \xi) \right] \frac{e^{-jkL(\psi)}}{L(\psi)} e^{jk\hat{\mathbf{e}}_r(\theta,\varphi)\cdot\hat{\mathbf{r}}''} \mathrm{d}A'', \tag{5.5}$$

where $L(\psi)$, $\vec{\mathbf{P}}_d$, and $C(r)$ are given by (2.12), (2.14), and (2.16) respectively. Using Appendix A, the far-field components yield (2.18) – (2.23):

$$E_\theta(\theta, \varphi) = -\pi C_f \cos\varphi \sum_m \int_{\psi_m}^{\psi_{m+1}} O_d(\psi) e^{M_d(\psi)} I_\theta(\theta, \psi) \mathrm{d}\psi \tag{5.6}$$

$$E_\varphi(\theta, \varphi) = -\pi C_f \sin\varphi \cos\theta \sum_m \int_{\psi_m}^{\psi_{m+1}} O_d(\psi) e^{M_d(\psi)} I_\varphi(\theta, \psi) \mathrm{d}\psi, \tag{5.7}$$

with

$$M_d(\psi) = -jkL(\psi) \tag{5.8}$$

$$N_d(\theta,\psi) = k\sin\theta\left(F\tan\psi + \frac{\tilde{\epsilon}_r d\sin(\psi)}{\sqrt{\tilde{\epsilon}_r - \sin^2\psi}}\right) \tag{5.9}$$

$$O_d(\psi) = \sqrt{G_f(\psi,m)}\left(F\tan\psi + \frac{\tilde{\epsilon}_r d\sin(\psi)}{\sqrt{\tilde{\epsilon}_r - \sin^2\psi}}\right), \tag{5.10}$$

and

$$\begin{aligned} I_\theta(\theta,\psi) &= -(t'_M\cos\psi + t'_E)J_0[N_d(\theta,\psi)]\ldots \\ &\quad +(t'_M\cos\psi - t'_E)J_2[N_d(\theta,\psi)] \end{aligned} \tag{5.11}$$

$$\begin{aligned} I_\varphi(\theta,\psi) &= (t'_M\cos\psi + t'_E)J_0[N_d(\theta,\psi)]\ldots \\ &\quad +(t'_M\cos\psi - t'_E)J_2[N_d(\theta,\psi)], \end{aligned} \tag{5.12}$$

all terms having been defined in Chapter 2. Note that the zone thickness is now given by the substrate thickness, d. The planar structure of the piFZPA requires modification of the complex Fresnel transmission coefficient, $t_{M,E}$ (A.3), following the Wood-Wiltse Fresnel-Kirchhoff analysis [121]; thus

$$t'_{M,E} = \frac{t_{M,E}}{s_d}, \tag{5.13}$$

where s_d defines the phase delay factor, defined by (A.4).

The far-field (co- and/or cross-polar) antenna pattern of a transmission-type piFZPA may then be simulated for a given opto-excited semiconductor substrate. This method is subject to the aforementioned limitations presented by the physical optics approach, and further assumes a homogeneous plasma profile. For substrates in which this may not be the case, i.e. $L_a \ll d$, the accuracy of this method may be improved by setting the substrate thickness equal to that of the effective plasma density [53]. Homogenous plasma distribution is assumed herein, which is a reasonable approximation for the wafer

thicknesses and lifetimes analysed in this work. In addition, this method does not account for radial diffusion, and thus maximum accuracy of this model will occur for zone plate designs which result in zone widths much greater than the diffusion length.

This model may also be extended to simulate the far-field antenna pattern in terms of the irradiance, where the relationship between the effective plasma density and the optical excitation level is given by (3.14).

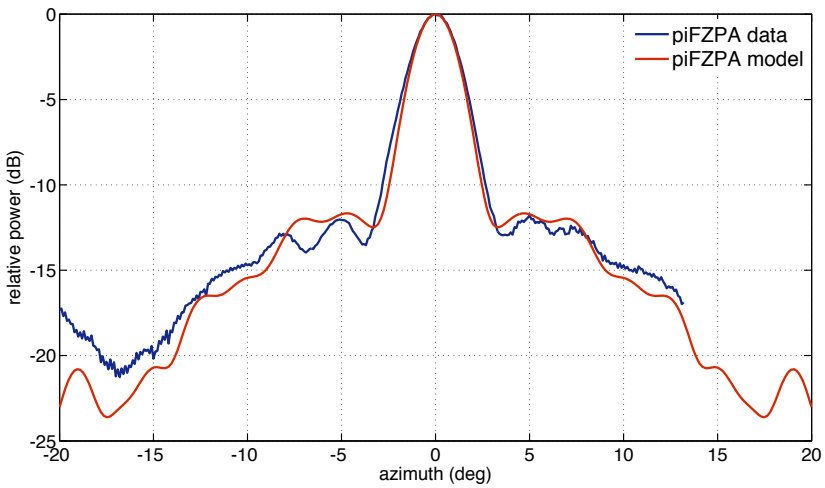

Figure 5.2: Comparison between measured and modelled antenna pattern of a F/1.2, 100 mm aperture piFZPA, at 94 GHz. The comparison demonstrate excellent agreement, highlighting the significance of this new approach, which thus serves as a invaluable tool in the design and optimisation process.

Figure 5.2 displays a comparison between the measured antenna pattern for a F/D = 1.2 (F/1.2), 100 mm diameter piFZPA (Chapter 6) and a simulated pattern obtained by the above model. The comparison shows excellent agreement. The effective plasma density was estimated as $\Delta n \approx 1.5\,\mathrm{x}10^{15}\ \mathrm{cm}^{-3}$ based on an measured minimum optical irradiance of $70\ \mathrm{mW/cm}^2$. The feed design, with an -13 dB edge taper, resulted in a 6-zone FZP design. The substrate thickness was taken as $d = 600\ \mu\mathrm{m}$. The slight discrepancy between the low-level region of the mainlobe (≈ -12 dB), can be attributed to lateral carrier diffusion effects resulting from the high lifetime wafer, which is not accounted for within the model. The discrepancy in the general level of the sidelobe envelope results from the approximations used in converting the

measured irradiance (assumed to be monochromatic) to the effective plasma density.

This technique thus serves as an invaluable tool for the design and characterisation of transmission-type piFZPAs, applicable to any frequency range. This new method also enables one to answer some fundamental questions relating to the gain, and general antenna performance, as a function of the opto-excited plasma density, which are addressed in the following sections. This method will also be used in subsequent comparisons to experimental data, which will be discussed in the next chapter.

5.2.3 Effective plasma density requirements

As noted previously, the irradiance required in order to generate a metallic effect can be unreasonably high for use in most systems, where irradiation densities can be as high as $2\ \mathrm{W/cm^2}$ depending on the substrate, its thickness, lifetime ($\tau_{\mathrm{eff}} = 100\ \mu\mathrm{s}$ assumed), and the illuminating wavelength (800 nm assumed). Thus, the relative tradeoff in antenna gain, and sidelobe level, is of importance for practical piFZPAs. Using the above modified Fresnel-Kirchhoff model, the relative tradeoff in performance can be investigated.

Figure 5.3 displays the simulated far-field antenna patterns for an F/2, 100 mm diameter transmission-type piFZPA with a substrate thickness of $d = 466\ \mu\mathrm{m}$, for a range of effective plasma densities. It is evident that as the effective plasma density increases to a level such that greater than 6 dB attenuation is optically induced, the antenna pattern begins to form a well distinguished mainlobe, with an increase in gain and sidelobe suppression. From these simulations, a photo-injected attenuation of 6 dB ($\Delta n = 8.3\ \mathrm{x}10^{14}\ \mathrm{cm}^{-3}$ in this case) can be considered to be the minimum required attenuation level for reasonable piFZPA performance, which corresponds to a ∼3 dB reduction in the overall gain. This opto-excited state represents a practical compromise between the required irradiation level, the sidelobe suppression, directivity, and overall antenna efficiency ($\eta > 5\%$). Nonetheless, an opto-injected attenuation of 10 dB is shown to offer better performance, for a modest increase in irradiation, with better than 7% efficiency. An attenuation level of 10 dB

has been previously stated as the minimum required attenuation, based on an unknown analysis [232]. The minimal opto-injected attenuation level will depend on the available optical power and the required antenna performance for the given application.

However, and most importantly, this analysis indicates that a much lower effected plasma density can be tolerated, whilst maintaining reasonable antenna performance. Thus a full optically induced metallic zone plate is not required, albeit with a reduced antenna performance.

5.2.4 Optimisation

The following discussion focuses on the optimisation of the transmission-type piFZPA, which in addition to the previous optimisation of the zone plate design as a result of the substrate diffusion length, requires consideration to the effective plasma density and the substrate thickness. Although both the substrate thickness and effective plasma density have been discussed above, it will be pertinent to give a more general discussion of the global impact of the transmission-type piFZPA as a continued variation of both of these

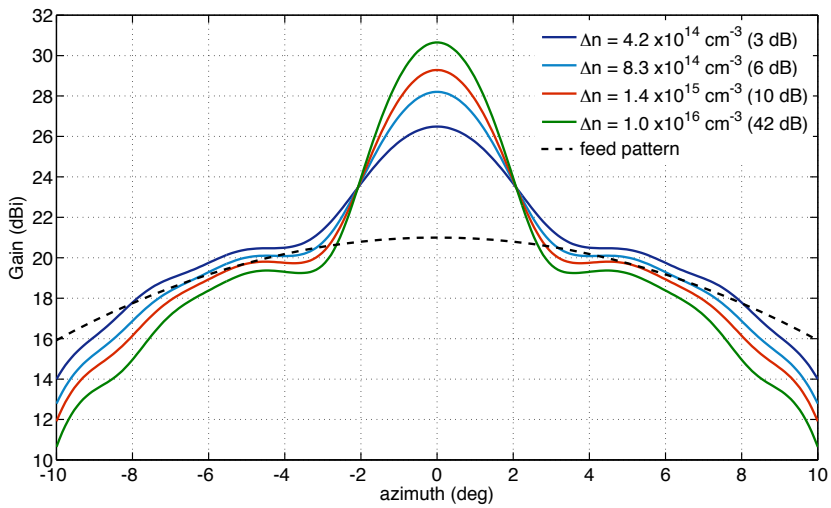

Figure 5.3: Simulated far-field patterns for a $d = 466\ \mu\mathrm{m}$ thick substrate, F/2 100 mm aperture piFZPA. Simulations suggest beam formation for optically injected losses exceeding ~ 6 dB ($\Delta n = 8.3\ \mathrm{x}10^{14}\ \mathrm{cm}^{-3}$), with increased sidelobe suppression for losses exceeding 10 dB.

parameters. The following insights have been obtained by implementing the composite Fresnel-Kirchhoff model. In addition, the following optimisation enables a conclusive overview of the performance degradations as a result of non-optimal choice of either one of these parameters.

Optimisation of the effective plasma density, Δn, is presented in Figure 5.4(a) while the optimisation of the substrate thickness is given in Figure 5.4(b). In both figures, the simulations of the transmission-type piFZPA far-field antenna pattern were performed at 94 GHz, with a F/2, 100 mm diameter piFZPA, and -13 dB amplitude taper. The substrate was assumed to be high-resistivity silicon, which gives a dark state effective plasma density of approximately 10^{11} cm^{-3}. The following focuses on the antenna gain as a function of both parameters, which has been extracted from each individual antenna pattern that was calculated, as a function of either parameter.

Considering the optimisation of the effective plasma density first; Figure 5.4(a) displays the gain as a function of the effective plasma density, Δn, for substrate thicknesses of $d = 300$ $\mu\mathrm{m}$, $d = 466$ $\mu\mathrm{m}$, $d = 600$ $\mu\mathrm{m}$, and $d = 932$ $\mu\mathrm{m}$. Here, $d = 466$, and 932 $\mu\mathrm{m}$ correspond to substrate thicknesses which are resonantly matched at 94 GHz, as defined by (5.1) with $m = 1, 2$ respectively. The relative change in antenna gain, for each substrate thickness, is observed to rise gradually as the effective plasma density increases – as would be expected due to the increased loss through the substrate. The antenna gain is also shown to saturate in all cases beyond a carrier density of $\Delta n = 10^{16}$ cm^{-3}, corresponding to alternate opto-excited metallic-like zones, i.e. a classical Soret type. Moreover, for resonantly matched substrate thicknesses ($d = 466, 932$ $\mu\mathrm{m}$), the saturation level is shown to peak at 31 dBi, corresponding to an approximate aperture efficiency of 11%; this agrees with what should be expected from this zone plate design (Chapter 2). The 1% overestimation is likely to result from the approximate method used to calculate the efficiency [133].

An increased gradient, and lowered effective plasma density transition period, is observed for $d = 932$ $\mu\mathrm{m}$ ($\lambda/\sqrt{\epsilon_r'}$), in comparison to $d = 466$ $\mu\mathrm{m}$ ($\lambda/2\sqrt{\epsilon_r'}$). Both effects result from the increased attenuation, at a given injection level, due to the increased substrate thickness, and the (longitudinal)

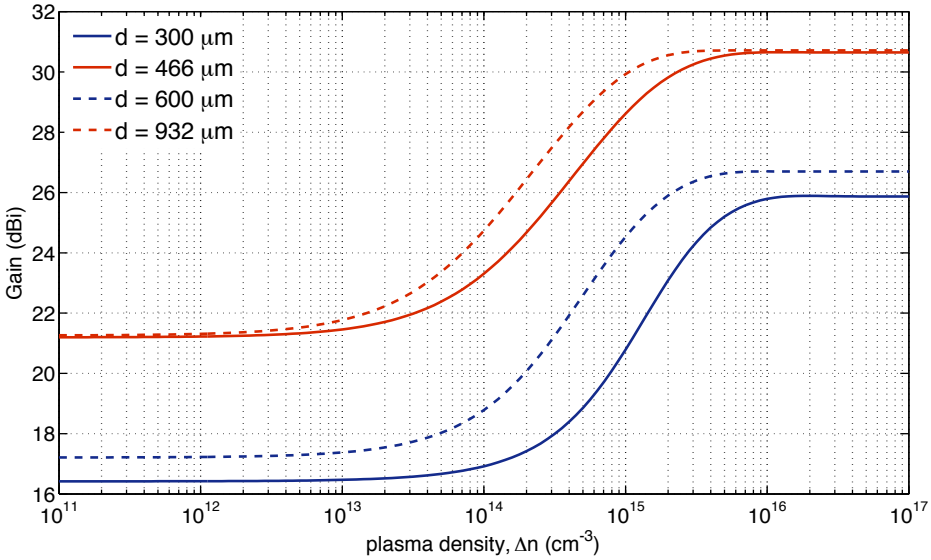

(a)

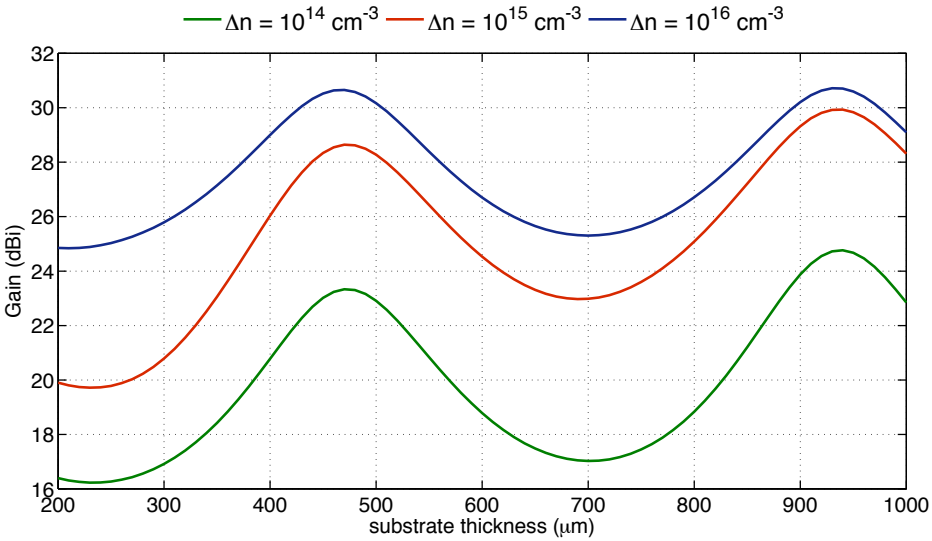

(b)

Figure 5.4: Simulated gain variation for a F/2, 100 mm diameter transmission-type piFZPA as (a) a function of the effective plasma density (Δn), and (b) a function of substrate thickness (d).

homogeneous plasma distribution which has been assumed in both cases. As the substrate thickness increases, the assumption of a homogeneous plasma distribution begins to break down, expect in the cases of large effective lifetimes. For example a diffusion length of 1 mm (L_a) requires an effective lifetime $\tau_{\text{eff}} \geq 350\ \mu\text{s}$, depending on the substrate.

Non-resonantly matched substrates are shown to yield reduced piFZPA gain due to increased loss through the un-injected regions of the semiconductor etalon. This gives rise to the lowered gain observed for the $d = 300,\ 600\ \mu\text{m}$ cases, and gives rise to the apparent reduced feed gain (< 21 dBi).

Considering the substrate thickness further, Figure 5.4(b) displays the corresponding gain as a function of substrate thickness, d, with effective plasma densities $\Delta n = 10^{14}\ \text{cm}^{-3}$, $\Delta n = 10^{15}\ \text{cm}^{-3}$, and $\Delta n = 10^{16}\ \text{cm}^{-3}$. The piFZPA gain is shown to oscillate as a function of substrate thickness, where maximum gain is observed at substrate thicknesses satisfying (5.1). The oscillations, and peak gain, correspond to the matching of the semiconductor etalon (Chapter 4). Furthermore, the peak gain in the oscillations are shown to be invariant for the $\Delta n = 10^{16}\ \text{cm}^{-3}$ case, whilst higher gain is observed at higher order ($m > 1$) matched substrate thicknesses for effective plasma densities $\Delta n < 10^{16}\ \text{cm}^{-3}$. The gain invariance of the $\Delta n = 10^{16}\ \text{cm}^{-3}$ case results from the saturation of the transmission-type piFZPA efficiency, while the higher gain for substrates of increased thickness ($m > 1$) result from the increased attenuation at the given effective plasma density; again a homogeneous plasma distribution has been assumed.

Thus it is clear that both substrate thickness and the effective photo-injected plasma density significantly affect the overall gain of the transmission-type piFZPA.

5.3 Reflection-type

The reflection-type piFZPA is the second of the two main piFZPA configurations. The reflection-type piFZPA, while more difficult to realise in practice due to low substrate thickness and alignment tolerances, features two modes

of operation: the improved blocking-type piFZPA, and the phase-reversal piFZPA. The former features the same 10% efficiency of the transmission-type piFZPA, but with a lower plasma density requirement, while the latter, which was first identified in US patents [234, 235, 237] (two of which are assigned to Webb), yields increased antenna efficiencies of up to 40%, with a corresponding increase in the required plasma density. As a result, the reflection-type piFZPA may be more attractive to most applications. Both configurations of the reflection-type piFZPA are depicted in Figure 5.5.

The reflection-type piFZPA typically leads to an on-axis feed, and thus suffers from aperture blockage effects. However, such effects are only significant in situations where the dimensions of the feed are greater than approximately 10% of the piFZPA aperture [135], and thus the reflection-type is suited to larger aperture sizes than the transmission-type.

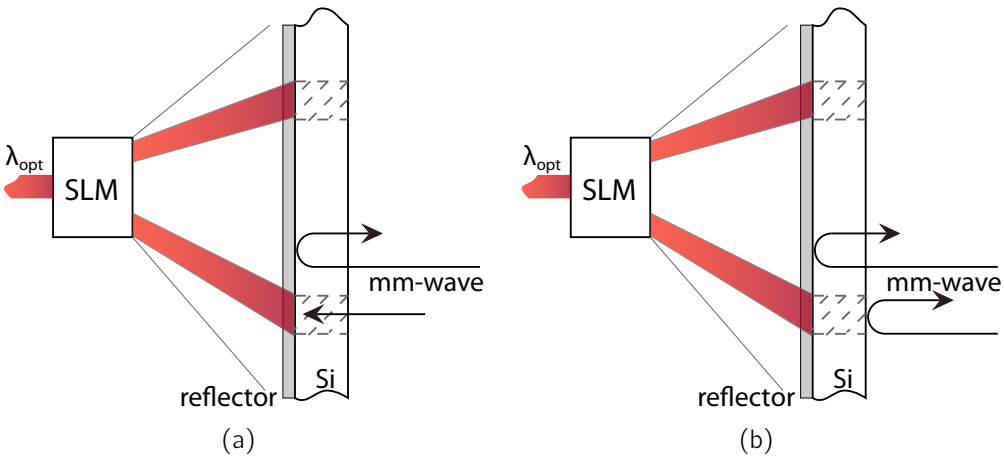

Figure 5.5: Depiction of the reflection-type piFZPA illustrating the (a) improved blocking-type, and (b) the phase-reversal subgroups.

The components and operation of the reflection-type piFZPA configuration follow the transmission-type piFZPA, where a suitable optically transparent mm-wave reflector becomes a requirement due to the prime-fed configuration. Typical optically transparent mm-wave reflectors include either a fine wired polariser mesh or grid, or a conductive polymer film such as indium tin oxide or silvered polymer films. In general, conductive polymer films are preferred due to their high optical transmission and high mm-wave reflectivity.

5.3.1 Design

Design of reflection-type piFZPAs require calculation of both the zone plate design and substrate thickness, with the zone plate design defining the overall antenna performance, and the substrate thickness ensuring minimised loss through the etalon. Optimal substrate thicknesses are, again, given by the matched etalon condition, which for maximum reflection requires (4.27) to be satisfied:

$$d = \frac{m\lambda}{4\sqrt{\epsilon_r'}} \qquad m = 1, 3, 5, ... \tag{5.14}$$

where each term has been defined in Section 5.2.1. The zone plate design follows from either (5.2) or (5.3), again subject to the limits imposed by the substrate diffusion length, as discussed in the transmission-type configuration.

In addition, reduced substrate thicknesses, resulting from the reflection mode etalon, present an increased sensitivity to surface defects; thus passivation (or a large substrate thickness) is generally required in order to reduce the surface mediated loss of optically excited carriers.

5.3.2 Modelling by the ABCD matrix method

The requirements of the reflection-type piFZPA are most readily obtained by modelling the piFZPA etalon using the ABCD matrix method, discussed in Chapter 4. These initial requirements, in a bid to support the reconfiguration-type piFZPA, were eluded by patents assigned to Webb [234, 235]. However, no detail was given to how the results were obtained; the following is believed to be a similar formalism used in the original patents, where initial conclusions of [234, 235] have also been found during this work. The following discussion extends the initial insights presented by Webb, and details the optimisation of the reflection-type piFZPA.

The modelled transmission line includes the semiconductor substrate and the back reflector, which has been assumed to be perfectly reflecting at the design (mm-wave) frequency. The reflection properties of the transmission line can then be analysed using the lossy ABCD matrix, which is restated for

clarity and context,

$$\begin{bmatrix} A & B \\ C & D \end{bmatrix} = \begin{bmatrix} \cosh\tilde{\gamma}d & \tilde{Z}_L \sinh\tilde{\gamma}d \\ \frac{1}{\tilde{Z}_L}\sinh\tilde{\gamma}d & \cosh\tilde{\gamma}d \end{bmatrix}, \tag{5.15}$$

with substrate thickness, d, complex wave impedance[1] $\tilde{Z}_L = \sqrt{1/\tilde{\epsilon}_r}$, and the complex propagation parameter, $\tilde{\gamma} = \alpha + j\beta$; components α, β were defined previously by (4.19) and (4.20) respectively. The complex substrate permittivity is again given by the Lorentz-Drude model. From [229], the complex (amplitude) transmission and reflectivity are given by[2]

$$t = \frac{2}{A + B + C + D} \tag{5.16}$$

and

$$r = \frac{A + B - C - D}{A + B + C + D}, \tag{5.17}$$

respectively.

Perfect mm-wave reflectivity from the optically transparent reflector is modelled by co-location of the input and output transmission line ports, thus the amplitude reflectivity is given by $r' = r - t$, where the virtual forward transmission port, t, has been *folded* back on the input port, depicted in Figure 5.6. The phase change through the transmission line is then given by $\phi = \arg(r')$. This model assumes plane wave propagation through the transmission line as before, zero SRV, a longitudinal homogeneous plasma distribution, and no radial diffusion.

[1] non-magnetic material, $\tilde{\mu}_r = 1$

[2] not to be confused with the Fresnel coefficients t, r

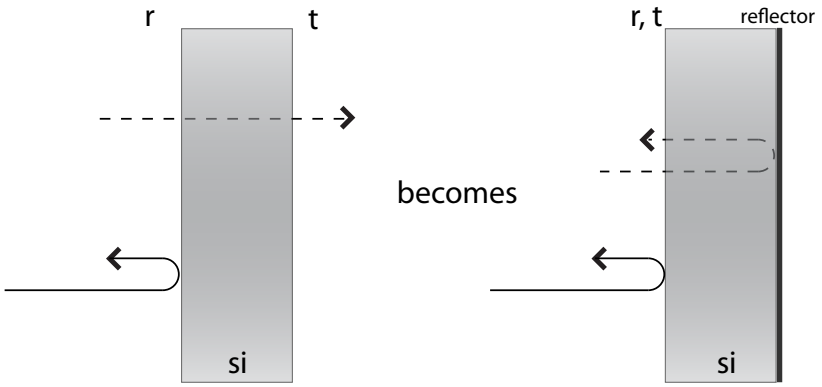

Figure 5.6: Modelling the reflection-type piFZPA: the perfect reflector folds the transmission port, t, back to the reflection port, r.

5.3.3 Effective plasma density requirements: improved blocking, and phase-reversal, piFZPAs

Using the above transmission line model, the requirements and corresponding advantages of both reflection-type configurations (Figure 5.5(a), (b)) can be found.

Figure 5.7 displays the simulated fractional field reflectivity, r', and the corresponding phase change, ϕ, through the reflection-type piFZPA transmission line as a function of the photo-injected plasma density, Δn, for a substrate thickness $d = 233\ \mu\mathrm{m}$ [m = 1, (5.14)] at 94 GHz. Simulations show that the reflectivity is maximal for a high-resistivity sample, which is expected as the chosen substrate thickness represents a matched etalon for maximum reflection, and the high-resistivity (doping density $< 10^{12}\ \mathrm{cm}^{-3}$) substrate has been shown to behave as a low-loss dielectric in the pseudo low-frequency limit (Chapter 4). Using this point as reference (amplitude and phase), the amplitude reflectivity is shown to approach zero as the plasma density increases, reaching a minimum at $\Delta n = 6.9\ \mathrm{x}10^{14}\ \mathrm{cm}^{-3}$, due to the increased loss presented by the opto-excited substrate. At this carrier density, the matched etalon thickness gives near-perfect ($r' \sim 0.01$) cancellation of the reflected beam with a near $180°$ phase change through the transmission line. Fractional adjustment of the substrate thickness may yield further cancellation of the

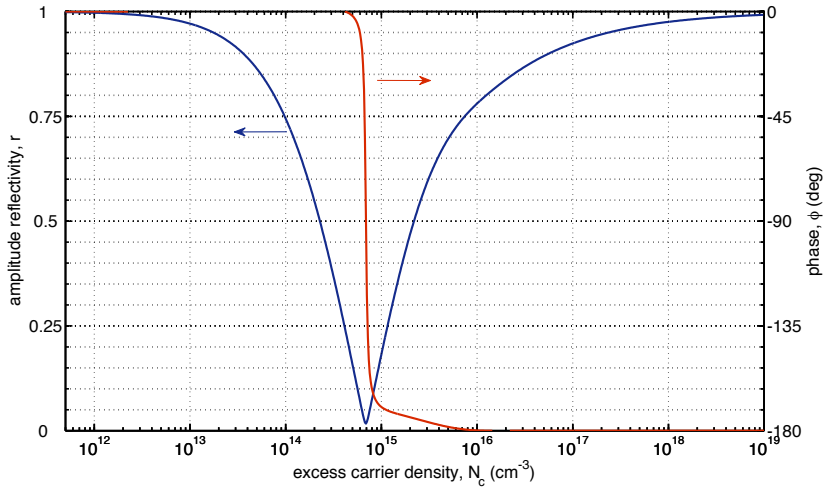

Figure 5.7: Simulated reflectivity and phase from a reflection-type piFZPA transmission line. The reflection-type etalon yields increased sensitivity to changes in the complex permittivity leading to minimised reflection at lower carrier densities. A $180°$ phase change is shown, with near unity reflected amplitude due to an opto-excited metallic state.

reflected beam, with increased phase change [234, 235]. Increased effective carrier densities beyond the reflection minimum ($\Delta n > 6.9\ \mathrm{x}10^{14}\ \mathrm{cm}^{-3}$) result in a continued increase in the amplitude reflectivity, whilst maintaining a constant $180°$ phase change. The transition towards perfect amplitude reflectivity, with a $180°$ phase change, results from the transition to the standard low-frequency limit ($\omega_p \geq \Gamma$) where the opto-excited zones begin to produce metallic-like behaviour.

Thus using Figure 5.7 as an example reflection-type piFZPA design, a blocking reflection-type piFZPA can then be realised for opto-excited zones with an effective plasma density of $\Delta n = 6.9\ \mathrm{x}10^{14}\ \mathrm{cm}^{-3}$, with the un-illuminated zones corresponding to $\Delta n \geq 10^{11}\ \mathrm{cm}^{-3}$ (depending on resistivity). The reflection minimum, which gives 1% reflection in the matched etalon case shown in the figure, corresponds to a 40 dB contrast between the illuminated and un-illuminated zones. This is equivalent to the 10% maximum efficiency case of the half-wave blocking correction scheme, c.f. transmission-type piFZPA. Most importantly, the required effective plasma density is more than an order of magnitude lower for the reflection-type piFZPA than the

transmission-type piFZPA ($\Delta n = 6.9$ x10^{14} cm^{-3} vs. $\Delta n \geq 10^{16}$ cm^{-3}), due to the increased finesse of the reflection mode etalon; coined 'the improved blocking Fresnel zone plate antenna' [235]. Degradation of the antenna efficiency from its maximum value, for effective plasma densities located at either side of the minimum point, follows the effective plasma density degradation shown in the transmission-type configuration discussed above.

The second subgroup configuration of the reflection-type piFZPA is also evident from Figure 5.7. The phase-reversal piFZPA, depicted in Figure 5.5(b), yields a maximum efficiency of 40% due to a half-wave correction zone plate scheme and full use of the incident energy from the feed, c.f. P = 2 phase-correcting WZP/folded SZP. From Figure 5.7 perfect amplitude reflectivity and $180°$ phase change is shown to require an effective plasma density of $\Delta n \approx 10^{19}$ cm^{-3}. However, this very large plasma density may be relaxed to plasma densities exceeding 10^{16} cm^{-3}, which yields greater than 80% amplitude reflectivity. A reflection-type, phase-reversal piFZPA with illuminated zones greater than this density would suffer a modest degradation from the maximum efficiency, with the power reflectivity dropping by less than 2 dB. Thus a higher efficiency reflection-type piFZPA can be realised for a similar effective plasma density as that required in the transmission-type piFZPA!

Furthermore, improved efficiency at lower effective plasma densities may be possible for a matched reflector reflectivity, such that the front and rear reflectivity of the reflection mode etalon are matched, i.e. $r' \neq 1.0$. The current model is however unable to simulate this effect.

5.3.4 Optimisation

Current discussions on the reflection-type piFZPA are concluded with details of optimisation, which is subject to the constraints imposed by the substrate diffusion length, and thus the practical F/D ratio of the zone plate design, as discussed for the transmission-type piFZPA. The discussion, in particular, details the reduced tolerance on the substrate thickness due to the increased finesse of the reflection-mode etalon. In addition, the improved blocking-type piFZPA will also be discussed, whereby the effective plasma density require-

ment changes depending on the substrate thickness, i.e. $m = 1, 3, 5$, etc.

Figure 5.8(a) indicates both the change in amplitude reflectivity and phase change for slight deviations in the matched substrate thickness, given by (5.14). The tolerance on substrate thickness deviations has been modelled for a first order (m = 1) substrate thickness at 94 GHz, i.e. $d = 233\ \mu\mathrm{m}$.

From Figure 5.8(a), small deviations in substrate thickness are shown to increase the reflection minimum and phase. For example, an attenuation contrast between the reflection minimum and the dark state ($\Delta n \approx 10^{11}\ \mathrm{cm}^{-3}$) changes from 40 dB on resonance, to 17 dB for a 5% ($12\ \mu\mathrm{m}$) deviation from the matched substrate thickness, reducing to 12 dB for a 10% ($24\ \mu\mathrm{m}$) deviation in substrate thickness. Thus, small changes in the substrate thickness, from the matched case, result in reduced aperture efficiency similar to the transmission-type, where for example the 5% case would yield an aperture efficiency $7\% \geq \eta \geq 10\%$, c.f. Figure 5.4(a). A similar effect (for a resonantly matched thickness) would also be observed if the opto-excited plasma density were to correspond to either side of the reflection minimum. Additionally, a similar degradation will be expected for the phase-reversal case due to the lowered phase change as a result of the deviation, i.e. $\eta < 40\%$.

Assuming homogeneous plasma distribution, higher order substrate thicknesses ($m = 3, 5, \ldots$) result in a shift of the reflection minimum to lower effective plasma densities due to the increased loss through the substrate. The shift is observed for both the improved blocking and phase reversal pi-FZPA, as illustrated in Figure 5.8(b) which displays the amplitude and phase for the $m = 1$, and $m = 3$ cases at 94 GHz. However, in practice this will only be the case for high lifetime wafers.

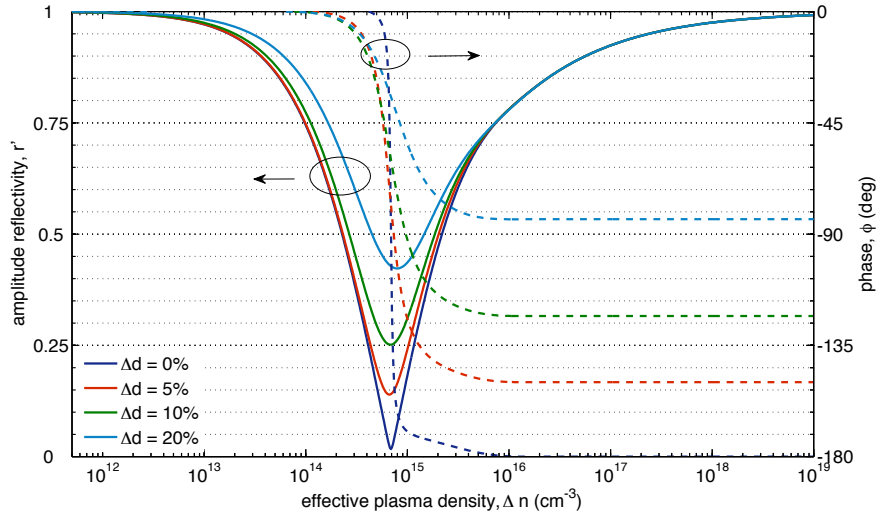

(a)

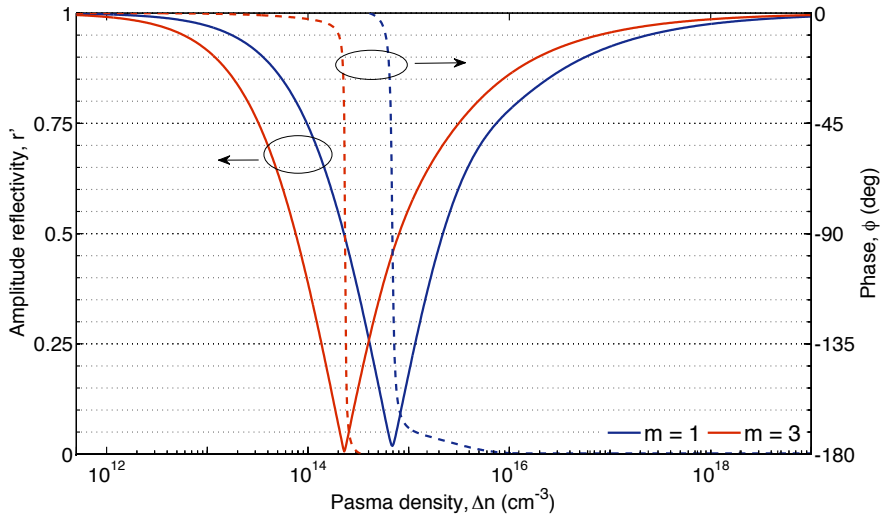

(b)

Figure 5.8: Simulated transmission line properties for the reflection-type piFZPA, highlighting the required selection of the substrate thickness; (a) illustrates the loss in *contrast* for small deviations in substrate thickness, d, and (b) illustrates the change in required plasma density, Δn, for a change in the resonant matched substrate thickness.

5.4 Algorithm for generating the zone plate masks

The following discussion details the algorithm used for generating the Fresnel zone plate masks, which are then projected onto the surface of the semiconductor substrate.

The goal of utilising well established display technologies simplifies the optical encoding to the generation of a binary image. The binary image can then be simply projected onto the substrate surface using standard image projection methods. Dynamic reconfiguration of the opto-excited substrate then requires generation of binary masks in a predefined sequence which can then be projected onto the substrate surface using standard video projection methods.

The algorithm used for calculating the binary images, which represent the zone plate design, requires several coordinate transformations including translation of the polar coordinate design of the zone plate (*real* space) to a cartesian image coordinate frame (*image* space). The following method extends the basic principle outlined by Hajian *et al.* [236], where additional raster scanning and phase reference (Appendix D) features have been added.

At the core of this method is the intermediate transformation to a *zone* sub-space, n. The zone sub-space transformation follows from the general inequality which gives rise to the Fresnel half-wave boundary condition, namely:

$$\frac{n\lambda}{2} + F \leq r \leq \frac{(n+1)\lambda}{2} + F; \tag{5.18}$$

F, λ, r define the focal length, free-space wavelength, nth path length to zone number n, and with the zone number n. The zone sub-space is then obtained by re-arranging for n, giving

$$n = \frac{2}{\lambda}\left[\sqrt{\rho_n^2 + F^2} - F\right]. \tag{5.19}$$

Equation (5.19) gives the zone number as a function of substrate coordinate, ρ, where the zone number is invariant with respect to the substrate polar angle coordinate, i.e. the zones are circularly symmetric. Circular symmetric zones are known to be a special case of the Fresnel zone plate design, which

arises for normal incidence. In the general case, where the beam direction is oblique to the zone plate aperture, the design results in an asymmetric zone pattern. However, as the feed and zone plate aperture remain orthogonal, the asymmetric design is different to that of the classical off-axis zone plate, which is discussed in [108, 238–240].

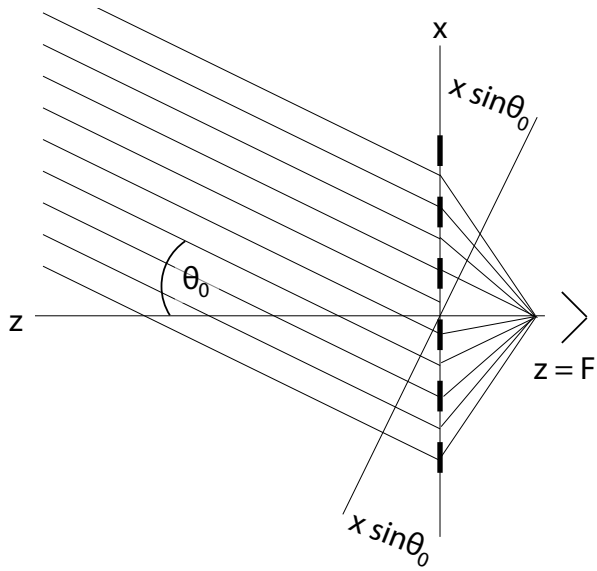

Figure 5.9: Cross section of the zone plate configuration depicting the beam direction in the azimuth plane for oblique incidence, which results in a pathlength change of $x \sin\theta_0$ in the azimuth case.

With the feed and aperture fixed, an off-axis beam then results in a pathlength change, depicted in Figure 5.9 for the azimuth direction, which varies depending on the location on the aperture. From geometry [236], the pathlength variation across the aperture is given by $\Delta x = x \sin\theta_0$, in the x-direction (azimuth), and $\Delta y = y \sin\varphi_0$ in the y-direction (elevation). Converting to polar coordinates, (5.19) can then be written as

$$n = \frac{2}{\lambda}\left[\sqrt{\rho_n^2 + F^2} - \rho\cos\phi\sin\theta_0 + \rho\sin\phi\sin\varphi_0 - F\right], \tag{5.20}$$

where θ_0 and φ_0 are the off-axis angles in azimuth and elevation, respectively, and ϕ denotes the polar angle in the aperture *image* space. Here the oblique

incidence in both azimuth and elevation have been explicitly separated to allow for the generation of raster sequences (c.f. form presented in [236]), which is utilised in the next chapter for beam pattern measurements.

Finally, incorporating the reference phase/radius discussed in Appendix D, the general zone sub-space transformation can be shown to be written as

$$\begin{aligned} n &= \frac{2}{\lambda}\Bigg[\sqrt{\rho_n^2 + F^2} - \sqrt{F^2 + r_0^2}\ldots \\ &\qquad -\rho\cos\phi\sin\theta_0 + \rho\sin\phi\sin\varphi_0\Bigg], \end{aligned} \tag{5.21}$$

where the reference radius, r_0, is given by (D.1) for a given reference phase, ϕ_{ref}.

Figure 5.10 demonstrates example zone sub-space diagrams for a F/1.5, 100 mm diameter, zero reference phase[3], zone plate for normal incidence $(\theta_0, \varphi_0) = (0°, 0°)$ – Figure 5.10(a), and oblique incidence $(\theta_0, \varphi_0) = (20°, 0°)$ – Figure 5.10(b). The dotted line in both figures indicates the 100 mm aperture size of the piFZPA. The asymmetry of the zone mask design becomes clearly evident as beam direction becomes oblique to the zone plate aperture.

The final transformation involves truncating the image mask to the zone plate aperture size, and compressing the zone sub-space diagram to the final binary image. The sub-space compression can be achieved by implementing a simple *is even* binary modulator in which the zone sub-space is translated into logical values depending on the parity of the nearest integer. By assigning a binary value to either integer parity, and truncating the sub-space outside the zone plate aperture, the final binary image can be computed; this was implemented using Matlab. The corresponding binary images for the zone sub-space examples of Figure 5.10(a), 5.10(b) are shown in Figure 5.10(c) (normal incidence), and Figure 5.10(d) (oblique incidence). Thus each binary image represents a separate pointing direction for the (sub) mm-wave beam.

[3]example non-zero reference phase masks are shown in Appendix D.

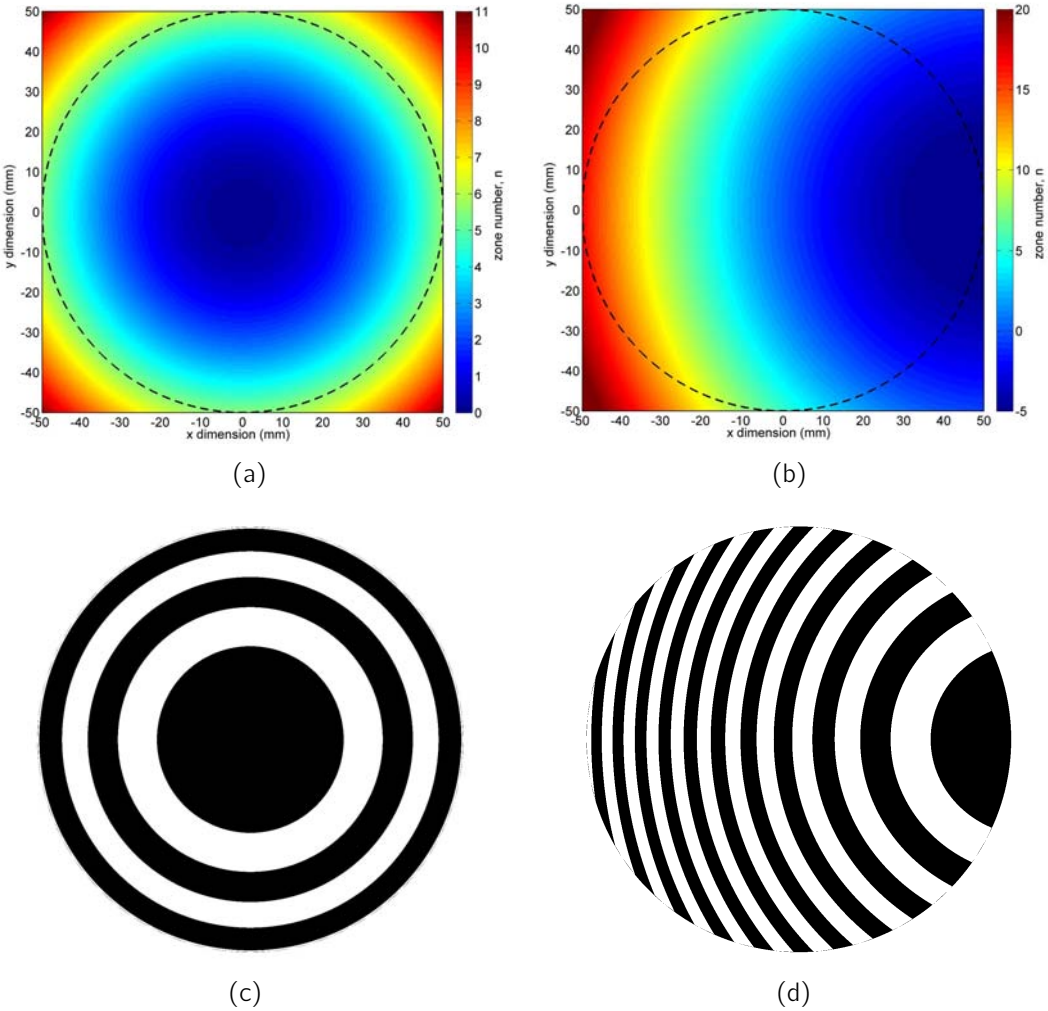

Figure 5.10: Example zone sub-space diagrams for a F/1.5, 100 mm diameter piFZPA design at 94 GHz, with zero reference phase, for (a) normal incidence, $(\theta_0, \varphi_0) = (0°, 0°)$, and (b) oblique incidence, $(\theta_0, \varphi_0) = (20°, 0°)$. The corresponding binary zone masks are shown for (c) normal, and (d) oblique incidence.

5.5 Summary

The concept and design of the piFZPA has been introduced, which can be separated into either a transmission- or reflection-type configuration. The inherent differences, and benefits, of each design have been detailed where the reflection-type designs feature reduced effective plasma density requirements yielding an improved blocking-type piFZPA, whilst also permitting higher efficiency phase-reversal embodiments, albeit with a required increased effective plasma density (irradiation level). The overall antenna efficiency is shown to be limited to 10% for the blocking-type piFZPA and 40% for the reflection-type phase-reversal configuration.

A composite analytical model has been introduced which details the performance of the transmission-type piFZPA as a function of zone plate design, substrate thickness **and** the effective plasma density. This model has been shown to yield excellent agreement with experimental data, and is also discussed further in the next chapter. In addition, the overall antenna gain is shown to gradually increase as a function of the effective plasma density, saturating at a plasma density exceeding $10^{16}\ \mathrm{cm}^{-3}$, which corresponds to a reconfigurable analogue to the Soret zone plate with 10% maximum aperture efficiency. Using this new composite model, a photo-injected loss of 6 dB has been suggested as a minimum requirement for a transmission-type piFZPA, which represents a compromise between antenna gain, directivity, sidelobe suppression, and the required irradiation level, although a level of 10 dB or greater is preferred.

Using the ABCD matrix method and the Lorentz-Drude model, the substrate thickness and effective plasma density dependence of the reflection-type piFZPA has been discussed. The required effective plasma density is shown to be approximately an order of magnitude lower than in the transmission case due to the increased finesse of the reflection mode etalon. The increased finesse of the reflection-type piFZPA also imposes stricter requirements on the substrate thickness than for a transmission-type configuration, requiring also either a thicker substrate or a high quality passivation layer in order to circumvent surface mediated free-carrier losses. The required density

for the improved blocking reflection-type piFZPA is shown to reduce with an increased substrate thickness, assuming a homogeneous plasma distribution.

An algorithm has been described which can be used to generate the necessary zone plate masks. The algorithm has been improved whereby the ability to generate sequential raster scans, and the inclusion of the reference phase parameter, have been added.

Finally, an attempt has been made to answer fundamental questions regarding the requirements, limitations, optimisation, and efficiency of piFZPAs based on an optically excited semiconductor substrate, which provides a theoretical framework for realising optimised piFZPAs in a given application.

chapter 6

Experiments on a transmission-type piFZPA

The realisation and characterisation of a range of photo-injected Fresnel zone plate antennas (piFZPAs) is presented, demonstrating high fidelity beam control over a 2-dimensional area.

The following results have been obtained using a visible data projector as a broadband light source and spatial light modulator, which are believed to be the first demonstrations of dynamic optoelectronic mm-wave beam manipulation of their kind.

6.1 Introduction

The following sections detail characterisations which were performed on several transmission-type piFZPA designs. Although the high-resistivity wafers were more suited for an optimised reflection-type piFZPA, at 94 GHz, due to their thickness, transmission-type piFZPAs have been investigated due to their simplicity. As a result, the non-resonantly matched substrate thicknesses lead to reduced performance, as discussed in the previous chapter.

6.2 Setup and measurement scheme

The far-field measurements of several transmission-type piFZPAs (piFZPAs from hereon) were performed using the standard far-field technique discussed in Chapter 2. The piFZPA arrangement, conceptualised in Figure 5.1, was based on a folded feed arrangement operating at 94 GHz. The folded feed arrangement was chosen to reduce blockage effects of both the mm-wave beam and the projected zone plate mask. The folded arrangement was implemented by use of an optically transparent mm-wave reflector comprised of a thin ITO coated polyester film (CPFilms OC200), which had a $200\ \Omega/\mathrm{sq}$ sheet resistance and a $175\ \mu\mathrm{m}$ thickness. Initial reflectors included either a vertical polariser grid or a silvered polymer film (CPFilms HgHT-4: $4\ \Omega/\mathrm{sq}$, $450\ \mu\mathrm{m}$). However the ITO film provided the best compromise between reflectivity at 94 GHz, approximately 85%, and optical transparency, $> 80\ \%$. Both the polariser grid and silvered film yielded better mm-wave reflectivity but significantly reduced the optical transmission in comparison to the ITO. The ITO film was chosen in order to maximise the irradiance on the silicon wafers, with power from the projector being limited ($< 20\ \mathrm{W}$).

The Sanyo data projector used in previous experiments was used a broadband visible light source and optical spatial light modulator. The W-band feedhorn was either a 20 dBi corrugated horn, or a custom smooth wall conical horn. Because of their different aperture sizes, these feeds offered different output tapers, enabling a range of piFZPAs with optimal amplitude taper and zone plate design to be investigated.

The transmitter and receiver hardware from the far-field measurements discussed in Chapter 2 were used. Measurements were performed using the HP spectrum analyser as before, and a detector diode (Eclipse microwave EZM0118PA3) and digital volt meter (HP34401A DVM), which offered increased sensitivity and response speeds. In particular, the improved GPIB poling speed of the DVM, enabled faster refresh rates in software, which increased from less than one point/sec to a maximum of 20 points/sec.

Two modes of characterisation were used: measurement of the far-field pattern by the rotation of the piFZPA assembly, with the transmitter fixed,

or by scanning the piFZPA with both piFZPA and transmitter fixed. Both methods were tested and verified to yield the same response. For practical reasons, the latter method will be used for the remainder of measurements discussed in this chapter.

The semiconductor substrate was wafer $w6$ due to its high effective lifetime ($\tau_{\text{eff}} \approx 1500\ \mu\text{s}$) and good lifetime spatial homogeneity (see Figure 3.15(b)). The semiconductor substrate was held upright with the aid of a bespoke HDPE frame.

The piFZPA assembly was then configured as follows: the ITO film, housed in a custom frame, was angled $45°$ to the silicon substrate, with the chosen W-band feed was angled $90°$ to the substrate, feeding the substrate via the tilted ITO film. The W-band feedhorn was attached to either the transmitter or receiver hardware depending on the measurement configuration; the zone plate masks were then optically projected onto the silicon surface by projection through the ITO film, using the Sanyo data projector. The setup, configured in receive mode, and with the smoothed wall conical horn, is shown in Figure 6.1.

Control software was developed using the C programming language and featured a graphical interface that was developed using the National Instru-

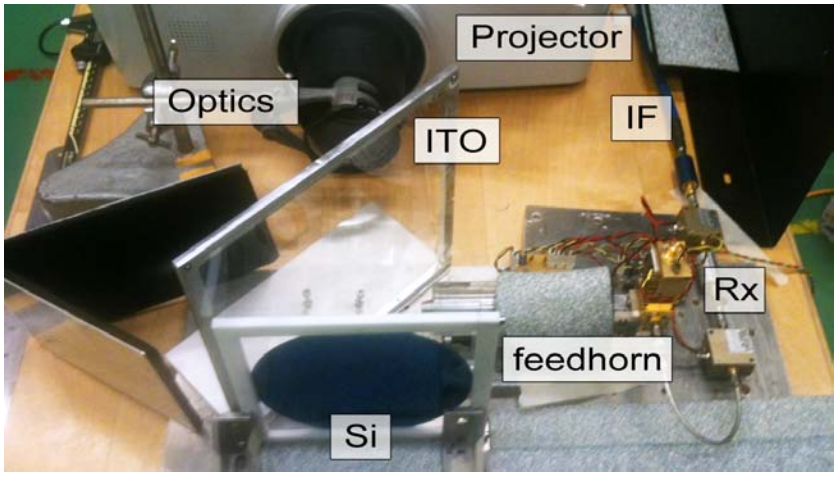

Figure 6.1: Photograph of the transmission-type piFZPA configured in receive mode. The piFZPA featured a folded-feed arrangement for simultaneous illumination of the silicon wafer.

ments LabWindows CVI IDE [241]. The software provided a basic platform which could be used to demonstrate proof-of-principle results and thus was not optimally configured for maximum scan rates. Additional Matlab routines were created which constructed a directory containing the relevant zone plate images for the intended piFZPA design and field-of-view, using the modified algorithm discussed in Section 5.4. The directory was then loaded by the control software for measuring the antenna response. The original implementation of the Matlab routines created single masks based on an 8-bit JPEG image file, which resulted in un-necessarily large image files, approximately 100 kB per mask at the native resolution of the projector (1024 x 768). Smaller image sizes could be achieved by adopting a 1-bit binary file, which can be produced by the Matlab image processing toolbox, which would produce file sizes of approximately 20 kB (e.g. a PNG format). However, this improvement was not initially realised during the setup of the system, and thus the larger JPEG files were implemented. The large number of required image files, with each image file/mask representing a single pointing direction, required significant memory management within the control software and thus limited the refresh rate.

Appropriate memory management was achieved by limiting the number of images held in memory to those required for a single elevation slice. Subsequent images where then dynamically loaded in place of images which had already been used/displayed by the control software; once displayed, each image was successively deleted from memory. The combination of this approach to manage the large amounts of required memory, and the use of the DVM/diode detector enabled maximum scan rates of up to 20 points/sec. However, marked improvements can be expected for implementation of the PNG file format, although this has yet to be tested. Figure 6.2 depicts a schematic block diagram summarising the operation of the control generation and handling software used in the piFZPA experiments. The figure also indicates the subroutine section which cause the largest time overheads. Further optimisation of the control software, such as multithreading, would be required in order to increase the scan rate of this piFZPA configuration.

As an example, 6,561 images are required to cover a 2D scan area of $\pm 20^{\circ}$

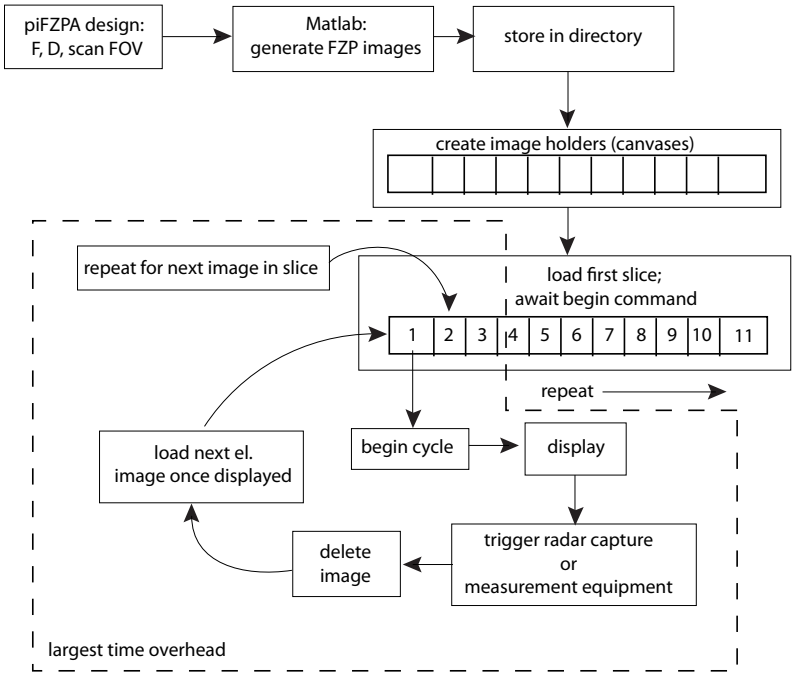

Figure 6.2: Block diagram depicting the generation and handling software used throughout all piFZPA based experiments.

in both azimuth and elevation at $0.5°$ angular increments. Using the JPEG file format (100 kB per image), this yields continued control of up to 8 MB in each elevation slice, or 641 MB for the total scan area.

6.3 Adaptive beam forming

The piFZPA enables adaptive beamforming of highly directive beams and non-mechanical steering of the directive beam by alteration of the optically excited plasma structure. The following presents a summary of the collective work which has been performed on several piFZPA designs. Using both feeds and a range of optical lenses, transmission-type piFZPAs (and small aperture focusing lenses) have been investigated for aperture sizes ranging from 40 mm up to 120 mm.

Initial investigations measured the on-axis beam forming for a given pi-

FZPA design, characterised in both transmit and receive modes, thus demonstrating reciprocity. The piFZPA used the corrugated feed and featured a F/1.63 design with a 70 mm effective aperture size, using wafer $w6$ as the substrate. The F/D ratio was chosen as a compromise between the amplitude taper and the resulting zone widths for the zone plate design. The zone plate design featured 3.3 zones, and is shown in the inset of Figure 6.3.

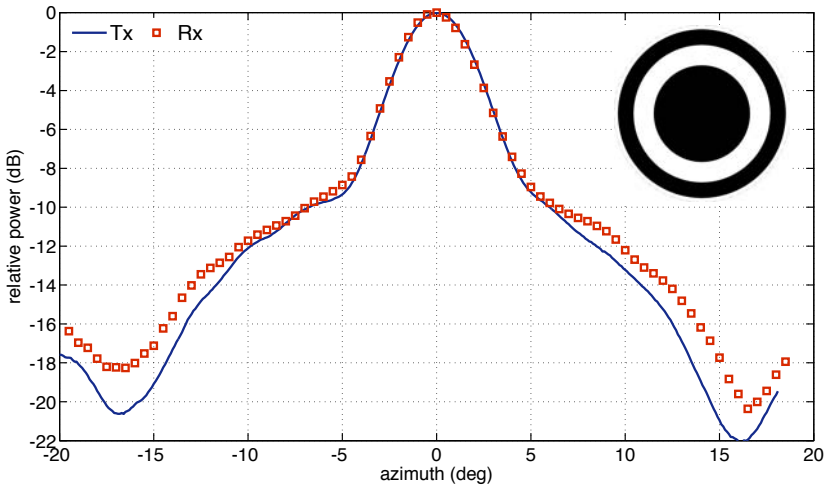

Figure 6.3: Measured (normalised) H-plane patterns for a F/1.63, 70 mm diameter transmission-type piFZPA, measured in both transmit (Tx) and receive (Rx) modes.

Figure 6.3 displays the measured H-plane patterns for both transmit and receive modes, where the formed directional beam is shown to be similar in both cases. The optical irradiance, measured at 550 nm, was $100\ \mathrm{mW/cm^2}$ in the receive mode (Rx), and $130\ \mathrm{mW/cm^2}$ in the transmit mode (Tx), giving rise to the discrepancy in the low-level sidelobes. For practical reasons, the following measurements were performed with the piFZPA operating in receive mode.

The following details the demonstration of a controllable directive beam over a 2D area, illustrated by a few of the piFZPA designs tested. Initial tests implemented the corrugated feedhorn, which resulted in higher F/D ratios in order to maintain reasonable amplitude tapers. Figure 6.4 displays the measured 2D antenna pattern for an F/1.63, 70 mm diameter piFZPA. The optical density was measured (at 550 nm) as approximately $100\ \mathrm{mW/cm^2}$, which

resulted in an approximate effective plasma density of $\Delta n \approx 2$ x10^{15} cm^{-3}. The zone plate design was the same used in Figure 6.3, which featured an amplitude taper of approximately -13 dB. The pattern was measured over $\pm 20°$ in both azimuth and elevation at $0.5°$ increments, requiring 6,561 masks (641 MB total); the scan rate was approximately 15 points/sec ($\sim$8 min acquisition time). Slight alignment errors in both azimuth and elevation of the transmitter location resulted in an offset from boresight.

The measured pattern features a peak sidelobe level of $\approx$ -8 dB, and a half power beamwidth of $\theta_{\mathrm{hpbw}} = 4.51°$ ($R^2 = 1.00$) and $\theta_{\mathrm{hpbw}} = 4.25°$ ($R^2 = 1.00$) in both the E- and H-plane respectively; the directivity is then 32.8 dBi. Using the gain transfer method the gain of the antenna was measured as 21.5 dBi, excluding the 4 dB loss due to the substrate thickness, which gives an effective 7.5% aperture efficiency. The reasonably high efficiency resulted from the relatively high carrier injection level, and is in agreement with the optimisation discussed in the previous chapter.

Figure 6.5 displays a comparison between the measured H-plane pattern and the simulated pattern, obtained from the new model developed in Section 5.2.2. The simulated pattern was obtained assuming the following parameters: F = 114 mm, D = 70 mm, amplitude taper = -13 dB, $d = 600\ \mu\mathrm{m}$, and $\Delta n = 2$ x10^{15} cm^{-3}. The simulated pattern yielded a gain of 23.5 dBi, and is shown to be in reasonable agreement with the measured data. The slight error in gain and the deviation from the simulated pattern is believed to have arisen from lateral diffusion effects, whereby the zone plate design, having only a few zones with comparable zone widths to the diffusion length (~ 2 mm), resulted in degradation of the measured piFZPA performance.

Improved designs were attempted by using the smoothed conical horn, which enabled smaller F/D ratios, whilst maintaining a good amplitude taper, due to the reduced aperture size. One such design comprised a 120 mm focal length, 100 mm effective aperture (F/1.2), with a -10 dB edge taper. The zone plate design then featured 6.3 zones, with the corresponding mask shown in Figure 6.6(a). Furthermore, improved optical lenses, which involved standard 77 mm diameter close-up camera lenses (Hoya) of either +2, +3, and +4 diopters, yielded enhanced irradiance and good focus at the reduced

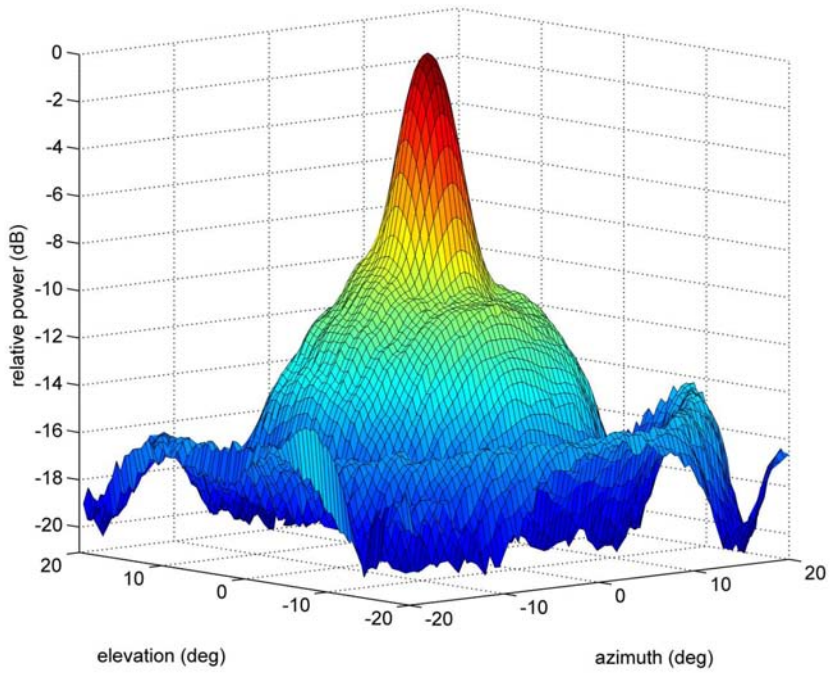

(a)

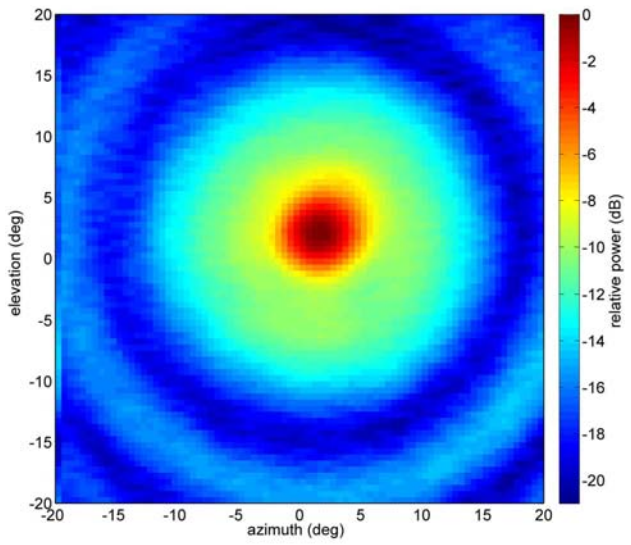

(b)

Figure 6.4: Measured 2D antenna pattern for an F/1.63, 70 mm diameter piFZPA using a visible data projector as a programmable broadband light source and spatial light modulator. The pattern was measured at $\Delta = 0.5°$ angular increments.

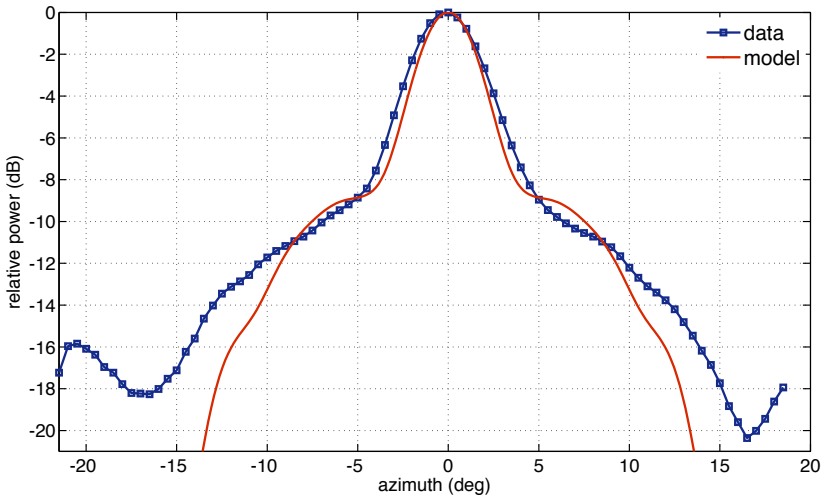

Figure 6.5: Measured and simulated H-plane pattern for the F/1.63, 70 mm diameter piFZPA displayed in Figure 6.3.

focal plane distance, with the increased aperture size. The maximum effective plasma density was then expected to be $\Delta n \approx 1.4 \text{ x}10^{15} \text{ cm}^{-3}$ with an increased aperture size of 100 mm.

The measured far-field pattern was performed over a 2D area surrounding the fixed transmitter, spanning $\pm$ 20° in both azimuth and elevation, in $0.25°$ steps in both planes. This particular scan required 25,921 zone masks, which resulted in a total sequence memory of 3 GB, or 16 MB per elevation slice! The increased memory requirement slowed the control software to less than 8 points/sec. The total scan time was approximately 1 hour.

Figure 6.6 displays the measured 2D antenna pattern for the improved piFZPA design, which demonstrates an excellently formed, highly symmetrical beam with a distinct highly directive mainlobe, and low level sidelobes. The increased number of zones resulted in an improved sidelobe suppression, yielding a peak sidelobe level of approximately -12 dB. The half-power beamwidth was measured as $2.80°$, and $2.89°$ in the H- and E- plane respectively, yielding an $R^2 = 1.00$ in both cases, with slight asymmetry arising from the feed. This then gives a directivity of 36.5 dBi. The gain of the piFZPA was found to be 23.7 dBi, measured as before, which gives an effective 5.2% aperture efficiency. The increased gain, in comparison to the F/1.63 design, resulted

(a)

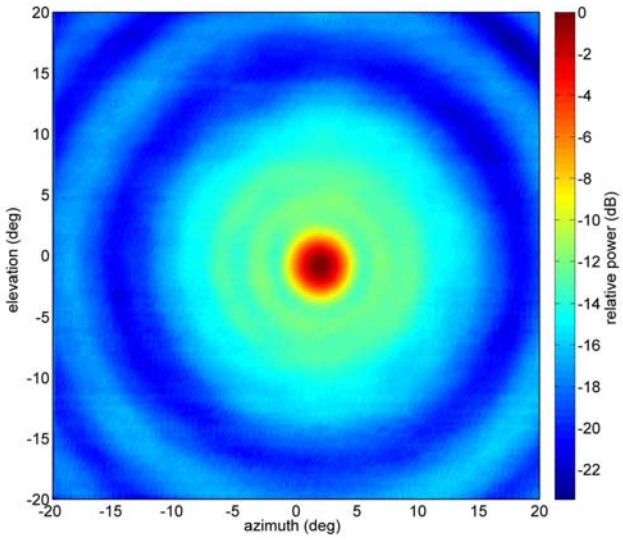

(b)

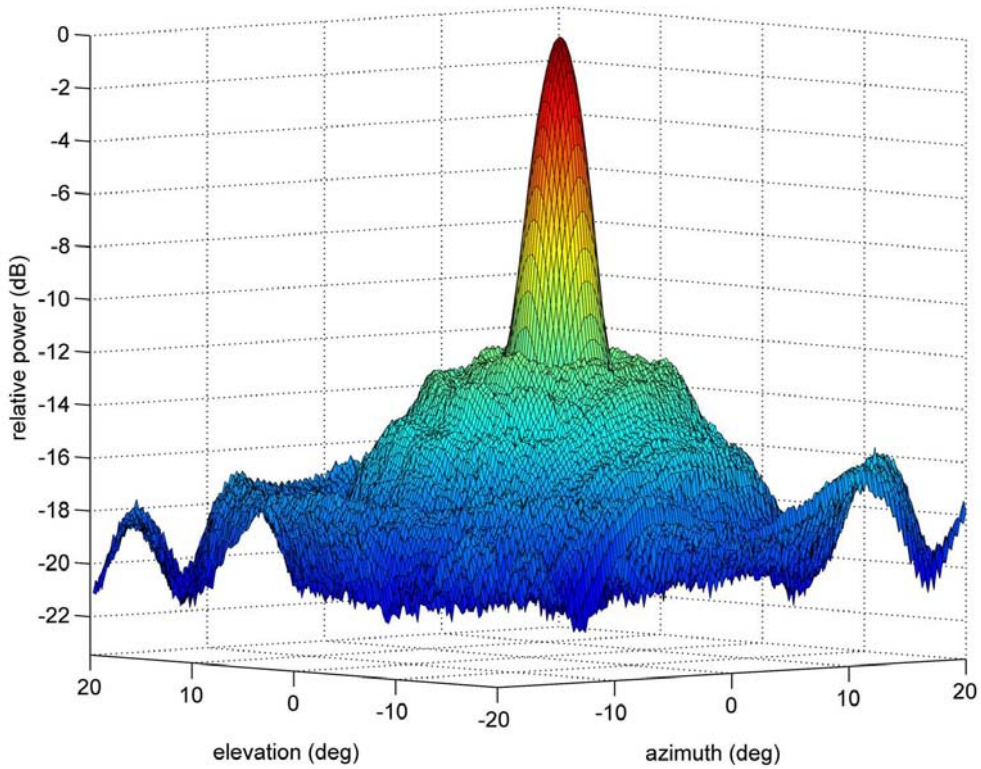

(c)

Figure 6.6: Measured 2D antenna pattern for an F/1.2, 100 mm diameter piFZPA using the visible data projector. The measured pattern was measured at $\Delta = 0.25°$ angular increments.

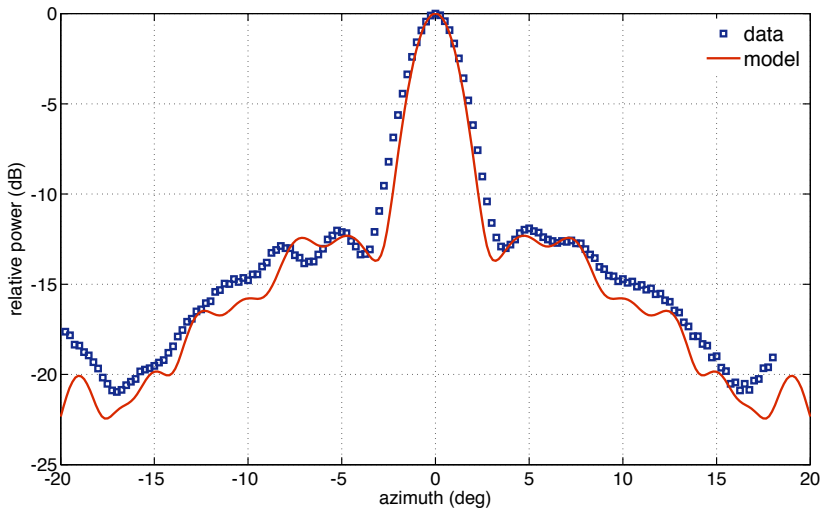

Figure 6.7: Measured and simulated H-plane patterns for the F/1.2, 100 mm diameter transmission-type piFZPA displayed in Figure 6.6. The simulations were performed using the new analytical model introduced in Chapter 5.2.2.

from the larger aperture, whilst the lower efficiency resulted from the reduced irradiance, as per Figure 5.4(a).

Figure 6.7 displays a comparison between the measured and simulated H-plane pattern; the measured pattern is from Figure 6.6. The simulated pattern assumed the following parameters: F = 120 mm, D = 100 mm, amplitude taper = -10 dB, $d = 600\ \mu\mathrm{m}$, and $\Delta n = 1.4\ \mathrm{x}10^{15}\ \mathrm{cm}^{-3}$. The comparison is shown to be in excellent agreement, where slight deviations of the measured pattern are believed to result from lateral diffusion effects due to the similarity in zone widths and the diffusion length of the wafer. The simulated gain was 24.2 dBi, again, close to that measured. While both measurements have shown to suffer from degradations due to carrier diffusion effects, it appears that a piFZPA design with an increased number of zones yields increased tolerance to the diffusion effects, maintaining reasonable performance, as observed by comparing Figures 6.5 and 6.7. The smaller F/D ratio piFZPA is believed to feature less degradation due to the increased number of zones, and possible the smaller illumination density. While diffusion degrades the zone plate plasma, a larger number of zones will remain in the short F/D case thus giving better performance. The lower irradiance will

also reduce the attenuation induced in un-illuminated regions caused by the diffusion of carriers.

6.4 Characterisation of the off-axis beam degradation

Scanning antennas are known to suffer from beam degradations which increase as the beam is deflected further from boresight. The following discussion presents the results from a range of off-axis characterisations that were performed for a number of piFZPA designs using the same transmission-type configuration outlined above.

As an example of controlled beamsteering, Figure 6.8 displays the measured 2D antenna pattern, as before, with the transmitter location fixed at either $0°$, $5°$, and $10°$, with the measurements performed over a 2D area spanning $\pm 20°$, at $0.5°$ increments. The zone plate design featured a 100 mm aperture, 160 mm focal length (F/1.6), and a -14 dB amplitude taper using the corrugated feed; this resulted in 4.8 zones (not shown). The measured irradiation level was approximately $70\ \mathrm{mW/cm^2}$, measured at 550 nm, and positional errors in locating the transmitter resulted in deviations of the beam from the intended angles; the transmitter location was instead $2°$, $7°$, and $12°$ as a result.

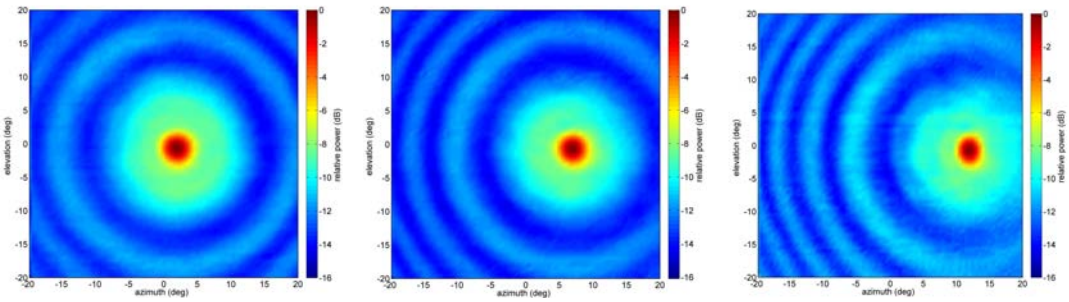

(a) (b) (c)

Figure 6.8: Measured 2D antenna pattern for a transmission-type F/1.6, 100 mm diameter piFZPA, with the transmitter located at (a) $0°$, (b) $+5°$, and (c) $+10°$.

Figure 6.8 clearly demonstrates beam steering using the piFZPA.

The scan loss for the piFZPAs were then obtained by comparing the relative degradation in the beam quality with various transmitter locations. The distance to the transmitter remained constant, and the transmitter rotated in an arc centred on the piFZPA to maintain collinear alignment of both antenna boresights. The measurement procedure is shown in Figure 6.9. The measured antenna patterns were performed in a single axis only. The largest offset transmitter location yielded an off-axis deflection of the mainlobe of approximately $45°$.

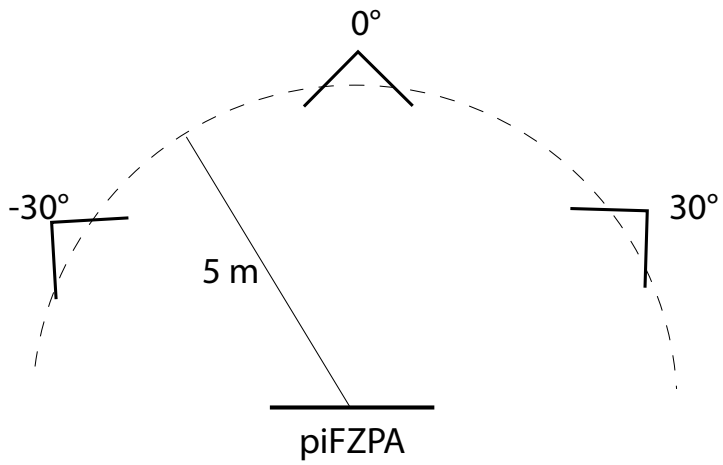

Figure 6.9: Off-axis beam degradation characterisation measurement scheme.

Figure 6.10 displays the measured scan loss characterisations for two example piFZPA designs. Figure 6.10(a) displays the measured H-plane patterns for an F/1.31, 80 mm diameter piFZPA as a function of off-axis scan angles of up to $30°$. The principle plane patterns were measured for azimuth angles spanning $-40° \leq \theta \leq +10°$ in $0.1°$ angular increments. The irradiation level was measured (at 550 nm) to be approximately $70\ \mathrm{mW/cm^2}$. The on-axis pattern featured a half-power beamwidth of $3.11°$ corresponding to 35.7 dBi directivity. Positional errors of the transmitter location changed the azimuth off-axis angles, θ_0, from those which were intended, which were instead $\theta_0 = -4.3°, -9.0°, -13.8°, -18.2°, -22.7°$, and $-26.8°$.

The measured H-plane patterns, normalised to the measured on-axis peak,

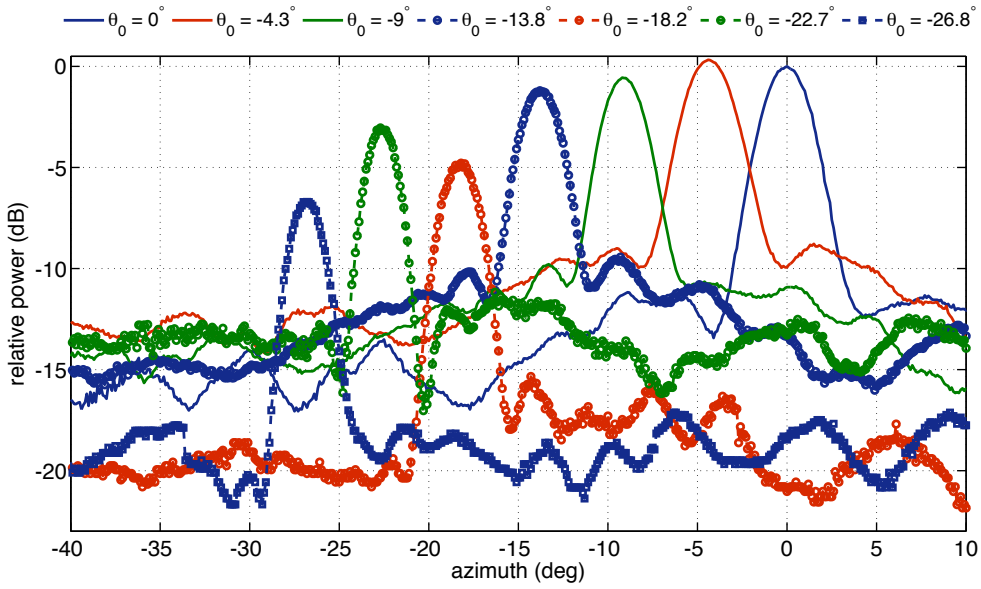

(a)

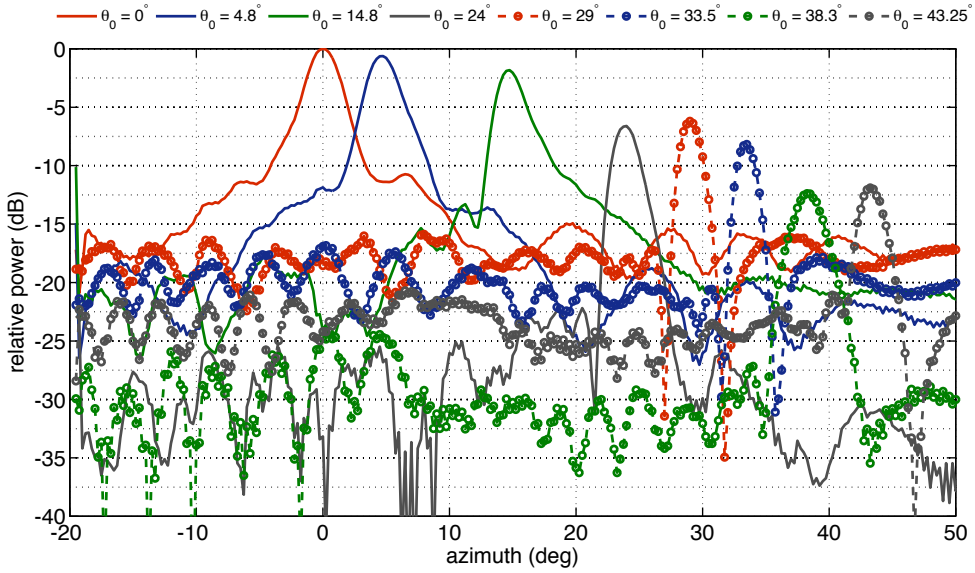

(b)

Figure 6.10: Measured scan loss for a transmission-type piFZPA with (a) F/1.31, 80 mm effective aperture, and (b) F/1.2, 100 mm effective aperture.

display the characteristic fall-off of the mainlobe peak as the transmitter is moved off axis. The measured off-axis antenna patterns illustrate a gradual drop in gain, with a maximum drop of ≈7 dB measured at near $30°$ offset, and a reduction in the half-power beamwidth of up to 30%, while the relative peak sidelobe level remained constant.

Figure 6.10(b) displays the off-axis scan loss for an F/1.2, 100 mm diameter piFZPA, measured for scan angles of up to $45°$ from boresight. Each H-plane pattern was measured between $-20°$ and $+50°$, at $0.25°$ increments. The irradiation level was measured (at 550 nm) to be approximately $80\ \mathrm{mW/cm^2}$. The on-axis pattern featured a half-power beamwidth of $2.90°$ corresponding to 36.3 dBi directivity. Positional errors of the transmitter location changed the off-axis angles from those which were intended to $\theta_0 = 4.8°$, $14.8°$, $24.0°$, $29.0°$, $33.5°$, $38.3°$, and $43.3°$.

Similarly, the gain is shown to gradually drop as the scan angle increases with a maximum gain loss of less than 12 dB observed at $43°$ offset, a change of up to 30% in the half-power beamwidth, and a constant sidelobe level.

Increased astigmatism at off-axis angles results from an inefficient zone plate mask. It has been suggested that increased zone eccentricity would remove such degradation [232], where constant beamwidths and similar gain drops have been shown experimentally in [75].

Alternative eccentric masking methods appear to be extremely sparse within the open literature, with current publications being restricted to [242] (in Chinese). Current implementations of the new masking algorithm have currently been unsuccessful and should be pursued in future work.

From the piFZPA designs which were investigated, the relative gain reduction was found to follow the trend discussed above, with small variation between designs. However, it is still unclear to what extent, if any, the scan loss is a function of the irradiance of the piFZPA; the details of this relation should be of interest in future work.

6.5 High fidelity beam control

The piFZPA technique permits high precision arbitrary scanning of a directive beam within a 2D area, thus making it a particularly attractive non-mechanical scanning method. Limitation of the pointing resolution of a directive beam using this method has yet to be defined, while previous demonstrations have shown resolutions of $\Delta\theta = 0.005°$ [75]. The pointing resolution of a piFZPA is expected to be limited by the method in which the zone plate masks are optically encoded onto the substrate, e.g. the number of LEDs in an array, or the resolution of the SLM, and potentially the diffusion length of the substrate. Given the high density of illuminating pixels used in this work, the pointing resolution of the masks is thus exceptionally high. This is one particular advantage of implementing modern display technologies, which inherently benefit from a high pixel density, i.e. the XGA projector used for this work featured over 785, 000 pixels, contrasted to the 2,335 LEDs used by Webb.

However, the finite resolution (0.01 dB) of the power measurement equipment used within this work restricted investigations into the possible limits imposed by the substrate. For instance, pointing resolutions which matched that demonstrated by Webb *et. al.* indicated that the resolution of the measurement equipment was being reached, and thus further work is required in order to ascertain possible substrate, or irradiance, dependencies that may limit the pointing resolution of the piFZPA.

For illustration, the measured H-plane pattern performed at $\Delta\theta = 0.005°$ is shown in Figure 6.11. The piFZPA design featured a 70 mm effective aperture, 114 mm focal length (F/1.63), and a -14 dB amplitude taper. The measured irradiation level was approximately $70\ \mathrm{mW/cm^2}$. The measured H-plane pattern was performed over a $12°$ field-of-view, which resulted in 2,401 masks with a total memory of 234 MB. It should be pointed out that the plotted data have no overlaying line joining the data points.

From the figure, the resolution limit of the power measurement device is being approached. Time did not permit further improvements to these measurements.

Finally, preliminary measurements were also performed which indicated the

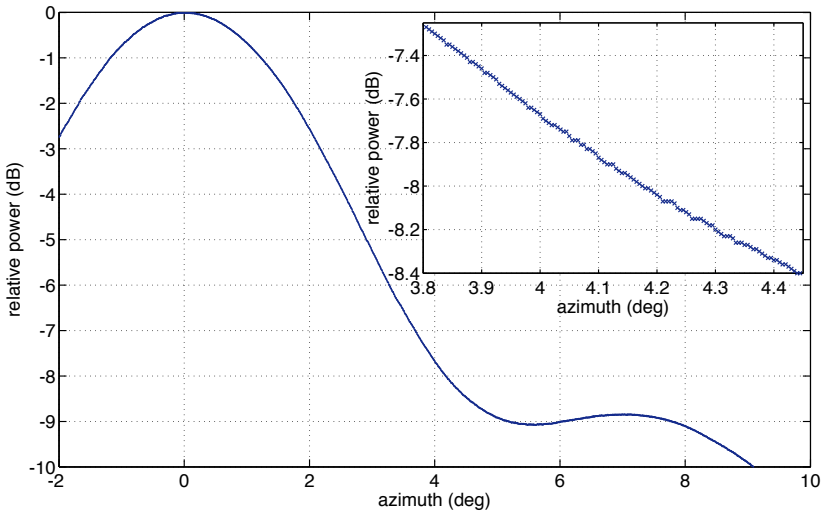

Figure 6.11: Measured principle plane pattern of an F/1.63, 70 mm aperture, transmission-type piFZPA with an angular increment of $0.005°$.

beam control repeatability. The mainlobe of the piFZPA was scanned between two points, one of which corresponded with the location of the fixed transmitter. The separation of both points spanned $23°$, and resulted in a measured power fluctuation of more than 15 dB. Repetition of these measurements with several piFZPA designs consistently demonstrated high repeatability between locations; the measured power over consecutive switching yielded less than 1% fluctuation in the measured power. The repeatability was found to be consistent at a range of reconfiguration speeds, which was limited to 20 points/sec due to the software.

These initial experiments readily demonstrate that the piFZPA technique enables high fidelity control of a given beam within a 2D area, although further characterisations are required in order to fully determine the limits of such control.

6.6 Summary

Several transmission-type piFZPA designs have been demonstrated and characterised using a standard visible data projector as the visible light source and spatial light modulator. Using this configuration the following demonstrations have been characterised:

- reciprocity of the piFZPA using visible excitation wavelengths,
- measured 2D patterns, both on and off-axis,
- high pointing resolution of a directive beam,
- excellent repeatability,
- excellent agreement with the composite Fresnel-Kirchoff model introduce in the previous chapter,
- characterisation of the beam degradation as a function of scan angles,
- initial results on a variable reference phase.

In particular, adaptive beamforming and non-mechanical beam steering has been demonstrated with a precision of up to $0.005°$, which has been shown to be highly repeatable over large deflection angles. Off-axis beam degradations have been found to yield gain reductions of up to 7 dB at $30°$ from boresight, increasing to less than 12 dB at $45°$, with reductions of the beamwidth of up to 30%, whilst maintaining a constant sidelobe level. Improved off-axis performance is expected for modification to the masks, in particular increased eccentricity of each zone.

Initial investigations of the effects of a non-zero reference phase, discussed in Appendix D, has shown similar trends to what would be expected by theory. However, the full benefits of this parameter were limited in practice due to the large diffusion length of the substrate used. Further work on shorter lifetime wafers, in addition to determining the limitations imposed on the modulation of the mainlobe phase, is required in order to fully realise the benefits of the reference phase parameter.

Finally, while initial investigations of the piFZPA technique highlighted the potential benefits of this method, the extension of this method to a system which utilises well-established visible display technologies further enhances the potential of this technique. The high pixel density and availability of conventional visible display technologies enables high flexibility and fidelity, low costs, and the ability to scale the piFZPA technique to higher frequencies, thus increasing the attractiveness of the piFZPA method to a host of applications.

chapter 7

Active imaging using a piFZPA

The following chapter discusses initial proof-of-principle results which have been obtained by integrating a piFZPA and a close-range imaging FMCW radar. The details of the implementation, and a range of preliminary images which were obtained, are discussed. This is believed to be the first demonstration of a piFZPA being integrated into an imaging system.

Some of the following results are to be presented at the SPIE Defence, Security and Sensing symposium 2012 on April 26th.

7.1 Configuration

A close range imaging system was initially chosen due to the limited gain of the piFZPA and the current test configuration which limited suitable environments to indoor testing. The chosen radar was the St Andrews fast imaging radar equipment, or SAFIRE [243]. SAFIRE is a single antenna, 94 GHz FMCW radar with a maximum chirp bandwidth of 2 GHz, yielding a 7.5 cm range resolution. The system is circularly polarised, and can image ranges of up to a maximum of 25 m.

The SAFIRE FMCW transceiver was removed from the antenna and in-

tegrated with the piFZPA. The circular polariser was removed and the radar WR10 homodyne transceiver hardware was attached to the smooth walled conical feed of the piFZPA, as shown in Figure 7.1. The SAFIRE processor was used to capture, process and display the radar data. Minor software changes were also required as the original data acquisition and plotting routines were configured for the $360°$ field-of-view plots which are generated by the mechanically rotating SAFIRE antenna assembly.

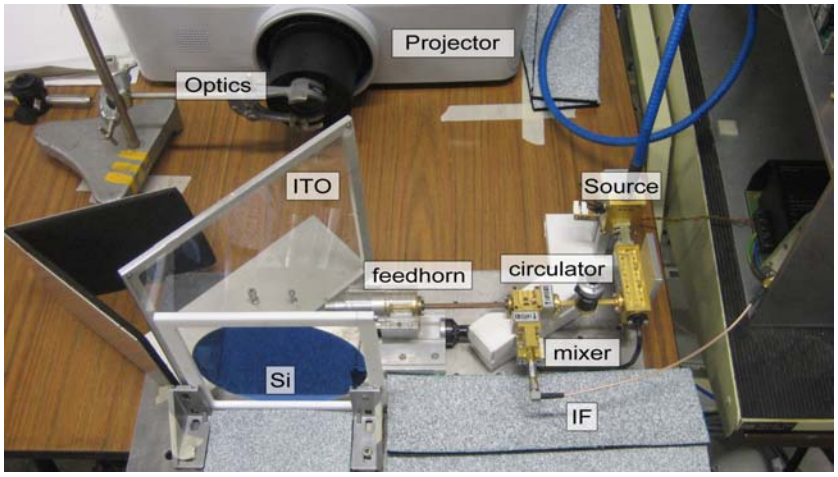

Figure 7.1: Photograph depicting the reconfigurable radar and piFZPA setup. The silicon substrate used was wafer $w6$ due to its good lifetime homogeneity.

Synchronisation of the data acquisition and the piFZPA was achieved by a software controlled digital IO line, which was configured at the beginning of each piFZPA frame/mask. The radar control computer then captured each line-of-sight produced by the FMCW chirp, which yielded raw time series data of the FMCW transit; FFT processing was then performed on each time series data, converting to the frequency (range) domain, before finally saving and displaying the peak power response within the measured range. Sorting of the output data (image) was then performed in Matlab.

The piFZPA comprised a 100 mm effective aperture, with a 120 mm focal length (F/1.2). The use of the smoothed wall horn yielded a -10 dB edge taper. The measured irradiance was approximately $70\ \mathrm{mW/cm^2}$, measured at 550 nm, which corresponded to an effective plasma density of $\Delta n \approx 1.4\ \mathrm{x10^{15}\ cm^{-3}}$. From the previous chapter, the *true* gain of the piFZPA

is approximately 20 dBi, including the 4 dB (one-way) loss through the unmatched silicon wafer and arising fro the limited irradiance from the projector. The beamwidth of the piFZPA was approximately $2.85°$, averaged between both planes (see Figure 6.6).

The limited gain, and angular resolution, restricted targets to standard corner reflectors which have high reflectivity and a point-like response. A range of corner reflectors with a +20 dBsm radar cross section (RCS) were then used as the targets of interest within a given scene.

7.2 Preliminary results

Preliminary results involved active imaging of a scene with a known distribution of corner reflectors. The first scene employed two corner reflectors distributed around the piFZPA boresight. The corner reflectors were placed in the far-field of the piFZPA at a constant lateral distance (5 m), and were separated by approximately 42 cm centre-to-centre. The scene is shown in Figure 7.2. The scene was then imaged using the piFZPA and SAFIRE radar.

Figure 7.2: Photograph of two 20 dBsm corner reflectors separated by 42 cm.

The field-of-view spanned $\pm 10°$ in both azimuth and elevation which was scanned in $0.25°$ increments, requiring 6,561 zone plate masks, totalling 641 MB of JPEG images. The required memory management (min. 8 MB at any given time) resulted in a maximum scan rate of 15 points/sec, limited

by the software as discussed in the previous chapter. The image acquisition time was of order 8 min.

Figure 7.3(a) displays the radar image obtained using SAFIRE and the piFZPA. The radar image shows two distinct peaks corresponding to the pair of corner reflectors. Fitting a Gaussian to both peaks, shown in Figure 7.3(b), yields the two-way antenna pattern of the piFZPA; the numerical fits yield $2.02°$ ($2.86°$ one-way) for the left target, and $2.17°$ ($3.07°$ one-way) for the right target. These values are similar to what was measured in the previous chapter ($2.80°$ in the H-plane, and $2.89°$ in the E-plane), with the discrepancy on the right target believed to have resulted from alignment errors. Further, the limited gain of the piFZPA resulted in the two-way sidelobe level to fall below the noise floor of the system.

Additional corner reflectors were added (located 5 m from the piFZPA), creating a distribution in both azimuth and elevation. Two reflectors were placed in close proximity to one another, and two other reflectors were well separated, one near boresight and the other in the far lower corner of the scene. The distribution of the reflectors is shown in Figure 7.4; the upper left reflectors were separated by 26 cm centre-to-centre.

Figure 7.5(a) displays the acquired radar image of the scene containing all four corner reflectors, measured in a range $3.0 \leq R \leq 5.5\,\mathrm{m}$. The piFZPA was scanned over $\pm 20°$ in both azimuth and elevation, in $\Delta\theta = 0.5°$ increments, at a rate of 15 points/second. The scan sequence required the same number of masks and thus memory as before.

Figure 7.5(b) displays the azimuth slice through each corner reflector. The angular separation of the upper left targets was approximately $1.49°$, much greater than the resolution limit of the piFZPA based imager ($\approx 1°$, or half the radar beamwidth), which lead to the large separation between the targets (≈ 14 dB), as highlighted in Figure 7.5(b). The slight drop in power from the far left target was the result of a slight angular alignment error of the corner reflector relative to the radar. The overall drop in the peak power for the off-axis reflectors was approximately -1.5 dB for corner reflector located at $(\theta, \phi) = (+12.5°, -8°)$, and -3.7 dB for the upper corner reflector located at $(\theta, \phi) = (-12.3°, +4.5°)$. The drop in peak power is inline with the gain

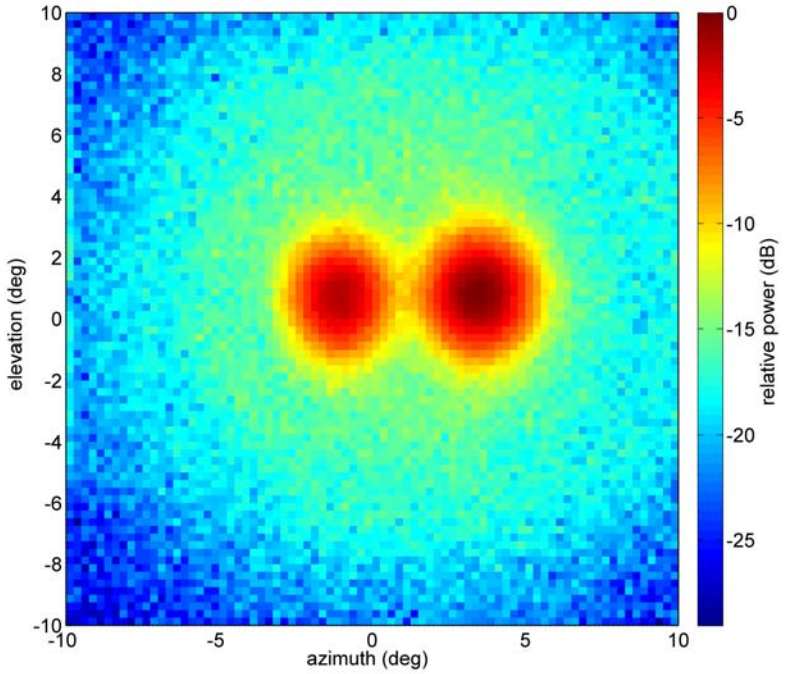

(a)

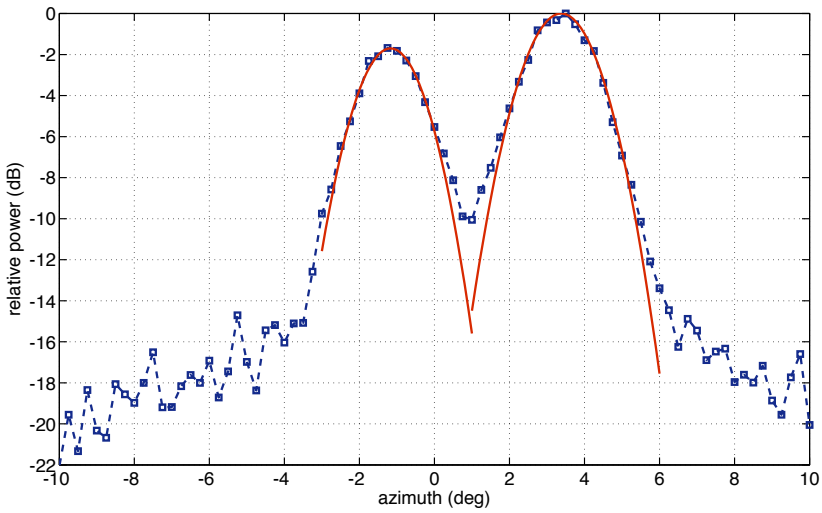

(b)

Figure 7.3: Scene involving two +20 dBsm corner reflectors separated by 42 cm, located 5 m from the radar, with (a) the acquired radar image using SAFIRE and the piFZPA, and (b) the central azimuth slice with a Gaussian fit to both peaks.

Figure 7.4: Photograph of four +20 dBsm corner reflectors; the pair of corner reflectors (top left) were separated by 26 cm.

reduction measured in the previous chapter (see Figure 6.10(b)), with a minor discrepancy being due to alignment of the reflectors.

The angular width of each peak was found by fitting a Gaussian to the data. Running from left to right in Figure 7.5(b), the two-way half-power beamwidths were found to be $1.28°$ ($1.81°$ one-way), $1.51°$ ($2.14°$ one-way), $2.02°$ ($2.86°$ one-way), and $2.03°$ ($2.87°$ one-way) respectively. The large change in the half-power beamwidths of the upper left corner reflectors are larger than would be expected for the piFZPA beam '*degradation*', with the change representing approximately 30% reduction at $12°$ from boresight. This *degradation* is much larger than found in the previous chapter, and its origin is currently unknown. The change may have resulted from the alignment of the reflectors relative to piFZPA, or mutual coupling between the reflectors. Very little change in the half-power beamwidth which was observed for the reflector located at $(\theta, \phi) = (+12.5°, -8°)$ which is inline with that measured previously, at this deflection angle. Figure 7.5(b) also displays the measured one-way antenna pattern (green) which has been scaled to the equivalent two-way pattern. The agreement for the on-axis reflector is shown to be excellent between the (scaled) one-way antenna pattern (see Figure 6.6(c)) and the measured two-way radar antenna pattern. In addition, the two-way sidelobe level of the piFZPA is shown to be below the noise floor of the radar.

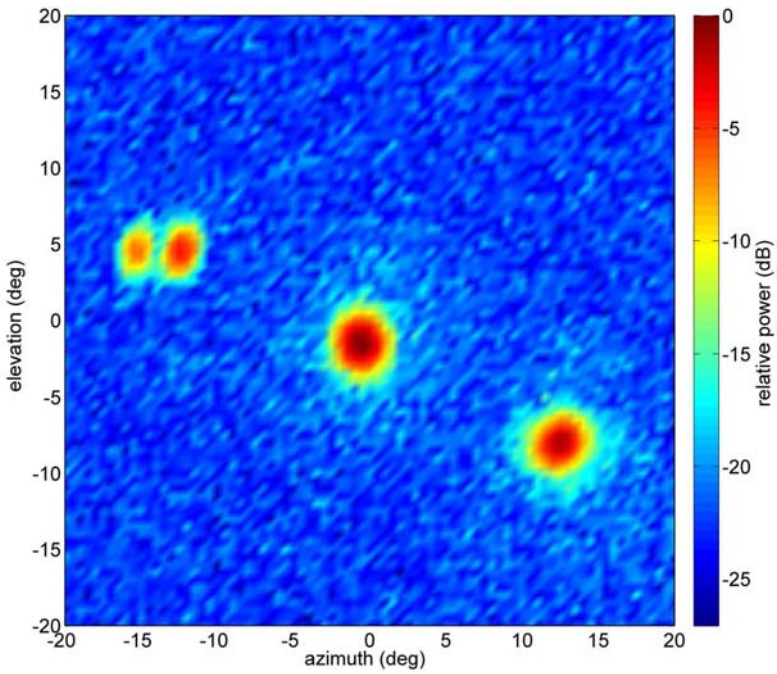

(a)

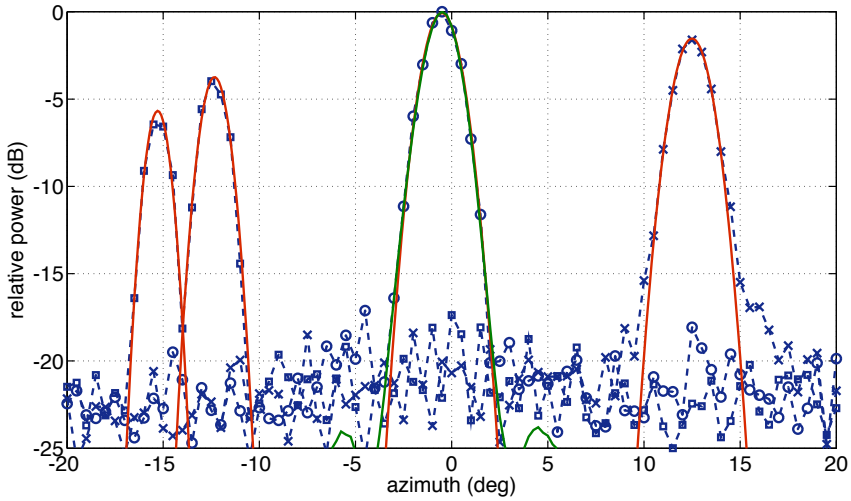

(b)

Figure 7.5: (a) Radar image for the scene presented in Figure 7.4; (b) azimuth slice through each corner reflector.

7.3 Summary

Preliminary results have been obtained based on a successful integration of a transmission-type piFZPA and a 94 GHz FMCW close-range imaging radar. Limited gain and directivity of the piFZPA restricted imaging to high reflectivity corner reflectors at moderately short ranges.

The basic imagery obtained by the piFZPA radar, while far from optimal, have provided the initial step in realising a high performance system with a non-mechanically steered piFZPA. The reasonable bandwidth performance of the piFZPA, the ability to arbitrarily scan a directive beam over a 2D area, and the potential frequency scalability with established display technologies highlights the piFZPA technique as a low-cost, highly flexible, and attractive solution for systems requiring adaptive beamforming capabilities.

chapter 8

Conclusions & further work

The motivation for the work presented in this thesis was to investigate the piFZPA technique; to provide a clear theoretical understanding detailing the requirements, limitations, and suitability of this particular method for use at mm-wave and submm-wave frequencies. The work outlined in this thesis has attempted to definitively answer these fundamental questions, highlighting the potential and limitations of this technology.

The following discussion summarises the results of this work, and the scope for future work is discussed.

Section 8.2 forms parts of a discussion which is to be presented at the European Microwave Week in October 2012, as an invited paper within the focused session on adaptive submm-wave beam forming.

8.1 Summary

Fresnel zone plates offer a low-cost, simple, planar alternative to traditional components such as lenses and reflectors with comparable performance, and are categorised as either blocking or phase-correcting depending on their construction. While the latter offer higher efficiency and performance, the simplicity and planar form factor of all zone plates have ensured continued interest spanning a wide range of applications.

The optimisation of zone plates is determined by the F/D ratio, total number of zones, and in the case of the phase-correcting plates the lens permittivity and thickness.

A range of phase-correcting zone plates were designed, fabricated, and characterised at 94 GHz. Wood zone plate antennas constructed from PMMA were found to yield up to 26 dB sidelobe suppression, 46 dBi gain, and 67% aperture efficiency, for the quarter-wave (P = 4) design.

Further, excellent agreement has been observed between measured data and the analytical model developed for simulating grooved zone plate antennas.

Modulation of (sub) mm-wave beams can be achieved via control of the complex permittivity of a suitable substrate. The work presented in this thesis has focused on optically excited semiconductors as the chosen substrate. Optical control of the free-carrier plasma density has been shown to depend on both the spatial and temporal distribution of the plasma, which is also dependent on the substrate effective lifetime, surface recombination velocity (SRV), and irradiation wavelength. Suitable modification of these parameters can yield optimised substrates for a range of applications, which balance the required irradiance, substrate refresh rate, and plasma resolution. Higher effective lifetimes, which generally require lowered SRVs, feature lower irradiance requirements ($I_{\mathrm{opt}} \propto 1/\tau_{\mathrm{eff}}$), but limit the spatial features which are supported by the optically excited plasma. The plasma resolution (L_a) then defines the overall performance of the substrate, whether it be an optically induced grating, zone plate, or other spatial modulating device.

Furthermore, lowered SRVs are of particular interest as enabling sufficient plasma densities by means of visible optical excitation, which may then be realised using lower cost, highly flexible, well established visible display technologies. Effective lifetimes are limited, in general, by the bulk lifetime of the material, and thus low lifetime substrates can still be maintained with low SRVs. This enables fast refresh rates whilst implementing short visible wavelength technology – visible excitation does not require slow refresh rate substrates!

A brief review of suitable passivation schemes has been presented, where focus has been restricted to current industry standards. Of the current standards which are routinely applied to photovoltaics, thin film deposition of hydrogenated $\mathrm{SiN_x}$:H appears to be the most relevant for optoelectronic (sub) mm-wave devices. The $\mathrm{SiN_x}$ can be passivated using PECVD techniques, and is cheap, quick, UV stable, with good passivation quality ($S \leq 100\ \mathrm{cm/s}$), and high thermal stability, suitable for further processing whilst additionally permitting optimal control of the thin film refractive index for optimised optical transmission onto the substrate surface. Characterisations presented within this thesis suggest good long term stability against decay (years) with simple, and cheap, reset methods. Hence this particular method features high quality passivation with low maintenance, and is thus attractive for mm-wave optoelectronic devices. Thin film passivation of hydrogenated amorphous silicon (a-Si:H) has also been shown to yield a high passivation quality, and stability, but the lower UV and thermal stability may render this method un-suitable, except for applications which do not require further high temperature processing of the substrate, such as metallisation.

W-band transmission line characterisation of both un-passivated and passivated high-resistivity silicon wafers have demonstrated the significance of surface recombination effects. High SRVs ($S \geq 10^6\ \mathrm{cm/s}$) of the un-passivated wafers resulted in significantly lowered effective plasma densities and thus yielded very low attenuation at both visible and NIR excitation wavelengths. Passivation of the wafers which produced SRVs of $S < 250\ \mathrm{cm/s}$ showed significant improvements in the optically injected attenuation at both NIR

and visible excitation wavelengths due to the increased effective lifetime, and lowered SRVs. Attenuations of up to 25 dB for NIR irradiation, and 15 dB for visible irradiation, have been experimentally observed as a result.

A model based on the Lorentz-Drude, lossy ABCD matrix method, and generalised optical property equations has shown excellent agreement with experimental results agreeing well for a range of substrate qualities, irradiance, and wavelengths. The model is thus invaluable for designing optoelectronic devices, in which the optical requirements can be inferred from the model based on the required optically controlled transmission line properties.

Optimised optoelectronic devices can thus be realised for a given application in which the control of (sub) mm-wave beams using an optically excited Fresnel zone plate has been of particular interest throughout this thesis. Such devices have been termed photo-injected Fresnel zone plate antennas, or "piFZPAs", within this work.

The piFZPA comprises two main configurations: transmission, or reflection-types. Transmission-type piFZPAs are simpler in construction with lower tolerances, and do not suffer from aperture blockage effects. However, high effective plasma densities ($\Delta n \geq 10^{16}\ \mathrm{cm}^{-3}$) are required in order to achieve the maximum 10% efficiency. Nonetheless, reduced effective plasma densities can be utilised, albeit with less efficiency. Using a newly developed analytical model, the minimum plasma density required was found such that the total loss through the substrate becomes approximately 6 dB. This value represents the lowest tolerable efficiency (∼5%) with minimal irradiance requirements. In general, 10 dB attenuation yields marked improvements to the antenna performance, representing approximately 7% efficiency, where the efficiency and performance of the transmission-type piFZPA gradually increases as the attenuation is increased beyond 10 dB, albeit with a continued increase in the required irradiation level.

In comparison, the reflection-type configuration permits significantly reduced effective plasma density requirements due to an increased finesse of the etalon. In effect, maximum efficiency of the blocking-type (10%) can be realised with an order of magnitude reduction in the required effective plasma

density than for an equivalent transmission-type piFZPA. The reflection-type is then attractive from a practical viewpoint whereby lower irradiation densities can be maintained.

Moreover, the reflection-type configuration also has the potential of yielding increased efficiencies of up to 40% when used as a phase-reversal zone plate antenna, albeit with an increased irradiation (plasma density) requirement. However, the required irradiance has been shown to be comparable with the requirement of the blocking transmission-type piFZPA, which yields an inferior 10% aperture efficiency.

Using lowered surface recombination velocity wafers within a piFZPA setup has enabled demonstration of the piFZPA technique using a low cost visible data projector as the light source and programmable optical spatial light modulator, emphasising the potential of this technique.

Using the transmission-type piFZPA, dynamic control of a mm-wave beam at 94 GHz over a 2D area has been demonstrated, and characterised. The efficiency of all demonstrations has been limited by the available power from the data projector, and an additional loss of 4 dB resulting from the unmatched substrate thickness. The high diffusion length of the substrates used ($\sim 2\ \mathrm{mm}$), and the limited aperture size of the piFZPAs tested (70 mm to 120 mm), resulted in diffusion degraded effects which included broadening of the mainlobe from the diffraction limit.

The limited aperture sizes restricted the number of zone that could be practically realised due to the diffusion length of the substrate, which resulted in sidelobe suppressions not exceeding -12 dB. Nonetheless, the rapid variation in the number of zones for a given zone plate design, as shown in Figure 8.1, can significantly improve this figure to a level which may be more attractive for real-world applications. For example, changes to the substrate lifetime, or marginal increase in aperture size (irradiance), such that a piFZPA design may feature a F/D ≈ 0.5 (N $\approx$ 13 for D = 100 mm) can result in significantly improved sidelobe suppression of up to 20 dB, versus the 10 dB suppression observed for $F/D \approx 1.5$ (N = 5), which was predicted in Figure 2.3(a). However, the overall performance of the piFZPA will be largely determined

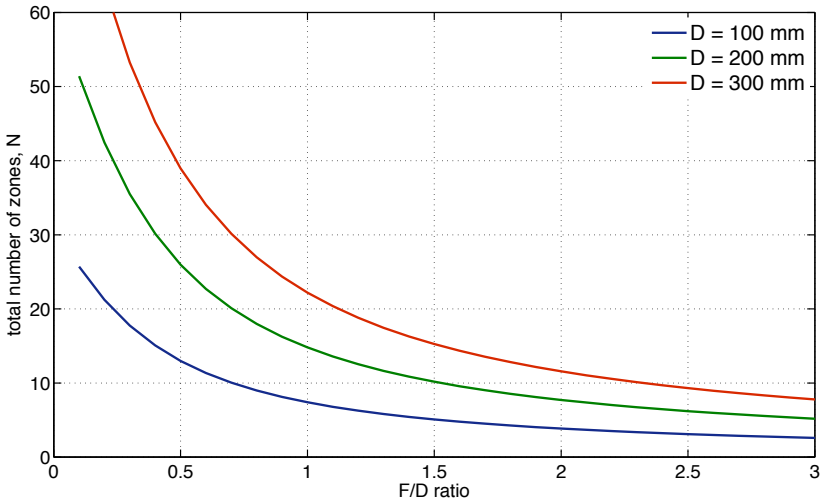

Figure 8.1: Calculated total number of zones as a function of the zone plate F/D ratio for a 100, 200, and 300 mm aperture size at 94 GHz.

by the optical budget of the given application. Nevertheless, reduced F/D designs may also introduce reduced off-axis performance of the piFZPA due to the *fast* lens design; although the details of such limitations are subject to further investigation.

Off-axis characterisations on several piFZPA designs have found gain reductions of up to 7 dB at $30°$ off-axis, and up to 12 dB at $45°$ off-axis, with a reduction of the half-power beamwidth of up to 30% being observed, while maintaining a constant sidelobe level. Improvements to the zone plate mask are known to yield improved off-axis performance, but have yet to be demonstrated using this architecture.

Preliminary results have been obtained based on successful integration of a piFZPA and a close-range FMCW imaging radar. Initial imagery was limited to scenes involving high reflectivity corner reflectors, due to the limited gain of the piFZPA. Nonetheless, these demonstrations provide the initial step towards realising a high performance system featuring a non-mechanical steering piFZPA. The piFZPA technique, and in particular implementations based on established visible display technologies, is thus an attractive solution to adaptive beamforming and non-mechanical beam steering.

8.2 Suitability at submm-wave frequencies

The suitability of the piFZPA technique at higher mm-wave and submm-wave frequencies is of particular interest. The following brief discussion outlines the requirements and limitations of the piFZPA as the design frequency is increased towards 1,000 GHz.

The effective plasma density requirements can be found by simulating the piFZPA gain as a function of plasma density for a range of design frequencies. Figure 8.2 displays the simulated antenna gain for a transmission-type piFZPA as a function of the effective plasma density, Δn, at a range of mm and submm-wave frequencies using the model introduced in Chapter 5. The piFZPA design for each simulated frequency has been adjusted such that the overall maximum antenna gain was maintained. Simulations were performed with all designs featuring a -12 dB edge taper and F/D $= 1.5$; the substrate thicknesses were $d = 466,\ 399,\ 387$, and $337\ \mu\mathrm{m}$, with apertures of $D = 315,\ 133,\ 87$, and $45\ \mathrm{mm}$, for designs at frequencies of $f = 94,\ 220,\ 340$ and $650\ \mathrm{GHz}$ respectively.

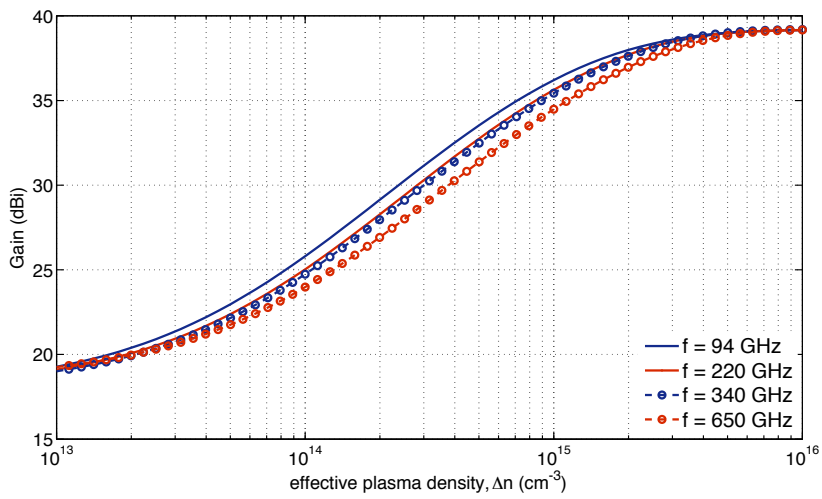

Figure 8.2: Simulated piFZPA gain as a function of the effective plasma density, Δn. Gain is shown for free-space design frequencies of 94, 220, 340, and 650 GHz. A longitudinal homogeneous plasma distribution has been assumed.

The piFZPA gain is shown to increase gradually as the effective plasma density increases, with maximum efficiency (10%) occurring for optically ex-

cited metallic zones ($\Delta n > 10^{16}$ cm^{-3}).

The transition towards increased gain is shown to translate slowly to higher effective plasma densities, resulting from the slow dispersion in the complex permittivity. Table 8.1 summarises the corresponding effective plasma density, irradiation level, and total optical power required to achieve the range of antenna efficiencies demonstrated by Figure 8.2.

Table 8.1: Summary of the piFZPA requirements for rated antenna efficiency: 4%, 6%, and 10% as per Figure 8.2. Irradiation densities, $\mathrm{I_{opt}}$, have been calculated assuming an illumination wavelength $\lambda = 900$ nm and effective carrier lifetime $\tau_{\mathrm{eff}} = 100$ μs.

f (GHz)	η	Δn (cm^{-3})	$\mathrm{I_{opt}}$ ($\mathrm{mW/cm^2}$)	$\mathrm{P_{tot}}$ (W)
94	4%	8.3 x10^{14}	118	92
	6%	1.4 x10^{15}	198	154
	10%	1.0 x10^{16}	1410	1099
220	4%	9.8 x10^{14}	132	18
	6%	1.6 x10^{15}	215	30
	10%	1.0 x10^{16}	1343	187
340	4%	1.0 x10^{15}	134	8
	6%	1.7 x10^{15}	227	13
	10%	1.1 x10^{16}	1464	87
650	4%	1.3 x10^{15}	167	3
	6%	2.3 x10^{15}	296	5
	10%	1.4 x10^{16}	1796	29

It is interesting to note from Table 8.1 that the total required optical power, $\mathrm{P_{tot}}$, for a given antenna gain is dominated by the effective aperture size of the piFZPA rather than the effective plasma density, due to the slow permittivity dispersion at mm and submm-wave frequencies (c.f. high frequency limit). In particular, the required total optical power can be seen to be much less for a maximum efficiency (10%) piFZPA at 650 GHz than any of the piFZPA efficiencies at 94 GHz. However, in practice such large 'savings' in the optical power may not be fully realised due to the diffusion limit imposed by the substrate.

Comparatively, a fixed aperture size piFZPA would require a marginal in-

crease in the total optical power due to the increased effective plasma density, with a corresponding increase in gain. For example, using the 6% efficiency 94 GHz example ($D = 315$ mm, $\mathrm{P_{tot}} = 154$ W), the total power required would then be 168, 177, and 231 W for the 220, 340, and 650 GHz cases respectively.

Figure 8.3 displays the simulated attenuation per unit length (dB/mm) as a function of frequency, for several effective plasma densities, Δn, for high resistivity silicon ($\epsilon_r = 11.7$).

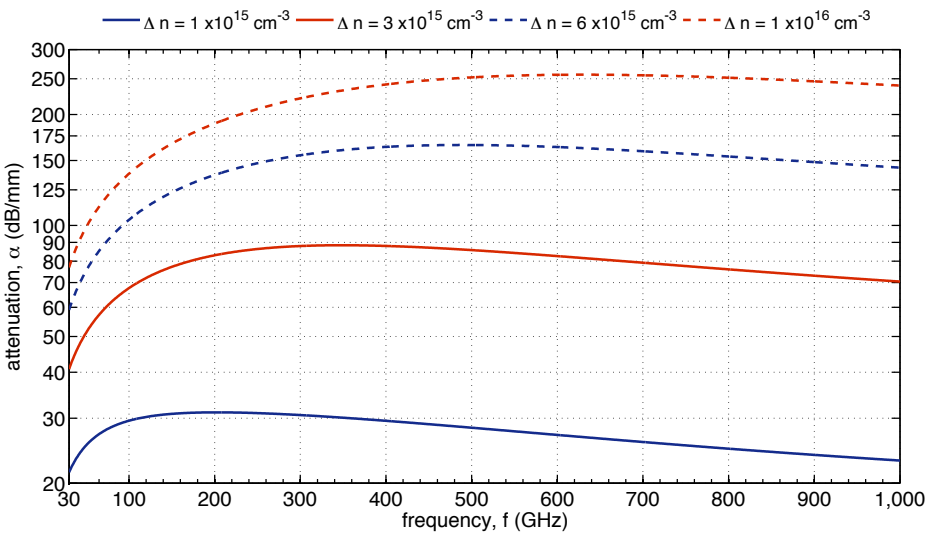

Figure 8.3: Simulated attenuation per unit length, α, as a function of design frequency, f, calculated at effective plasma densities $\Delta n = 1\ \mathrm{x}10^{15}\ \mathrm{cm}^{-3}$, $3\ \mathrm{x}10^{15}\ \mathrm{cm}^{-3}$, $6\ \mathrm{x}10^{15}\ \mathrm{cm}^{-3}$, and $1\ \mathrm{x}10^{16}\ \mathrm{cm}^{-3}$.

The attenuation per unit length is shown to vary slowly as a function of frequency, with a maximum corresponding to the plasma resonance of the free carrier system, ω_p, where $\omega_p \propto \sqrt{\Delta n}$. Although the attenuation, for sufficient carrier densities, is shown to be a slowly varying function above the plasma resonance, which is well into the submm-wave band, the attenuation is shown to vary significantly at lower mm wave frequencies. Thus, for limited plasma densities (irradiation levels), consideration of the design frequency can yield optimum loss within the substrate, increasing the antenna efficiency. For example, for $\Delta n = 3\ \mathrm{x}10^{15}\ \mathrm{cm}^{-3}$ ($\omega_p/2\pi \approx 360$ GHz) the attenuation at 94 GHz is found to be 66 dB/mm contrasted to the 88 dB/mm at 300 to

400 GHz.

For sufficiently large plasma frequencies, $\omega_p > 2$ THz ($\Delta n > 10^{17}$ cm^{-3}) for silicon, and (sub) mm-wave frequencies, the conventional low-frequency limit applies and the substrate becomes metallic due to the dominance of the Drude free-carrier contribution.

Furthermore, limited plasma resolution requires optimisation of the zone plate design, where, in general, zone widths decrease with increasing design frequency.

Hence, the zone plate design, similarly, plays an important role in the overall performance of the piFZPA at higher submm-wave frequencies, since for either an increased effective lifetime or an increase in frequency, the relative zone widths become equal to, or less than, the resolution limit of the plasma, leading to reduced performance. Figure 8.4 displays the zone plate designs for an F/1.5, 100 mm aperture piFZPA at 94, 340, and 650 GHz.

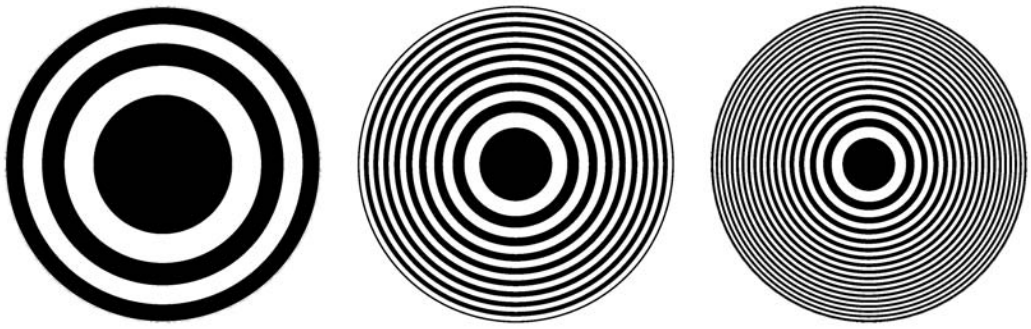

(a) 94 GHz (b) 340 GHz (c) 650 GHz

Figure 8.4: Zone plate designs for an F/1.5, 100 mm aperture piFZPA at three different design frequencies.

For a given substrate diffusion limit and an increase in the design frequency, the corresponding F/D ratio must be increased in order to maintain full transfer of the zone plate design to the optically excited plasma. As a result, the limited number of zones then leads to a reduced sidelobe performance, and possibly gain. Whilst a shorter diffusion length (through reduced effective carrier lifetimes) improves the zone plate performance, a corresponding increase in the irradiance would be required, and thus the optimisation will

depend on the given application, and the optical budget.

The optimisation process is thus similar for all frequency regimes, where the antenna performance is limited by the plasma resolution limit. As the design frequency increases, the required irradiance increases marginally for a fixed gain antenna, where optimal design frequencies exist around (or above) the plasma resonance; this is particularly important in circumstances when the irradiance is limited.

Finally, as the frequency increases to sub-mm wave bands, the optimal zone plate design requires a slower focal design (large F/D) due to the limited plasma resolution, and thus designs begin to approach that of conventional optical zone plates. The piFZPA technique is thus a potentially attractive solution for a range of submm-wave applications, benefiting from reasonable costs, low complexity, high flexibility, tailored performance, and high beam fidelity.

8.3 Further work

While the work presented within this thesis has attempted to provide a detailed insight into the piFZPA technique, the piFZPA method remains an infant technology, with extensive work still to be pursued. The following discussion outlines some possible work which should be considered in the future in order to fully realise the benefits of this technology.

Future interest in optimised zone masks designs are of particular importance, where alteration to the zone plate algorithm introduced in Section 5.4 should be pursued as a means of improving the off-axis performance of the piFZPA, as suggested in [232].

Various improvements could be extended to a range of models which have been developed within this thesis. In particular, the inclusion of the plasma penetration depth within all models would yield improved applicability to low lifetime and/or thick substrates. One possible approach would be the simple modification of the substrate thickness with the effective plasma penetration depth as developed by W. Platte [53]. Inclusion of lateral diffusion effects

within the piFZPA model would also further enhance the accuracy of the model to piFZPA designs which violate the plasma resolution limit.

Identification of other suitable semiconductor substrates could also be beneficial. However, the wide availability, large scope of standardised processing methods, and low insertion loss of silicon substrates may make finding an alternative difficult. Nonetheless, compound semiconductors such as gallium arsenide (GaAs) may prove to be interesting. The increased base carrier density results in lowered plasma densities which produce 'metallic-like' behaviour [228]. However, lowered lifetimes, due to increased radiative recombination, may cause practical problems due to increased irradiance requirements.

Alternatively, other suitable reconfigurable substrates may be of interest. In particular, appropriate substrates may be used which can overcome the practical problems imposed by the substrate diffusion length, and in addition may be able to produce higher efficiencies by implementing higher phase correcting designs. Such realisations have been previously demonstrated using mechanically actuated solenoid driven reflectors [244, 245]. While these demonstrations are capable of increased efficiencies beyond 40% ($P = 2$), the number of components, and system architecture, lead to increased complexity and limited flexibility, which may restrict their suitability to some applications, particularly at (sub) mm-wave frequencies.

Electronic paper, or 'e-ink', display technologies has been identified during this work as a promising alternative technology. Initial W-band transmission line results performed on an e-ink display which was extracted from a standard 1st generation Amazon kindle® e-reader has shown to be promising, although further investigations are required. For example, Figure 8.5 displays the measured reflection properties of the e-ink display across W-band, using the QO-VNA of Chapter 4. Transmission through the display was approximately constant across the full W-band, with a measured S_{21} of -10 dB for both white and black screens, while a S_{11} contrast of 5 dB was observed at 94 GHz.

The display was removed from the consumer device and was positioned within the W-band QO beam. Control electronics remained connected to

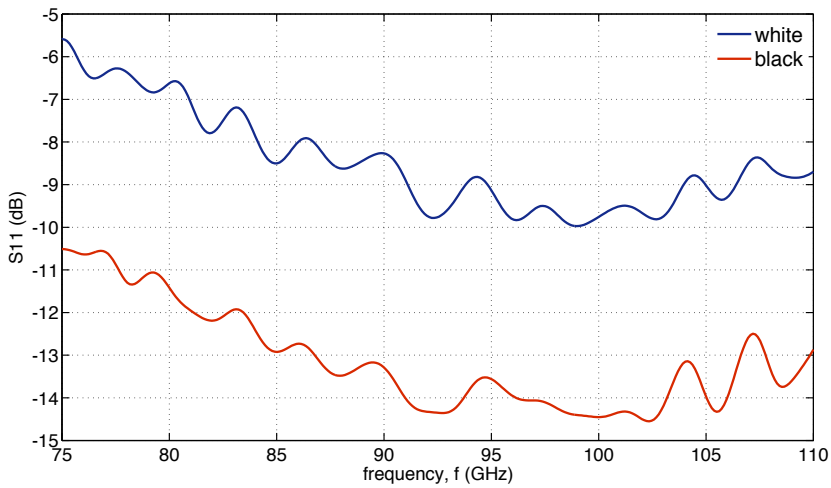

Figure 8.5: Measured reflection from a 1st generation e-ink display at W-band frequencies using the QO-VNA setup of Chapter 4.

the main motherboard, and a simple 'black' and 'white' PDF file was loaded onto the onboard memory, and displayed by the e-ink display. The sinusoidal modulation of the measured reflection resulted from the thickness of the e-ink display.

The implications of these results are quite significant: if the reflection contrast of the e-ink display can be increased at W-band frequencies such that the change in reflection between white and black can exceed 10 dB, then reasonable aperture efficiency, and antenna performance, can be realised using these devices. In particular, such realisations would not be subject to a 'plasma resolution', being limited only by the pixel density of the display, and thus higher performance piFZPAs may be realised by implementing smaller F/D ratios. Furthermore, if such a reflection contrast can be maintained while removing the backing metallic film, stacked e-ink displays can yield efficiencies approaching 80% ($P \geq 4$). Moreover, such 'piFZPAs' would maintain low costs, power consumption, high flexibility, and simplicity with high efficiencies. Scalability of this technology to larger apertures would also be of low-cost, where suitability at higher submm-wave frequencies would only be limited by the pixel pitch of the display technology, defining the limit at which grating lobes appear.

Conversely, the response time of e-ink displays are known to be slow (milliseconds) which have prevented them from being adopted within video based devices. However, the fundamental requirement for faster displays, driven by the display industry, will only increase the refresh rates over time, and thus this particular approach could be a potential option in the future.

Finally, improvements over current demonstrations are to be performed in a future project which has recently received short term EPSRC funding. The short term project aims to develop the demonstrations presented within this thesis, and is expected to improve the piFZPA efficiency ($\sim 10\%$) and also increase the scan rate to greater than 10,000 beams/sec. The theoretical groundwork and models that have been developed within this thesis will thus be crucial for realising the optimised piFZPA.

appendix A

Fresnel-Kirchoff derivation for the grooved WZP

The following presents the derivation of the new analytical model used for simulating the far-field antenna patterns of a grooved dielectric Wood zone plate, with arbitrary lens (complex) permittivity, $\tilde{\epsilon}_r$, and lens thickness, t_L, which was summaried in Chapter 2.

The grooved Wood zone plate follows the geometry depicted in Figure 2.5:

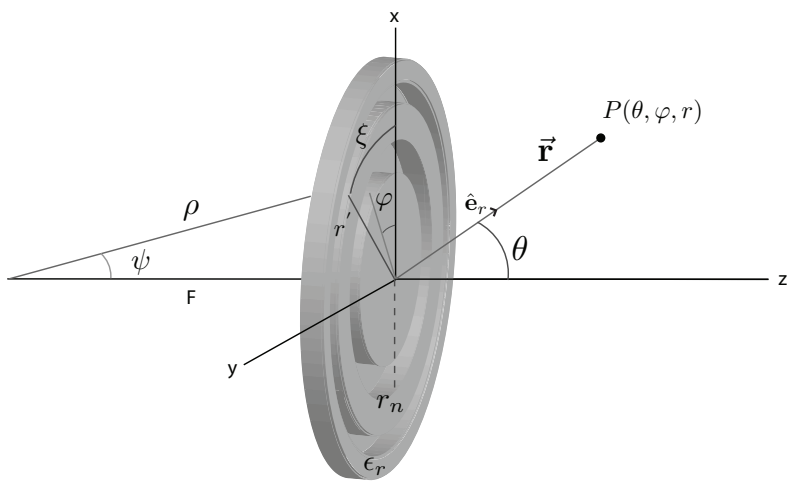

Figure A.1: Geometry of the grooved dielectric WZP.

where the transmission through, and reflection from, a given dielectric zone

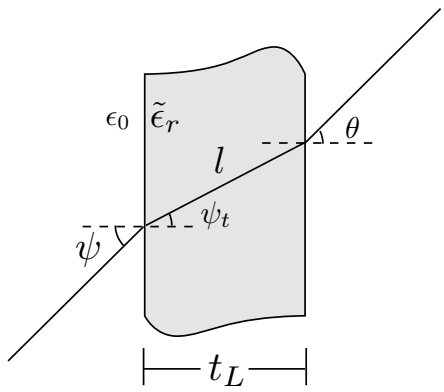

Figure A.2: Depiction of a propagating beam transmitting through a dielectric zone

is depicted in Figure A.2:

Transmission through the dielectric slab is determined by the standard Fresnel transmission and reflection coefficients t, r; the polarisation dependent reflection coefficients (oblique incidence) are given by[1] [88, 108, 246]

$$r_{\mathrm{E}} = \frac{\cos\psi - \sqrt{\tilde{\epsilon}_r - \sin^2\psi}}{\cos\psi + \sqrt{\tilde{\epsilon}_r - \sin^2\psi}} \tag{A.1}$$

$$r_{\mathrm{M}} = \frac{\tilde{\epsilon}_r\cos\psi - \sqrt{\tilde{\epsilon}_r - \sin^2\psi}}{\tilde{\epsilon}_r\cos\psi + \sqrt{\tilde{\epsilon}_r - \sin^2\psi}}, \tag{A.2}$$

where subscripts E, M correspond to the electric (perpendicular) and magnetic (parallel) polarisations respectively; the angle ψ defines the input angle from the feed. The corresponding transmission coefficient is the series convergence of the infinite sum of internal reflections [88, 108], and is given by

$$t_{E,M} = \frac{s_d(1 - r_{E,M}^2)}{1 - r_{E,M}^2 s_d^2 s_a}, \tag{A.3}$$

where s_d defines the phase delay through the dielectric for a pathlength, l, and s_a defines the pathlength change to the far-field point; both are defined as [88, 108]

[1] typographical error in [246]

$$s_d = \exp\left(\frac{-jk\tilde{\epsilon}_r t_L}{\sqrt{\tilde{\epsilon}_r - \sin^2\psi}}\right) \tag{A.4}$$

and

$$s_a = \exp\left(\frac{2jkt_L \sin^2\psi}{\sqrt{\tilde{\epsilon}_r - \sin^2\psi}}\right), \tag{A.5}$$

with

$$k = \frac{2\pi}{\lambda}, \tag{A.6}$$

where the dielectric thickness $t_L = t_{\text{base}} + w$, for groove depth w, (2.8), which has been substituted for the effective path length, l, using the relation:

$$l = \frac{t_L}{\cos\psi_t} \tag{A.7}$$

$$= \frac{t_L\sqrt{\tilde{\epsilon}_r}}{\sqrt{\tilde{\epsilon}_r - \sin\psi}}, \tag{A.8}$$

arising from the geometry depicted in Figure A.2; the following relations hold

$$\cos\psi_t = \frac{\sqrt{\tilde{\epsilon}_r - \sin^2\psi}}{\sqrt{\tilde{\epsilon}_r}} \tag{A.9}$$

$$\sin\psi = \sqrt{\tilde{\epsilon}_r}\sin\psi_t. \tag{A.10}$$

The amplitude divergence factor, detailing the field fall-off at the output plane of the aperture, includes propagation through both free-space, ρ, and the permittivity of the WZP zones, and can be written as [121]

$$L(\psi) = \rho + l\sqrt{\tilde{\epsilon}_r} \tag{A.11}$$

$$= \frac{F}{\cos\psi} + \frac{\tilde{\epsilon}_r t_L}{\sqrt{\tilde{\epsilon}_r - \sin^2\psi}}, \tag{A.12}$$

with focal length, F.

Calculation of the far-field is simplified by adopting spherical coordinates, which leads to the following unit vectors:

$$\hat{\mathbf{e}}_\xi = \begin{pmatrix} -\sin\xi \\ \cos\xi \\ 0 \end{pmatrix}, \quad \hat{\mathbf{e}}_\psi = \begin{pmatrix} \cos\xi\cos\psi \\ \sin\xi\cos\psi \\ -\sin\psi \end{pmatrix}, \quad \hat{\mathbf{e}}_r = \begin{pmatrix} \sin\theta\cos\varphi \\ \sin\theta\sin\varphi \\ \cos\theta \end{pmatrix} \tag{A.13}$$

where $\hat{\mathbf{e}}_\psi$ and $\hat{\mathbf{e}}_\xi$ are unit vectors in the frame of the input feed, and $\hat{\mathbf{e}}_r$ denotes the unit vector in the far-field observation point, $P(r, \theta, \varphi)$; the unit normal vector of the zone plate is given as

$$\hat{\mathbf{n}} = \begin{pmatrix} 0 \\ 0 \\ 1 \end{pmatrix}. \tag{A.14}$$

Using the expression for the polarisation vector, $\vec{\mathbf{P}}_d(\psi, \xi)$, which is defined for a Huygen's source, (2.14):

$$\vec{\mathbf{P}}_d(\psi, \xi) = -t_M \cos\xi \cdot \hat{\mathbf{e}}_\psi + t_E \sin\xi \cdot \hat{\mathbf{e}}_\xi;$$

the product $\hat{\mathbf{n}}$ x $\vec{\mathbf{P}}_d(\psi, \xi)$ can then be shown to yield

$$\hat{\mathbf{n}} \text{ x } \vec{\mathbf{P}}_d(\psi, \xi) = \begin{pmatrix} [t_M \cos\psi - t_E]\sin\xi\cos\xi \\ -t_M \cos\psi\cos^2\xi - t_E \sin^2\xi \\ 0 \end{pmatrix}. \tag{A.15}$$

The radial vector in spherical coordinates is given by

$$\vec{r} = \begin{pmatrix} r' \sin\psi\cos\xi \\ r' \sin\psi\sin\xi \\ 0 \end{pmatrix}, \tag{A.16}$$

for the general radial length, r', which yields the following vectors:

$$\vec{r}^{\,'} = \begin{pmatrix} F\tan\psi\cos\xi \\ F\tan\psi\sin\xi \\ 0 \end{pmatrix} \tag{A.17}$$

$$\vec{r}^{\,''} = \begin{pmatrix} \left[F\tan\psi + \frac{\epsilon_r t_L \sin\psi}{\sqrt{\tilde{\epsilon}_r - \sin^2\psi}}\right]\cos\xi \\ \left[F\tan\psi + \frac{\tilde{\epsilon}_r t_L \sin\psi}{\sqrt{\tilde{\epsilon}_r - \sin^2\psi}}\right]\sin\xi \\ 0 \end{pmatrix} \tag{A.18}$$

for the input, $r^{'} = \rho(\psi)$, and output, $r^{'} = L(\psi)$, planes of the zone plate. The far-field product $\hat{\mathbf{e}}_r \cdot \vec{r}^{\,''}$, can be shown to yield

$$\hat{\mathbf{e}}_r \cdot \vec{r}^{\,''} = \sin\theta \left(F\tan\psi + \frac{\tilde{\epsilon}_r t_L \sin\psi}{\sqrt{\tilde{\epsilon}_r - \sin^2\psi}}\right)\cos(\xi - \varphi); \tag{A.19}$$

where finally, the aperture area element in spherical coordinates is given by

$$\mathrm{d}A'' = L^2(\psi)\sin\psi\ \mathrm{d}\psi\mathrm{d}\xi. \tag{A.20}$$

Hence, substituting (A.1) – (A.20) into the general far-field expression, (2.15):

$$\vec{\mathbf{E}}_d(\theta,\varphi) = C_f(r)\hat{\mathbf{e}}_r(\theta,\varphi) \times \iint_{A'} \left[\hat{\mathbf{n}} \times \vec{\mathbf{P}}_d(\psi,\xi)\right] \frac{e^{-jkL(\psi)}}{L(\psi)} e^{jk\hat{\mathbf{e}}_r(\theta,\varphi)\cdot\hat{\mathbf{r}}''} \mathrm{d}A^{''},$$

yields the general form for the far-field electric field vector

$$\begin{aligned} \vec{E}_d(\theta,\varphi) &= C_f(r)\hat{\mathbf{e}}_r(\theta,\varphi) \\ &\times \int_0^{2\pi}\int_{\psi_m}^{\psi_{m+1}} \begin{pmatrix} [t_M\cos\psi - t_E]\cos\xi\sin\xi \\ -t_M\cos\psi\cos^2\xi - t_E\sin^2\xi \\ 0 \end{pmatrix} \ldots \\ &\quad O_d(\psi)e^{M_d(\psi)}e^{jN_d(\theta,\psi)\cos(\xi-\varphi)}\mathrm{d}\psi\mathrm{d}\xi, \end{aligned} \tag{A.21}$$

where $M_d(\psi), N_d(\theta,\psi), O_d(\psi)$ have been defined in the main text: (2.20) – (2.22):

$$M_d(\psi) = -jkL(\psi) \tag{A.22}$$

$$N_d(\theta,\psi) = k\sin\theta\left(F\tan\psi + \frac{\tilde{\epsilon}_r t_L \sin(\psi)}{\sqrt{\tilde{\epsilon}_r - \sin^2\psi}}\right) \tag{A.23}$$

$$O_d(\psi) = \sqrt{G_f(\psi,m)}\left(F\tan\psi + \frac{\tilde{\epsilon}_r t_L \sin(\psi)}{\sqrt{\tilde{\epsilon}_r - \sin^2\psi}}\right) \tag{A.24}$$

Solving (A.21) requires performing the ξ integral analytically for each vector component, where the full solution, i.e. ψ integral, requires numerical methods. The ξ integral is then performed analytically as follows: collecting the partial constants in ψ, which gives the temporary constants

$$A(\psi) = t_M \cos\psi\ O_d(\psi)e^{M_d(\psi)} \tag{A.25}$$

$$B(\psi) = t_E\ O_d(\psi)e^{M_d(\psi)}; \tag{A.26}$$

and performing the integral over $-\pi \rightarrow +\pi$, thus removing odd terms, the ith vector component of (A.21), with the vector notation:

$$\begin{pmatrix} i \\ j \\ 0 \end{pmatrix} \tag{A.27}$$

can be shown to yield

$$(A-B)\sin 2\varphi \int_0^{\pi} \cos 2\xi e^{jN_d(\theta,\psi)\cos\xi}\ \mathrm{d}\xi \tag{A.28}$$

where an offset angle $\Delta = +\varphi$ has been included to simplify the exponent dependency. Noting that (A.28) is a standard integral whose solution is a second order Bessel function, of the first kind, $J_2(N_d(\theta,\psi))$, the analytical solution, in ξ, for the ith vector component then becomes:

$$(A-B)\sin 2\varphi \int_0^{\pi} \cos 2\xi e^{jN_d(\theta,\psi)\cos\xi} \mathrm{d}\xi = (A-B)\sin 2\varphi J_2(N_d(\theta,\psi)). \quad \text{(A.29)}$$

Repeating for the jth vector component requires solving two integral components; the first can be shown to give the pair

$$-A\int_0^{\pi} e^{jN_d(\theta,\psi)\cos\xi}\mathrm{d}\xi \quad \text{(A.30)}$$

$$-A\cos 2\varphi \int_0^{p} i\cos 2\xi e^{jN_d(\theta,\psi)\cos\xi}\mathrm{d}\xi, \quad \text{(A.31)}$$

whose solutions are the zeroth and second order Bessel functions of the first kind, giving

$$-A\int_0^{\pi} e^{jN_d(\theta,\psi)\cos\xi}\mathrm{d}\xi = \pi A J_0(N_d(\theta,\psi)) \quad \text{(A.32)}$$

$$-A\cos 2\varphi \int_0^{p} i\cos 2\xi e^{jN_d(\theta,\psi)\cos\xi}\mathrm{d}\xi = -\pi A\cos 2\varphi J_2(N_d(\theta,\psi)). \quad \text{(A.33)}$$

The second pair can similarly be shown to yield

$$-B\int_0^{\pi} e^{jN_d(\theta,\psi)\cos\xi}\mathrm{d}\xi = \pi B J_0(N_d(\theta,\psi)) \quad \text{(A.34)}$$

$$+B\cos 2\varphi \int_0^{p} i\cos 2\xi e^{jN_d(\theta,\psi)\cos\xi}\mathrm{d}\xi = -\pi B\cos 2\varphi J_2(N_d(\theta,\psi)). \quad \text{(A.35)}$$

Hence, substituting back into (A.21), we get

$$\vec{E}_d(\theta,\varphi) = C_f(r)\hat{\mathbf{e}}_r(\theta,\varphi) \times \int_{\psi_m}^{\psi_{m+1}} \ldots$$
$$\ldots \begin{pmatrix} -\pi\sin 2\varphi(A-B)J_2(N_d(\theta,\psi)) \\ \pi(-A-B)J_0(N_d(\theta,\psi)) + \pi(A-B)\cos 2\varphi J_2(N_d(\theta,\psi)) \\ 0 \end{pmatrix} \mathrm{d}\psi \quad \text{(A.36)}$$

where A, B are given above.

Finally, performing the cross product yields the general vectorial form of the electric far-field, where the components θ and φ are obtained by performing the dot product as defined by (2.17):

$$\mathbf{E}(\mathbf{r}, m) = \mathbf{E}_\theta(\mathbf{r}, m) \cdot \hat{\mathbf{e}}_\theta + \mathbf{E}_\varphi(\mathbf{r}, m) \cdot \hat{\mathbf{e}}_\varphi;$$

noting that the unit far-field vectors in θ, φ are given in spherical coordinates by

$$\hat{\mathbf{e}}_\theta = \begin{pmatrix} \cos\theta\cos\varphi \\ \cos\theta\sin\varphi \\ -\sin\theta \end{pmatrix}, \qquad \hat{\mathbf{e}}_\varphi = \begin{pmatrix} -\sin\varphi \\ \cos\varphi \\ 0 \end{pmatrix}, \tag{A.37}$$

the solutions can then be shown to yield (2.18) and (2.19):

$$\begin{aligned} E_\theta(\theta, \varphi) &= -\pi C_f \cos\varphi \sum_m \int_{\psi_m}^{\psi_{m+1}} O_d(\psi) e^{M_d(\psi)} I_\theta(\theta, \psi) \mathrm{d}\psi \\ E_\varphi(\theta, \varphi) &= -\pi C_f \sin\varphi \cos\theta \sum_m \int_{\psi_m}^{\psi_{m+1}} O_d(\psi) e^{M_d(\psi)} I_\varphi(\theta, \psi) \mathrm{d}\psi \end{aligned}$$

with

$$\begin{aligned} I_\theta(\theta, \psi) &= -(t_M \cos\psi + t_E) J_0[N_d(\theta, \psi)] \ldots \\ &\qquad +(t_M \cos\psi - t_E) J_2[N_d(\theta, \psi)] \qquad \text{(A.38)} \\ I_\varphi(\theta, \psi) &= (t_M \cos\psi + t_E) J_0[N_d(\theta, \psi)] \ldots \\ &\qquad +(t_M \cos\psi - t_E) J_2[N_d(\theta, \psi)], \qquad \text{(A.39)} \end{aligned}$$

where $J_0[x], J_2[x]$ are the zeroth and second order Bessel functions of the first kind, of argument x, respectively.

The solutions can then be found numerically using the *quadgk* function in Matlab, giving the results presented in the main text.

appendix B

Efficiency expressions for the grooved WZP

The following gives the expressions for the efficiency components of the grooved dielectric Wood zone plate, discussed in the main text. The following solutions have been derived based on the original formulation presented in [108], which describes the Wood-Wiltse zone plate model.

B.1 Spillover efficiency, η_s

The spillover efficiency is defined as: "*ratio of the power radiated by the feed that reaches the antenna surface, and the total power radiated by the feed*", and is given by

$$\eta_s = \frac{\int_0^{\psi_0} G_f(\psi)\mathrm{d}\psi}{\int_0^{\pi} G_f(\psi)\ \mathrm{d}\psi}. \tag{B.1}$$

The spillover efficiency is independent of the zone plate details, and is defined, only, by the subtended angle of the antenna aperture, which is given by

$$\psi_0 = \tan\left(\frac{D}{2F}\right).$$

B.2 Phase efficiency, η_p

The phase efficiency is defined as: "*the ratio of the radiated power in the forward direction and the radiated power in the forward direction on the condition that the phase of the field in the antenna aperture is constant*", and is given by

$$\eta_p = \left| \frac{\sum_n \int_{\psi_n}^{\psi_{n+1}} (t_M \cos\psi + t_E) O_d(\psi) e^{M_d(\psi)} \, \mathrm{d}\psi}{\sum_n \int_{\psi_n}^{\psi_{n+1}} |t_M \cos\psi + t_E| O_d(\psi) \, \mathrm{d}\psi} \right|^2 , \tag{B.2}$$

where $t_{M,E}, M_d(\psi), O_d(\psi)$ are defined by (A.3), (2.20) and (2.22) respectively.

B.3 Illumination efficiency, η_i

The illumination efficiency defines the distribution of the field over the antenna surface, and is given by

$$\eta_i = \frac{1}{\eta_s} \left| \frac{1}{D} \sum_n \int_{\psi_n}^{\psi_{n+1}} |t_M \cos\psi + t_E| O_d(\psi) \, \mathrm{d}\psi \right|^2 , \tag{B.3}$$

where D denotes the zone plate aperture size.

B.4 Aperture Efficiency, η

The total aperture efficiency is then the product of the above efficiencies: $\eta = \eta_s \cdot \eta_p \cdot \eta_i$, which can be readily observed to be defined as

$$\eta = \left| \frac{1}{D} \sum_n \int_{\psi_n}^{\psi_{n+1}} |t_M \cos\psi + t_E| O_d(\psi) e^{M_d(\psi)} \, \mathrm{d}\psi \right|^2 , \tag{B.4}$$

all terms retaining the usual meanings.

appendix C

3D plasma distribution based on the top-hat function

The following equations define the solutions to the transform performed in Chapter 3, but with a 'top-hat' illumination function. As a result of the discontinuity in the illumination function, this solution is subject to long numerical integration times, and Gibbs phenomenon. In certain circumstances Gibbs oscillations can mask particular features which are of interest. The following has been included for completeness.

The generation function, $G(r, z)$, for a top-hat function can be defined as

$$G(r, z) = \begin{cases} 1 & \text{if } 0 \leq r \leq a \\ 0 & \text{otherwise} \end{cases} . \tag{C.1}$$

Substituting into (3.16):

$$D_a \nabla^2 \Delta n(r, z) - \frac{\Delta n(r, z)}{\tau_a} = -G(r, z),$$

gives

$$D_a \nabla^2 \Delta n(r,z) - \frac{\Delta n(r,z)}{\tau_a} = -g\Theta(r)\exp(-\alpha z), \tag{C.2}$$

where $\Theta(r)$ denotes the radial top-hat function. Converting to a dimensionless form using the following parameters, as per the main text: $\rho = r/L_a$, $\xi = z/L_a$, $\varepsilon = \alpha_\lambda L_a$, $\delta n = g\tau_a$, $h(\rho,\xi) = \Delta n(r,z)/\delta n$, with $\eta = a/L_a$ for the top-hat function, and noting the following Hankel transform for the top-hat function [154]

$$\int_0^\infty \rho J_0(\nu\rho)\Theta(r)\mathrm{d}\rho = \frac{\eta J_1(2\pi\eta\nu)}{\nu}, \tag{C.3}$$

the dimensionless continuity equation becomes in Hankel space (c.f. (3.20))

$$\frac{\mathrm{d}^2}{\mathrm{d}\xi^2}\bar{h}(\nu,\xi) - (\nu^2+1)\bar{h}(\nu,\xi) = -\frac{\eta J_1(2\pi\eta\nu)}{\nu}\exp(-\varepsilon\xi). \tag{C.4}$$

This is solved to give the sum of a homogeneous and particular solution, with the general form

$$\bar{h}(\nu,\xi) = A_1 e^{\left(-\xi\sqrt{\nu^2+1}\right)} + A_2 e^{\left(\xi\sqrt{\nu^2+1}\right)} + A_p e^{(-\varepsilon\xi)}, \tag{C.5}$$

where the particular coefficient, A_p, is given as

$$A_p = -\frac{1}{\varepsilon^2}\left[\frac{\eta J_1(2\pi\eta\nu)}{\nu} + (\nu^2+1)\right]. \tag{C.6}$$

Using the boundary conditions of (3.27):

$$\begin{aligned} S_0\bar{h}(\nu,\xi=0) &= \chi\frac{\partial}{\partial\xi}\bar{h}(\nu,\xi)\bigg|_{\xi=0} \\ S_b\bar{h}(\nu,\xi=b) &= -\chi\frac{\partial}{\partial\xi}\bar{h}(\nu,\xi)\bigg|_{\xi=b}, \end{aligned}$$

the homogeneous coefficients, A_1, A_2 can be shown to give

$$A_2 = A_p \frac{(S_0+\chi\varepsilon)(S_b-\chi\varpi)e^{-b\varpi}+(\chi\varepsilon-S_b)(S_0+\chi\varpi)e^{-\varepsilon b}}{(S_b+\chi\varpi)(S_0+\chi\varpi)e^{b\varpi}-(S_0-\chi\varpi)(S_b-\chi\varpi)e^{-b\varpi}} \quad \text{(C.7)}$$

$$A_1 = -\frac{A_2(S_0-\chi\varpi)+A_p(S_0+\chi\varepsilon)}{S_0+\chi\varpi} \quad \text{(C.8)}$$

with the following constant added for simplicity, as per the main text:

$$\varpi = \sqrt{\nu^2+1},$$

where [153]

$$\chi = \frac{L_a}{\tau_a},$$

and with the front and rear surface recombination velocities S_0, S_b.

Figure C.1 displays the excess carrier profile for an optically excited silicon wafer. The simulations were performed using the following parameters: a = 3 cm, Dia = 5 cm, $t_{si} = 500\ \mu\mathrm{m}$, $\tau_{\mathrm{eff}} = 10\ \mu\mathrm{s}$, $\lambda = 800\ \mathrm{nm}$, $P_{\mathrm{opt}} = 100\ \mathrm{mW/cm^2}$, and with $S_0 = S_d = 0\ \mathrm{cm/s}$. The excited plasma distribution is shown to feature oscillations, which are artefacts of the discontinuous top-hat function.

Ignoring the oscillations, the plasma profile is shown to be uniform radially, as one would expect, with a gradual drop in plasma density throughout the thickness of the wafer. The effective plasma depth is shown to be approximate to that defined by the diffusion length, $175\ \mu\mathrm{m}$ in this case, arising from the condition $\alpha L_a \gg 1$, as outlined in the main text, i.e. diffusion is non-negligible.

Radially the plasma profile is shown to equal the width of the initial top-hat function, resulting from negligible radial diffusion, i.e. $a \gg L_a$. Simulating the case in which radial diffusion dominates, did not always produce clear results due to Gibbs oscillations, thus interpretation of these results was often difficult. For these reasons, the main text focused on a continuous function in order to highlight the significance of the diffusion length and the corresponding plasma resolution.

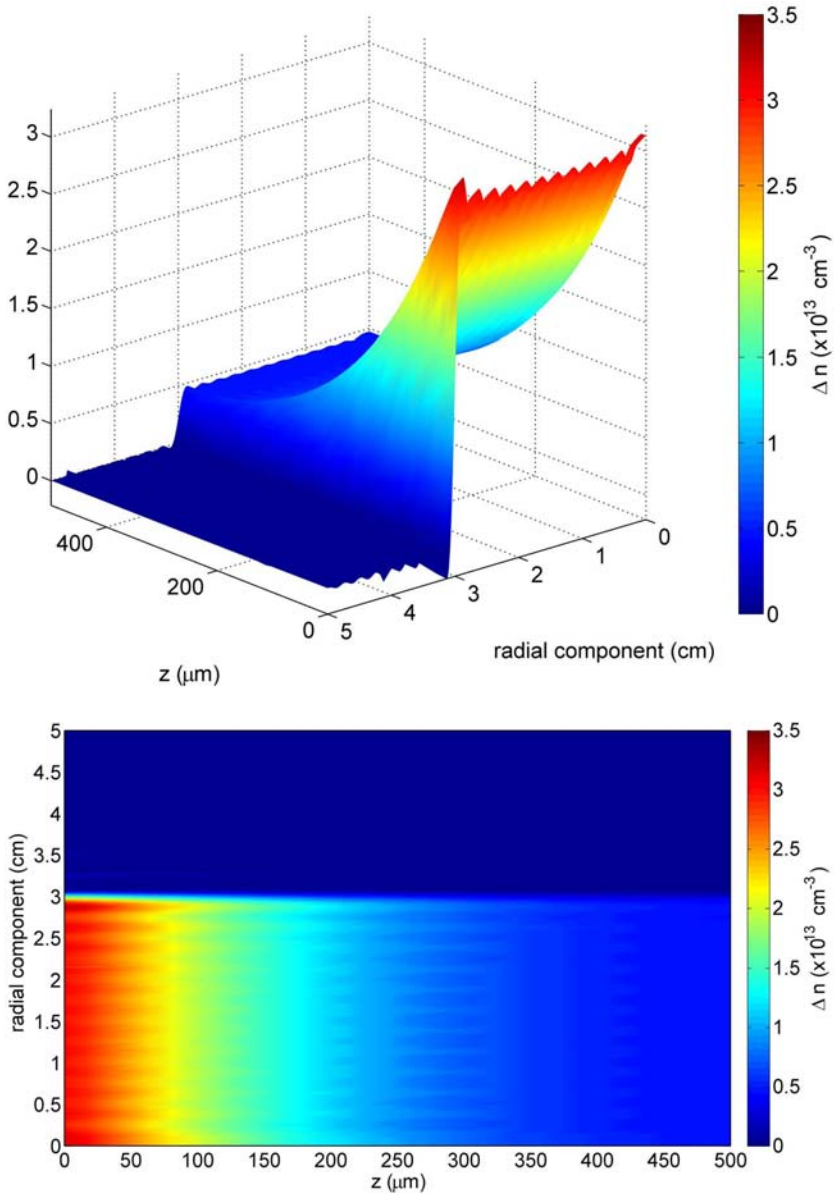

Figure C.1: Simulated plasma profile for a top-hat illumination function. The top-hat width, a, was 3 cm; the diameter of the wafer, Dia, was 5 cm, which was $500\ \mu\mathrm{m}$ thick.

appendix D

The reference phase parameter

The reference phase parameter enables control of the mainlobe phase, whilst also improving the zone plate performance. The following discussion introduces the reference phase parameter and its effects. Initial results are also presented for a transmission-type piFZPA with non-zero reference phase values.

D.1 Reference phase concept

The reference phase [247], or radius [248], provides a method for optimising the design of Fresnel zone plates, based on an improved zoning rule, which has shown greater potential than previous schemes [115, 249]. The improved scheme originates from the way in which zone plates are conventionally designed, where traditionally the zone plate design is referenced to the shortest pathlength connecting zone plate foci, which was treated as a $0°$ phase reference by Fresnel and carried forward thereafter [250]. However, modification of this approach can yield improvements to the zone plate performance.

Previous discussions have indicated that the choice of the reference phase may be arbitrary, chosen to assume any value between $0°$ and $360°$ [247, 251].

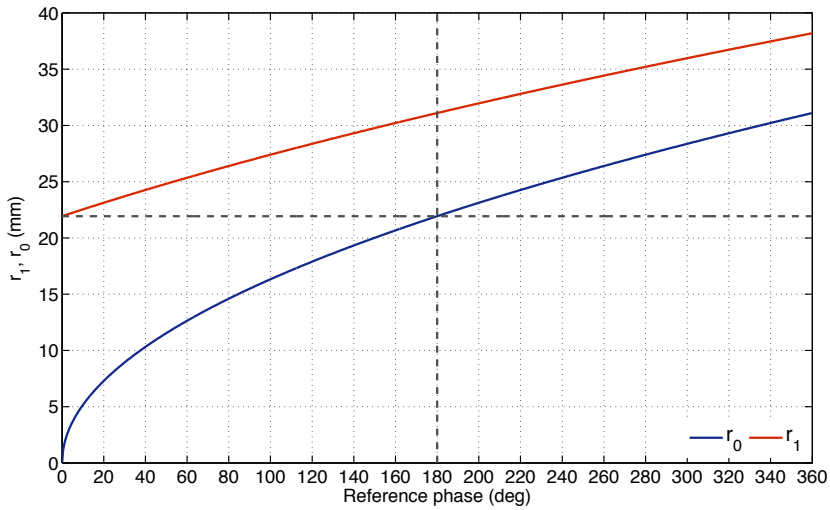

Figure D.1: Calculation of the reference radius, r_0, and comparison to the first Fresnel zone radius, r_1, as a function of reference phase ϕ_{ref}. Comparison of both radii indicate that the reference phase should assume any value between $0°$ and $180°$ in order to reduce loss through apodization.

However, limitations such that the reference radius, r_0, assumes dimensions less than the first Fresnel zone radius, r_1 [250], restrict the reference phase to values between $0°$ and $180°$, as illustrated in Figure D.1.

A non-zero reference phase (radius) results in adjustments to the first, and thus successive, zones such that they no longer coincide with Fresnel half-wave boundaries; and if chosen appropriately can reduce the phase error across the first zone. Control of the reference phase then permits optimisation of a range of zone plate features [252]. Various studies [247, 250–254] have shown control over the zone plate performance through an appropriate choice of this reference parameter, which lends their suitability for a wide range of interesting applications.

The reference phase and radius approaches have been developed separately, but have recently been joined [250, 254]; both approaches have been shown to be related by

$$r_0 = \sqrt{\left(\frac{\phi_{\mathrm{ref}}\lambda}{360°} + F\right)^2 - F^2}, \tag{D.1}$$

with reference phase ϕ_{ref} (deg), wavelength λ, and focal length F. The classical zone plate equation (2.6) can then be modified to give

$$r_n = \left[\frac{2n\lambda}{P} \sqrt{F^2 + r_0^2} + \left(\frac{n\lambda}{P} \right)^2 + r_0^2 \right]^{1/2}, \tag{D.2}$$

where all terms have been previously defined. Using the Fresnel-Kirchoff diffraction integral for the SZP[1], the effects of a non-zero reference phase can be simulated.

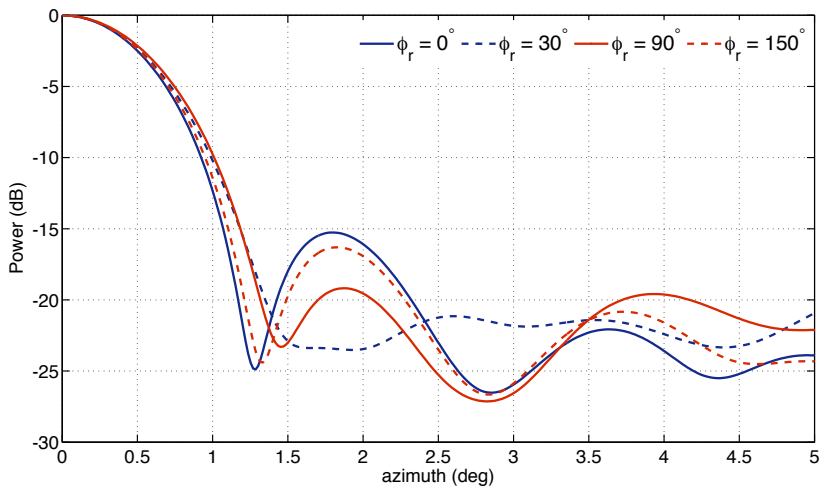

Figure D.2: Normalised numerical simulations of the 1D normalised far-field patterns for a 200mm aperture, F/1.5 *negative* SZP antenna with reference phase varying between $0°$ and $150°$. Non-zero reference phase values indicate the ability to further enhance the zone plate antenna performance, where an increase of 4 dB sidelobe suppression is observed for $\phi_{\text{ref}} = 30°$.

Figure D.2 displays the normalised far-field patterns for *negative* SZP designs featuring a 300 mm focal length, and 200 mm diameter (F/1.5). Simulations were performed with a -11 dB edge taper, over a range of reference phase values with $\phi_{\text{ref}} = 0°,\ 30°,\ 90°,\ 150°$. These simulations show that using this optimisation approach to improved zone plate designs, it is possible to alter the sidelobe level of the antenna with little change in other parameters; a 2 dB gain variation, and less than 2% change in half-power

[1]the SZP was chosen for the reduced degree of freedom (design), but this technique is equally applicable to WZPs

beamwidth. Figure D.2 demonstrates a 4 dB improvement in sidelobe suppression, with a corresponding 2 dB increase in gain, although not shown in the figure, for an optimal reference phase of $30°$, albeit with a marginal increase in beamwidth.

Prior studies have indicated that ϕ_{ref} is unique to each zone plate design, and thus simulations are required in order to find the optimal value of ϕ_{ref} for a given F/D [252].

Improvements to the zone plate performance, plus the ability to alter the mainlobe phase, whilst keeping the phase of the sidelobe regions constant [250, 251, 254], may benefit a range of zone plate applications, such as: multipath fading mitigation [250, 255, 256], improved performance of non-circularly symmetric zone plates [78, 250, 257], increased efficiency of soft X-ray photon sieves [250], reduction of sidelobe clutter in radar and perimeter security systems [254], and potential phase modulated continuous wave (c.f. FMCW) radar applications [254]. The reference phase is thus a new and promising tool that extends a range of zone plate applications.

D.2 piFZPA with a non-zero reference phase

Applications that could benefit from continuous phase modulation of the mainlobe, such as multipath fading mitigation and secure communications, require a reconfigurable device. The following section details preliminary results obtained using a piFZPA with non-zero reference phase.

The following investigations were performed on the F/1.2 piFZPA antenna discussed previously (see Figure 6.6). The corresponding change in the antenna performance of the transmission-type piFZPA was analysed based on the measured principle H-plane pattern. The antenna patterns were measured in receive mode, with the transmitter fixed at $0°$ in the far-field, with wafer $w6$ as the substrate. The antenna measurements were performed over $\pm 15°$ in azimuth, at $0.25°$ increments. The FZP masks were generated using (5.21) with $0° \leq \phi_{ref} \leq 360°$; Figure D.3 displays a set of the resulting masks indicating the corresponding change to the zone plate mask as a result

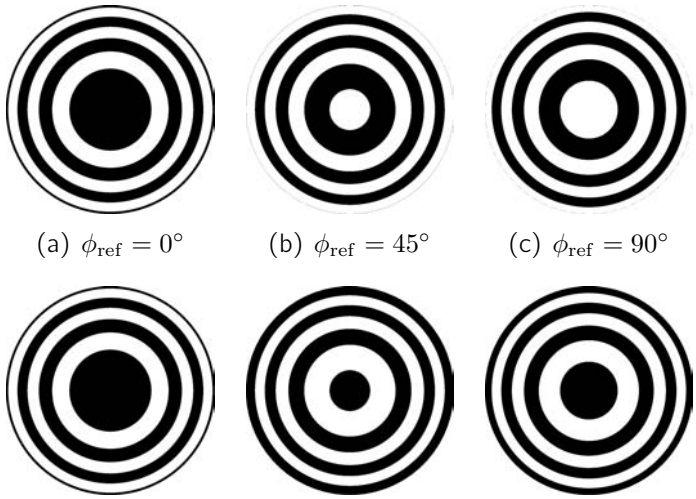

(a) $\phi_{\mathrm{ref}} = 0°$ (b) $\phi_{\mathrm{ref}} = 45°$ (c) $\phi_{\mathrm{ref}} = 90°$

(f) $\phi_{\mathrm{ref}} = 360°$ (e) $\phi_{\mathrm{ref}} = 270°$ (d) $\phi_{\mathrm{ref}} = 225°$

Figure D.3: Calculated zone plate masks for a range of reference phases, ϕ_{ref}.

of the non-zero reference phase; each mask is shown for an on-axis beam, i.e. $\theta_0 = 0°$.

Figure D.4(a) displays the measured gain and sidelobe level for the F/1.2 piFZPA over the full reference phase range. The measured peak power is shown to fall by up to 7 dB as the reference phase increases from $0°$, with the minimum observed at $\phi_{\mathrm{ref}} = 220°$. The gain loss results from increased blockage of the central zone, i.e. as the *positive* zone plate design slowly transitions to the *negative* zone plate design. The increase in gain beyond $\phi_{\mathrm{ref}} = 220°$ results from an increased centrally transparent zone. While these trends agree with what would be expected (see Section D.1), the turning point is observed at $\phi_{\mathrm{ref}} = 220°$ instead of $\phi_{\mathrm{ref}} = 180°$. This is believed to result from pattern washout of the central zone.

The corresponding sidelobe level is also observed to vary as a function of reference phase, where only a marginal improvement (~ 1 dB) has be achieved for non-zero reference phases. The limited improvements, in comparison to the original discussion of Section D.1, is thought to arise from the large diffusion length of the substrate. The large increase in the sidelobe level in the range $200°$ to $260°$ arose from a spurious sidelobe appearing within the mainlobe region of the antenna patterns; the origin of this effect is currently

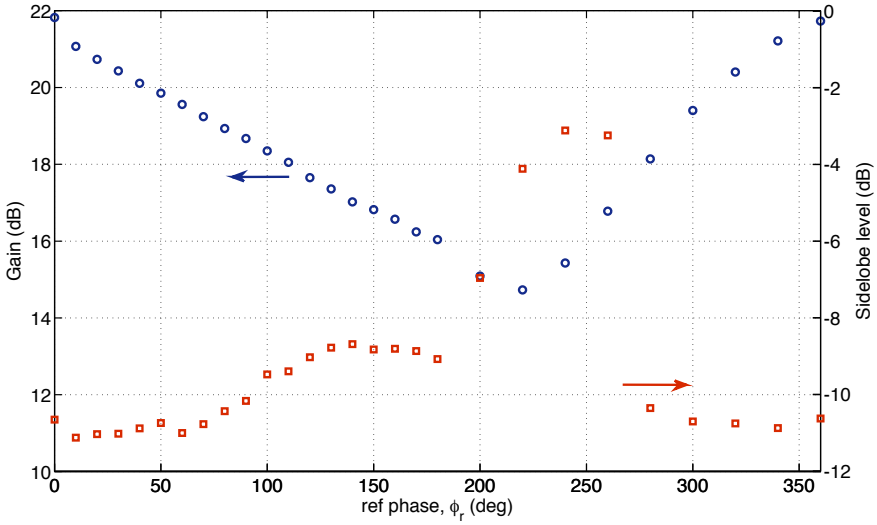

(a)

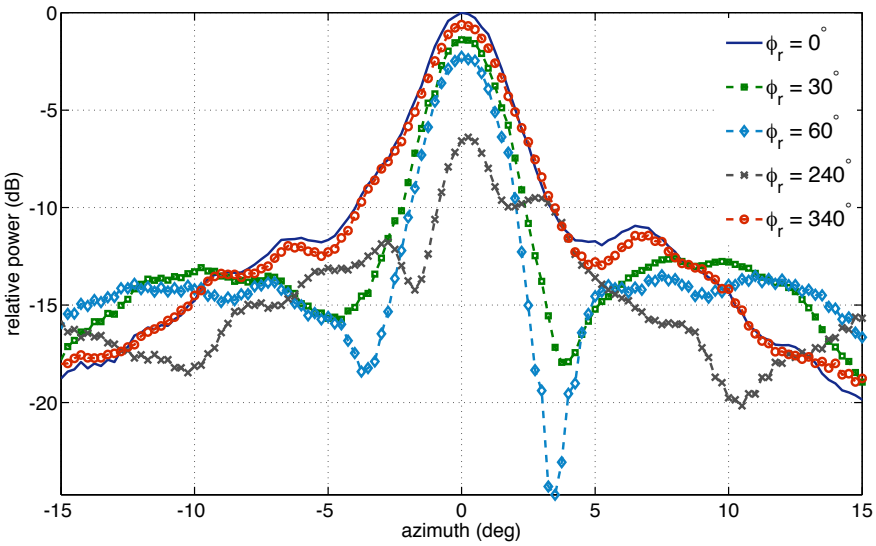

(b)

Figure D.4: (a) Measured change in gain and sidelobe level as a function of reference phase, ϕ_{ref}, and (b) measured H-plane patterns with a reference phase $\phi_{ref} = 0^\circ,\ 30^\circ,\ 60^\circ,\ 240^\circ$, and 340°.

unknown. Example H-plane patterns which were measured at various reference phase values are displayed in Figure D.4(b). The reduced beamwidth observed for $\phi_{\mathrm{ref}} = 30^\circ$ and 60° result from the *negative* zone plate design (see Chapter 2).

While larger improvements were observed in Section D.1, and have been demonstrated experimentally (at 35 GHz) for mechanical zone plates [250, 252, 254, 257], it is believed that the small changes in the zone masks which yield such improvements are limited, in practice, by the diffusion length of the substrate. Thus further work must be performed on lower lifetime wafers in order to realise the full potential of the reference phase parameter. Additional work is also required in order to ascertain the effects on the relative phase change in the mainlobe as a result of the plasma diffusion length, which has not been addressed here.

References

[1] P. Smulders, "Exploiting the 60 ghz band for local wireless multimedia access: prospects and future directions," *IEEE Communications magazine*, vol. 40, no. 1, pp. 140 – 147, 2002.

[2] D. G. Macfarlane, G. Wadge, D. A. Robertson, M. R. James, and H. Pinkerton, "Application of a portable topographic mapping millimetre wave radar to an active lava flow," *Geophysical Research Letters*, vol. 33, no. L03301, 2006.

[3] M. R. Fetterman, J. Grata, G. Jubic, W. L. Kiser, and A. Visnansky, "Simulation, acquisition and analysis of passive millimeter-wave images in remote sensing applicaitons," *Optics Express*, vol. 16, no. 25, pp. 20503 – 20515, 2008.

[4] G. Brooker, "A w-band airborne interrupted fmcw imaging radar," *Proceedings of SPIE*, vol. 5081, pp. 11 – 22, 2003.

[5] B. Korn and H.-U. Doehler, "Passive landing aids for precision EVS approach and landing," *22nd Digital Avionics Systems Conference*, vol. 2, pp. 9.D–1 – 9.1–8, 2003.

[6] L. Q. Bui, D. Uecker, E. Loose, and Y. Alon, "Test results of an experimental autonomous aircraft landing system utilizing a 94 GHz FM-CW imaging radar," *IEEE MTT-S International Microwave Symposium Digest*, vol. 2, pp. 857 – 860, 1993.

[7] A. Pagels, M. Hagelen, G. Briese, and A. Tessmann, "Helicopter assisted landing system - millimeter-wave against brown-out," *Proceedings of the German Microwave Conference*, pp. 1 – 3, March 2009.

[8] D. G. Mackrides, C. A. Schuetz, R. D. Martin, T. E. Dillon, P. Yao, and D. W. Prather, "Progress towards a video-rate passive millimeter-wave imager for brownout mitigation," *Passive Millimeter-Wave Imaging Technology XIV, Proc. of SPIE*, vol. 802203, pp. 1 – 7, 2011.

[9] S. Schmerwitz, N. Peinecke, U. Doehler, T. Lueken, and B. Korn, "Discussing millimeter wave pencil beam radar for terrain visualization," *IEEE/AIAA 30th Digital Avionics Systems Conference*, vol. 8D5, pp. 1 – 10, 2011.

[10] C. A. Martin, V. Kolinko, and J. A. Lovberg, "Millimeter-wave radar for brown-out landings using passive imager components," *Passive Millimeter-Wave Imaging Technology XIII, Proc. of SPIE*, vol. 7670, no. 767007, 2010.

[11] C. A. Shuetz, E. L. Stein, J. Samluk, D. G. Mackrides, J. P. Wilson, R. D. Martin, T. E. Dillon, and D. W. Prather, "Studies of millimeter wave phenomenology for helicopter brown-out mitigation," *Millimeter Wave and Terahertz Sensors and Technology II, Proc. of SPIE*, vol. 7485, no. 74850F, pp. 1 – 8, 2009.

[12] N. Yonemoto, A. Kohmura, and S. Futatsuomri, "76 GHz millimeter wave radar system for helicopter obstacle detection," *International Radar Symposium*, pp. 161 – 166, September 2011.

[13] R. Appleby, "Passive millimetre-wave imaging and how it differs from terahertz imaging," *Philosophical Transactions of The Royal Society A*, no. 362, pp. 379 – 392, 2004.

[14] R. Appleby and R. N. Anderton, "Millimetre-wave and submillimetre-wave imaging for security and surveillance," *Proceedings of the IEEE*, vol. 95, no. 8, pp. 1683 – 1690, 2007.

[15] R. Appleby and B. Wallacer, "Standoff detection of weapons and contraband in the 100GHz to 1THz region," *IEEE Antennas and Propagation Magazine*, vol. 55, no. 11, pp. 2944 – 2955, 2007.

[16] D. A. Wikner, "Progress in millimeter-wave imaging," *Proceedings of SPIE*, vol. 7936, no. 79360D, 2011.

[17] D. M. Sheen, D. L. McMakin, and T. E. Hall, "Three-dimensional millimeter-wave imaging for concealed weapon detection," *IEEE Transactions on Microwave Theory and Techniques*, vol. 49, no. 9, pp. 1581 – 1592, 2001.

[18] P. Corredoura, Z. Baharav, B. Taber, and G. Lee, "Millimeter-wave imaging system for personnel screening: scanning $10\hat{7}$ points a second using no moving parts," *Passive Millimeter-Wave Imaging Technology IX, Proc. of SPIE*, vol. 6211, no. 62110B, pp. 1 – 8, 2006.

[19] D. M. Sheen, D. L. McMakin, W. M. Lechelt, and J. W. Griffin, "Circularly polarized millimeter-wave imaging for personnel screening," *Passive Millimeter-Wave Imaging Technology VIII, Proc. of SPIE*, vol. 5789, pp. 1 – 10, 2005.

[20] C. T. Rodenbeck, M.-y. Li, and K. C. Chang, "A novel multibeam grating antenna with applications to low-cost millimeter-wave beam-steering," *IEEE MTT-S International Microwave Symposium Digest*, vol. 1, pp. 57 – 60, 2002.

[21] C. T. Rodenbeck, M.-y. Li, and K. C. Chang, "Design and analysis of a reconfigurable dual-beam grating antenna for low-cost millimeter-wave beam-steering," *IEEE Transactions on Antennas and Propagation*, vol. 52, no. 4, pp. 999 – 1006, 2004.

[22] H. Kamoda, T. Kuki, H. Fujikake, and T. Nomoto, "Millimeter-wave beam former using liquid crystal," *Electronics and Communicaitons in Japan, Part II*, vol. 88, no. 8, pp. 34 – 41, 2005.

[23] C. A. Schuetz, J. Murakowski, G. J. Schneider, and D. W. Prather, "Radiometric millimeter-wave detection via optical upconversion and carrier suppression," *IEEE Transactions on Microwave Theory and Techniques*, vol. 53, no. 5, pp. 1732 – 1738, 2005.

[24] M. Sterner, D. Chicherin, A. V. Raisanen, G. Stemme, and J. Oberhammer, "RF MEMS high-impedance tunable metamaterials for millimeter-wave beam steering," *IEEE 22nd International Conference on Micro Electro Mechanical Systems*, vol. 1, pp. 896 – 899, 2009.

[25] Z. Du, D. Chicherin, and A. V. Raisanen, "Millimeter wave beam steering with a MEMS-based high impedance surface," *Proceedings of the 41st European Microwave Conference*, vol. 1, pp. 1043 – 1046, 2011.

[26] M. Hoefle, M. Koeberle, A. Penirschke, and R. Jakoby, "Improved millimeter wave Vivaldi antenna array element with high performance liquid crystals," *36th International Conference on Infrared, Millimeter and Terahertz Waves (IRMMW-THz)*, vol. 1, pp. 1 – 2, 2011.

[27] A. A. Tamijani, L. Zhang, G. Pan, H. K. Pan, and H. Alavi, "Lens-enhanced phased array antenna systems for high directivity beam steering," *IEEE International Symposium on Antennas and Propagation*, vol. 1, pp. 3275 – 3278, 2011.

[28] A. Abdellatif and S. Safavi-Naeini, "Novel millimetre-wave low cost multi-beam dielectric grating antenna (mb-dga)," *36th International Conference on Infrared, Millimeter and Terahertz Waves (IRMMW-THz)*, pp. 1 – 2, 2011.

[29] D. Parker and D. C. Zimmermann, "Phased arrays – part I: Theory and architectures," *IEEE Transactions on Microwave Theory and Techniques*, vol. 50, no. 3, pp. 678 – 687, 2002.

[30] D. Parker and D. C. Zimmermann, "Phased arrays – part II: Implementations, applications, and future trends," *IEEE Transactions on Microwave Theory and Techniques*, vol. 50, no. 3, pp. 688 – 698, 2002.

[31] E. Carpentieri, U. F. D'Ella, E. De Stefano, L. Di Guida, and R. Vitiello, "Millimetre-wave phased array antennas," *IEEE Radar Conference*, vol. 1, pp. 1 – 5, 2008.

[32] M. F. Jahromi, *Optical and Microwave Beamforming for Phased Array Antennas*. PhD thesis, University of Waterloo, Canada, 2008.

[33] J. W. Kuo and Y. E. Wang, "A low cost wafer based w-band phased array," *IEEE Antennas and Propagation Society International Symposium*, pp. 1 – 4, July 2010.

[34] A. Babakhani, D. B. Rutledge, and A. Hajimir, "mm-wave phased arrays in silicon with integrated antennas," *IEEE Antennas and Propagation Society International Symposium*, pp. 4369 – 4372, June 2007.

[35] H. R. Raemer, *Radar Systems Principles*. CRC press, 1997.

[36] J. Shaker, M. R. Chaharmir, M. Cuhaci, and A. Ittipiboon, "Reflectarray research at the communications research centre canada," *IEEE Antennas and Propagation Magazine*, vol. 50, no. 4, pp. 31 – 52, 2008.

[37] S. Weiss and R. Dahlstrom, "Rotman lens development at the army research lab," *IEEE Aerospace Conference*, pp. 1 – 7, March 2006.

[38] D. G. Berry, R. G. Malech, and W. A. Kennedy, "The reflectarray antenna," *IEEE Transactions on Antennas and Propagation*, vol. 11, no. 6, pp. 645 – 651, 1963.

[39] S. Mueller, F. Goelden, P. Scheele, M. Wittek, C. Hock, and R. Jakoby, "Passive phase shifter for w-band applications using liquid crystals," *36th European Microwave Conference*, pp. 306 – 309, September 2006.

[40] R. Marin, *Investigations on Liquid Crystal Reconfigurable Unit Cells for mm-Wave Reflectarrays*. PhD thesis, Vom Fachbereich 18 Elecktrotechnik und Informationstechnick der Technischen Universitat Darmstadt, 2008.

[41] A. Luukanen, J. P. S. Ala-Laurinaho, D. Gomes-Martin, J. Hakli, P. Koivisto, P. Pursula, J. Saily, A. Tamminen, R. Tuovinen, and M. Sipila, "Rapid beamsteering reflectarrays for mm-wave and submm-wave imaging radars," *Proceedings of SPIE*, vol. 8022, no. 80220M, 2011.

[42] W. Rotman and R. Turner, "Wide-angle microwave lens for line source applications," *IEEE Transactions on Antennas and Propagation*, vol. 11, no. 6, pp. 623 – 632, 1963.

[43] E. O. Rausch and A. F. Peterson and W. Wiebach, "Electronically scanned millimeter wave antenna using a Rotman lens," *IEEE Radar Conference*, no. 449, pp. 374 – 378, 1997.

[44] E. O. Rausch, A. F. Peterson, and W. Wiebach, "Millimeter wave rotman lens," *IEEE National Radar Conference*, pp. 78 – 81, 1997.

[45] L. Hall, H. Hansen, and D. Abbott, "Rotman lens for mm-wavelengths," *Proceedings of SPIE*, vol. 4935, pp. 215 – 221, 2002.

[46] "2d millimeter-wave phased array radar." http://www.savium.com, Savium Technologies.

[47] W. Lee, Y. S. Kim, J. Km, and Y. J. Yoon, "Multi-layer beamforming lens antenna array with a new line design for millimeter-wave systems in package applications," *Proceedings of the 5th European Conference on Antennas and Propagation (EuCAP)*, pp. 2954 – 2958, April 2011.

[48] J.-G. Lee, J.-H. Lee, and H.-S. Tae, "Design of nonradiative dielectric Rotman lens in the millimeter wave frequency," *IEEE MTT-S International Microwave Symposium Digest*, vol. 1, pp. 551 – 554, 2001.

[49] L. Hall, H. Hansen, and D. Abbott, "Design and simulation of a high efficiency Rotman lens for mm-wave collision avoidance sensor," *Microelectronics Journal*, vol. 33, pp. 153 – 159, 2002.

[50] W. Platte, "An optimization of semiconductor film thickness in light-controlled microstrip devices," *Solid-State Electronics*, vol. 20, no. 1, pp. 57 – 60, 1977.

[51] W. Platte, "Diffusion-controlled decay of laser-excited photoconductivity in optoelectronic switches," *Electronic Letters*, vol. 13, no. 11, pp. 321 – 323, 1977.

[52] W. Platte, "Spectral dependence of microwave power transmission in laser-controlled solid-state microstrip switches," *Solid-state and electron devices*, vol. 2, no. 4, pp. 97 – 103, 1978.

[53] W. Platte, "Effective photoconductivity and plasma depth in optically qausi-CW controlled microwave switching," *IEE proceedings*, vol. 135, no. 3, pp. 251 – 254, 1988.

[54] W. Platte and B. Sauerer, "Optically cw-induced losses in semiconductor coplanar waveguides," *IEEE Transactions on Microwave Theory and Techniques*, vol. 37, no. 1, pp. 139 –149, 1989.

[55] A. M. Yurek, C. D. Striffler, and C. H. Lee, "Optoelectronic devices for millimeter waves," in *Infrared and Millimeter waves*, vol. 14 of *Millimeter components and techniques, part V*, pp. 249 – 290, Academic Press, 1985.

[56] W. Platte, "Optoelectronic microwave switching," *IEE proceedings*, vol. 132, no. 2, pp. 126 – 132, 1985.

[57] A. P. DeFonzo, C. H. Lee, and P. S. Mak, "Optically controllable millimeter wave phase shifter," *Applied physics letters*, vol. 35, no. 8, pp. 575 – 577, 1979.

[58] C. H. Lee, P. S. Mak, and A. P. DeFonzo, "Optical control of millimeter-wave propagation in dielectric waveguides," *IEEE Journal of Quantum Electronics*, vol. QE-16, no. 3, pp. 277 – 288, 1980.

[59] C. H. Lee, A. M. Vaucher, M. G. Li, and C. D. Striffler, "Ultrafast optoelectronic devices for millimeter-waves," *IEEE MTT-S International Microwave Symposium Digest*, vol. 1, pp. 103 – 105, 1983.

[60] A. M. Vaucher, C. D. Striffler, and C. H. Lee, "Theory of optically controlled millimeter-wave phase shifters," *IEEE Transactions on Antennas and Propagation*, vol. 31, no. 2, pp. 209 – 216, 1983.

[61] V. A. Manasson and L. S. Sadovnik, "Optically controlled phase shifter and phased array antenna for use therewith." Us Patent: No. 5694498, December 1997.

[62] C. H. Lee, P. S. Mak, and A. P. DeFonzo, "Millimetre-wave switching by optically generated plasma in silicon," *Electronic Letters*, vol. 14, no. 23, pp. 733 – 734, 1978.

[63] W. Platte, "Optical control of microwaves by led-induced dbr structures in silicon coplanar waveguides," *Electronic Letters*, vol. 25, no. 3, pp. 177 – 179, 1989.

[64] W. Platte, "Effect of surface recombination on microwave performance of laser-induced dbr gratings in silicon coplanar waveguides," *IEE proceedings*, vol. 139, no. 6, pp. 399 – 401, 1992.

[65] W. Platte, "Spectral dependence of light-induced microwave reflection coefficient from optoelectronic waveguide gratings," *IEEE Transactions on Microwave Theory and Techniques*, vol. 43, no. 1, pp. 106 – 111, 1995.

[66] V. A. Manasson, L. S. Sadovnik, A. Moussessian, and D. B. Rutledge, "Millimeter-wave diffraction by a photo-induced plasma grating," *IEEE Transactions on Microwave Theory and Techniques*, vol. 43, no. 9, pp. 2288 – 2290, 1995.

[67] V. A. Manasson, L. S. Sadovnik, and V. Yepishin, "Optically controlled scanning antennas comprising a plasma grating," *IEEE Antennas and*

Propagation Society International Symposium, vol. 2, no. 1, pp. 1228 – 1231, 1997.

[68] V. A. Manasson and L. S. Sadovnik and V. Yepishin, "Antenna with plasma-grating." US Patent: No. 5982334, November 1999.

[69] G. F. Brand, "Remote millimeter-wave beam control by the illumination of a semiconductor," *IEEE Transactions on Microwave Theory and Techniques*, vol. 48, no. 5, pp. 855 – 857, 2000.

[70] V. A. Manasson and L. S. Sadovnik, "Monolithic millimeter-wave beam-steering antenna." US Patent: No. 6313803, November 2001.

[71] M. R. Chaharmir, A. R. Sebak, J. Shaker, and M. Cuhaci, "Novel reflectarray antennas for beam steering," *22nd National Radio Science Conference (NRSC)*, vol. 1, pp. 17 – 34, 2005.

[72] M. R. Chaharmir, J. Shaker, M. Cuhaci, and A. R. Sebak, "Novel photonically-controlled reflectarray antenna," *IEEE Transactions on Antennas and Propagation*, vol. 54, no. 4, pp. 1134 – 1141, 2006.

[73] M. Khaldi, F. Podevin, and A. Vilcot, "Optically controlled microstrip phased arrays," *International Topical Meeting on Microwave Photonics*, vol. 1, pp. 193 – 196, 2005.

[74] G. W. Webb and L. H. Pinck, "Light-controlled mmw beam scanner," *SMBO International Microwave Conference Brazil*, pp. 417 – 422, 1993.

[75] G. W. Webb, S. C. Rose, M. S. Sanchez, and J. M. Osterwalder, "Experiments on an optically controlled 2-d scanning antenna," *Antenna Applications Sysmposium, Allerton Park, Monticello II*, September 16 - 18 1998.

[76] G. W. Webb, W. Vernon, M. S. Sanchez, S. C. Rose, and S. Angello, "Optically controlled millimeter wave antenna," *International Topical Meeting on Microwave Photonics*, pp. 275 – 278, 1999.

[77] G. W. Webb, S. Angello, W. Vernon, M. S. Sanchez, and S. C. Rose, "Novel photonically controlled antenna for MMW communication," *International Topical Meeting on Microwave Photonics*, pp. 97 – 100, September 2000.

[78] I. V. Minin and O. V. Minin, *Basic Principles of Fresnel Antenna Arrays*. Lecture Notes in Electrical Engineering 19, Springer, 2008.

[79] G. R. Folwes, *Introduction to Modern Optics*. Dover Publications Inc., 1989.

[80] J. Wiltse, "History and evolution of Fresnel zone plate antennas for microwaves and millimeter waves," *IEEE Antennas and Propagation Society International Symposium. 1999 Digest. Held in conjunction with: USNC/URSI National Radio Science Meeting (Cat. No.99CH37010)*, vol. 2, pp. 722–725, 1999.

[81] F. Wentworth, J. Wiltse, and F. Sobel, "Quasi-optical surface waveguide and other components for the 100- to 300-gc region," *IEEE Transactions on Microwave Theory and Techniques*, vol. 9, pp. 512–518, November 1961.

[82] P. F. Goldsmith, "Zone plate lens antennas for millimeter and submillimeter wavelengths," *The Third International symposium on Space Terahertz Technology*, pp. 345 – 361, 1992.

[83] M. H. A. J. Herben and H. Hristov, "Some developments in Fresnel zone plate lens antennas," *IEEE Antennas and Propagation Society International Symposium. 1999 Digest. Held in conjunction with: USNC/URSI National Radio Science Meeting (Cat. No.99CH37010)*, vol. 2, pp. 726–729, 1999.

[84] L. F. van Buskirk, "Zone plate radio transmission system." US Patent: No. 3189907, August 1965.

[85] G. Collinge and T. M. B. Wright, "Phase correcting reflection zone plate for focusing microwave." US Patent: No. 5389944, February 1995.

[86] G. Collinge, "Phase correcting zone plate." US Patent: No. 5486950, January 1996.

[87] K. F. Peterson, "Reflective Fresnel lens for sub-millimeter wave power distribution." US Patent: No. 7339551, March 2008.

[88] H. Hristov, *Fresnel Zones in wireless links, zone plate lenses and antennas*. Artech House Inc., 2000.

[89] Y. J. Guo and S. K. Barton, *Fresnel Zon Antennas*. Kluwer Academic Publishers, 2002.

[90] O. Minin and I. Minin, *Diffractional Optics of Millimetre Waves*. Series in Optics and Optoelectronics, IoP Publishing Ltd, 2004.

[91] I. V. Minin and O. V. Minin, "Fresnel zone plate lens and antennas for millimeter waves: history and evolutions of developments and applications," *25th International Conference on Infrared and Millimeter Waves*, pp. 409 – 410, 2000.

[92] D. Stigliani, R. Mittra, and R. G. Semonin, "Resolving power of a zone plate," *Journal of the Optical Society of America*, vol. 57, p. 610, 1967.

[93] B. Huder and W. Menzel, "Flat printed reflector antenna for mm-wave applications," *Electronic Letters*, vol. 24, no. 6, p. 318, 1988.

[94] M. Gouker and G. Smith, "A millimeter-wave integrated circuit antenna based on the Fresnel zone plate," *IEEE Transactions on Microwave Theory and Techniques*, vol. 40, no. 5, p. 968, 1991.

[95] Y. J. Guo, S. K. Barton, and T. M. B. Wright, "Design of high efficiency Fresnel zone plate antennas," *Antennas and Propagation Society Symposium 1991 Digest*, vol. 1, pp. 182–185, 1991.

[96] Y. J. Guo and S. K. Barton, "A high-efficiency quarter-wave zone plate reflector," *IEEE Microwave and Guided Wave Letters*, vol. 2, no. 12, 1992.

[97] Y. Guo and S. Barton, "Fresnel zone plate reflector incorporating rings," *IEEE Microwave and Guided Wave Letters*, vol. 3, pp. 417–419, 1993.

[98] D. R. Reid and G. S. Smith, "A full electromagnetic analysis for the soret and folded zone plate antennas," *IEEE Transactions on Antennas and Propagation*, vol. 54, pp. 3638–3646, 2006.

[99] J. E. Garrett and J. C. Wiltse, "Fresnel zone plate antennas at millimeter wavelengths," *International Journal of Infrared and Millimeter Waves*, vol. 12, no. 3, pp. 195 – 220, 1991.

[100] M. Young, "Zone plates and their abberations," *Journal of the Optical Society of America*, vol. 62, no. 8, p. 972, 1972.

[101] J. C. Wiltse, "Advanced zone plate antenna design," in *Terahertz and Gigahertz Electronics and Photonics II*, vol. 4111, pp. 201 – 209, proc. SPIE, 2000.

[102] J. Wiltse, "Analysis of the properties of large-angle zone plate antennas," *IEEE Antennas and Propagation Society International Symposium. 2001 Digest. Held in conjunction with: USNC/URSI National Radio Science Meeting (Cat. No.01CH37229)*, pp. 284–287, 2001.

[103] M. Sussman, "Elementary diffraction theory of zone plates," *American Journal of Physics*, vol. 28, no. 4, p. 394, 1960.

[104] O. E. Myers, "Studies of transmission zone plates," *American Journal of Physics*, vol. 19, p. 359, 1951.

[105] Y. J. Guo and S. K. Barton, "On the sidelobe performance of Fresnel zone plate antennas," *IEEE Antennas and Propagation Society International Symposium 1992 Digest*, vol. 4, pp. 2175–2178, 1992.

[106] C. F. Ye and W. X. Zhang, "On the radiation characteristics of the Fresnel zone plate antenna," *Antennas and Propagation Society International Symposium*, vol. 3, pp. 2236 – 2239, 1994.

[107] L. Leyten and M. H. A. J. Herben, "Vectorial far-field analysis of the Fresnel-zone plate antenna: a comparison with the parabolic reflector antenna," *Microwave and Optical Technology Letters*, vol. 5, no. 2, pp. 49 – 56, 1992.

[108] J. M. van Houten, "Analysis of phase correcting and elliptical Fresnel-zone plate antennas," Master's thesis, Eindhoven University of Technology, 1993.

[109] L. C. J. Baggen, "The Fresnel zone plate antenna: Design and analysis," Master's thesis, Eindhoven University of Technology, 1992.

[110] P. F. Goldsmith, *Qausioptical Systems*. Microwave Technology and Techniques, IEEE Press and Chapman & Hall, 1998.

[111] P. F. Goldsmith, "Quasi-optical techniques," *Proceedings of the IEEE*, vol. 80, no. 11, pp. 1729 – 1747, 1992.

[112] J. C. Wiltse, "Performance characteristics of phase-correcting Fresnel zone plates," *Microwave Symposium Digest, MTT-S International*, vol. 2, pp. 797 – 800, 1990.

[113] D. N. Black and J. C. Wiltse, "Millimeter-wave characteristics of phase-correcting Fresnel zone plates," *IEEE Transactions On Microwave Theory And Techniques*, vol. 35, no. 12, pp. 1122 – 1129, 1987.

[114] J. C. Wiltse, "High efficiency, high gain Fresnel zone plate antennas," in *Targets and Backgrounds: Characterization and Representation IV*, vol. 3375, pp. 286 – 290, proc. SPIE, 1998.

[115] P. D. Kearney and A. G. Klein, "Resolving power of zone plates," *Journal of Modern Optics*, vol. 36, pp. 261 – 267, 1989.

[116] A. Petosa and A. Ittipiboon, "Shadow blockage effects on the aperture efficiency of dielectric Fresnel lenses.," *IEE Proceedings Microwave antennas and propagation*, vol. 147, no. 6, pp. 451 – 454, 2000.

[117] D. R. Reid and G. S. Smith, "A comparison of the focusing properties of a Fresnel zone plate with a doubly-hyperbolic lens for application in a free-space, focused-beam measurement system," *IEEE Transactions on Antennas and Propagation*, vol. 57, no. 2, pp. 499 – 507, 2009.

[118] C. A. Barrett and J. C. Wiltse, "Design parameters for zone plate antennas," *Antennas and Propagation Society Symposium 1992 Digest*, vol. 1, pp. 608 – 611, 1992.

[119] L. P. Kamburov, H. D. Hristov, and R. Feick, "Optimum design of millimeter-wave doube-dielectric Fresnel zone-plate lens and antenna," *International Journal of Infrared and Millimeter Waves*, vol. 25, no. 2, pp. 301 – 316, 2004.

[120] D. R. Reid and G. S. Smith, "A full electromagnetic analysis of grooved-dielectric fresnel zone plate antennas for microwave and millimeter-wave applications," *IEEE Transactions on Antennas and Propagation*, vol. 55, no. 8, pp. 2138 – 2146, 2007.

[121] H. D. Hristov and M. H. A. J. Herben, "Millimeter-wave Fresnel-zone plate lens and antenna," *IEEE Transactions on Microwave Theory and Techniques*, vol. 43, pp. 2779–2785, 1995.

[122] H. D. Hristov and M. H. A. J. Herben, "Quarter-wave Fresnel zone planar lens and antenna," *IEEE Microwave and Guided Wave Letters*, vol. 5, pp. 249–251, 1995.

[123] I. V. Minin and O. V. Minin, "Beam control in Fresnel zone plate antennas," *Proceedings of the 9th Russian-Korean International Symposium on Sicence and Technology*, pp. 786 – 790, 2005.

[124] J. M. van Houten and M. H. A. J. Herben, "Analysis of phase-correcting Fresnel-zone plate antenna with dielectric/transparent zones," *Journal*

of Electromagnetic waves and Applications, vol. 8, no. 7, pp. 847 – 858, 1994.

[125] D. N. Black and J. C. Wiltse, "Millimter wave characteristics of Fresnel zone plates," *Microwave Symposium Digest, MTT-S International*, vol. 1, pp. 437 – 440, 1987.

[126] J. Sluijter, "Analysis of and measurements on basic configurations of the Fresnel zone plate antenna," Master's thesis, Eindhoven University of Technology, 1994.

[127] J. Sluijter, M. H. A. J. Herben, and O. J. G. Vullers, "Experimental validation of PO/UTD applied to Fresnel-zone plate antennas," *Microwave and Optical Technology Letters*, vol. 9, no. 2, pp. 111 – 113, 1995.

[128] S. Silver, ed., *Microwave Antenna Theory and Design*. IEE Electromagnetic Waves Series 19, Peter Peregrinus Ltd, 1987.

[129] "CST computer simulation technology AG." http://www.cst.com.

[130] R. I. Hunter, *Characterisation of Ferrite and Dielectric Materials and their use in Millimetre-wave Qausi-optical Devices*. PhD thesis, University of St Andrews, 2004.

[131] J. W. Lamb, "Miscellaneous data on materials for millimetre and submillimetre optics," *International Journal of Infrared and Millimeter Waves*, vol. 17, no. 12, pp. 1997 – 2034, 1996.

[132] A. Petosa and A. Ittipiboon, "Effects of Fresnel lens thickness on aperture efficiency," *ANTEM 2004*, pp. 175 – 178, Ottawa Cannada 2004.

[133] J. D. Kraus, *Antennas*. McGraw-Hill Series in Electical Engineering, McGraw-Hill, Inc, 1988.

[134] NPL, "A guide to power flux density and field strength measurement." The Institute of Measurement and control, ISBN 0 904457 39 7, 2004.

[135] A. W. Rudge, K. Milne, A. D. Olver, and P. Knight, eds., *The Handbook of Antenna Design*, vol. 1 of *IEE Electromagnetic Waves Series 15*. Peter Peregrinus Ltd, 1982.

[136] S. Rein, *Lifetime spectroscopy: A method of defect characterization in silicon for photo-voltaic applications*. Materials science, Springer, 2005.

[137] D. K. Schroder, "Carrier lifetimes in silicon," *IEEE Transactions on Electron Devices*, vol. 44, no. 1, pp. 160 – 170, 1997.

[138] D. K. Schroder, *Semiconductor Material and Device Characterisation*. Wiley-Interscience, third ed., 2006.

[139] C. Kittel, *Introduction to Solid State Physics*. John Wiley & Sons, seventh ed., 1996.

[140] W. Schockley and W. T. Read, "Statistics of the recombinations of holes and electrons," *Physical review*, vol. 87, no. 5, pp. 835 – 842, 1952.

[141] R. N. Hall, "Electron-hole recombination in Germanium," *Physical review*, vol. 87, p. 397, 1952.

[142] J. P. McKelvey, *Solid state and semiconductor physics*. Harper & Row, 1966.

[143] K. L. Luke and L.-J. Cheng, "Analysis of the interaction of a laser pulse with a silicon wafer: determination of bulk lifetime and surface recombination velocity," *Journal of Applied Physics*, vol. 61, no. 6, pp. 2282 – 2293, 1987.

[144] A. B. Sproul, "Dimensionless solution of the equation describing the effect of surface recombination on carrier decay in semiconductors," *Journal of Applied Physics*, vol. 76, no. 5, pp. 2851 – 2854, 1994.

[145] D. A. Neamen, *Semiconductor physics and devices*. McGraw-Hill, Inc, third ed., 2003.

[146] M. A. Green and M. J. Keevers, "Optical properties of intrinsic silicon at 300 K," *Progress in photovotaics: research and applications*, vol. 3, no. 3, pp. 189 – 192, 1995.

[147] G. S. Kousik, Z. G. Ling, and P. K. Ajmera, "Nondestructive technique to measure bulk lifetime and surface recombination velocities at the two surfaces by infrared absoprtion due to pulsed optical excitation," *Journal of Applied Physics*, vol. 72, no. 1, pp. 141 – 146, 1992.

[148] L. Sirleto, A. Irace, G. Vitale, L. Zeni, and A. Cutolo, "All-optical mulitwavelength technique for the simultaneous measurement of bulk recombination lifetimes and front/rear surface recombination velocity in single crystal silicon samples," *Journal of Applied Physics*, vol. 93, no. 6, pp. 3407 – 3413, 2003.

[149] A. Buczkowski, Z. J. Radzimski, G. A. Rozgonyi, and F. Shimura, "Bulk and surface components of recombination lifetime based on a two-laser microwave reflection technique," *Journal of Applied Physics*, vol. 69, no. 9, pp. 6495 – 6499, 1991.

[150] L. Sirleto, A. Irace, G. Vitale, L. Zeni, and A. Cutolo, "Separation of bulk lifetime and surface recombination velocity obtained by transverse optical probing and multi-wavelength technique," *Optics and Lasers in engineering*, vol. 38, pp. 461 – 472, 2002.

[151] Z. G. Ling and P. K. Ajmera, "Measurement of bulk lifetime and surface recombination velocity by infrared absoprtion due to pulsed optical excitation," *Journal of Applied Physics*, vol. 69, no. 1, pp. 519 –521, 1991.

[152] Z. G. Ling, P. K. Ajmera, and G. S. Kousik, "Simultaneous extraction of bulk lifetime and surface recombination velocities from free carrier absorption transients," *Journal of Applied Physics*, vol. 75, no. 5, pp. 2718 – 2720, 1994.

[153] R. Gary, J.-D. Arnould, and A. Vilcot, "Semi-analytical modeling and analysis in 3-dimensions of the optical carriers injection and diffusion

in a semiconductor substrate," *IEEE Journal of Lightwave technology*, vol. 24, no. 5, pp. 2163 – 2170, 2006.

[154] H. Gross, W. Singer, and M. Totzeck, eds., *Handbook of Optical Systems: Physical Image Formation*, vol. 2. Wiley, 2005.

[155] R. Gary, J.-D. Arnould, A. Perron, G. Pananakakis, and A. Vilcot, "Fast modeling of 3D-optical carriers injection and permittivity in semiconductor substrate," *International topical meeting on microwave photonics*, vol. 1, pp. 169 – 172, 2005.

[156] R. Gary, J.-D. Arnould, G. Pananakakis, and A. Vilcot, "3-dimensional anaylitical modelling of the optical carriers injection in a semiconductor substrate," *IEEE International symposium on microwave, antenna, propagation and EMC technologies for wireless communications*, vol. 1, pp. 462 – 465, 2005.

[157] M. Guizar-Sicairos and J. C. Gutierrez-Vega, "Computation of qausi-discrete Hankel transforms of integer order for propagating optical wave fields," *Journal of the Optical Society of America*, vol. 21, no. 1, pp. 53 – 58, 2004.

[158] T. M. Pritchett, "Fast Hankel transform algorithms for optical beam propagation," Tech. Rep. ARL-TR-2492, Army Research Laboratory, December 2001.

[159] J. A. Ferrari, D. Perciante, and A. Dubra, "Fast Hankel transform of nth order," *Journal of the Optical Society of America A*, vol. 16, no. 10, pp. 2581 – 2582, 1999.

[160] D. C. Perciante and J. A. Ferrari, "Fast Hankel transform of nth order with improved performance," *Journal of the Optical Society of America A*, vol. 21, no. 9, pp. 1811 – 1812, 2004.

[161] J. I. Pankove, *Optical Processes in Semiconductors*. Dover Publications, 1975.

[162] A. G. Aberle, "Surface passivation of crystalline silicon solar cells: a review," *Progress in photovotaics: research and applications*, vol. 8, pp. 473 – 487, 2000.

[163] J. Y. Lee, *Rapid thermal processing of silicon solar cells - passivation and diffusion*. PhD thesis, Institute for solar energy (ISE), 2003.

[164] M. Schøfthaler, R. Brendel, G. Langguth, and J. H. Werner, "High-quality surface passivation by corona-charged oxides for semiconductor surface characterization," *24th IEEE Photovoltaic specialists conference: Photovoltaic Energy Conversion*, vol. 2, pp. 1509 – 1512, 1994.

[165] E. Yablonovitch, D. L. Allara, C. C. Change, T. Gmitter, and T. B. Bright, "Unusually low surface-recombination velocity on silicon and germanium surfaces," *Physical review letters*, vol. 57, no. 2, pp. 249 – 252, 1986.

[166] I. Marin, M. Vetter, M. Garin, A. Orpella, C. Voz, J. Puigdollers, and R. Alcubilla, "Crystalline silicon surface passivation with amorphous $\mathrm{SiC_x : H}$ films deposited by plasma-enhanced chemical-vapour deposition," *Journal of Applied Physics*, vol. 98, no. 114912, pp. 114912–1 – 114912–10, 2005.

[167] S. Glunz, M. Hofmann, T. Roth, and G. Willeke, "Surface passivation of silicon solar cells using amorphous silicon carbide layers," *4th World conference on photovoltaic energy conversion*, pp. 1016 – 1019, 2006.

[168] A. B. Sieval, C. L. Huisman, A. Schønecker, F. M. Schuurmans, A. S. H. van der Heide, A. Goossens, W. C. Sinke, H. Zuilhof, and E. J. R. Sudhølter, "Silicon surface passivation by organic monolayers: minority charge carrier lifetime measurements and Kelvin probe investigations," *Journal of Physical chemistry B*, vol. 107, pp. 6846 – 6852, 2003.

[169] N. S. Lewis and W. J. Royea, "Electrical passivation of silicon-containing surfaces using organic layers." US Patent: No. 7564120, September 2009.

[170] S. Avasthi, G. Vertelov, J. Schwartz, and J. C. Sturm, "Reduction of minority carrier recombination at silicon surfaces and contacts using organic heterojunctions," *34th IEEE PVSC Conference, Philadelphia*, pp. 001681 – 001685, 2009.

[171] S. Avasthi, Y. Qi, G. K. Vertelov, J. Schwartz, A. Kahn, and J. C. Sturm, "Silicon surface passivation by an organic overlayer of 9,10-phenanthrenequinone," *Applied physics letters*, vol. 96, no. 222109, pp. 222109–1 – 222109–3, 2010.

[172] A. G. Aberle and R. Hezel, "Progress in low-temperature surface passivation of silicon solar cells using remote-plasma silicon nitride," *Progress in photovotaics: research and applications*, vol. 5, pp. 29 – 50, 1997.

[173] A. G. Aberle, S. Glunz, and W. Warta, "Impact of illuminaiton level and oxide parameters on shockley-read-hall recombination at the $\mathrm{Si} - \mathrm{SiO_2}$ interface," *Journal of Applied Physics*, vol. 71, no. 9, pp. 4422 – 4431, 1992.

[174] J. Brody and A. Rohatgi, "Comparison of dielectric surface passivation of monocrystalline and multicrystalline silicon," *29th IEEE Photovoltaic specialists conference*, vol. 1, pp. 243 – 246, 2002.

[175] M. J. Kerr and A. Cuevas, "Very low bulk and surface recombination in oxidized silicon wafers," *Semiconductor science and technology*, vol. 17, pp. 35 – 38, 2002.

[176] N. E. Grant and K. R. McIntosh, "Surface passivation attained by silicon dioxide grown at low temperature in nitric acid," *24th IEEE Photovoltaic specialists conference: Solar Energy Conversion*, pp. 1676 – 1679, 2009.

[177] R. Hezel and R. Schørner, "Plasma si nitride – a promising dielectric to achieve high quality silicon mis/il solar cells," *Journal of Applied Physics*, vol. 52, no. 4, pp. 3076 – 3079, 1981.

[178] W. Soppe, H. Rieffe, and A. Weeber, "Bulk and surface passivation of silicon solar cells accomplished by silicon nitride deposited on industrial scale by microwave PECVD," *Progress in photovotaics: research and applications*, vol. 13, pp. 551 – 569, 2005.

[179] M. J. Kerr and A. Cuevas, "Recombination at the interface between silicon and stoichiometric plasma silicon nitride," *Semiconductor science and technology*, vol. 17, pp. 166 – 172, 2002.

[180] T. Lauinger, J. Schmidt, A. G. Aberle, and R. Hezel, "Record low surface recombination velocity on $1\ \Omega\mathrm{cm}$ p-silicon using remote plasma silicon nitride passivation," *Applied physics letters*, vol. 68, no. 9, pp. 1232 – 1234, 1996.

[181] H. Mackel and R. Ludemann, "Detailed study of the composisition of hydrogenated $\mathrm{sin_x}$ layers for high-quality silicon surface passivation," *Journal of Applied Physics*, vol. 92, no. 5, pp. 2602 – 2609, 2002.

[182] K. J. Weber and H. Jin, "Improved silicon surface passivation achieved by negatively charged silicon nitride films," *Applied physics letters*, vol. 94, no. 063509, pp. 1 – 3, 2009.

[183] A. G. Aberle, *Crystalline silicon solar cells – advanced surface passivation and analysis*. Centre for photovoltaic engineering, university of New Sout Wales, Austraila, 1999.

[184] C. Li, B. Sopori, P. Rupnowski, A. T. Fiory, and N. M. Ravindra, "Surface and bulk passivation layer of silicon nitride for solar cell applications." web: www.njit.edu, 2005.

[185] J. Schmidt, M. J. Kerr, and A. Cuevas, "Surface passivation of silicon solar cells using plasma-enchanced chemical-vapour-deposited sin films and thin thermal $\mathrm{sio_2}$/plasma sin stacks," *Semiconductor science and technology*, vol. 16, pp. 164 – 170, 2001.

[186] K. Koyama, K. Ohdaira, and H. Matsumura, "Extremely low surface recombination velocities on crystalline silicon wafers realized by catalytic

chemical vapor deposited $\mathrm{sin_x}$/a-si stacked passivation layers," *Applied physics letters*, vol. 97, no. 082108, pp. 082108–1 – 082108–3, 2010.

[187] Y. Larionova, V. Mertens, N.-P. Harder, and R. Brendel, "Surface passivation of n-type czochralski silicon substrates by thermal-$\mathrm{sio_2}$/plasma-enhanced chemical vapor deposition sin stacks," *Applied physics letters*, vol. 96, no. 032105, pp. 032105–1 – 032105–3, 2010.

[188] C. Leguijt, P. Lolgen, J. A. Eikelboom, A. W. Weeber, F. M. Schuurmans, W. C. Sinke, P. F. A. Alkemade, P. M. Sarro, C. H. M. Maree, and L. A. Verhoef, "Low temperature surface passivation for silicon solar cells," *Solar energy materials and solar cells*, vol. 40, pp. 297 – 345, 1996.

[189] M. McCann, K. Weber, and A. Blakers, "Surface passivation by rehydrogenation of silicon-nitride-coated silicon wafers," *Progress in photovotaics: research and applications*, vol. 13, pp. 195 – 200, 2005.

[190] S. Dauwe, J. Schmidt, and R. Hezel, "Very low surface recombination velocities on p- and n-type silicon wafers passivated with hydrogenated amorphous silicon films," *29th IEEE Photovoltaic specialists conference*, pp. 1246 – 1249, 2002.

[191] M. Hofmann, S. Glunz, R. Preu, and G. Willeke, "21% efficient silicon solar cells using amorphous silicon rear side passivation," *21st European photovoltaic solar energy conference*, pp. 609 – 612, 2006.

[192] J.-W. A. Schuttauf, K. H. M. van der Werf, and I. M. Kielen, "Excellent crystalline silicon surface passivation by amorphous silicon irrespective of the technique used for chemical vapour deposition," *Applied physics letters*, vol. 98, no. 153514, pp. 153514–1 – 153514–3, 2011.

[193] T. F. Schulze, H. N. Beushausen, C. Leendertz, A. Dobrich, B. Rech, and L. Korte, "Interplay of amorphous silicon disorder and hydrogen content with interface defects in amorphous/crystalline silicon heterojunctions," *Applied physics letters*, vol. 96, no. 252102, 2010.

[194] S. de Wolf, S. Olibet, and C. Balif, "Stretched-exponential a-si:h/c-si interface recombination decay," *Applied physics letters*, vol. 93, no. 032101, 2008.

[195] B. Hoex, S. B. S. Heil, E. Langereis, M. C. M. van de Sanden, and W. M. M. Kessels, "Ultralow surface recombination of c-Si substrates passivated by plasma-assisted atomic layer deposited $\mathrm{Al_2O_3}$," *Applied physics letters*, vol. 89, no. 042112, pp. 042112–1 – 042112–3, 2006.

[196] A. Focsa, A. Slaoui, H. Charifi, J. P. Stoquert, and S. Roques, "Surface passivation at low temperature of p- and n-type silicon wafers using a double layer a-si:h/sinx:h," *Materials Science and Engineering B*, vol. 159 - 160, pp. 242 – 247, 2009.

[197] R. R. King, R. A. Sinton, and R. M. Swanson, "Front and back surface fields for point-contact solar cells," *20th IEEE Photovoltaic specialists conference*, vol. 1, pp. 538 – 544, 1988.

[198] J. Zhao, A. Wang, and M. A. Green, "24.5% efficiency PERT silicon solar cells on SEH MCZ substrates and cell performance on other SEH CZ and FZ substrates," *Solar energy materials and solar cells*, vol. 6, pp. 27 – 36, 2001.

[199] B. Hoex, J. Schmidt, R. Bock, P. P. Altermatt, M. C. M. van de Sanden, and W. M. M. Kessels, "Excellent passivation of highly doped p-type Si surfaces by the negative-charge-dielectric $\mathrm{Al_2O_3}$," *Applied physics letters*, vol. 91, no. 112107, pp. 112107–1 – 112107–3, 2007.

[200] S. Glunz, "High-efficiency crystalline silicon solar cells," in *Advances in Optoelectronics*, Hindawi publishing corporation, 2007.

[201] B. Hoex, J. Schmidt, P. Pohl, M. C. M. van de Sanden, and W. M. M. Kessels, "Silicon surface passivation by atomic layer deposited $\mathrm{Al_2O_3}$," *Journal of Applied Physics*, vol. 104, no. 044903, pp. 044903–1 – 044903–12, 2008.

[202] J. Schmidt, A. Merkle, R. Bock, P. P. Altermatt, and A. Cuevas, "Progress in the surface passivation of silicon solar cells," *23rd European Photovoltaic solar energy conference*, pp. 974 –981, 2008.

[203] G. Dingemans and W. M. M. Kessels, "Recent progress in the development and understanding of silicon surface passivation by aluminium oxide for photovoltaics," *25th European Photovoltaic solar energy conference*, vol. 1, pp. 1083 – 1090, 2010.

[204] J. Schmidt, A. Merkle, R. Bock, P. P. Altermatt, A. Cuevas, N.-P. Harder, B. Hoex, R. van de Sanden, E. Kessels, and R. Brendel, "Progress in th surface passivation of silicon solar cells," *23rd European solar energy conference*, 2008.

[205] B. Veith, F. Werner, D. Zielke, R. Brendel, and J. Schmidt, "Comparison of the thermal stability of single $\mathrm{Al_2O_3}$ layers and $\mathrm{Al_2O_3/SiN_x}$ stacks for the surface passivation of silicon," *SiliconPV: Energy procedia 8*, pp. 307 – 312, 2011.

[206] P. A. Basore and B. R. Hansen, "Microwave-detected photoconductance decay," *Photovoltaic specialists conference*, vol. 1, pp. 374 – 379, May 1990.

[207] M. Schofthaler and R. Brendel, "Sensitivity and transient response of microwave reflection measurements," *Journal of Applied Physics*, vol. 77, pp. 3162 – 3173, April 1994.

[208] Kunst, M. and Beck, G., "The study of charge carrier kinetics in semiconductors by microwave conductivity measurements," *Journal of Applied Physics*, vol. 60, no. 10, pp. 3558 – 3566, 1986.

[209] Kunst, M. and Beck, G., "The study of charge carrier kinetics in semiconductors by microwave conductivity measurements. II.," *Journal of Applied Physics*, vol. 63, no. 4, pp. 1093 – 1098, 1986.

[210] C. Swiatkowski, A. Sanders, K.-D. Buhre, and M. Kunst, "Charge-carrier kinetics in semiconductors by microwave conductivity measure-

ments," *Journal of Applied Physics*, vol. 78, no. 3, pp. 1763 – 1775, 1995.

[211] D. Klein, F. Wuensch, and M. Kunst, "The determination of charge-carrier lifetime in silicon," *Physics Status Solidi b*, vol. 245, no. 9, pp. 1865 – 1876, 2008.

[212] E. Gaubas and A. Kaniava, "Determination of recombination parameters in silicon wafers by transient microwave absorption," *Rev. Sci. Instrum.*, vol. 67, no. 6, pp. 2339 –2345, 1996.

[213] K. Lauer, A. Laades, H. Ubensee, H. Metzner, and A. Lawerenz, "Detailed analysis of the microwave-detected photoconductance decay in crystalline silicon," *Journal of Applied Physics*, vol. 104, no. 104503, 2008.

[214] N. Derhacobian, J. T. Walton, P. N. Luke, Y. K. Wong, and C. S. Rossington, "Proper interpretation of photoconductive decay transients in semiconductors having finite surface recombination velocity," *Journal of Applied Physics*, vol. 76, no. 8, pp. 4663 – 4669, 1994.

[215] R. A. Sinton, A. Cuevas, and M. Stuckings, "Quasi-steady-state photoconductance, a new method for solar cell material device characterization," *25th IEEE photovoltaic specialists conference*, pp. 457 – 460, 1996.

[216] J. Schmidt, "Measurement of differential and actual recombination parameters on crystalline silicon wafers," *IEEE Transactions on Electron Devices*, vol. 46, no. 10, pp. 2018 – 2025, 1999.

[217] "http://www.topsil.com." TOPSiL Semiconductor Materials A/S.

[218] "Private converstaions with Rune Søndenå, IFE, Norway.."

[219] W. Culshaw, "The Fabry-Perot interferometer at millimetre wavelengths," *Proceedings of the Physical Society B*, vol. 66, no. 7, pp. 597 – 608, 1953.

[220] W. Culshaw, "High resolution millimeter wave Fabry-Perot interferometer," *IRE Transactions on Microwave Theory and Techniques*, vol. 8, no. 2, pp. 182 – 189, 1959.

[221] D. K. Ghodgaonkar, V. V. Varadan, and V. K. Varadan, "Free-space measurement of complex permittivity and complex permeability of magnetic materials at microwave frequencies," *IEEE Transactions on Instrumentation and Measurement*, vol. 39, no. 2, pp. 387 – 394, 1990.

[222] J. D. Kraus, *Electromagnetics*. Electrical Engineering, McGraw-Hill International Edition, fourth ed., 1991.

[223] D. J. Griffiths, *Introduction to Electrodynamics*. Prentice Hall International, Inc, third ed., 1999.

[224] F. Stern, *Solid state physics: advances in research and applications*, vol. 15 of *Solid State Physics*, ch. Elementary Theory of the Optical Properties of Solids. Academic Press, 1963.

[225] A. M. Fox, *Optical Properties of Solids*. Oxford Master Series in Condensed Matter Physics, Oxford University Press, 2003.

[226] P. Y. Yu and M. Cardona, *Fundamentals of Semiconductors*. Physics and Materials Properties, Springer Berlin Heidelberg, fourth ed., 2010.

[227] M. S. Dresselhaus, "Solid state physics pt. 2: Optical properties of solids." Lecture series - Massachusetts Institue of Technology (MIT), 2001.

[228] A. M. Yurek, C. D. Striffler, and C. H. Lee, "Optoelectronic devices for millimeter waves," in *Infrared and Millimeter waves* (K. J. Button, ed.), vol. 14 of *Millimeter components and techniques, part V*, pp. 249 – 290, Academic Press, 1985.

[229] B. C. Wadell, *Transmission Line Design Handbook*. Artech House, 1991.

[230] L. J. Peter Linnér, "Exact formulas for wave impedance and propagation constants of homogeneous, lossy dielectric and/or magnetic materials," *IEEE Transactions on Antennas and Propagation*, vol. 37, no. 3, pp. 410 – 411, 1989.

[231] D. G. Macfarlane, *Close range passive millimetre wave imaging*. PhD thesis, University of St Andrews, 2002.

[232] G. W. Webb, "Millimeter wave beam deflector." Int. Patent: No. WO 93/26059, 1993.

[233] G. W. Webb, "Millimeter wave beam deflector." US Patent: No. 5360973, November 1994.

[234] G. W. Webb and S. Angello, "Plasma controlled antenna." US Patent: No. 0140624, October 2002.

[235] G. W. Webb and S. G. Angello, "Plasma controlled antenna." US Patent: No. 6621459, September 2003.

[236] M. Hajian, G. A. de Vree, and L. P. Ligthart, "Electromagnetic analysis of beam-scanning antenna at millimeter-wave band based on photoconductivity using Fresnel-zone plate technique," *IEEE Antennas and Propagation Magazine*, vol. 45, no. 5, pp. 13 – 25, 2003.

[237] B. J. Reits, "Adjustable microwave antenna." US Patent: No. 5736966, April 1998.

[238] Y. J. Guo, I. H. Sassi, and S. K. Barton, "Offset Frensel lens antenna," *IEEE Proceedings - Microwaves, Antennas and Propagation*, vol. 141, no. 6, pp. 517 – 522, 1994.

[239] Y. J. Guo and S. K. Barton, "Offset Fresnel zone plate antennas," *International Journal of Satellite Communications*, vol. 12, pp. 381 – 385, 1994.

[240] J. M. van Houten and M. H. A. J. Herben, "The elliptical Fresnel zone plate antenna," *Ninth International Conference on Antennas and Propagation (ICAP)*, no. CP407, pp. 97 – 101, 1995.

[241] "National Instruments LabWindows, CVI." http://www.ni.com.

[242] Z.-G. Ke, X.-J. Zhou, Z.-G. Zhang, Z.-Y. Zhang, and D. Liu, "Optically controlled frensel zone plate scanning antenna," *Chinese Infrared Montly (in Chinese)*, vol. 31, no. 5, pp. 23 – 27, 2010.

[243] D. G. Macfarlane and D. A. Robertson, "SAFIRE: A real time close range millimetre wave exhibition radar," *35th International Conference on Infrared Millimeter and Terahertz Waves (IRMMW-THz)*, vol. 1, pp. 1 – 2, 2010.

[244] L. Cabria, J. A. Garcia, J. Gutierrez-Rios, A. Tazon, and J. Vassal'lo, "Active reflectors: Possible solutions based on reflectarrays and fresnel reflectors," *International Journal of Antennas and Propagation*, vol. 2009, no. 653952, 2009.

[245] J. Gutierrez-Rios and J. V. Sanz, "Algorithms for synthesis of radiation patterns using reconfigurable reflectors," *3rd European Conference on Antennas and Propagation*, pp. 3024 – 3028, March 2009.

[246] E. Hecht, *Optics*. Addison Wesley, third ed., 1998.

[247] G. W. Webb, "New variable for Fresnel zone plate antennas," in *Proceedings of the 2003 Antenna Applications Symposium*, vol. 1, pp. 92 – 106, 2003.

[248] I. V. Minin and O. V. Minin, "Control of focusing properties of diffraction elements," *Sov. J. Quantum Electron*, vol. 20, no. 2, pp. 198 – 199, 1990.

[249] W. X. Zhang, "An improved zoning rule of the Fresnel zone plate," *Microwave and Optical Technology Letters*, vol. 23, no. 2, pp. 69 – 73, 1999.

[250] I. V. Minin and O. V. Minin, "Reference phase in diffractive lens antennas: A review," *Journal of Infrared, Millimetre, and Terahertz waves*, vol. 32, no. 6, pp. 801 – 822, 2011.

[251] G. W. Webb, "Reference phase of Fresnel zone plates," *ArXiv physics e-prints*, arXiv:physics/0303002, 2003.

[252] S. M. Stout-Grandy, A. Petosa, I. V. Minin, O. V. Minin, and J. Wight, "A systematic study of varying reference phase in the design of circular Fresnel zone plate antennas," *IEEE Transactions on Antennas and Propagation*, vol. 54, no. 12, pp. 3629 – 3637, 2006.

[253] I. Minin, O. Minin, and G. Webb, "Flat and conformal zone plate antennas with new capabilities," *2005 18th International Conference on Applied Electromagnetics and Communications*, vol. 2, pp. 1–4, 2005.

[254] G. Webb, I. V. Minin, and O. V. Minin, "Variable reference phase in diffractive antennas: Review, applications, new results," *IEEE Antennas and Propagation Magazine*, vol. 53, no. 2, pp. 77 – 94, 2011.

[255] G. W. Webb, "Technologies of millimeter-wave road-vehicle and vehicle-vehicle communications," *Infrared Millimeter waves and 14th International Conference on Terahertz electronics*, p. 357, 2006.

[256] G. W. Webb, I. V. Minin, and O. V. Minin, "Eliminating multipath fading improves wireless signal reception," *International Society for Optical Engineering*, vol. SPIE Newsroom, August 2006.

[257] S. M. Stout-Grandy, A. Petosa, I. V. Minin, I. V. Minin, and J. Wight, "Recent advances in Fresnel zone plate antenna technology," *Microwave Journal*, March 2008.